

Biochemical Sensing
based on
Metal–Organic Architectures

INAUGURALDISSERTATION

zur
Erlangung der Würde eines Doktors der Philosophie
vorgelegt der
Philosophisch-Naturwissenschaftlichen Fakultät
der Universität Basel

von

Lars Lüder

Basel, 2023

Genehmigt von der Philosophisch-Naturwissenschaftlichen Fakultät
auf Antrag von

Prof. Dr. Michel Calame

Prof. Dr. Marcel Mayor

Prof. Dr. Wendy L. Queen

Basel, den 18.10.2022

Prof. Dr. Marcel Mayor
Dekan

Contents

| | | |
|----------|--|-----------|
| 1 | Introduction | 1 |
| 2 | Metal–organic frameworks | 5 |
| 2.1 | Introduction to MOFs | 6 |
| 2.2 | Chemical Structure | 6 |
| 2.3 | Material properties of MOFs | 8 |
| 2.3.1 | Nanoporosity | 8 |
| 2.3.2 | Chemical functionality of the framework | 9 |
| 2.3.3 | Intrinsic conductivity | 9 |
| 2.3.4 | Optical, magnetic and soft mechanical properties | 14 |
| 2.4 | Applications of MOFs | 15 |
| 2.5 | Outlook and future approaches | 16 |
| 3 | Sensing approaches based on MOFs | 19 |
| 3.1 | Basics of sensing | 20 |
| 3.2 | MOF-based sensing | 23 |
| 3.3 | Signal transduction | 24 |
| 3.3.1 | Non-electrical signal transduction | 25 |
| 3.3.2 | Electrical signal transduction | 26 |
| 3.4 | MOFs for biosensing purposes | 28 |
| 3.5 | Outlook | 30 |
| 4 | Characterization techniques | 31 |
| 4.1 | Raman spectroscopy | 32 |
| 4.2 | Scanning electron microscopy | 36 |
| 4.2.1 | Energy dispersive X-ray spectroscopy | 38 |
| 4.3 | X-ray diffraction | 39 |
| 4.3.1 | Grazing-incidence small-angle X-ray scattering | 41 |
| 4.4 | Atomic force microscopy | 41 |
| 4.5 | Gas adsorption | 43 |
| 4.6 | Concluding remarks | 46 |
| 5 | Design, synthesis and characterization of conductive MOFs for sensing | 47 |
| 5.1 | Introduction | 48 |
| 5.2 | Synthesis approach | 49 |

| | | |
|----------|---|------------|
| 5.3 | Structural characterization | 50 |
| 5.4 | Chemical characterization | 55 |
| 5.5 | Electrical characterization | 59 |
| 5.6 | Conclusion and Outlook | 63 |
| 5.A | Supporting Information | 65 |
| 5.A.1 | Additional Figures | 65 |
| 5.A.2 | Measurement details and parameters | 68 |
| 6 | MOF-particle integration into fibrous layers for wearables | 71 |
| 6.1 | Introduction | 72 |
| 6.2 | Fabrication approach | 73 |
| 6.3 | Characterization of MOF@NC layers | 74 |
| 6.4 | Raman spectroscopy | 79 |
| 6.5 | Sensing experiments | 83 |
| 6.6 | Conclusion and Outlook | 93 |
| 6.A | Supporting Information | 94 |
| 6.A.1 | Additional Figures | 94 |
| 6.A.2 | Measurement details and parameters | 100 |
| 7 | Exploiting MOFs towards protein sensing in body fluids | 101 |
| 7.1 | Introduction | 102 |
| 7.2 | Cerebrospinal fluid analytics | 103 |
| 7.3 | MOF-based protein analytics | 109 |
| 7.4 | Conclusion and Outlook | 111 |
| 7.A | Supporting Information | 113 |
| 7.A.1 | Additional Figures | 113 |
| 7.A.2 | Measurement details and parameters | 115 |
| 8 | Conclusion and Outlook | 117 |
| | References | 123 |
| A | Fabrication recipes | 147 |
| A.1 | Synthesis of Cu-HHTP-TCNQ films | 147 |
| A.2 | Fabrication of glass chips with gold electrodes | 148 |
| A.3 | Electrospraying of MOF particles | 149 |
| A.4 | Electrospinning of nitrocellulose | 149 |

| | |
|---------------------------------------|------------|
| Curriculum Vitae | 151 |
| List of Publications | 152 |
| Acknowledgements | 155 |

CHAPTER 1

Introduction



This research work is about the use of metal–organic architectures as a platform for biochemical sensing purposes.

The following chapter provides an overview of the subject area and relevance of this work and introduces the reader to the content of this thesis.

In today's life, the sensing of biochemical and physiological parameters in humans plays an increasingly important role in healthcare, as the monitoring of vital indicators and metabolic products enables the creation of health profiles of the individual.¹⁻³ For instance, screening and monitoring of target analytes in body fluids such as sweat, breath and saliva allow conclusions to be drawn about fitness and health status by measuring changes in the analyte concentration.^{4,5} The comprehensive collection of physiological data can thus improve disease diagnosis and create personalized healthcare solutions such as treatment tailored to the person, thereby improving the patient's quality of life.⁶

In general, human body fluids are rich in diverse biomarkers, i.e. analytes that reflect specific processes in the body and thus indicate a person's condition. Blood is the hallmark example of clinical health assessment, but it requires an invasive procedure for blood collection, which is why noninvasive alternatives are readily used when possible.^{7,8} For example, it is no longer necessary for diabetic patients to take blood several times a day to measure glucose levels, as nowadays glucose levels can also be determined from saliva, tears or sweat.^{9,10} Sweat alone provides a lot of information about biochemical relations, since it contains numerous metabolites (e.g. glucose and lactate), electrolytes (e.g. sodium chloride and potassium chloride), and other molecules with biological relevance (e.g. proteins and peptides).^{11,12}

As a result, there is an increasing demand for wearable sensors that can be used for health monitoring and fitness tracking in everyday life. This need is also reflected in the rapidly growing global market for wearable sensors, which is expected to be worth \$2.86 billion by 2025.^{1,13} A variety of innovative wearable sensors have already been tested and applied to different body fluids, such as smart wound dressings to monitor the wound healing process,^{14,15} mouthguards for sensing metabolites in saliva¹⁶ and wearable sweat bands to track the level of medication in the body (for example Levodopa for Parkinson's disease patients).¹⁷ An overview of examples of modern wearable sensors is shown in Figure 1.1a.

The ultimate future goal would be a wearable sensor that continuously detects and monitors noninvasively a wide range of biochemical analytes of interest on the body, allowing for the prompt identification of unhealthy conditions and medical assessment. Besides analysis of body fluids, the sensing of environmental conditions such as levels of harmful chemicals or particles in the air can also be an important aspect in the prediction and prevention of diseases.^{18,19} However, there are many challenges to overcome before such a sensor can be used in practice, as

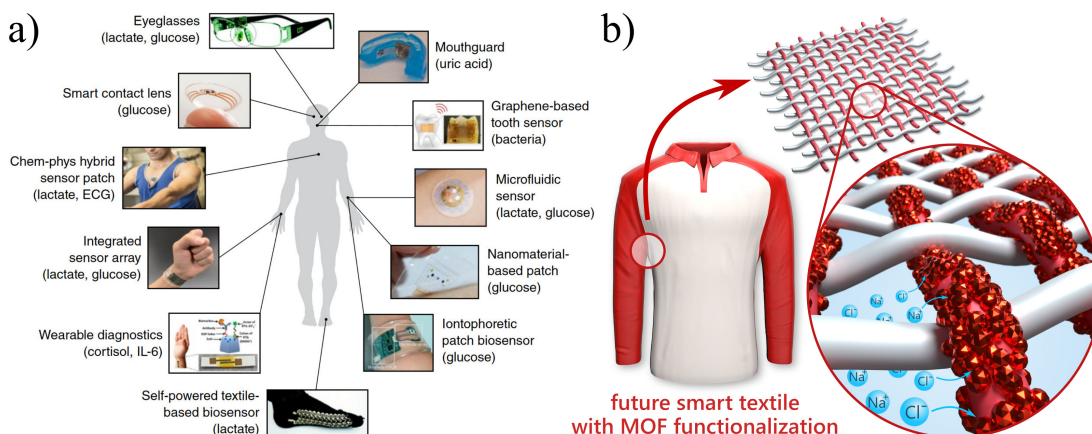


Figure 1.1: a) Examples of modern wearable sensors for noninvasive monitoring of biochemical analytes in various body fluids; reproduced from Kim et al.¹ b) Future vision of a textile-integrated MOF-sensor for monitoring health indicators in the wearer's daily life.

most examples at this stage represent more of a proof of concept. For instance, the sensing material should be easily integrable, while exhibiting high sensitivity and selectivity to a variety of target analytes.²⁰ Such requirements could be met by novel nanomaterials and nanocomposites.^{20,21}

An example in this context is the relatively new class of nanoporous materials called metal-organic frameworks (MOFs).^{22,23} MOFs exhibit extremely large surface areas and enormous porosities, which allow efficient uptake of analytes similar to a sponge.^{24,25} In addition, their material properties such as pore size, electrical conductivity or chemical functionality can be customized, making MOFs highly versatile in their application.²⁶⁻²⁸ These outstanding features render this type of material a promising candidate for diverse sensing applications.

The objective of this project is to explore the versatility of MOFs as sensing material, with the ultimate goal of integrating them into textiles in the context of personalized and remote health monitoring (Figure 1.1b). Several approaches using different metal-organic architectures for biochemical sensing are covered in this work. We present the synthesis and structural characteristics of a new hybrid MOF film that is electrically conductive and exhibits chemiresistive behavior to environmental changes. These properties are demonstrated even though the film lacks long-range crystalline ordering, which has the potential to be an advantage when integrated into flexible systems. Furthermore, we design and apply an integration process for MOF particles into fibrous polymer layers to fabricate MOF-containing flexible membranes. These membranes are examined for their

sensing ability of several sweat biomarkers using optical spectroscopy. In addition, we investigate the potential of the fabricated MOF platform for protein sensing by initial tests with amyloid proteins in cerebrospinal fluid, exploring the possibility of diagnosing neurodegenerative diseases in the future.

Dissertation outline

Following this introduction, Chapter 2 presents the material class of metal–organic frameworks and explains their basic structure, unique properties and fields of applications.

Chapter 3 covers the fundamentals of sensing and signal transduction and goes into detail about approaches for biochemical sensing based on MOFs.

In Chapter 4, the main characterization techniques that will occur in this work are depicted. In this context, the operating principles of the techniques are described and reference is made to the study of MOFs.

Next, Chapter 5 investigates a conductive MOF film with low crystalline order as a chemiresistive sensing material. This includes the synthesis of the hybrid MOF, the detailed characterization of the structural and electrical properties of the MOF film by various methods and the demonstration of its chemiresistive response to ambient changes.

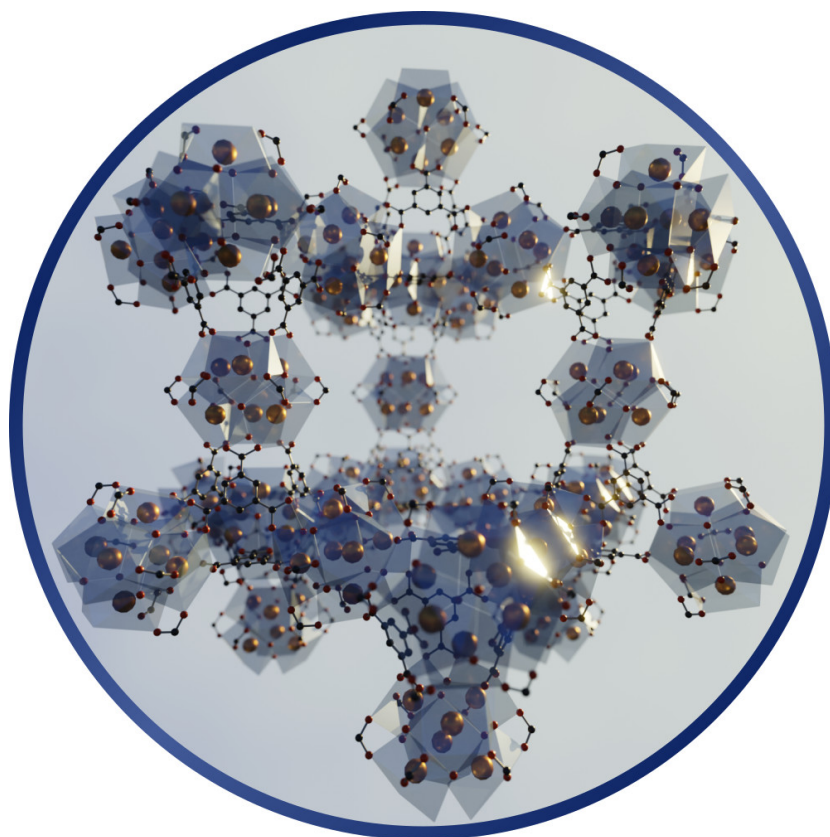
Chapter 6 focuses on the integration of MOF particles into a polymer membrane and evaluates its sensing ability of sweat biomarkers. In the investigation process to realize a MOF-based wearable sensor membrane, the integration process was developed using electrospraying and electrospinning, and Raman spectroscopy is used as sensing tool to study the spectral changes after the addition of the biomarkers NaCl, KCl and pyocyanin.

In Chapter 7, the possibilities of using MOFs for protein sensing are explored on the example of amyloid proteins in cerebrospinal fluid. Samples of cerebrospinal fluid from patients with Alzheimer pathology are examined for their morphological and chemical properties and the spectral differences of the previously presented MOF membranes are investigated after treatment with the samples and reference solutions.

Finally, Chapter 8 summarizes the main findings of the work and provides an outlook on possible future projects.

Furthermore, the interested reader will find supplementary information such as fabrication parameters and purchasing details in Appendix A.

Metal–organic frameworks



Metal–organic frameworks are an emerging class of materials in the field of coordination chemistry with unique physical, chemical and electronic properties that can be exploited in many fields ranging from catalysis to biochemical sensing. Their versatility makes them increasingly important for many applications, however, they are not yet well known beyond the boundaries of science and research. The purpose of this chapter is to give an introduction to metal–organic frameworks and explain their general structure and material properties.

2.1 Introduction to MOFs

Metal-organic frameworks (MOFs) are a class of materials that, as the name suggests, are composed of metal nodes and organic linker molecules to form extended crystalline structures. Similar to a scaffold for renovation works, which consists of individual parts that are assembled in an organized manner to create a large and stable scaffold, MOFs are also constructed from molecular building blocks that are connected by strong bonds such as coordination bonds creating a molecular framework system. This approach is known as reticular chemistry.²⁹

The first reports of MOFs date back to Kinoshita's work in 1959, although they were not yet called MOFs at that time.³⁰ It became quiet around this field for thirty years until Hoskins' and Robson's publication in 1989 elaborated on the idea and design of three-dimensional infinite polymeric frameworks.²² Finally, in 1995, it was Omar M. Yaghi, who synthesized extended coordination networks of $[\text{Cu}(4,4'\text{-bipyridine})_{1.5}](\text{NO}_3)$, coining the label of "metal-organic framework".²³ He became an important pioneer in the field of MOFs and, together with his co-workers, synthesized the first rigid MOFs with permanent porosity only a few years later (1998: MOF-2³¹, 1999: MOF-5³²). This can be regarded as the beginning of a broad research and investigation of this new class of materials.

2.2 Chemical Structure

The approach of reticular chemistry allows the usage of modular building units, which are assembled together to extended and ordered networks (Figure 2.1). The stability of the formed frameworks depends on the molecular units involved and their interaction. For example, basic coordination networks consisting of metal ions linked by neutral organic linkers often require counterions and solvent molecules in the pores to ensure charge neutrality and stability. When the pore filling is removed from such structures, the framework can collapse partially or completely.^{33,34} By using charged organic linkers, the cationic charge from the metal can be balanced, thus eliminating the necessity of counterions in the pores. Another advantage of using charged linkers is an increased framework stability due to higher bond strengths towards the metal nodes.³⁵

Single metal ions as metal nodes are usually accompanied by diverse coordination possibilities to the organic linkers due to different possible coordination numbers and geometries, which can complicate the synthesis control of the resulting MOF. Instead of using single metal ions, metallic node points can also be realized

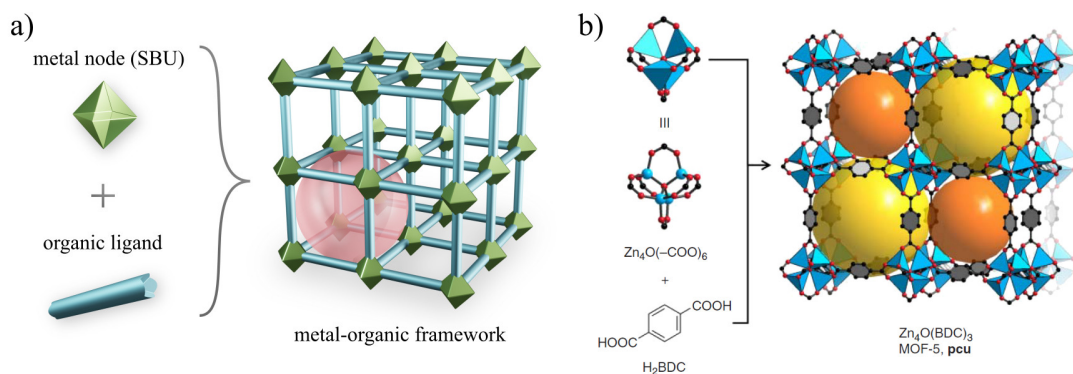


Figure 2.1: a) The general structure of a MOF is based on the coordination between metal node building units and organic linker molecules. The resulting framework architecture is porous with large pore volumes (values up to $5 \text{ cm}^3 \text{ g}^{-1}$ have been demonstrated, being an order of magnitude greater than typical values of zeolites²⁴), as illustrated by the red sphere. b) The 3D-structure of MOF-5, composed of $\text{Zn}_4\text{O}(-\text{COO})_6$ metallic cluster and benzenedicarboxylic acid as organic ligand, with cavities highlighted in yellow and orange; reproduced from Kaskel.³⁶

by poly-nuclear clusters, called secondary building units (SBUs). Originally, the term SBU describes a set of aluminosilicate groups from which zeolites can be constructed. In the context of MOF chemistry, the SBUs refer to the geometry, which is determined by the metallic cluster or rather its connection points (points of extension).^{29,37,38} The use of poly-nuclear clusters with their defined connection points and fixed position of the metal center increases directionality and rigidity and thus robustness of the framework.³⁹ The geometry of the SBU and its coordination environment thus play a key role in the construction of reticular structures. Considering these two concepts, i.e. the use of charged organic linker molecules and SBUs as building units, architecturally stable and robust frameworks can be realized that exhibit permanent porosity, as first demonstrated in 1998 with MOF-2.³¹ A major advantage of this reticular approach, and of MOFs in general, is the rich structural chemistry based on the wide range of possible building units. The structural diversity of SBUs, the many different linkers with variable functional groups and diverse combination possibilities lead to an almost unlimited number of feasible MOFs and framework types, each with individual adjustable properties.

2.3 Material properties of MOFs

2.3.1 Nanoporosity

What MOFs generally have in common in terms of their architecture are very high porosities, which is defined as the ratio of the pore volume to the total volume of the solid (Figure 2.2a). Depending on the MOF structure, there are either uniform pores or voids of different volumes with varying aperture sizes.⁴⁰ The associated large specific surface areas of MOFs thereby exceed that of most porous materials such as zeolites or porous ceramics, sometimes by up to two orders of magnitude.^{41–43} The record to date for the largest surface area of a metal–organic framework is held by DUT-60 with an BET surface area of $7839 \text{ m}^2 \text{ g}^{-1}$.²⁴ For comparison, the standard size of a soccer field is 7140 m^2 . The abbreviation BET stands for the scientists Brunauer, Emmett and Teller, who classified the gas adsorption/desorption isotherms from which surface areas are usually derived.^{44,45} More details about the BET gas adsorption method are given in Chapter 4.5. The high porosities generally give MOFs high uptake capacities, like a sponge but with nanopores. Many different applications are feasible in which guest molecules enter and possibly interact with the MOFs.⁴⁶ NU-1501-M is another MOF that also exhibits a very large BET surface area of $7310 \text{ m}^2 \text{ g}^{-1}$ while having a high volumetric BET area of $2060 \text{ m}^2 \text{ cm}^{-3}$.²⁵ This balance is advantageous, for example, when it comes to gas storage, such as for hydrogen or methane.

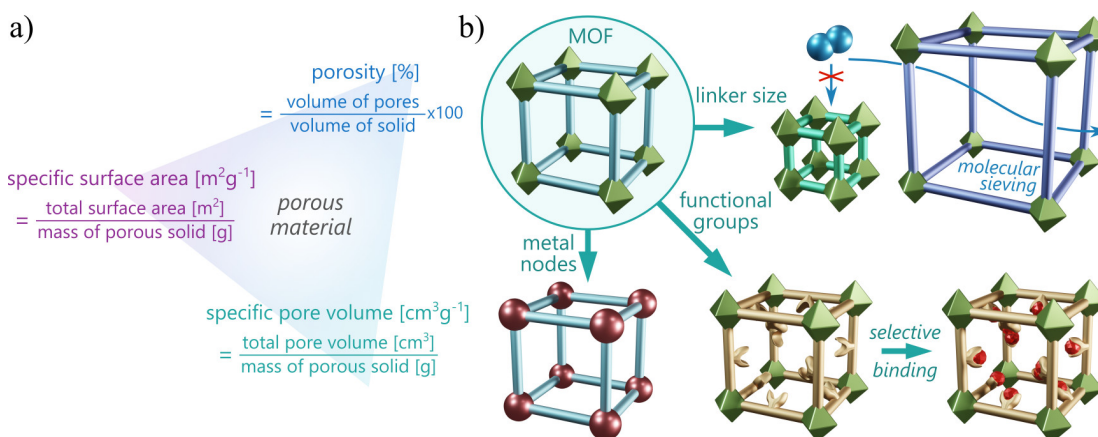


Figure 2.2: a) Porous materials can be described by different parameters, e.g. porosity, specific surface area and specific pore volume. b) The structural versatility of MOFs enables the introduction of functionality through different approaches, such as adjusting the linker size, chemical functionalization or choice of the metal node.

2.3.2 Chemical functionality of the framework

In addition to high porosities, there are further advantages of MOFs, such as their modularity and resulting structural versatility.⁴⁷ Appropriate choice of the building units allows to introduce functionality that can be adapted to a specific situation (Figure 2.2b). For example, by choosing ligands of different lengths, the size of the pores can be scaled, providing selectivity of the MOF towards certain analyte sizes (molecular sieving effect).²⁶

The selectivity of MOFs, that is the ability to differentiate different target analytes, can be realized not only by adjusting the pore size, but also by chemical functionalization. The attachment of different functional groups to the linker molecules changes the local properties of the MOF such as its polar character, Lewis acidity or hydrophobicity/hydrophilicity, which then modifies the individual sorption affinity.^{48,49} Such variation of functional groups may also involve the immobilization of larger molecules with binding sites or chelating function. For instance, it was shown that by grafting ethylenediaminetetraacetic acid (EDTA) into the pores of MOF-808, an efficient trap for the capture of heavy metal ions can be realized.⁵⁰ Further, the introduction of multiple functionalities within a single framework is also possible. "Multivariate MOFs" have already shown improved properties compared to the summarized individual parts.⁵¹

Specific functionality can be introduced into MOFs not only by the ligands but also by appropriate choice of metals. Just as with organic ligands, the different properties of the metal such as the ionic radius, electronic state, or coordination environment, among others, have a direct influence on the properties of the MOF. In the case of open metal coordination sites, an enhanced binding strength to certain molecules, such as nonpolar gases like hydrogen, is evident.⁵² In this aspect, variability in function can again be achieved by mixing several metals (mixed metal MOFs), whereby superior performances can be realized with respect to related single-metal MOFs.⁵³

2.3.3 Intrinsic conductivity

One property to be discussed in more detail here is the electrical conductivity of MOFs. Most MOFs are insulators, meaning there is no or very poor transport of electrical charges through the material. This significantly limits their usability for electronic or electrochemical devices. But in recent years, MOFs have been synthesized that are electrically conductive. By combining the unique properties

of MOFs with electrical conductivity, completely new areas of application emerge such as energy storage,⁵⁴ electrocatalysis⁵⁵ and chemiresistive sensing⁵⁶, which will be discussed later. A part of the research work presented in this thesis also covers the synthesis and characterization of a conductive MOF and the demonstration of its chemiresistive behavior (Chapter 5).⁵⁷

In general, the electrical conductivity σ of a material (unit: S cm^{-1}) depends on the density of charge carriers n (unit: cm^{-3}) and their mobility μ (unit: $\text{cm}^2 \text{V}^{-1} \text{s}^{-1}$) and can be written as

$$\sigma = en\mu \quad (1)$$

where e is the elementary charge ($1.602 \cdot 10^{-19} \text{ C}$). Both, organic ligand and metal ion can be provider of charge carriers. In solids, charge transport can commonly be described by two different transport regimes: hopping transport and band transport.⁵⁸

In hopping transport, the charge carriers are localized at discrete levels and jump from one electronic state to the adjacent electronic state, resulting in net current transport (Figure 2.3a). This type of transport often occurs in amorphous, disordered materials and organic semiconductors.⁵⁹ The hopping probability p between two states with energetic separation E and spatial separation R can be described as follows:^{60,61}

$$p(R, E) = e^{-\alpha R - \frac{E}{kT}} \quad (2)$$

k is the Boltzmann constant ($1.381 \cdot 10^{-23} \text{ J K}^{-1}$), T is the temperature (in Kelvin) and α is a constant, which depends on the characteristics of the hopping sites. From this, the formula for describing the hopping model conductivity can be derived:

$$\sigma = \sigma_0 e^{-\left(\frac{T_0}{T}\right)^{\frac{1}{1+d}}} \quad (3)$$

where σ_0 is a pre-exponential factor, T_0 is the Mott temperature largely dependent on the charge carrier localisation length, and d is the dimensionality of the transport. For a three-dimensional system, Mott's law is obtained with the characteristic temperature dependence of the conductivity $\sigma \propto T^{-1/4}$.^{60,62}

In the band transport regime, the charges no longer belong to a single unit, but to the entire crystal. Instead of having localized energy states, the charge carriers are delocalized by an energy band structure (Figure 2.3b). This mechanism is often present in highly ordered crystalline structures.⁵⁹ While the hopping-type conduc-

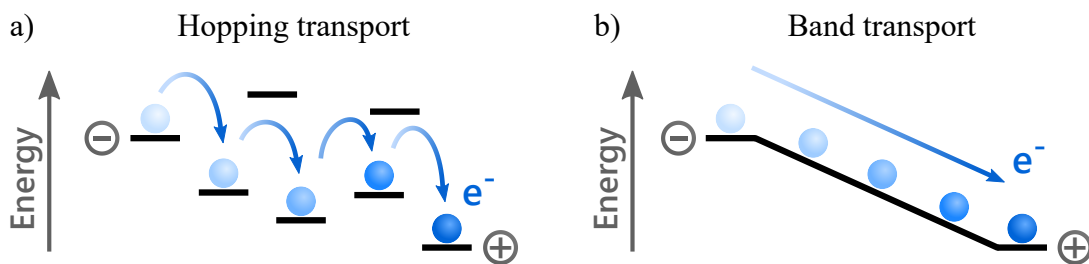


Figure 2.3: Schematic illustration of the hopping (a) and band-like (b) transport regime, where the charge carriers are moving from high to low potential energy. In hopping transport, the charge carriers hop from one localized electronic state to the next, while in band-like transport, the charge carriers move in a continuous energy band; adapted from Xie et al.⁵⁹

tivity is always thermally activated, for band-like transport it depends on whether one has a metallic or semiconducting material, i.e. whether the conduction band and the valence band are separated by a small band gap (ca. $< 3 \text{ eV}$ ⁶³). In metallic materials, the Fermi energy E_F crosses the conduction band and free charge carriers are available for current transport. The electrical conductivities achieved hereby are high (approx. 10 S cm^{-1} and larger^{64,65}), with increasing temperatures leading to stronger scattering effects and decreasing mobility and consequently conductivity.⁶³ If E_F lies in a gap between conduction and valence band, it represents a semiconductor. Beyond the absolute zero temperature, electrons can be promoted from the valence band into the conduction band by thermal (and optical) excitation, and become free charge carriers together with the holes created in the valence band. This refers to intrinsic, i.e. undoped semiconductors. Only a few MOFs show metallic behavior, most MOFs are semiconducting and their temperature dependent conductivity can be described by the Arrhenius law:^{58,65,66}

$$\sigma = \sigma_0 e^{-\frac{E_a}{kT}} \quad (4)$$

with E_a the activation energy (in Joules) defined as half of the band gap and σ_0 a pre-exponential factor.

Charge transport mechanisms

The careful choice of the organic and inorganic components allows the synthesis of conductive MOFs.^{27,67} In principle, low energy charge transport pathways are essential to achieve good electrical conductivity. Which transport pathway the charges take through the framework structure varies and depends individually on the MOF. One can distinguish between different approaches to efficient current

flow (Figure 2.4).

The first method is through-bond transport, in which the charges are transported through the continuous covalent and coordination bonds in the framework. In general this involves the bonding motifs of the metals and the ligands with their functional groups forming a continuous route. If the overlap between the orbitals of appropriate symmetry involved in the metal-ligand bond is both spatially and energetically favourable, this can lead to small band gaps and high charge mobilities and hence high conductivities.⁵⁹ An example thereof is MOF-74 and its analogues, in which infinite $(-M-O-)_{\infty}$ or $(-M-S-)_{\infty}$ chains are present through which the charges pass.^{68,69} It was shown that by exchanging the functional groups of the benzenedicarboxylate linkers from oxygen to sulfur residues, the energy levels of the ligand orbitals can be better matched to those of the metal and thus higher conductivities can be achieved ("redox matching"⁷⁰).

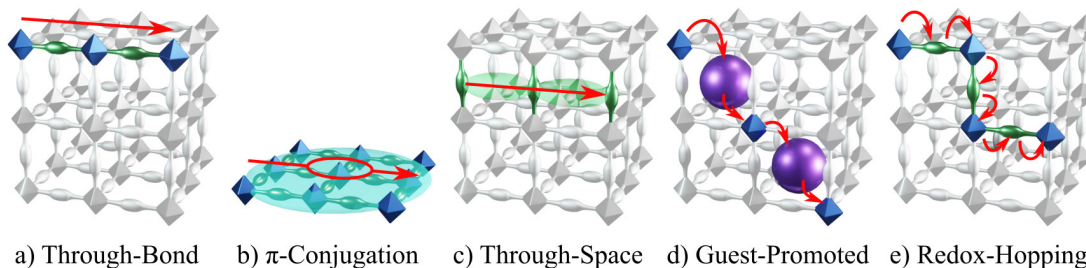


Figure 2.4: Schematic representation of the charge transport pathways through the MOF: a) through-bond transport that involves continuous bonds of the metal and ligand; b) π -conjugation in a 2D structure with delocalized charge carriers; c) through-space transport through non-covalent π - π -interactions; d) guest-promoted transport, when loaded guest molecules are interacting with the framework; e) redox-hopping enabled by redox-active building units. The red arrows illustrate the charge carrier flow.

A particular case of the through-bond approach is when the MOF has a two-dimensional structure with extended π -conjugation in the plane. Due to the enhanced orbital coupling, the charge carriers are efficiently delocalized throughout the whole framework structure, resulting in high conductivities.⁷¹ In fact, the most conductive MOFs to date have a planar structure, such as Cu-BHT (BHT: benzenehexathiol) achieving a record conductivity of around 2500 S cm^{-1} .⁷² Well known representatives of this category are also triphenylene-based MOFs that show graphene-like honeycomb lattices with efficient conjugation pathways (Figure 2.5). The first representation for this was accomplished with the ligand hexahydroxytriphenylene (HHTP), which, after forming a MOF, exhibits stacks of 2D layers with good conductivity due to its square-planar coordination to a wide

range of metals, e.g. cobalt, nickel and copper.⁷³ By substituting the functional groups of the ligand (here: hydroxy groups $-\text{OH}$) with other moieties such as amine groups ($-\text{NH}_2$) or thiol groups ($-\text{SH}$), new MOF combinations can be realized with high conductivities (Ni-HITP⁷⁴ film conductivity: 40 S cm^{-1}) and mobilities (Fe-HTTP⁷⁵ RT-mobility: $220 \text{ cm}^2 \text{ V}^{-1} \text{ s}^{-1}$).

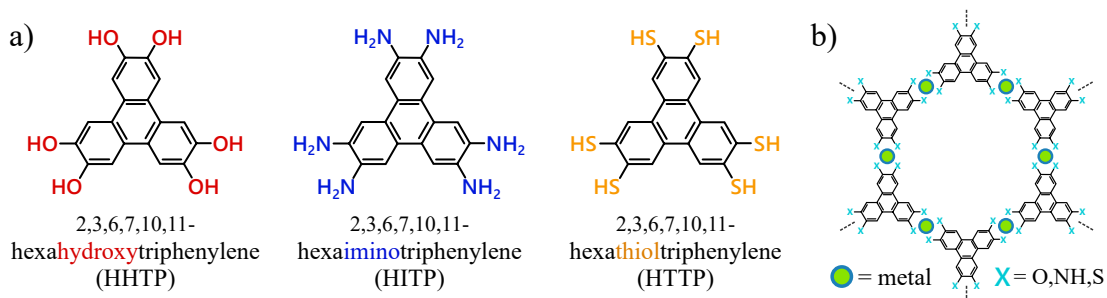


Figure 2.5: a) Triphenylene-based organic linker molecules with different functional groups: HHTP with hydroxy groups, HITP with amine groups and HTTP with thiol groups. b) The coordination of the triphenylene-based linker with specific metal ions results in a hexagonal 2D MOF, which is usually accompanied by good electrical conductivity.

The aromatic ligand also has redox-active properties, which is beneficial for conductivity. There are seven different redox states for the ligand HHTP⁷⁶ and when partially oxidized, additional charge carriers are induced into the system.^{58,59} In general, redox active components, including not only the ligand but also the metal ions, can affect conductivity. In the example of $\text{Fe}_2(\text{BDT})_3$ (BDT: benzenediyl-bistetrazole), the mixed-valency of the redox-active $\text{Fe}^{2+/3+}$ pairs leads to an intervalence charge transfer between the metal centers. The partial oxidation of the Fe^{2+} centers influences the conductivity, which can be improved by up to five orders of magnitude from $6 \cdot 10^{-5} \text{ S cm}^{-1}$ to 1.8 S cm^{-1} .⁷⁷

In parallel to the transport pathways mentioned above, charge carriers can also be transported through-space via non-covalent interactions. Often, it is the π - π interactions between the orbitals of the organic ligands that overlap as they take their place in the framework.⁵⁸ This can result in extended transport paths where the charges pass through space rather than through the bond backbone, as is the case with tetrathiafulvalene-based MOFs of the form $\text{M}_2(\text{TTFTB})$ (TTFTB: tetrathiafulvalene-tetrabenzoate).^{78,79} The tetrathiafulvalene linkers are electron-rich and stacked in helical columns allowing the orbitals of the sulfur atoms to come close and overlap. The size of the spatial overlap is defined by the radius of the metal ions and the consequent stacking distance. A larger ionic radius re-

duces the S··S distances and makes the conductivity increase.⁷⁹ Through-space transport also affects two-dimensional MOFs, where in-plane transport via π -conjugation predominates, but π - π -interactions between the stacked layers may play a considerable role regarding charge transport.^{58,59}

Since MOFs are extremely porous, there is also the possibility of guest molecules entering the pores and interacting with the MOF. The guests can have redox-active properties and thus induce free charge carriers in the MOF, they can in turn be charge carriers (e.g. in ionically conductive MOFs⁸⁰), or they are bridging the building units and create new transport pathways allowing the charge carriers to flow.^{58,59} A well-known example of this guest mediated approach is Cu-BTC ("HKUST-1"; BTC: benzenetricarboxylate) infiltrated by TCNQ molecules (TCNQ: tetracyanoquinodimethane).⁸¹ The TCNQ molecules bind to open metal sites and bridge the SBUs, forming new through-bond transport pathways. This increases the film conductivity by six orders of magnitude, from $10^{-8} \text{ S cm}^{-1}$ to 0.07 S cm^{-1} , which might not match the range of ten or eleven orders of magnitude when doping certain polymers such as polyacetylene^{82,83}, however, may very well outperform many other conductive polymers.^{84,85} Inducing or tuning electrical conductivity in MOFs by guest molecules, however, has the consequence that the porosity considerably suffers under the guest inclusion. The pores may be partially or completely blocked by the guests, which may not be desirable for some applications that require large surface areas. In the aforementioned example, only $\sim 12\%$ of the initial BET surface area is accessible after adsorption of TCNQ.⁸¹

2.3.4 Optical, magnetic and soft mechanical properties

It is probably not possible to list all kinds of MOF properties, but here are a few more worth mentioning. For example, luminescent MOFs can be produced by using optically active building units, by adsorbate-based emission or by surface functionalization, among others.⁸⁶ The large variety and variability in MOFs chemistry allow e.g. tuning of luminescence emission, making them attractive for diverse applications from light emission devices to chemical sensors.⁸⁷

The situation is similar with magnetic MOFs, for instance by involving paramagnetic metal centers.⁸⁸ Magnetic MOFs can then be manipulated by an external magnetic field, which can be used, for example, to align or guide cells, provided the MOFs are interlinked with the cells.⁸⁹

Other interesting features such as photoswitchable MOFs and structural deformation while maintaining crystalline order can be achieved by flexible MOFs.^{90,91}

Their ability to undergo dynamic structural transformation, e.g. upon guest molecule incorporation or mechanical pressure, makes them promising for high-selective gas separation, which has been demonstrated, for example, in the separation of CO₂/CH₄ gas mixtures with selectivity improved by a factor of about 10 compared to conventional MOFs.^{92,93}

2.4 Applications of MOFs

The wide range of possible building units and associated individual properties of MOFs allows them to be used in specific applications, some of which we have already learned about. It is obvious that the extreme porosities of MOFs make them suitable for all applications where large surface areas and high adsorption capacities are beneficial or even required. Prime examples of this are gas storage^{94,95} and catalysis such as heterogeneous catalysis⁹⁶, capture and conversion of gases like NO₂ to nitric acid⁹⁷ and detoxification.^{98,99} MOFs also find their place in filtration applications, whether filtering particles from the air¹⁰⁰, separating gases^{92,101} or removing toxic metals from water.^{50,102} An advantage here is the tunable selectivity toward specific analytes, which can be achieved by different functionalities. A novel application is water harvesting, in which moisture is absorbed from the air and fresh drinking water is generated.^{103–106} This application

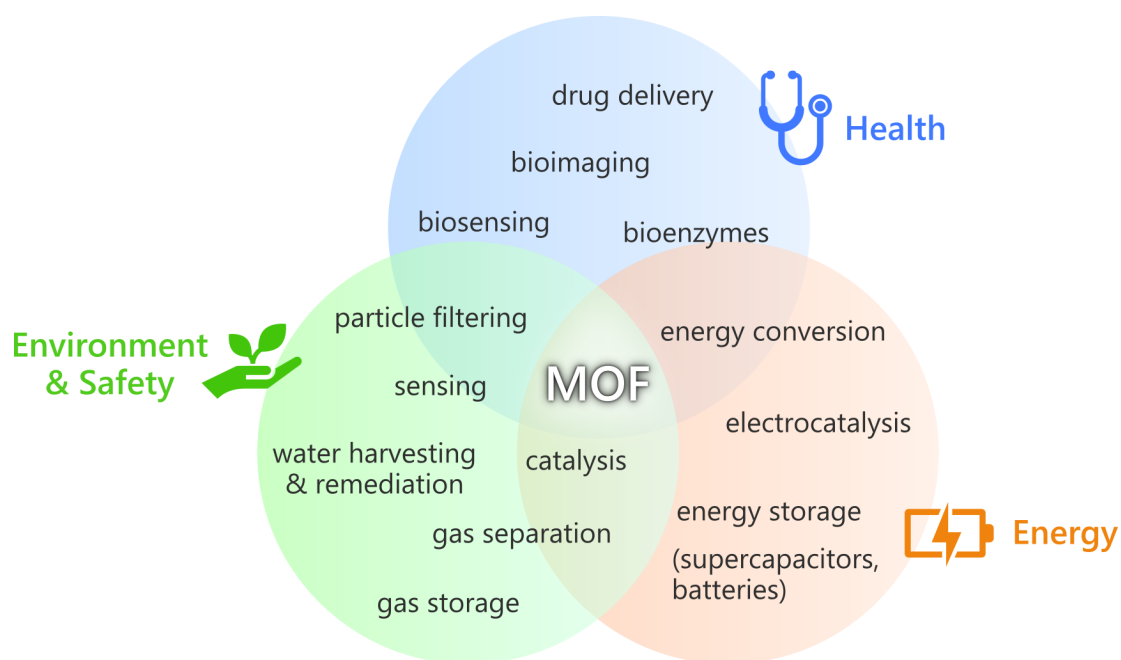


Figure 2.6: The large number of MOFs and their versatile properties lead to numerous applications, whether in the field of health, energy or environment and safety.

works even in desert regions with low humidity and prototype devices show a yield of around 40 L water per kilogram of MOF per day (Figure 2.7a).¹⁰⁷

So far, only examples have been listed which do not require intrinsic conductivity. As mentioned above, electric charge transport in MOFs opens up many other applications. Electrocatalysis is an obvious example of this. MOFs have already been successfully applied for example for electrochemical reduction of oxygen⁵⁵, hydrogen evolution¹⁰⁸ and water splitting.¹⁰⁹ MOFs are also attractive in the field of energy storage.^{54,110} MOF supercapacitors have been shown to have high volumetric and areal capacitances with values reaching 760 F cm^{-3} and 20 F cm^{-2} , while maintaining good chemical and cycling stability.^{111,112}

The chemical and electronic properties of MOFs have also been shown to be useful in photonic applications^{113,114}, including solar energy conversion¹¹⁵, light-emitting diodes¹¹⁶ and microlasers.¹¹⁷ Various biomedical applications also benefit from MOFs due to their features like rich surface chemistry, high loading capacities and possibly good biodegradability.¹¹⁸ For example, MOFs can be used as nanocarrier for drug delivery^{119,120} and for bioimaging purposes.¹²¹ Recently, it was shown how MOFs can significantly increase the efficiency of neuronal cell generation from neural stem cells due to the sustained and continuous delivery of necessary differentiation factors.¹²² Another application is a biocompatible MOF-based exoskeleton for native red blood cells (RBC) which gives them improved resistance to external stress factors like osmotic pressure or toxic nanoparticles while retaining the original properties of the RBC.⁸⁹ By varying the MOF design, the properties can be tuned to allow external magnetic manipulation or biosensing of nitric oxide in blood by NO-triggered fluorescence. The last example is associated to the field of sensing applications, hence the rationale to discuss this in detail in Chapter 3 of this thesis.

2.5 Outlook and future approaches

MOFs are an emerging class of materials that have increasingly been applied in numerous areas and have already been shown to exceed the performance of current materials such as zeolithes or carbon-based materials.^{42,111} Being in the early stages of development, it is not easy to predict what further applications and improvements may come in the future, but simply because of the chemical diversity of MOFs, they will certainly have significant impact. This can already be seen in part by the startup companies that are being founded and are working with MOF

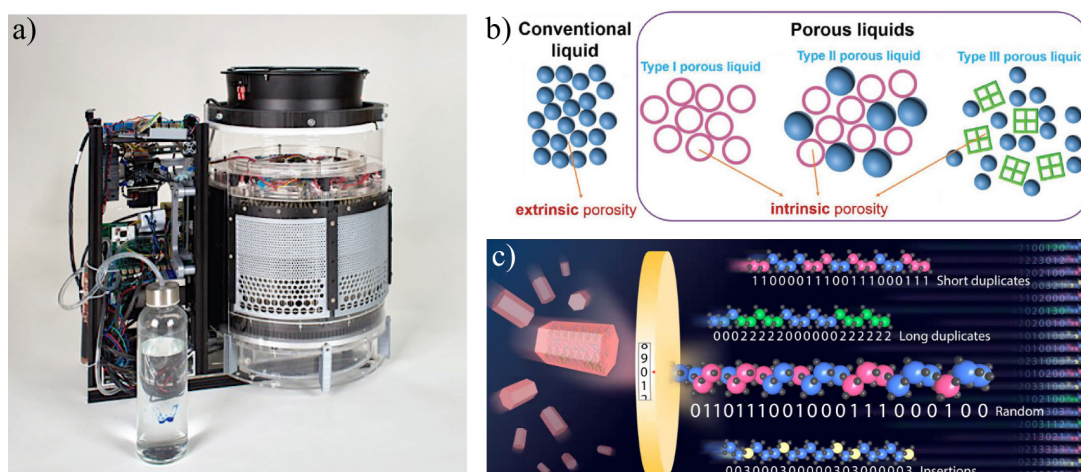


Figure 2.7: a) Prototype of MOF water harvester from Water Harvesting Inc., which is able to produce 4L water from air per 100 g MOF; reproduced from Yang et al.¹⁰⁷ b) Schematic representation of the types of porous liquids with different intrinsic porosities compared to a conventional liquid that has only extrinsic porosity; reproduced from Jie et al.¹²³ c) Illustration of a multivariate MOF with sequences of metal ions that could be used to encode information; image by Omar Yaghi and Zhe Ji, UC Berkeley.¹²⁴

technology.^{125–127}

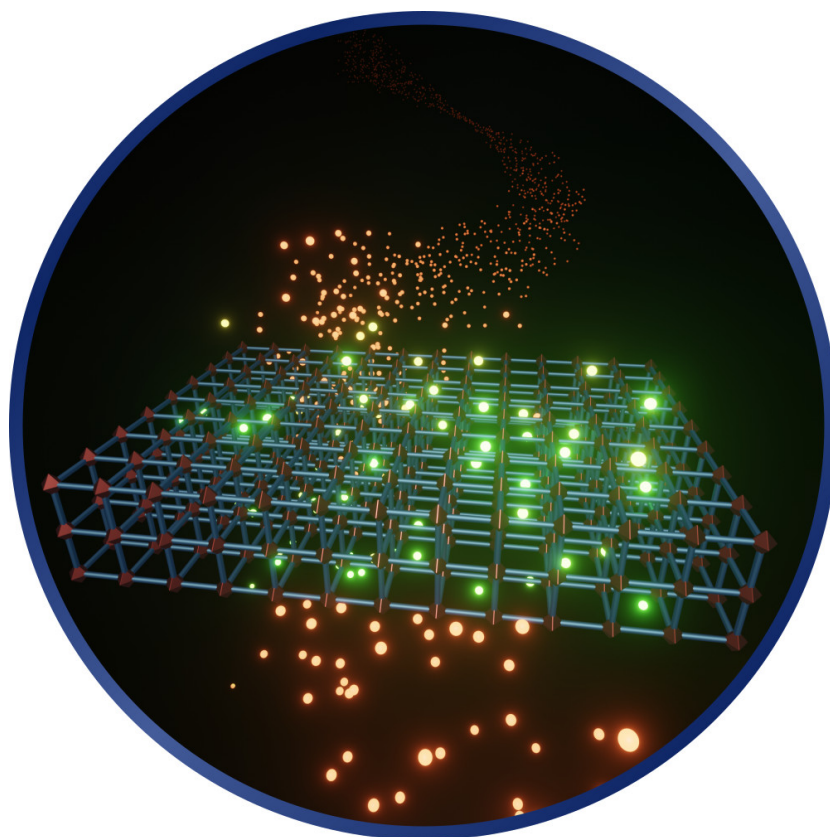
We have already learned about one example, namely water harvesting, which is currently being commercialized by *Water Harvesting Inc.* (Figure 2.7a) and is certainly having an impact on our society, as over two billion people live in countries with high water stress and the situation is aggravated by water pollution or climate change, for example.^{126,128} In a next step, water harvesting could be combined with CO₂ capturing and conversion powered by renewable energy such as solar energy in order to create a closed energy cycle for the production of fuels and chemicals.¹⁰⁷ The individual components of this cycle are already achievable today, thanks in part to reticular chemistry, and the vision for the future is clear: the production of clean air, water and energy.

Another example of MOF-based technology are porous liquids.^{123,129–131} These are liquids with permanent microporosity by dissolving particles of microporous frameworks or other materials with microcavities (Figure 2.7b). However, in contrast to the simple dissolution of the porous species, the pores are not filled with solvent molecules, but remain freely accessible. This retains the properties of porous materials, but now combines them with the advantages of a fluid that can circulate and be used in flow processes. This is a promising approach for industrial applications such as those offered by the company *Porous Liquid Technologies*.¹²⁷ Further insights into future applications can be provided by the first mapping

of the metal sequence in a multivariate MOF-74 via atom probe tomography.¹³² Multivariation, i.e. the concept of introducing multiple functionalities, allows information to be stored in the form of sequences; thereby, the functionalities are considered separately to the backbone. The sequence describes the spatial arrangement of functionalities incorporated into the backbone, similar to the nucleotide sequence in the DNA.¹³³ For the future, applications in data sequencing could emerge with different types of variants and shape of the sequences, for example in 3D (Figure 2.7c).

In general, the field of research in MOF-based materials is broadening even further than the established set picture. New fields of MOF science have emerged with the next generation of MOFs with properties such as spatiotemporal evolution of dynamic frameworks (4D-MOFs)¹³⁴ or future approaches to fabricate novel MOF materials like melting, downsizing or hybridization.^{135,136}

Sensing approaches based on MOFs



Sensors are found in various everyday objects and provide important information from the environment to the user, such as the presence of certain analytes or the concentration of a substance. High selectivity and sensitivity are desirable, which is why metal–organic frameworks with their nanoporosity and tunable functionality increasingly represent a promising sensing platform.

This chapter discusses the fundamentals of sensing and the exploration of MOF-based sensing platforms for chemical and biochemical sensing.

3.1 Basics of sensing

A sensor can be defined as a device that detects physical, chemical or biochemical properties and converts them into a measurable signal, such as an optical signal (e.g. change in light intensity, frequency, polarization, ...) or an electrical signal (e.g. resistance modulation, electrochemical current, ...).¹³⁷ A distinction can be made between quantitative and qualitative sensors. Qualitative sensors give a signal in case of presence or absence of a certain parameter or substance, such as a gas when a threshold value is exceeded, whereas quantitative sensors want to reflect the concentration of a certain substance like the glucose level in blood. The smallest initial increment in the measurand that results in a detectable signal output from the sensor is referred to as the threshold.

In the process of sensing, the principle is always the same and basically consists of three steps (Figure 3.1). First, the target analytes are recognized by selective

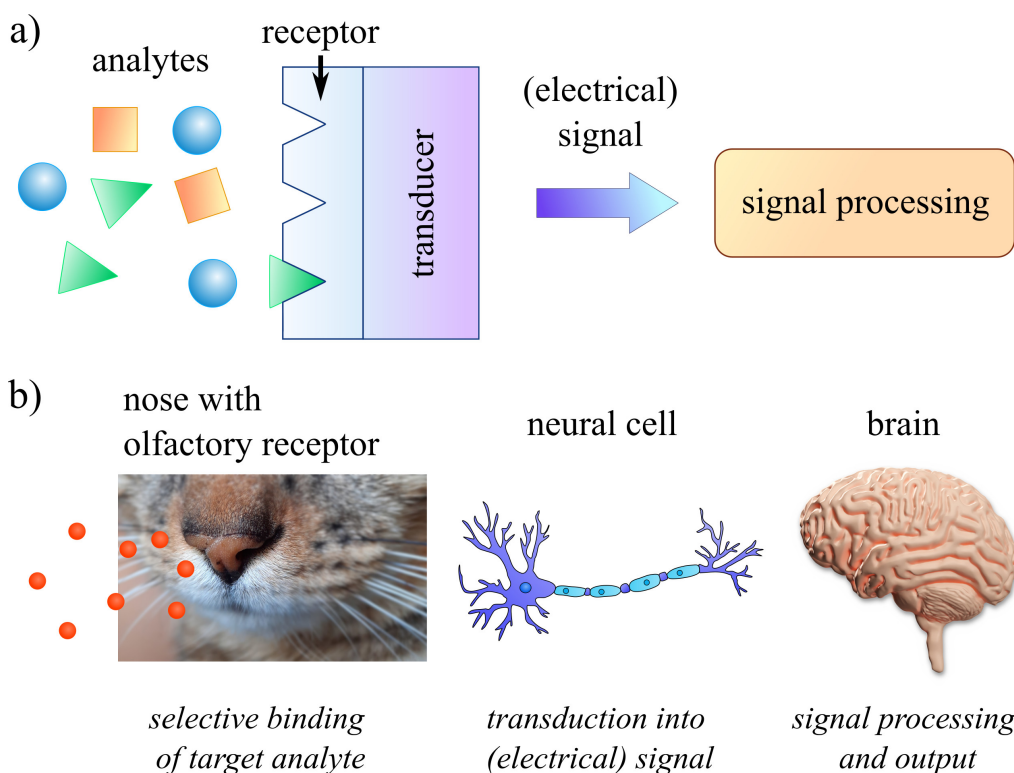


Figure 3.1: a) Schematic of the sensing principle. Target analytes bind selectively to a receptor, where a transducer converts the binding into a measurable signal, such as an electrical signal. The signal is then forwarded, processed and output. b) Our senses function according to the same principle. In the example of the nose, it is the olfactory receptors that recognize certain odors and convert them into electrical impulses. Nerve cells transmit these to the brain, where we recognize the smell.

binding to the receptor. Second, the transducer converts the binding into a measurable signal, such as an electrical signal. Third, this signal is routed where it can then be processed and output. The human senses are built on the same principle. They are our sensors with which we perceive the outside world.^{138,139}

There are several characteristics that have an impact on the optimization of sensor performances.^{137,140,141} Sensitivity determines the smallest amount that can be detected, while selectivity defines the specific identification of the target analyte, even if other analytes are present.¹⁴² Other important parameters of a sensor are stability, e.g. against external disturbance factors, reproducibility, even with multiple repetitions, and response time. Another aspect is the linearity, which indicates the linear dependence range between output signal and analyte concentration. For quantification, linearity is not mandatory, but it may facilitate the description of the transfer function, which mathematically describes the relationship between input and output within the sensing range.

In most cases, the sensor response can be described with a Sigmoidal calibration curve, which defines the operating range of the sensor, i.e. the ability to measure an analyte from the lowest value up to saturation (Figure 3.2).

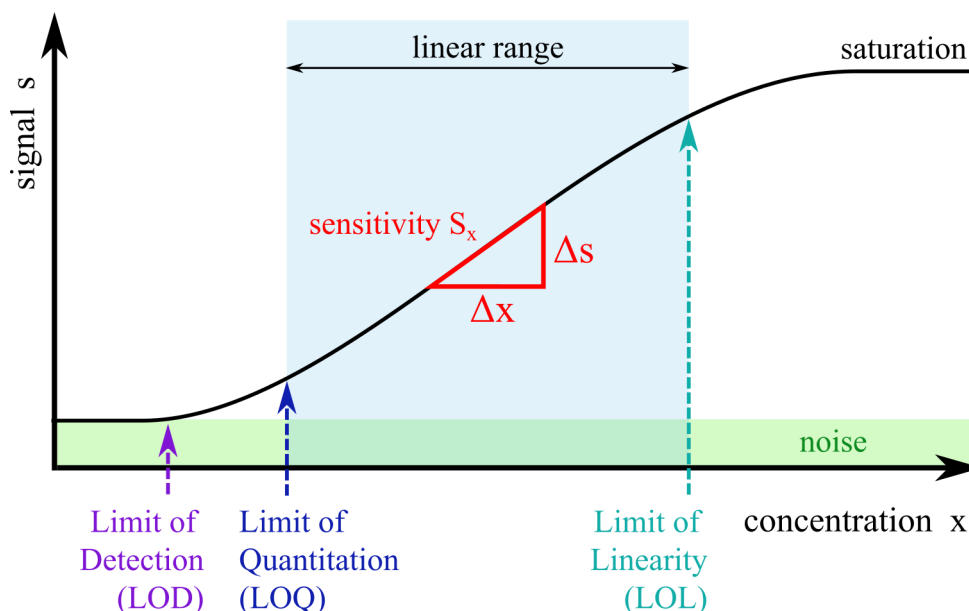


Figure 3.2: Schematic of a typical Sigmoidal calibration curve of a sensor, from which one can read parameters such as limit of detection, limit of quantification and linear range. The slope of the curve represents the sensitivity, means signal change upon a change in the concentration.

The slope of the curve reflects the sensitivity, meaning the resolution at which the smallest change in concentration causes a signal change. The sensitivity S_x can be written as the partial derivation of the signal s with respect to the target analyte x at a certain value and time:¹⁴³

$$S_x = \left. \frac{\partial s(x,y,t)}{\partial x} \right|_{x_0,y_0,t_0} \quad (5)$$

In this context, cross-sensitivity (or parasitic sensitivity) S_y is defined as the contribution of interferants y , i.e. other than the target analyte, to the signal:

$$S_y = \left. \frac{\partial s(x,y,t)}{\partial y} \right|_{x_0,y_0,t_0} \quad (6)$$

In general, y can be grouped as a family of multiple different interferants $\{y_1, y_2, \dots, y_i\}$. The selectivity of a sensor, which means the ability to selectively detect the target analytes in the presence of interferants, is the ratio between sensitivity and cross-sensitivity induced by each interferant:

$$Sel_x = \frac{S_x}{\sum_i S_{y_i}} = \left. \frac{\frac{\partial s(x,y,t)}{\partial x}}{\sum_i \frac{\partial s(x,y,t)}{\partial y_i}} \right|_{x_0,y_0,t_0} \quad (7)$$

The lowest possible concentration which can be detected is defined by the limit of detection (LOD). It is the threshold at which the signal can be distinguished from the noise, thus indicating the presence of the analyte (typically the LOD is equal to three times the standard deviation of the background noise).¹⁴⁴ In contrast, the limit of quantification (LOQ) describes the smallest possible concentration that can be quantified with suitable accuracy (precision and trueness), and is always higher than the limit of detection (typically ten times the standard deviation of the background noise). The limit of linearity (LOL) indicates the level in the calibration curve at which the signal ceases to be linearly proportional to the concentration and enters saturation. If the signal shifts in time without the concentration changing, it is called a drift. An example of this is the offset drift d_t , which can be given by the partial derivative of the signal s with respect to time t :

$$d_t = \left. \frac{\partial s(x,y,t)}{\partial t} \right|_{x_0,y_0,t_0} \quad (8)$$

3.2 MOF-based sensing

Many of the requirements of an efficient sensor, such as high sensitivity and selectivity, can be met with MOFs because of their large surface-to-volume ratio and unique chemistry. For example, due to their nanoporosity and large intrinsic surface area, most MOFs are able to concentrate the analytes to higher levels, which is very conducive to sensitivity.^{140,145} Apart from that, the sensitivity also depends on the strength of the binding between MOF and analyte, which can be influenced by the flexible chemistry of the MOFs as well.

This tunability also gives MOFs many advantages over other sensor materials in terms of selectivity. The simple exclusion of some analytes based on their size can be accomplished by adjusting the MOF pore size and is called molecular sieving. Specific detection sites can also be incorporated into the MOF by the choice of the building units, either already during synthesis or as post-synthetic modification. The wide variety of possible functionalities of organic linkers and metal centers allows their selective response to be tailored to specific chemical and biological stimuli.^{137,140,145,146}

Stability and reversibility are further important parameters of an efficient sensing device. MOFs enable sensor recyclability through reversible uptake and release of analytes, which are mostly physisorbents.^{140,145} The MOF can be reactivated by purging the material with a gas component or applying a vacuum (pressure depends on MOF structure, e.g. 10^{-3} mbar for activation of MIL-96¹⁴⁷), making it usable for a large number of cycles.^{147,148} Heating of the sample can also be applied to increase sensor regeneration, but in that case the thermal robustness of the MOF must be known. However, most MOFs, e.g. UiO-66 or nickel-tricarboxybenzene, are thermally stable up to a temperature of 350-400 °C, some even exceeding 500 °C, which is sufficient for most operation temperatures.^{140,149,150}

MOFs therefore have great potential for sensory applications. The success of MOF-based sensors can also be seen in the sharp increase in published works in recent years (Figure 3.3). And the trend is expected to continue because there is a wide range of analytes that can be efficiently detected using MOFs. Often it is about ion sensing¹⁵¹ or gas sensing^{152,153}, as these may have a biological relevance or a relevance for the environment.¹⁵⁴ Also, the discrimination between different classes of volatile organic compounds (VOCs) such as alcohols, amines or aromatics has been demonstrated with MOF-based sensors.^{56,155} However, sensing is of course not limited to gases or VOCs. Temperature¹⁵⁶, humidity¹⁵⁷ and pH¹⁵⁸ also

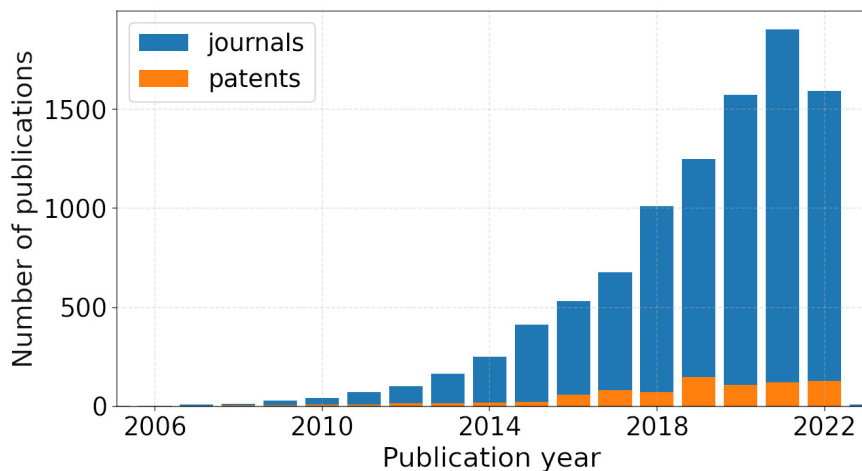


Figure 3.3: Number of yearly publications that include both concepts: "metal-organic framework" and "sensor" (source: SciFinder®, retrieved 12.09.2022). The growing number is one indication of the potential that MOF-based devices hold.

belong to the sensing repertoire of MOF-based sensors. In general, a very important aspect is how the signal is generated, i.e. what kind of signal transduction takes place.

3.3 Signal transduction

Signal transduction describes the generation of a measurable, usually electrical, signal as a result of the physico-chemical interaction between the MOF and the target analytes. There are several options for signal transduction. For MOF-based sensors, the transduction is often non-electrical as most MOFs are insulating, and can proceed in different ways such as optical, mechanical or thermal. The interaction between MOF and analytes leads to a change in the properties of MOF, which is detected by an external transducer and subsequently converted into a measurable physical signal (Figure 3.4a).¹⁴⁶

The emergence of electrically conductive MOFs allows their use in electrical or electrochemical sensing. The advantage here is that in most cases the conductive MOF is both receiver and transducer. In this way, changes in the electrical properties caused by the MOF-analyte interactions can be read directly without external transducer (Figure 3.4b).^{65,159}

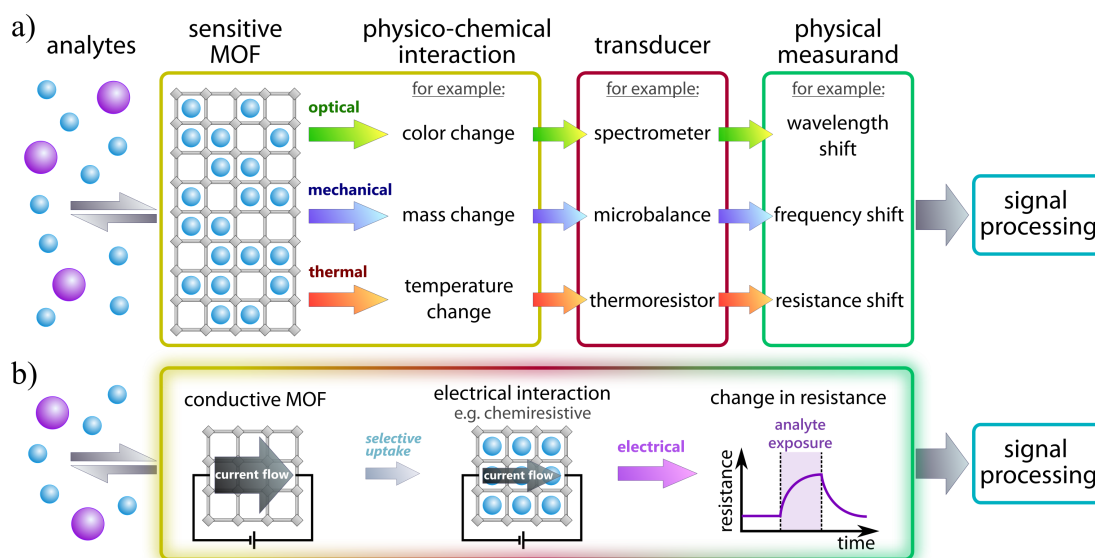


Figure 3.4: Sensing principle and signal transduction. a) The sensitive MOF layer enables the selective uptake of analytes, whose physico-chemical interactions lead to changes in the material properties. An external transducer converts this information into an electrical signal for readout and signal processing. b) Using conductive MOFs as sensing element benefit from being receiver and transducer at the same time, thus allowing a direct signal readout and analyte detection.

3.3.1 Non-electrical signal transduction

The most common way of non-electrical signal transduction is by optical means, for example by a change in color and absorption properties of the MOF material.^{160,161} The change in refractive index after uptake of guest molecules is also a convenient approach.¹⁶² One of the methods that can be used to detect this change is localized plasmon oscillations, i.e. collective electron density oscillations in metallic nanostructures. Their resonance frequency (localized surface plasmon resonance; LSPR), and hence their extinction spectra depend on the refractive index of the surrounding.¹⁶³ A further well known method of optical signal transduction is using luminescent MOFs and the variation of their emission color upon exposure.^{155,164} But also the quenching or enhancement of the photoinduced emission due to the MOF-analyte interaction has been demonstrated numerous times.^{165–167} Raman spectroscopy is another optical technique in which information about material properties can be obtained from the scattered light, which depends on the individual vibrational modes. For selectivity and signal enhancement, Surface-Enhanced Raman Spectroscopy (SERS) using MOFs can be employed, thus detecting signal changes based on interactions and bindings at

the molecular level.^{168,169}

Gravimetric signal transduction is a non-optical sensing option that typically converts changes in mass into a signal. The most obvious approach is to measure the weight change using piezoelectric materials, for example in sensitive quartz crystal microbalances (QCM).¹⁷⁰ A deposited MOF then serves as a selective host for the target analytes. Another approach is to use Surface Acoustic Waves (SAW) that, after being generated by a piezo, propagate across a surface and pass through the MOF. The mass uptake of the MOFs is then detected by the frequency shift of the acoustic wave.¹⁷¹

The large number of MOFs with their individual properties also allows several other signal transduction pathways, such as changes in magnetic properties in response to analyte uptake.¹⁷² In principle, thermal changes can also be used for calorimetric sensing, which is a well known sensing principle¹⁷³, however, to one's knowledge no MOF-based calorimetric sensor has yet been implemented.¹³⁷

3.3.2 Electrical signal transduction

In electrical signal transduction, detection in MOF-based electrical or electrochemical sensing is typically achieved by penetration of target analytes into the MOF pores, which alter certain electrical MOF properties upon interaction. It has the advantage that the MOF is both the receiver and transducer, which allows a direct signal readout. There are different categories, between which a distinction can be made (Figure 3.5):¹³⁷

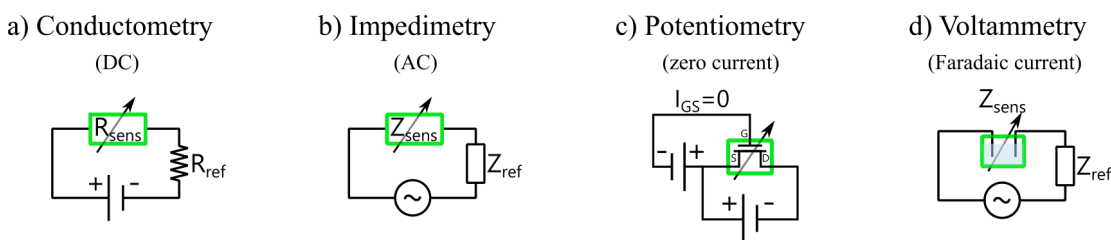


Figure 3.5: Schematic sensor circuits of the most relevant electrical and electrochemical MOF-based sensors: chemiresistors (a), chemicapacitors (b), chemitransistors (c) and electrochemical sensors (d). The green square indicates the position of the chemically sensitive MOF; adapted from Stassen et al.¹³⁷

- Conductometry and chemiresistors:
Chemiresistors measure a change in the conductance (or resistance), which is based on the manipulation of the charge carrier mobility or concentra-

tion. Usually, a constant voltage is applied and the direct current (DC) is monitored to detect alterations in the conductivity of the MOF, which must therefore be present to a certain extent.^{56,174}

- Impedimetry and chemicapacitors:
Chemicapacitors measure a change in the dielectric constant by studying the MOF behavior in the frequency domain. By applying an alternating current (AC), the imaginary part of the impedance can be analyzed, which reflects the capacitive reactance being inversely proportional to the dielectric constant. The real part of the impedance describes the resistance and does not contribute to the impedance, which is why electric current flow through the MOF is not absolutely necessary.^{147,175}
- Potentiometry and chemitransistors:
Chemitransistors such as chemically sensitive field effect transistors (CHEM-FETs) measure surface potential modulations caused by analytes near the electrode surface. In general, the potential difference between a chemically sensitive electrode and a reference electrode kept at constant potential is investigated. The potential between source and gate, the latter equipped with the sensitive MOF, modulates the current flow in the channel between source and drain, while zero current flows through the MOF.^{176–178}
- Voltammetry and electrochemical sensors:
Electrochemical sensors measure the Faradaic current generated during the reduction or oxidation of the analytes. This distinguishes them from the other types of electrical sensors. The electrochemical cell includes two electrodes (potentially functionalized with MOFs) connected by a circuit on one side and an electrolyte on the other side, where an opposite ionic current is formed during the redox reaction.^{179,180}

A well-known example of MOF-based chemiresistive sensors is Cu-HITP and also its isomorphs Cu-HHTP and Ni-HITP.^{56,181} They belong to the triphenylene-based MOFs and are one of the first demonstrations of successful sensing based on conductive MOFs. The sensing device could discriminate between different classes of volatile organic compounds (VOCs). Chemiresistive sensing using other promising MOFs¹⁷⁴ or blends with other materials such as graphite¹⁸² are also known, and all of them show a selective response due to the unique properties of the MOF.

3.4 MOFs for biosensing purposes

The definition of a biosensor, and thus a distinction from ordinary chemical sensors, is that the sensor contains a biological component for its sensing function.^{183,184} Usually, the biological component takes the role of the receptor, taking advantage of the very specific affinity between certain biomolecules, such as antibody-antigen binding¹⁸⁵, complementary DNA strands¹⁸⁶ or the affinity of particular enzymes.⁹ Peptides¹⁹ and even whole cells¹⁸⁷ can be used as recognition elements as well, for example for ion detection. The idea for a biosensor originated with Dr. Leland Clark in 1962 for the detection of glucose based on the enzyme glucose oxidase.^{188,189}

In principle, biosensors can be used in many areas. This includes, for example, monitoring food quality or detecting environmental substances that may have biological relevance.¹⁹⁰ In particular, the detection of biomarkers, i.e. analytes that have a direct relationship to specific processes in the body and thus indicate a certain condition, such as a disease, are of enormous importance here. By generating a signal proportional to the analyte concentration, biosensors allow accurate diagnosis of diseases and associated pathological processes, representing one example of how biosensors can improve quality of life.^{1,118,141} The signal is thereby generated in the same way as with chemical sensors, i.e. by transduction of the biochemical interaction into a measurable signal such as electrochemically or optically.^{178,191,192}

Since specificity and sensitivity are important parameters for sensing, MOFs with their high surface area and versatile functionalization have become attractive alternative biosensors characterized by low detection limits, high sensitivity and recyclability.^{193,194} Their excellent performance has made MOF-based biosensors increasingly important in recent years, driving the development of sensors using MOFs as active element for efficient biomarker detection and disease diagnosis.^{195,196} A variety of biomolecules including bacteria¹⁹⁷, macromolecules such as nucleic acids¹⁹⁸ or proteins¹⁹⁹ and other small biologically relevant molecules^{179,200} have already been detected using MOF-based biosensors (Figure 3.6). Depending on the MOF, its role in sensing varies. In some cases, MOFs act as containers for the immobilization of molecules¹⁹⁸, in other cases the MOF serves as nanocarrier and amplifies the signal, be it e.g. electrochemically²⁰¹ or optically.¹⁶⁸ The MOF can also be the probe itself, for example with fluorescent ligands incorporated into the MOF¹⁵³ or by quenching of photoluminescence.¹⁹⁷ Some MOFs, for example

the two-dimensional architectures Ni-HITP or Cu-HHTP, are catalytically active and are used for the electrochemical detection of biologically relevant analytes.¹⁷⁹ Biocatalytic and enzymatic activity of MOFs is known as well (e.g. MOF-808) to be used for sensing of diverse analytes, for example glucose.^{40,202–204} Finally, it should be mentioned that before MOFs are deployed directly on or in the human body for biosensing or related biomedical applications, issues such as biocompatibility and toxicity must be addressed beforehand.^{118,205} The toxicity of a MOF greatly depends on its composition, i.e. the choice of the metal and the nature of the organic ligand.²⁰⁶ For example, the sustained release of certain metal ions like silver from the MOF framework can show biotoxic and antibacterial effects.²⁰⁷ Other factors also influence the toxicity of a MOF, including particle size, biodegradability, and morphology.²⁰⁵ Due to the diversity of different MOFs, toxicity must be evaluated individually, and this should not be limited to *in vitro* or short-term toxicity studies, but requires long-term *in vivo* experiments.^{118,208}

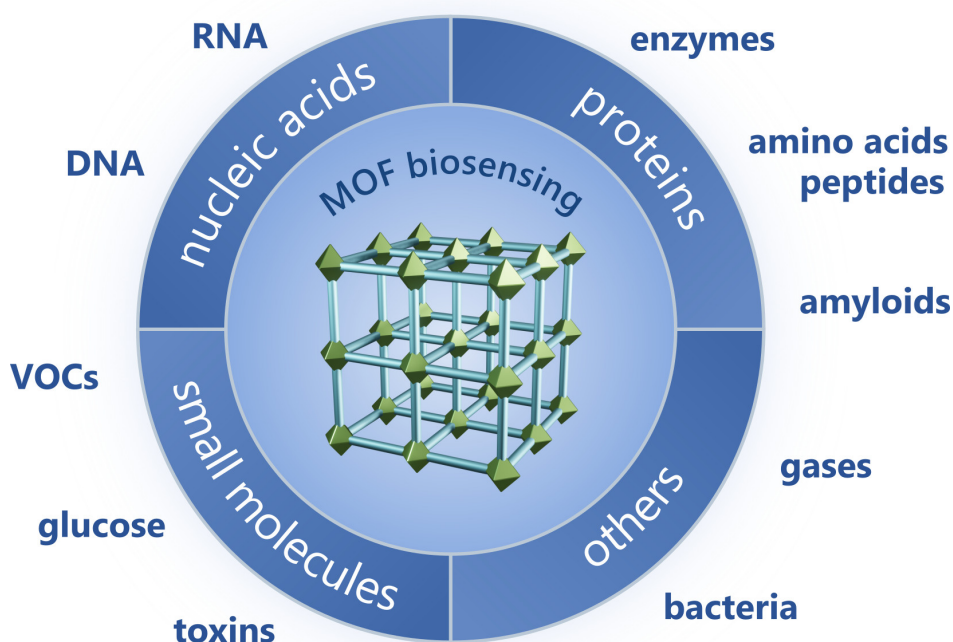


Figure 3.6: Overview of some examples of biomolecules that can be detected with MOF-based sensors, including DNA, peptides, bacteria or other molecules with biological relevance; inspired by Liu and Liu.¹⁹⁶

3.5 Outlook

The latest research and developments demonstrate the advantages of MOFs as an active platform in sensing, which is why they are also seen as promising for future applications. As sensing material in various fields of environmental monitoring and public health, there are already innovative approaches to combine MOFs with other materials or portable gadgets.^{118,146,209} One example of this is the use of smartphones to process the signal response of MOFs, e.g. optically or electrochemically.^{210,211} It has already been shown how the use of a MOF sensing platform integrated in a sweatband can monitor sweat glucose levels by connecting to a smartphone via Bluetooth (Figure 3.7).²¹² The field of wearable sensors in particular is gaining in importance, especially in point-of-care diagnosis due to their ability to precisely collect physical and (bio-)chemical data from the individual.^{12,213} This has direct implications for many fields, ranging from medicine²¹ and fitness³ to military applications.²¹⁴

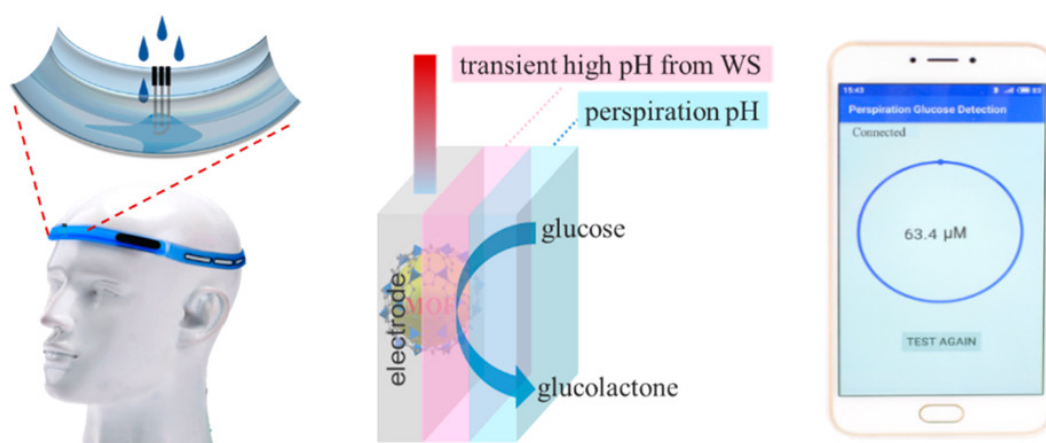
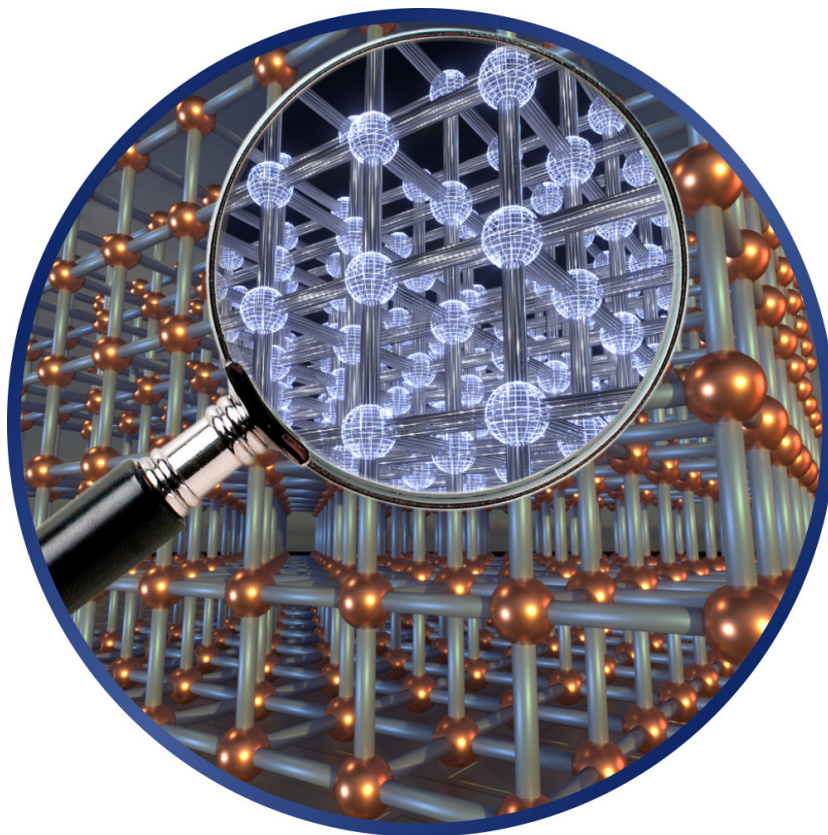


Figure 3.7: Schematic of a wearable and MOF-based electrochemical sensor for measuring the glucose level in sweat. The detection is based on a water splitting-assisted electrocatalytic reaction with Pd@ZIF-67. The data analysis is then performed by a smartphone connected with the sensor via Bluetooth; reproduced from Zhu et al.²¹²

Characterization techniques



The study of nanomaterials such as MOFs requires different characterization techniques like microscopy, spectroscopy or X-ray diffraction that allow insights into different aspects of the material to be obtained, thereby providing a deeper understanding of the material's properties.

In this chapter, the main characterization techniques used and their operation are presented with reference to the characterization of MOFs.

4.1 Raman spectroscopy

Raman spectroscopy is an optical analysis method in which information about material can be obtained from the scattering of light by molecules. The eponym of this spectroscopy method is Chandrasekhara Venkata Raman, who was the first to observe and describe this effect in 1928 together with his colleague Kariamanikkam Srinivasa Krishnan and also received the Nobel Prize in Physics for his discovery in 1930.²¹⁵ Light interacts with the material and is scattered inelastically by it, exciting vibrations in the molecules of the material. The energy transfer results in a shift in the wavelength of the light and because each molecule has distinct vibrational modes, the scattering spectrum contains an individual pattern of the material, like a fingerprint. Material defects, chemical reactions and interactions between the material and analytes at the molecular level lead for example to changes in the scattering spectrum and can be detected by Raman spectroscopy.^{216–218} Aqueous systems can also be characterized, for example biological samples, which is often difficult with infrared spectroscopy due to the strong IR absorption of water.²¹⁹ Besides, high reading speeds can be achieved by using faster data acquisition based on computational algorithms that read only the required part of the information, allowing quick large-area scans suitable for e.g. biological samples.^{220,221} Finally, it is possible nowadays to be mobile with Raman spectroscopy through the realization of portable Raman instruments, allowing on-site analysis.^{222,223} For these reasons, Raman spectroscopy has become a powerful and versatile analytical tool for fast and label-free material characterization in many fields beyond material science - down to the single molecule level.^{224,225}

In the following, the basic theoretical description of Raman scattering is discussed. The interested reader is referred to further literature in which the theory is treated in more detail.^{226–228}

When light interacts with a material, the incoming electromagnetic wave induces a dipole moment μ (unit: C m), which can be expressed as follows:

$$\vec{\mu} = \tilde{\alpha} \cdot \vec{E} \quad (9)$$

$\tilde{\alpha}$ is the polarizability of the molecules in the material (unit: C m² V⁻¹) and \vec{E} is the electric field of the incident electromagnetic wave (unit: V m⁻¹). It can be written as:

$$\vec{E}(t) = \vec{E}_0 \cdot \cos(\omega_0 t) \quad (10)$$

with the amplitude E_0 , the angular frequency ω_0 and the time t . In general, it is not a constant but a tensor and depends on the instantaneous position of the individual atoms: If they are displaced from their equilibrium positions, i.e. the positions they occupy when no external field is present, so does the electron density and the polarizability changes.

The oscillations of the atoms along each normal coordinate q can be written as:

$$q(t) = q_0 \cdot \cos(\omega_q t) \quad (11)$$

with angular frequency ω_q and amplitude q_0 . Q comprises all individual normal modes of vibration $\{q_1(t), q_2(t), \dots, q_i(t)\}$. For simplicity, the vector notation is dropped and the treatment is given in 1D with contribution along the normal coordinate q . For vibrations with small amplitude, the polarizability can be expressed into a Taylor series around the equilibrium positions $Q_0 = Q(t = 0)$:

$$\alpha(Q) = \alpha_0 + \sum_q \left(\frac{\partial \alpha}{\partial q} \right)_{q_0} q + \frac{1}{2} \sum_{q, q'} \left(\frac{\partial^2 \alpha}{\partial q \partial q'} \right)_{q_0 q'_0} q q' + \dots \quad (12)$$

with α_0 the equilibrium polarizability. For further consideration it is only of interest up to the linear Taylor term. Combining the equations gives us the formula for the time-dependent dipole moment $\mu(t)$:

$$\mu(t) = \left[\alpha_0 + \left(\frac{\partial \alpha}{\partial q} \right)_{q_0} \cdot q_0 \cdot \cos(\omega_q t) \right] \cdot E_0 \cdot \cos(\omega_0 t) \quad (13)$$

$$\begin{aligned} &= \alpha_0 \cdot E_0 \cdot \cos(\omega_0 t) \\ &\quad + \frac{1}{2} \left(\frac{\partial \alpha}{\partial q} \right)_{q_0} \cdot q_0 \cdot E_0 \cdot \cos[(\omega_0 - \omega_q)t] \\ &\quad + \frac{1}{2} \left(\frac{\partial \alpha}{\partial q} \right)_{q_0} \cdot q_0 \cdot E_0 \cdot \cos[(\omega_0 + \omega_q)t] \end{aligned} \quad (14)$$

This equation for the dipole moment describes the scattered radiation; the dipole acts as a source for the light re-emission. Therein, three terms with different oscillation frequencies are to be recognized:

- The first term $\alpha_0 \cdot E_0 \cdot \cos(\omega_0 t)$ describes the elastic *Rayleigh scattering*. The oscillation frequency and thus the frequency of the scattered light is the same as that of the incident radiation, namely ω_0 .

- The second term $\frac{1}{2} \left(\frac{\partial \alpha}{\partial q} \right)_{q_0} \cdot q_0 \cdot E_0 \cdot \cos[(\omega_0 - \omega_q)t]$ characterizes the inelastic *Stokes scattering*, where the oscillation frequency is red-shifted to the excitation frequency. The magnitude of the difference depends on the molecular system, i.e. ω_q , therefore representing the typical Raman spectrum.
- The third term $\frac{1}{2} \left(\frac{\partial \alpha}{\partial q} \right)_{q_0} \cdot q_0 \cdot E_0 \cdot \cos[(\omega_0 + \omega_q)t]$ differs from the second term in the sum $\omega_0 + \omega_q$. This means a blue shift of the frequency compared to the excitation frequency, which is then called *anti-Stokes scattering*. The spectrum is the same as in the Stokes scattering, however, the intensity is greatly reduced due to the lower probability of thermally excited vibrational states.

A look at the formula of the dipole moment also reveals the selection rule, which indicates whether a sample is Raman active or not. While the Rayleigh term depends on the equilibrium polarizability α_0 and is always non-zero, for Stokes and anti-Stokes there is only a contribution if the partial derivation of the polarizability with respect to the normal coordinate is not zero at equilibrium geometry $\left(\frac{\partial \alpha}{\partial q} \right)_{q_0} \neq 0$. Infrared-active samples differ in that the derivative of the dipole moment must not be zero $\left(\frac{\partial \mu}{\partial q} \right)_{q_0} \neq 0$. In contrast to Raman spectroscopy, infrared (IR) spectroscopy involves the absorption of infrared light by the sample through excitation of vibrations in the electronic ground state, with the absorption ana-

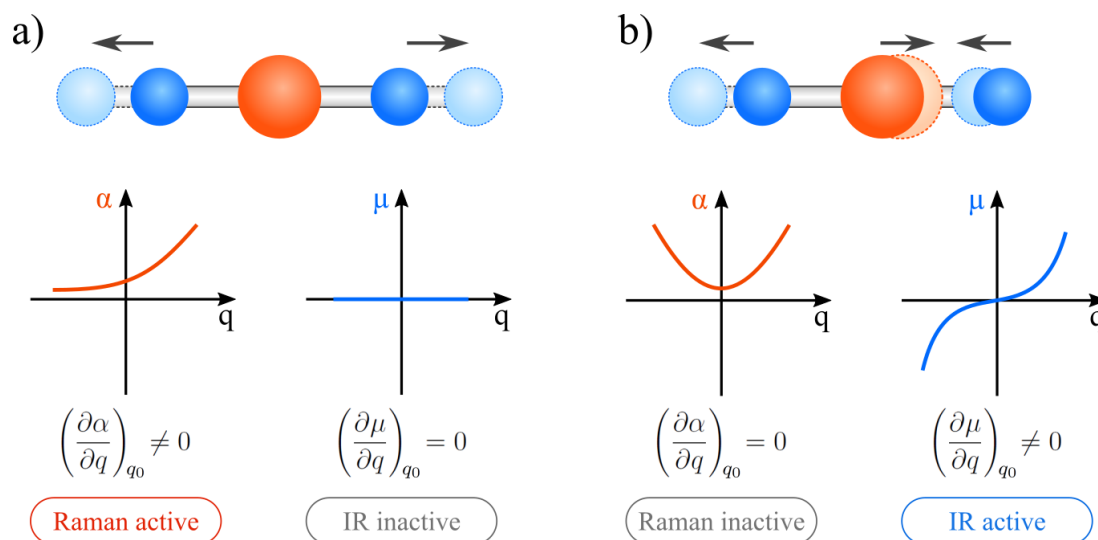


Figure 4.1: Two example vibrations of a linear triatomic molecule and the corresponding variations of polarizability (red) and dipole moment (blue). The partial derivative with respect to the normal coordinate at equilibrium position defines the Raman or IR activity of the molecule; adapted from Toporski et al.²²⁶

lyzed as a function of frequency. An illustrative comparison of the two cases is shown in Figure 4.1.

An example of a typical Raman spectrum is shown in Figure 4.2a. The energy shift becomes obvious when looking at the energy diagram, here simplified as a diatomic system. In Raman spectroscopy, the molecule is excited by the incoming photon. This does not require excitation to a discrete level of an electronically excited state, as is the case with fluorescence, for example, but excitation takes place to a virtual, intermediate state. Depending on whether the final position ends in an excited vibrational energy state or it starts from such a vibration state, the emitted photon has a red-shifted or blue-shifted frequency, representing the described Stokes or anti-Stokes scattering.

When the laser frequency, and thus its energy, matches an electronically excited state of the molecule, a significantly enhanced scattering intensity occurs. This is referred to as Resonant Raman scattering (Figure 4.2b). Not only the inelastically scattered light is observed, but after excitation to a discrete electronic level, fluorescence can occur. In fluorescence, the system relaxes after excitation to the lowest vibrational state without radiation, from where it then decays to the electronic ground state, emitting a photon (Figure 4.2b). In many cases, the fluorescence signal interferes as background with the evaluation of the Raman signal

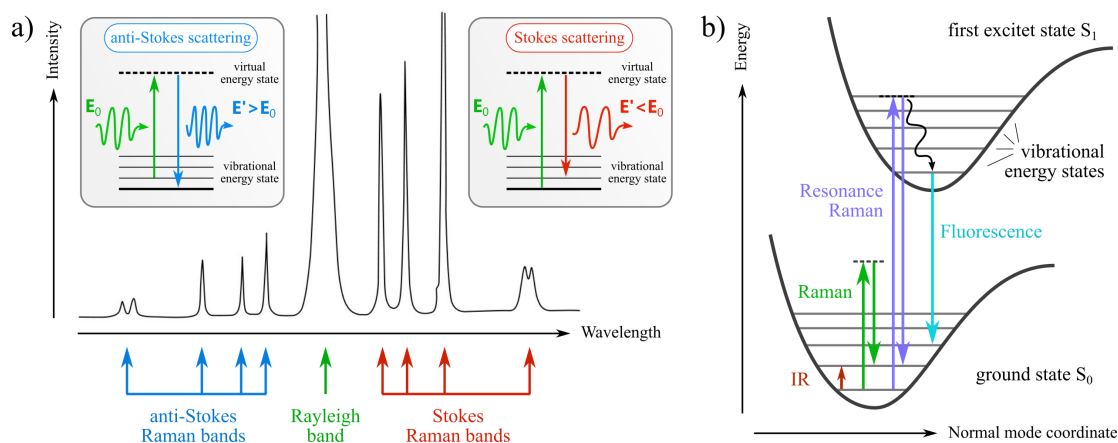


Figure 4.2: a) Raman spectra of liquid carbon tetrachloride (CCl₄), clearly showing the dominant Rayleigh peak in the center, the Stokes scattering peaks on the right, and the weaker anti-Stokes scattering peaks on the left (excitation by an Argon ion laser with wavelength of 488 nm). The insets show simplified Jablonski energy diagrams illustrating the process of Stokes and anti-Stokes scattering; spectra adapted from Long.²²⁸ b) Jablonski diagram of the electronic energy states for comparison between the different processes. Arrows indicate transitions of IR absorption, normal Raman, Resonant Raman, and fluorescence; adapted from Toporski et al.²²⁶

because, compared to Resonant Raman, fluorescence has a scattering cross section about six orders of magnitude larger.²²⁶

Besides Resonant Raman, it is possible to amplify the Raman signal by plasmonic resonances in metallic structures when the molecules are in their immediate vicinity. The strong field enhancement near the plasmonic structure results in enhanced excitation, and furthermore, the coupling leads to efficient emission of the Raman signal.^{229,230} Amplification factors of up to 15 orders of magnitude have been demonstrated in the example of the molecule rhodamine 6G in the vicinity of colloidal silver nanoparticles, proving the ability to detect even single molecules.²³¹ Well-known applications include Surface-Enhanced Raman Scattering (SERS), which employs a metallic surface or nanoparticles to amplify the signal, and Tip-Enhanced Raman Scattering (TERS), involving the tip of a scanning probe.

For MOFs, Raman spectroscopy is a valuable characterization technique²³² because the Raman scattering spectrum can provide insight into structural changes of the MOF or into the ligand-metal bonding relationship.^{233,234} Changes in vibrational modes of ligands caused by coordinative binding to the metal nodes can be exploited for purity control and ligand localization in the acquisition of two-dimensional Raman maps of a sample.⁵⁷ Raman spectroscopy can also be used during crystal growth to investigate the synthesis mechanism in more detail.²³⁵ In terms of sensing, one can analyze and detect interactions between MOFs and guest molecules using Raman spectroscopy, with the advantage of being label-free.^{236,237} As a SERS substrate, many MOFs are also capable of amplifying the Raman signal while bringing molecular selectivity to it.^{169,193,238}

4.2 Scanning electron microscopy

Scanning electron microscopy (SEM) uses high-energy electrons, rather than light as in optical microscopy, to produce an image of a sample. The image resolution and achievable magnification are considerably higher than with light microscopes. The resolution d generally depends on the wavelength λ of the beam used, as well as the numerical aperture NA, i.e. the refractive index n and the half aperture angle α , and can be written by Abbe's equation²³⁹:

$$d = \frac{0.612 \lambda}{n \sin(\alpha)} = \frac{0.612 \lambda}{\text{NA}} \quad (15)$$

Using visible light, the wavelength is about $\lambda = 500 \text{ nm}$, which gives a resolution in the micrometer range.

In quantum mechanics, not only light can be described by a wave, but also particles like the electron have a wave character and the sharp boundary between waves and particles becomes blurred. This phenomena is known as wave-particle duality. Just as light has a particle character (photons), other quantum objects, typically considered as particles, can be assigned a wavelength, the so-called *de Broglie* wavelength λ_{DB} ⁶³:

$$\lambda_{\text{DB}} = \frac{h}{p} = \frac{h}{\sqrt{2mE}} \quad (16)$$

Here, h is the Planck's constant ($6.626 \cdot 10^{-34} \text{ Js}$) and p is the momentum of the particle (unit: Ns), which can also be expressed by the particle mass m and the energy E . A typical electron energy for imaging of $E = 15 \text{ keV}$ then gives an electron wavelength of $\lambda_{\text{el}} \simeq 10 \text{ \AA}$, resulting in a resolution in the nanometer range, orders of magnitude smaller than with light.

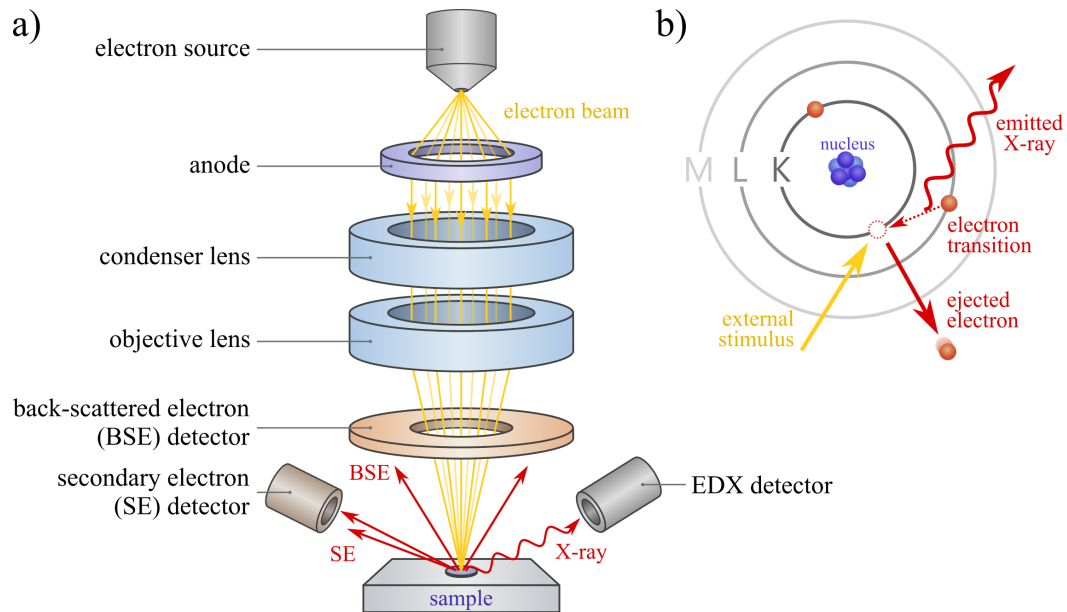


Figure 4.3: a) The general setup of an electron microscope. Electrons are emitted by a source and accelerated to the anode by a high voltage. Magnetic coils are used as lenses for the electrons to focus the electron beam onto the sample (here: condenser and objective lens). When they hit the sample, different interactions with the sample are possible, such as the emission of secondary electrons or the backscattering of electrons. Their detection leads to the creation of a monochrome picture. b) Simplified model of an atom showing the process of X-ray emission when electrons near the nucleus are ejected by external excitation. The resulting hole is immediately filled by electrons of outer shells with higher energy and the excess energy is released as a photon (X-ray).

The general setup of an electron microscope is shown in Figure 4.3a. The electron source (cathode) emits electrons which are accelerated to the anode by applying a high voltage. Magnetic coils, which serve as lenses for the electrons, are used to focus the electron beam onto the sample. When the electrons hit the sample, secondary electrons (SE) are ejected from the atoms on the surface and few nanometers below, which are then collected by a detector for image creation.²³⁹ This is how the topography of a sample is mapped, being the most common mapping method. Likewise, the back-scattered electrons (BSE) can be used for imaging. The strength of the backscatter depends on the mass of the element, which is why this method tends to reproduce the material contrast.

The image is generally formed by scanning the sample with the electron beam by magnetic deflection in the lateral plane. For each position, the scattering information as well as the energy of the detected electrons are then converted into gray scale information and translated into a monochrome picture. To avoid scattering of electrons with molecules in the air, the imaging process takes place in vacuum. SEM imaging is one of the standard analysis methods for MOF investigations, as a visual impression of the MOF crystals is obtained. At high resolution, even the crystal lattice geometry can be revealed.²⁴⁰ Tilting the sample stage during imaging also allows angled or lateral images of the sample to be taken, which is very useful e.g. when examining the profile of thin MOF films.²⁴¹ When processing MOFs into other structures, such as fibers or polymers, SEM can be used to evaluate the amount and efficiency of material functionalization.^{242,243}

4.2.1 Energy dispersive X-ray spectroscopy

In addition to the scattered electrons, it is also possible to detect emitted X-rays to obtain information about the material of the sample.²⁴⁴ The method is called energy dispersive X-ray spectroscopy (EDX) and is based on the fact that the energy of the X-rays is distinctive for the elements present. Emission is generated when the electron beam ejects electrons near the nucleus when it hits the sample. The resulting hole is filled directly by an electron from a higher orbital with increased energy, releasing the excess energy characteristic of the atom as a photon (Figure 4.3b). By detecting these X-rays, information about the element composition can be obtained.

Since MOFs always consist of metal nodes and organic ligands of a certain composition, EDX is very useful to map the MOF on the SEM image.²⁴⁵ For this, an element is usually targeted which is characteristic for the MOF, for example zir-

conium for UiO-66.²⁴³ This allows to determine the position of the MOF. If there are several distinct MOF architectures, they can be differentiated using EDX, such as for Cu-HHTP-TCNQ presented in Chapter 5.⁵⁷ The analysis also works for multivariate MOFs, i.e. structures consisting of multiple building units, and allows qualitative and quantitative study of their composition.^{246,247}

4.3 X-ray diffraction

X-ray diffraction is used to identify the atomic structure of a crystalline sample. Due to the wave properties of electromagnetic radiation, diffraction effects occur when the wavelength of the rays is of the order of the distance between the atoms. The lattice constant in a crystal lattice is in the Angstrom range, which is why no visible light ($\sim 400 \text{ nm} - 800 \text{ nm}$) but shorter wavelength X-rays are used for the sample examination.²⁴⁸

When X-rays encounter a crystalline object with a periodically ordered structure, the sample acts as a diffraction grating and the incoming radiation is scattered at the lattice planes. As a result, the incoming beams change their direction of propagation and interference occurs between the diffracted beams. Depending on the phase shift due to the path difference between the beams, constructive or destructive interference occurs (Figure 4.4a). Bragg's law describes the condition for

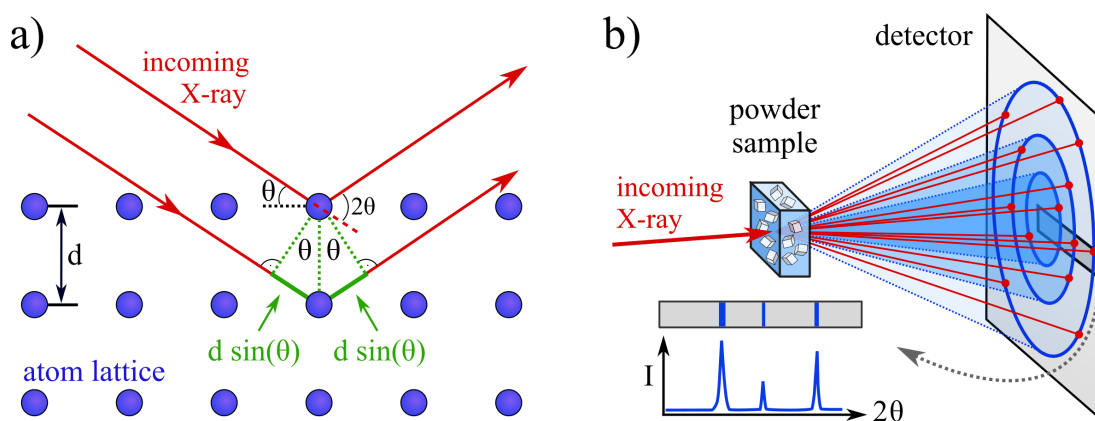


Figure 4.4: a) Schematic of the Bragg reflection. X-rays incident on an atomic crystal with lattice plane spacing d at angle θ are scattered and change their direction of propagation. The diffracted beams interfere with each other, with constructive Bragg reflection occurring when the path difference (here in green) is a multiple of the wavelength λ . b) Powder X-ray diffraction uses a powder sample consisting of many small randomly arranged crystals. Due to the random arrangement, some crystals always satisfy the Bragg condition and the diffracted beams lie rotationally symmetrically on the surface of cones, resulting in rings on the detector.

constructive interference, where the path difference is a multiple of the wavelength λ and intensity maxima can be found:

$$2d \sin(\theta) = n\lambda \quad (17)$$

with d the distance of the crystal planes, θ the angle between X-ray beam and lattice plane and n the order of the reflex.^{63,248}

The crystal structure and lattice parameter can then be determined from the diffraction pattern. Since there is more than one way to divide the crystal into lattice planes, there are different plane spacings d and thus scattering angles with constructive interference. Therefore, in a more detailed consideration, lattice planes are defined with the three *Miller indices* (h,k,l), which indicate the reciprocal plane intersections with the crystal axes. When examining a single crystal, a pattern of dots (intensity maxima) emerges, with each dot belonging to a specific lattice plane.⁶³

Often a powder sample is used instead of a single crystal, which consists of many small randomly arranged crystals. This approach is referred to as powder X-ray diffraction (PXRD, also Debye-Scherrer-approach) and has the consequence that there are always some crystals which satisfy Bragg's diffraction conditions.⁶³ As a result, the diffracted beams are rotationally symmetrical on the surface of cones with half opening angle 2θ (Figure 4.4b). Diffraction rings become visible on the detector, the diameter of which indicates the diffraction angle.

For MOFs, X-ray diffraction represents one of the most important analytical methods because their crystalline nature allows their structure and crystallinity to be determined. Most MOFs occur as powders, making PXRD the tool of choice. The individual scattering spectrum of each architecture makes the method very suitable for identifying the MOF, for example, after its synthesis.^{249,250} The evolution of MOF growth can be captured by taking snapshots during the synthesis process.⁹⁹ The sharpness of the peaks also gives information about the crystallinity of the MOF, which also makes X-ray diffraction a tool for determining amorphousness.^{251,252} Thin MOF films can be evaluated with XRD as well, but occasionally show weak signal strength due to the small amount of material.^{253,254} Most MOFs are stable to high-energy X-rays, however, irradiation of certain MOFs, e.g. from the ZIF family (zeolitic imidazolate frameworks) with high-energy radiation as in X-ray synchrotron studies can possibly lead to radiation damage such as amorphization and site specific structural damage and therefore radiation stability

should be tested in advance.²⁵⁵

4.3.1 Grazing-incidence small-angle X-ray scattering

Small-angle X-ray scattering (SAXS) is another method that uses X-rays to study larger mesoscopic structural features between about 1 nm and few 100 nm such as nanoparticles or nanopores, based on the fact that small scattering angles reflect larger dimensions.^{256,257} However, for samples with small scattering volumes such as thin films, the conventional transmission geometry of SAXS gives signals that are too weak. Grazing-incidence small-angle X-ray scattering (GI-SAXS) employs a reflection geometry for the study of film samples using an extremely flat X-ray incidence angle (typically below $< 1^\circ$).^{258,259} The grazing incidence approach leads to increased scattering cross-section and thus to a stronger signal. The measured scattering intensity at small exit angles then allows conclusions to be drawn about the structure such as in-plane lattice parameter and porosity of a material.

4.4 Atomic force microscopy

In general, atomic force microscopy (AFM) is a microscopy method in which a fine tip raster scans across the sample and by measuring the forces interacting between the tip and the sample, a topographic map is generated. Here, the achievable resolution depends on the tip diameter and can thus circumvent the resolution limit of diffraction-based methods. Nowadays, atomic resolution can be achieved by fabricating extremely pointed tips such as micromachined silicon cantilevers, allowing only few atoms at the tip to interact with the surface of the sample.^{260,261} The scan tip is attached to a cantilever, which bends due to the forces between the sample and the tip. The magnitude of the bending can be measured, for instance, by a laser that is pointed at the cantilever and reflected onto a photodetector. In this way, the surface profile of the specimen can be accurately reproduced. The basic construction of an AFM is shown in Figure 4.5a.

To perform the scan measurement, there are different approaches to direct the tip along the sample²⁶² (Figure 4.5b). In contact mode, the tip is in contact with the sample and moves over the surface, deflecting the cantilever to different degrees depending on the profile. The deflection of the cantilever can either be measured directly by a laser, or the cantilever can be held in the same position and the piezo current required to counteract the force is measured. In non-contact mode, the cantilever is excited by a periodic force (e.g. piezo element) to oscillate at a

frequency close to the resonance frequency. The tip has no contact to the sample, but near the surface interactions between tip and sample (e.g. van der Waals) lead to a change of the oscillation frequency, which then provides the surface information. The tapping mode is similar to non-contact mode, but the oscillation is closer to the surface and the tip intermittently taps the sample as it scans the surface, thereby reproducing the surface profile.

AFM is widely used to determine the thickness of MOF nanosheets or thin MOF films.^{250,263} For this purpose, a profile scan is performed either at the edge of the film or at a crack, be it a self-induced or a naturally occurring one. 2D AFM scans also allow the detection of the MOF film topology and surface roughness.²⁶⁴ However, this is not limited to thin films. In the functionalization of fibers, for example, AFM can also show the nature of the fiber surface, providing additional information to visual methods such as SEM.²⁶⁵ Furthermore, in situ AFM measurements were used to identify the crystal growth mechanism of MOFs like MOF-5.²⁶⁶ By combining AFM with spectroscopic methods such as Raman spectroscopy, topographic and chemical information can be linked to provide a better understanding of MOF architecture.^{267,268} A combined confocal Raman AFM even allows simultaneous acquisition of such material data, as demonstrated in the study of thin polymer films²⁶⁹ or nanocomposite films.²⁷⁰

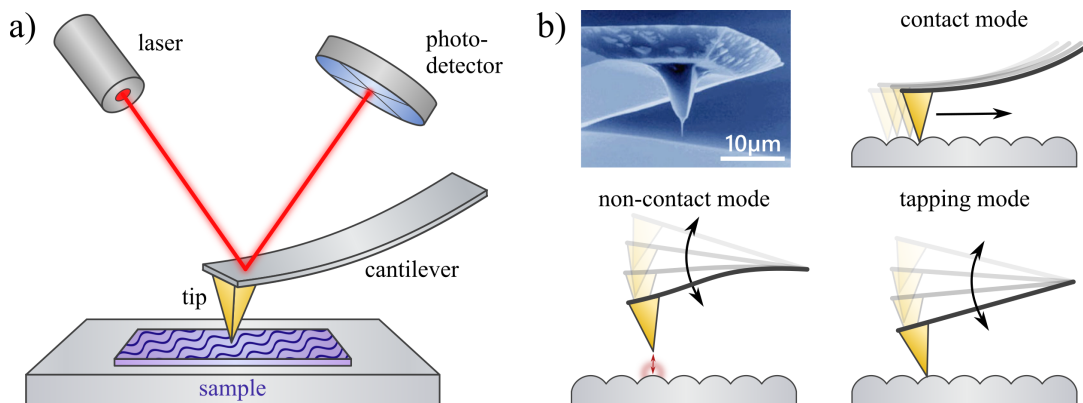


Figure 4.5: a) The general construction of an atomic force microscope. A cantilever with a sharp tip scans the surface profile of the sample. The resulting deflection of the cantilever can be measured by using a laser, which is directed at the cantilever and whose displacement is measured by a photodetector. b) Illustration of different imaging modes: contact mode, non-contact mode and tapping mode. The photo top left shows an extremely fine tip on a micromachined silicon cantilever, manufactured by Nanosensors GmbH und Co. KG Germany; adapted from Giessibl.²⁶⁰

4.5 Gas adsorption

A central question when working with porous materials such as MOFs is the characterization of the pore volume and the intrinsic surface area, because these are target properties for many applications. A common method for evaluating such material properties is gas adsorption and the application of the theory of Brunauer, Emmett and Teller, in short BET.^{44,271} Generally, the porous material is filled with a certain gas and the pressure is increased. The gas molecules adsorb on the surface and fill the pores with increasing pressure (Figure 4.6). From the amount of adsorbed gas molecules in relation to the pressure, the surface area can be inferred.

The pressure dependence of the adsorbed gas quantity also depends on the size of the pores. A distinction is made between micro-, meso- and macropores. Micropores are pores with widths smaller than 2 nm and macropores have widths larger than 50 nm. Everything in between is called mesopores.²⁷² During the adsorption process, monolayer formation and filling of small pores occurs, later also multilayer formation. The plot of the gas uptake against relative pressure (at constant temperature) leads to a certain curve, which is called sorption isotherm. From the shape of the curve, e.g. hysteresis occurring during the desorption process or plateaus, conclusions can be drawn about the size and structure of the pores. The isotherms were originally classified by Brunauer, Deming L., Deming W., and Teller into different categories, depending on the type of porosity present.^{45,272}

For a theoretical description of the physisorption of gases at the material surface, the model of Langmuir, which assumes a limited number of sites for adsorption, is used at the beginning.²⁷³ The gas molecules form a monolayer on the homogeneous surface of the adsorbent, thereby assuming strong interactions (chemisorption). The gas uptake goes into saturation and the isotherm that can be observed has the form of a type I (Figure 4.7a). However, the Langmuir model is not applicable for a real physisorption process, where usually weak adsorption occurs and multilayers are formed.^{35,274} For example, microporous materials exhibit an isotherm similar to type I, but it is less related to monolayer formation than to the filling of micropores.^{35,272}

For this reason, the Langmuir model was extended by Brunauer, Emmett and Teller such that the physisorption process is not limited to monolayer adsorption, which is important when it comes to larger pores.^{44,274,275} The idea behind the BET model is that the monolayer capacity can be extracted even though in reality

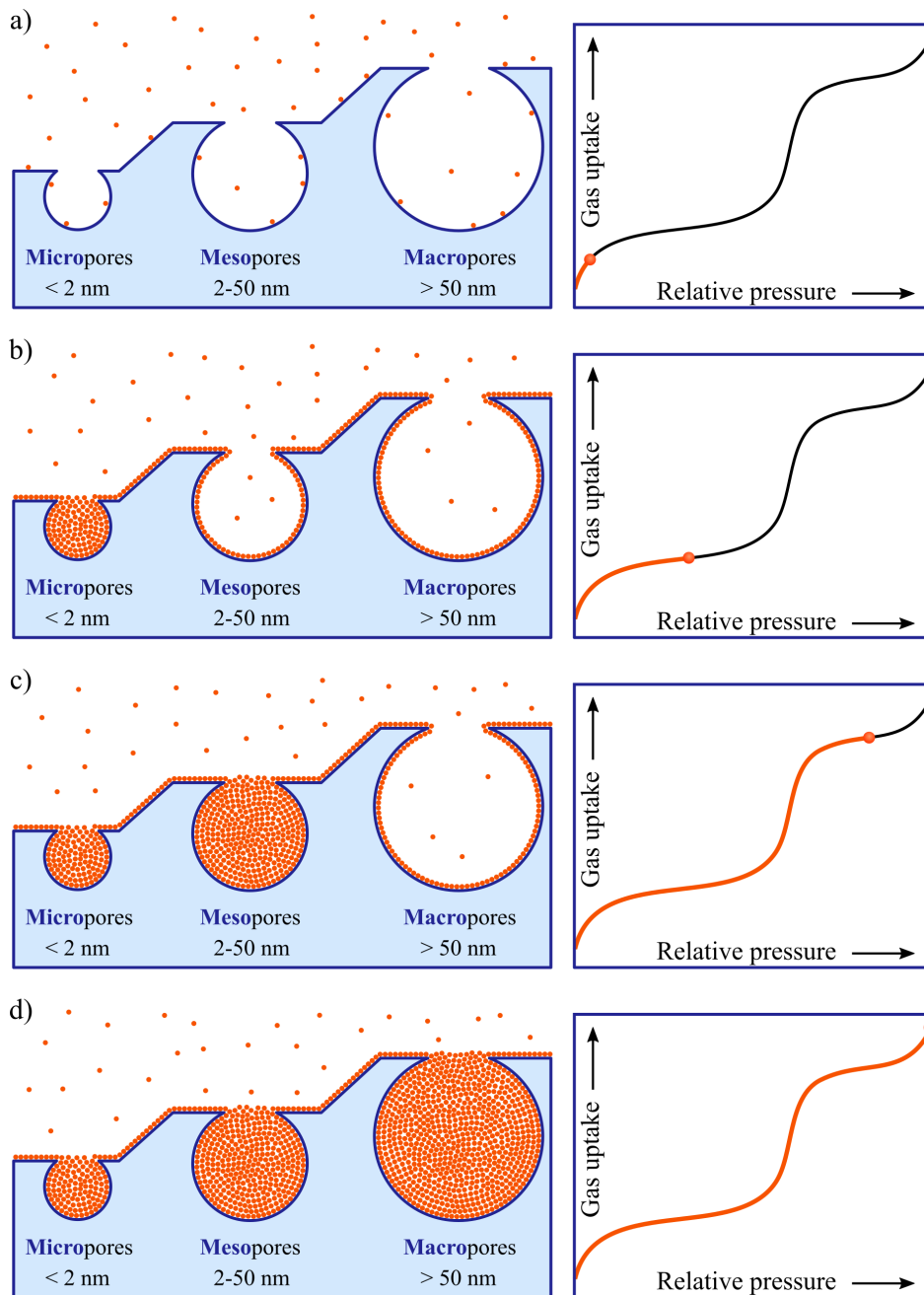


Figure 4.6: Simplified schematic representation of the gas adsorption process for a porous material with corresponding isotherms. a) At low pressure, only a few gas molecules are adsorbed on the material surface. b) When the pressure is increased, micropore filling occurs resulting in a plateau in the isotherm. c) When mesopores are filled at higher pressure, an increase in the isotherm can be observed, which then also turns into a plateau. d) Close to bulk saturation pressure, large macropores are filled; adapted from Yaghi et al.³⁵

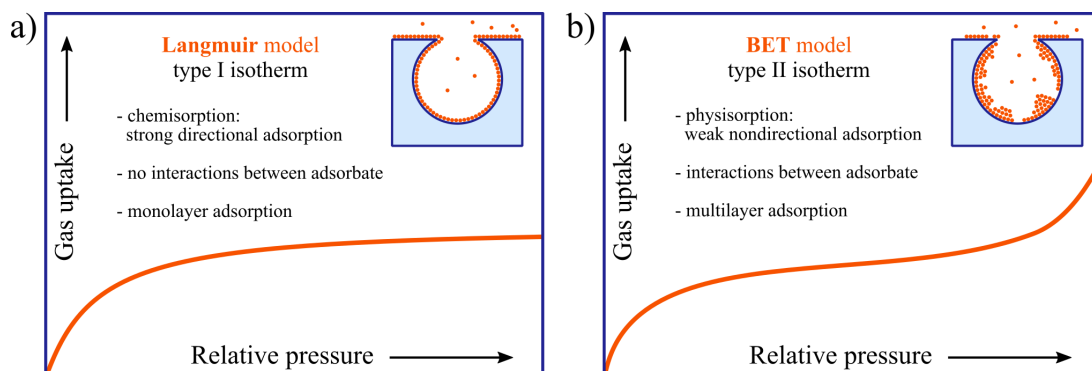


Figure 4.7: Illustration of the Langmuir and BET adsorption models. While the Langmuir model (a) describes the formation of monolayers of the gas molecules assuming strong adsorption (chemisorption), the BET model (b) takes multilayer formation into account due to undirected physisorption and interactions between the adsorbate; adapted from Yaghi et al.³⁵

a monolayer is never formed. Therefore, the BET model has become one of the most commonly used models for determining surface areas of porous materials (Figure 4.7b).^{35,271,272} The BET equation in its linear form is as follows (for the detailed derivation, the interested reader is referred to further literature^{35,275}):

$$\frac{P}{n(P_0 - P)} = \frac{1}{n_m c} + \frac{c - 1}{n_m c} \frac{P}{P_0} \quad (18)$$

$\frac{P}{P_0}$ is the relative pressure with P_0 indicating the saturation pressure, c is a constant that is related to the enthalpy of adsorption, n is the total amount of adsorbed gas (in moles) and n_m declares the monolayer capacity, means the amount of gas adsorbed within a monolayer (in moles). The latter is related to the surface area and can be obtained from a linear regression in the BET plot $\frac{P}{n(P_0 - P)}$ versus $\frac{P}{P_0}$. With the knowledge of the gas used (mostly nitrogen, sometimes argon) and the size of the cross-section area taken up by a single gas molecule a_m , the BET surface area A_{BET} can be calculated:²⁷²

$$A_{\text{BET}} = n_m N_A a_m \quad (19)$$

with N_A the Avogadro constant ($6.022 \cdot 10^{23} \text{ mol}^{-1}$).

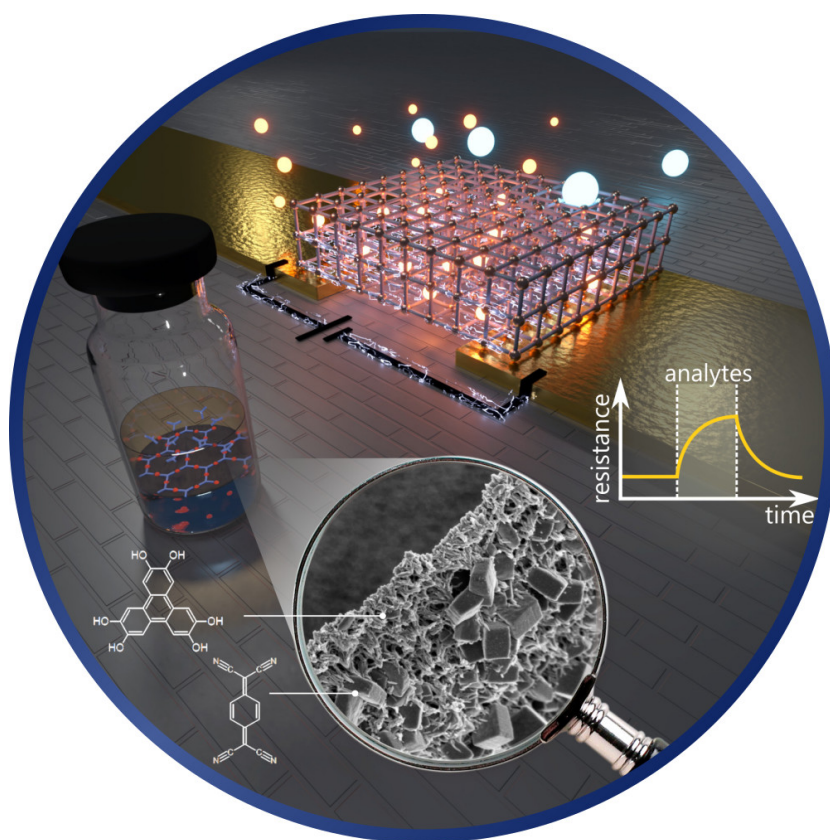
Since porosity is an important property for MOFs, the intrinsic surface is almost always assessed by gas adsorption and often compared to simulated values, especially after synthesis of new MOF types.^{25,276} When decorating other materials with MOFs, such as fibers, gas adsorption is also used as a method to see to what

degree the functionalization has been successful. The higher the evaluated surface area, the more accessible the MOF and its pores for the target application.^{99,242,265}

4.6 Concluding remarks

We already know that the large number of different MOFs is associated with diverse properties, which is precisely why it is essential to use many different characterization methods to gain a complete picture of the material properties. It is comparable to a jigsaw puzzle, in which the final picture can only be seen when all the pieces of the puzzle have been correctly assembled. Similarly, a multiparametric analysis of a nanomaterial such as MOFs using different characterization methods, where each method depicts a different aspect, allows a deeper understanding of the material properties. These include the techniques already mentioned for obtaining information on crystallinity, surface properties, and chemical composition, which is why we will encounter them in the following chapters.

Design, synthesis and characterization of conductive MOFs for sensing



Hybrid structures are obtained by combining different building units, which offers a broader range of options for adjusting the structure and thus the properties such as electrical properties.

In this chapter, we present the synthesis and characterization of a conductive hybrid MOF film, composed of copper ions and two different organic ligands and demonstrate its chemiresistive sensing response towards ambient changes.

Parts of this chapter have been published in *Advanced Electronic Materials* (Lüder et al.⁵⁷). Supporting information is included at the end of this chapter.

5.1 Introduction

We have already seen that conductive MOFs and MOF-like coordination polymers are an emerging class of materials in the field of sensing because they also bring their unique properties and advantages such as nanoporosity or tailoring to specific properties. In general, highly crystalline defect-free MOFs are preferred for electrical charge transport over randomly arranged architectures because their periodic structure leads to high mobility.^{58,277,278} Nickel (II) hexaiminotriphenylene (Ni-HITP)⁷⁴ and copper (II) hexahydroxytriphenylene (Cu-HHTP)^{73,250} are two examples from other work where it has been shown that single crystals and well-grown MOF films with high structural order generally exhibit better conductivities than pressed powder.

However, the inherent crystallinity of MOFs also typically makes them brittle, which often complicates their integration into flexible systems. Amorphous MOFs, i.e., MOFs without long-range periodic order, usually exhibit higher mechanical robustness and isotropy than their crystalline equivalents.^{251,279,280} This allows them to be used in a wider range of applications, for example, for incorporation into flexible devices.^{281–283}

The presented approach of using copper ions and two different organic ligands hexahydroxytriphenylene (HHTP) and tetracyanoquinodimethane (TCNQ) enables the formation of a heterogeneous hybrid MOF structure that lacks long-range ordering without sacrificing conductivity (hereon referred to as Cu-HHTP-TCNQ). MOF hybrids have great potential, as they have already demonstrated improved characteristics, such as enhanced performance in separation, energy conversion, or catalysis.²⁸⁴ The Cu-HHTP-TCNQ hybrid film structure presented in this work exhibits a good compromise between structural order and conductivity, providing an average conductivity of 0.033 S cm^{-1} and a chemiresistive response toward ambient changes, despite its discontinuous architecture and its highly amorphous phase. The heterogeneous nature of the film was studied multi-parametrically, yielding information about its structural, chemical, and electrical properties. Glass substrates with prepatterned gold electrodes were fabricated for the electrical and chemiresistive measurement in a four-wire configuration on the deposited Cu-HHTP-TCNQ films. In summary, this work shows that hybrid framework architectures are promising active materials for chemiresistive sensors without the need for high crystallinity.

5.2 Synthesis approach

For the synthesis of the MOF films, an interfacial approach was chosen, consisting of two immiscible liquid phases (Figure 5.1a). This synthesis has been used successfully before and has the advantage that the film thickness increases uniformly over time.^{241,285} The principle is based on the dissolution of the organic ligands in one solvent and the metal source in the other solvent. At the interface, the ligands and the ions meet and coordinate to form a MOF. The end result is a free-standing film that can be deposited on a wide variety of substrates.

In our case, water and ethyl acetate were used as solvents. Cu(II) nitrate was dissolved in water, and both ligands 2,3,6,7,10,11-hexahydroxytriphenylene (HHTP) and 7,7,8,8-tetracyanoquinodimethane (TCNQ) were dissolved in the organic solvent (Figure 5.1b). Details on quantities and exact procedure are given in the

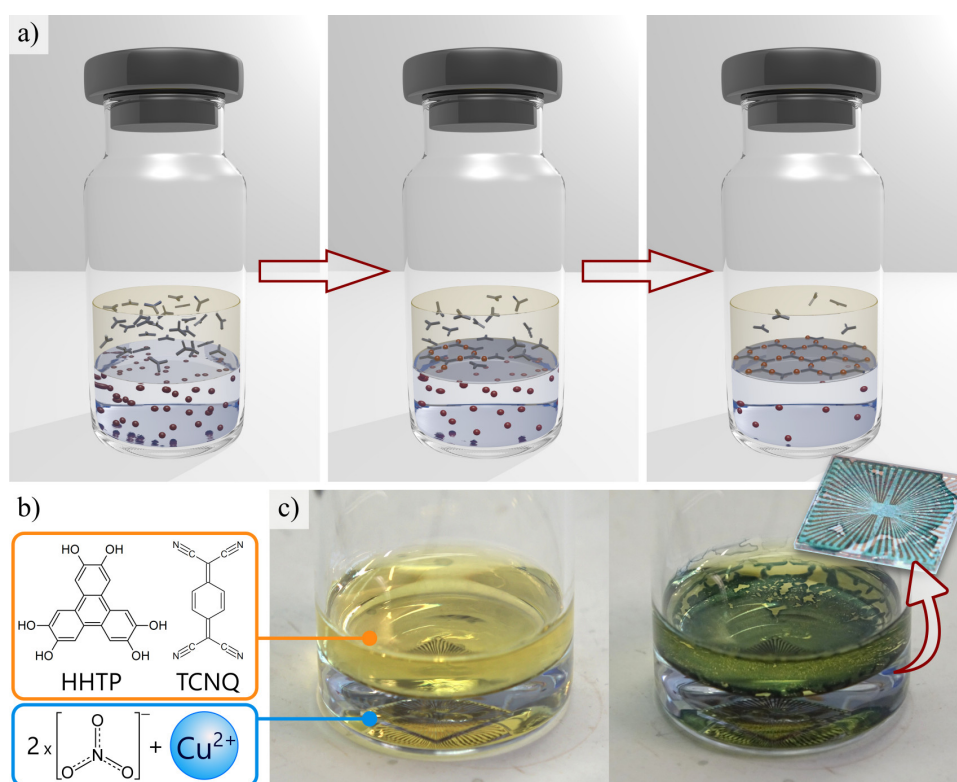


Figure 5.1: a) Schematic illustration of the formation process of thin Cu-HHTP-TCNQ MOF films at the interface between bottom aqueous and top organic phase. Diffusion lets the separately dissolved metal ions and organic ligands meet at the interface, forming a coordinative bond. b) Molecular structures of the organic ligands HHTP and TCNQ as well as copper nitrate as metal source. c) Photograph of interfacial film growth of Cu-HHTP-TCNQ at starting time (left) and after 15 min (right), showing the fast growth of the dark film. Inset: Photograph of the film directly after deposition on a glass chip with gold electrodes.

Appendix A.1. When the phases were combined, the coordination reaction between Cu^{2+} -ions and the ligands began and a film formed was visible within 1 min at 0 °C. Since the film was still very thin at the beginning, it was almost transparent, but already after 15 min at the latest, a black film has emerged (Figure 5.1c). The size of the film is determined by the dimensions of the reaction vessel; in our case it covered an area of about 5 cm². This film will from now on be referred to as Cu-HHTTP-TCNQ hybrid films. The formation of a continuous film started only when both ligands HHTTP and TCNQ were added in combination. The addition of TCNQ alone had not started any macroscopic reaction with the copper ions and HHTTP alone resulted in the slow formation (after 1 h) of an unconnected powder known to consist of multiple nanosheets.²⁶⁴

After synthesis of the freestanding Cu-HHTTP-TCNQ film, it had to be transferred to a substrate for structural and electrical measurements. During this step, the film can easily break if the mechanical shocks are too strong while it is still floating. Before starting the reaction, a substrate of choice has been placed on the bottom of the reaction vial. After film formation, the liquid was carefully removed with a syringe so that the film slowly sank down and remained on the substrate. Glass substrates with prepatterned gold electrodes were used as substrates for electrical and other structural investigations (Figure 5.1c inset; fabrication details in Appendix A.2), but other substrates such as silicon wafers were also used. Depending on the substrate, the wetting properties may differ and complicate the deposition of the film. A short air plasma on the substrate before placing into the vial facilitated film deposition, in part because it completely removed any resist residues on the chip (Supporting Information Figure 5.20). Once the film is transferred, it stays stable for analysis.

5.3 Structural characterization

Scanning electron microscopy

First, the Cu-HHTTP-TCNQ film is subjected to a visual examination via SEM. Figure 5.2 shows a top view and a side view of the film. On the one hand, you can see many filamentous features, which are mostly arranged vertically with respect to the film extension. This creates a continuous film that has gaps in some places. On the back side of this layer, i.e. on the side which was facing the water during the reaction, there are many crystalline cubes. This can be deduced from the parts of the film that were folded over during deposition, thus allowing a view of the

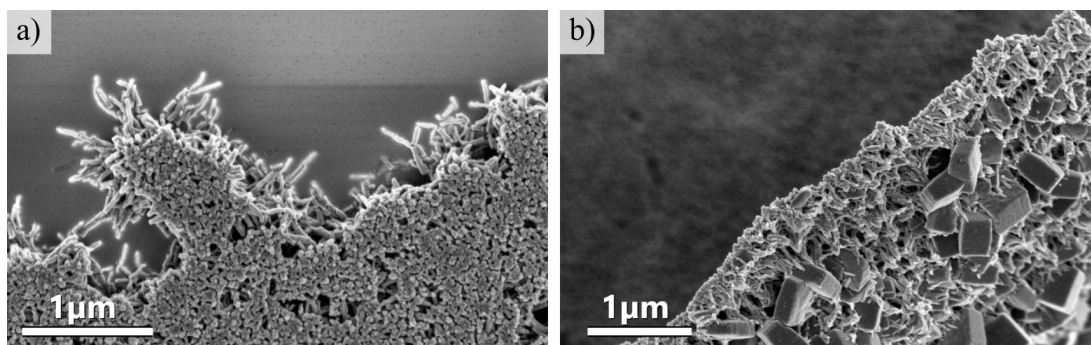


Figure 5.2: Scanning electron microscopy (SEM) images of Cu-HHTP-TCNQ thin films with 60 min reaction time from the top (a) and from the bottom (angled) (b), showing filamentous features substantially aligned in parallel and cubic crystals on the film downside.

back. There is no regular arrangement of the cubes, which extend over the entire film. Films with only 10min reaction time were examined and already showed the appearance of the cubes (Supporting Information Figure 5.16a). In some places, there are long crystals that seem to have their origin in the film backside at the cubes. Their anisotropic growth in length makes them stand out perpendicular to the film (Supporting Information Figure 5.16c,d).

Atomic force microscopy

To get a more detailed understanding on the morphology and thickness of the film, AFM measurements were performed on films with different synthesis times. The AFM topographs are shown in Figure 5.3. The thinnest film had a reaction time of 10 min and was just manageable (Figure 5.3a). It was not yet completely closed and still had holes in some places. Already after 20 min reaction time the film was closed and continuous (Figure 5.3b). The reaction time was increased to 80 min until no major change was observed anymore (Figure 5.3f). The elevations formed are probably due to the cubic crystals in addition to the continuous film. Due to limitations in the large area AFM scan, the film with 60 min reaction time is shown in Figure 5.3e with a different scale. High resolution images are also displayed in Figure 5.17 in the Supporting Information. Line profile scans were performed on each film at the border and then the mean film thickness was correlated with the reaction time (Figure 5.3g and Supporting Information Figure 5.18) It can be seen that thicker films are measured for longer reaction times. Film growth is initially faster due to the easy diffusion of the reagents, but slows down with increasing film thickness. Further, fluctuations in synthesis and variations in

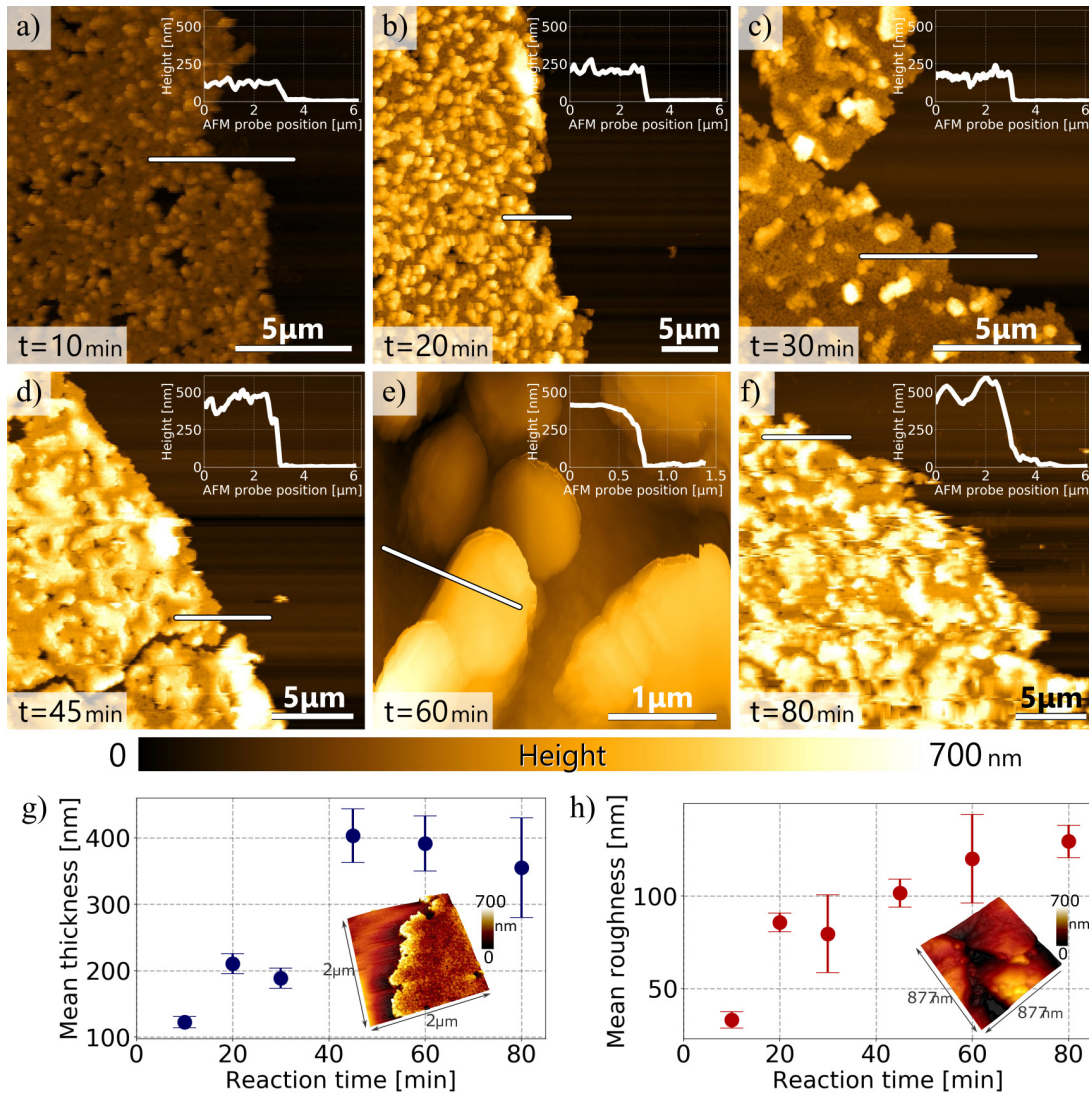


Figure 5.3: Topography of Cu-HHTP-TCNQ films measured by atomic force microscopy (AFM). Films have reaction times from 10 min (a) to 80 min (f). Profile line scans were performed on all scanned areas to evaluate film thickness. Selected profiles are shown as inset. g) Mean film thickness over reaction time, evaluated from profile scans at five different edge positions. Film thickness increases for longer reaction times. Inset: 3D topography of selected film border for better overview. h) Root mean square roughness over reaction time, evaluated at five film sections. Film roughness increases for longer reaction times. Inset: 3D topography of selected film section for better overview.

the heterogeneous material result in a non-steady increase in thickness over time. The continued growth in the liquid phase also leads to a roughening of the film. This is shown in Figure 5.3h, where the root mean square roughness of the film is plotted against reaction time.

X-ray diffraction

Different diffraction methods such as X-ray diffraction (XRD) were performed to get a more accurate picture of the structure of Cu-HHTTP-TCNQ. The XRD signal is shown in Figure 5.4 and shows a relatively strong background signal. This is due to the high amorphous content of the sample and could be caused by the combination of two different ligands, which disrupts the order of the film and leads to a lower crystalline structure and less long-range order. To exclude weak peaks from the sample environment, a background measurement was performed. Although X-ray characterization of amorphous MOFs is more difficult because of to the absence of Bragg peaks in the diffraction patterns²⁵¹, the results reveal the presence of coordinated HHTTP and TCNQ ligands, which form two crystalline phases within the film. The diffraction peaks of the individual components Cu-HHTTP and Cu-TCNQ are known from the literature and can be assigned to the measured peaks. For example, the reflections (100), (200), and (001) belong to known diffraction peaks of crystalline Cu-HHTTP^{250,264} and correspond to the 2D polymer in-plane long-range ordering, or π - π stacking in the latter case. In the case of Cu-TCNQ, it is known that two different phases with different crystal structures can be formed (phase I and II). The reflections (011), (002), (012), and

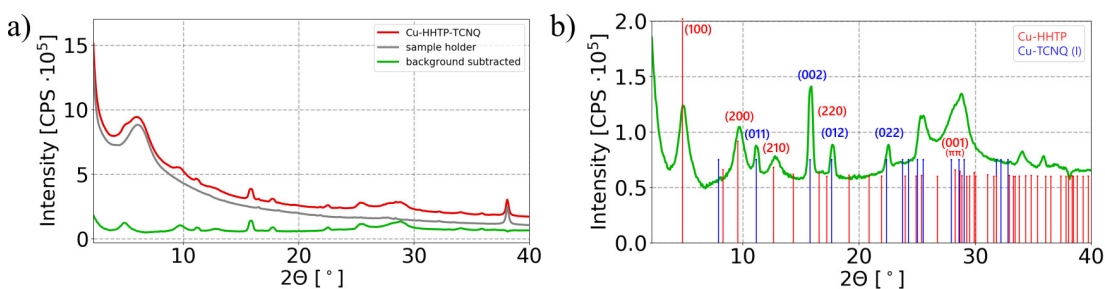


Figure 5.4: a) X-ray diffraction (XRD) pattern of Cu-HHTTP-TCNQ, which is measured as powder in reflection mode for 60 h. A background measurement (sample holder without sample) was carried out with same parameters and background subtraction from the Cu-HHTTP-TCNQ signal was performed. b) Zoom-in for the background subtracted pattern. Peaks representing the crystalline part can be seen on a background, which indicates the amorphous quantity. The lines show the position of known reflections from Cu-HHTTP (red) and Cu-TCNQ (I) (blue).

(022), among others, can be clearly assigned to Cu-TCNQ (phase I).^{286,287} For the quantification of the phase I we would require atomic coordinates, which are not available to the best of our knowledge. Features of Cu-TCNQ phase II were not detected in the XRD pattern. The Scherrer formula can be used to estimate the crystallite size for selected crystal orientations. For Cu-HHTTP ((200)-reflection) it gave a crystallite size of 12 nm and for Cu-TCNQ (I) ((002)-reflection) a crystallite size of 24 nm. No changes in the XRD pattern were measured when Cu-HHTTP-TCNQ was washed and dried compared to the signal measured immediately after synthesis. This indicates a stable and reproducible structure.

Another indication of the largely amorphous structure of the films can be obtained by transmission electron microscopy (TEM) and corresponding selected area electron diffraction (SAED). The examination showed no diffraction peaks for the most part of the film, with a few exceptions, but these occur randomly. As can be seen in Figure 5.5, the diffraction signal cannot be assigned to the crystalline cubes or the continuous film.

Often the porosity is determined with BET gas sorption methods. In this case, however, the amount of Cu-HHTTP-TCNQ was too low. Grazing-incidence small-angle X-ray scattering (GI-SAXS) can be used to determine the presence of porosity. Figure 5.6 shows the scattering intensities of a Cu-HHTTP-TCNQ film deposited on a silicon substrate in the range of $0.1\text{-}1\text{ nm}^{-1}$. The scattering intensity is about five times stronger than that of a reference silicon substrate, indicating the presence of nanoscale pores in the sample.

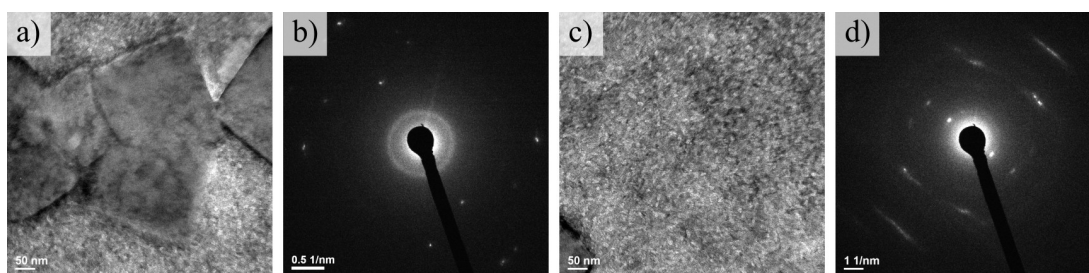


Figure 5.5: Transmission electron microscopy (TEM) images of Cu-HHTTP-TCNQ (a,c) and the corresponding selected area electron diffraction (SAED) signals (b,d). a) and b) show regions with crystalline cubes, whereas c) and d) display a location without cubic crystals. The camera lengths are 100 cm (b) and 60 cm (d) respectively.

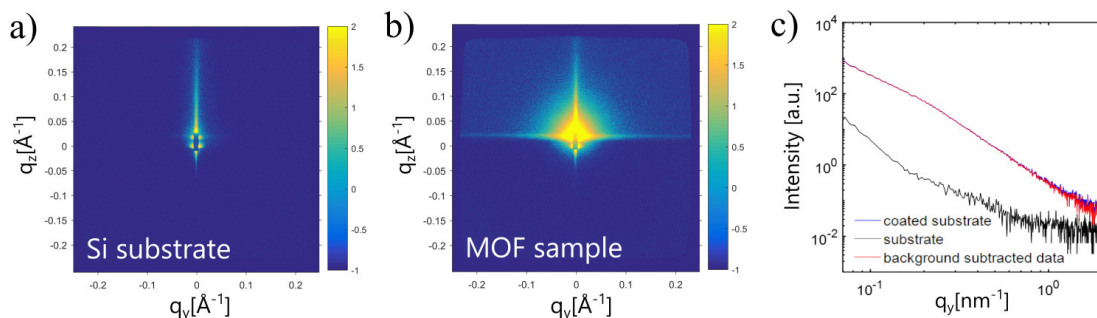


Figure 5.6: Grazing-incidence small-angle X-ray scattering (GI-SAXS) intensity plots of pure silicon substrate (a) and Cu-HHTTP-TCNQ film deposited onto a silicon substrate (b). c) Lateral scattering intensities (in plane, q_y), obtained by line integration along the lateral direction for both substrate and MOF coated samples.

5.4 Chemical characterization

Energy dispersive X-ray spectroscopy

Energy dispersive X-ray spectroscopy (EDX) can be used to map the elemental distribution. Since oxygen occurs only in HHTTP and nitrogen only in TCNQ, the EDX analysis allowed the localization of their occurrence within the film. A region of the continuous film that contained crystalline cubes as well is shown in Figure 5.7. EDX analysis revealed that oxygen is exclusively present in the continuous film. However, no oxygen was measured in the crystalline cubes (Figure 5.7b). This indicates the presence of the ligand HHTTP in the continuous part, which is further supported by the fact that this part of the film consisted of elongated rods, since Cu-HHTTP is known to form hexagonal-shaped filamentous rods.^{73,240} In contrast, the mapping of nitrogen showed an inverse picture. Nitrogen was in fact clearly concentrated in the cubes, but only weakly in the continuous part. Besides TCNQ, residual nitrate salt could also be the source of the nitrogen signal. However, oxygen is also present in the molecular structure of nitrate, which is why the signal in the cubes could be attributed to TCNQ. The distinction between the organic ligands HHTTP and TCNQ and their localization does not yet say anything about their coordination to copper. EDX analysis showed that copper and carbon were homogeneously distributed throughout the film, which makes it difficult to say anything about the nature of their coordination.

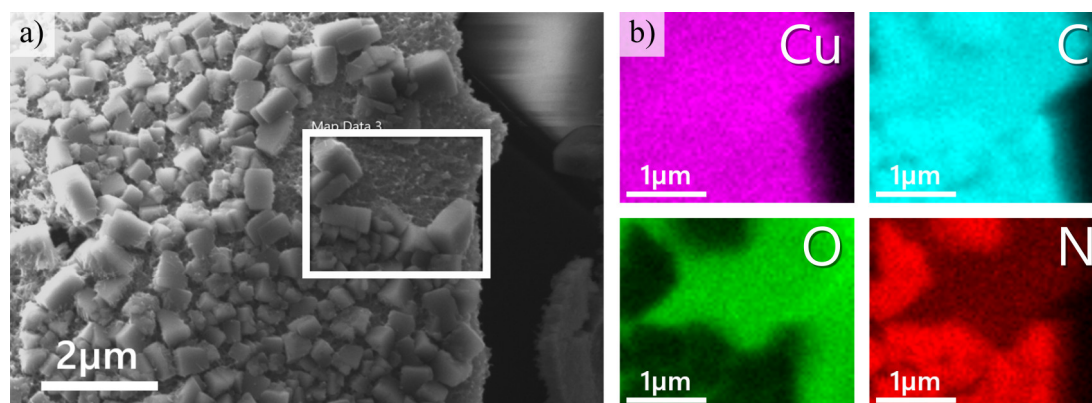


Figure 5.7: a) SEM image of Cu-HHTTP-TCNQ, showing the continuous film with cubic crystal structures. The white box shows the position of performed EDX measurement. b) Energy dispersive X-ray (EDX) spectroscopy maps of the elements copper (purple, Cu), carbon (cyan, C), oxygen (green, O) and nitrogen (red, N). The distribution shows an accumulation of nitrogen in the cubic crystals, whereas oxygen is entirely present in the filamentary features. Copper and carbon are evenly distributed over the film.

Raman spectroscopy

The coordination between the organic linkers and the copper ions can be identified using Raman spectroscopy. Figure 5.8 shows the Raman signals acquired at different positions of the Cu-HHTTP-TCNQ film. The compound Cu-HHTTP alone has no distinct Raman peaks according to literature.²⁸⁸ It is known that the ligand HHTTP can exist in seven different oxidation states, resulting in the blending of several vibrational modes.⁷⁶ In contrast, TCNQ and Cu-TCNQ show clear Raman spectra with mainly four different vibrational modes.^{234,287,289} The blue spectrum in Figure 5.8 agrees very well with literature data for noncoordinated TCNQ. The red spectrum shows a similar pattern to the blue, with the C–CN stretching mode at the wavenumber 1450 cm^{-1} (blue box) shifted to a lower wavenumber 1380 cm^{-1} (red box). The shift can be attributed to a charge transfer due to the coordination of TCNQ with copper ions.²⁸⁷ The Raman signal of Cu-TCNQ also includes another shift of the C–N stretching mode at 2225 cm^{-1} to lower frequencies and the appearance of a new mode at 735 cm^{-1} . The green spectrum shows a different pattern than that of the other two. It is likely the weak signal coming from Cu-HHTTP, as the signal is consistent with positions where Cu-HHTTP is known to be Raman active.²⁸⁸

Information about the location of the Raman signal can be obtained by a 2D Raman scan. An area of cubic crystals in the continuous film, as identified by optical microscopy, was selected for a Raman scan (Figure 5.9a). SEM images were

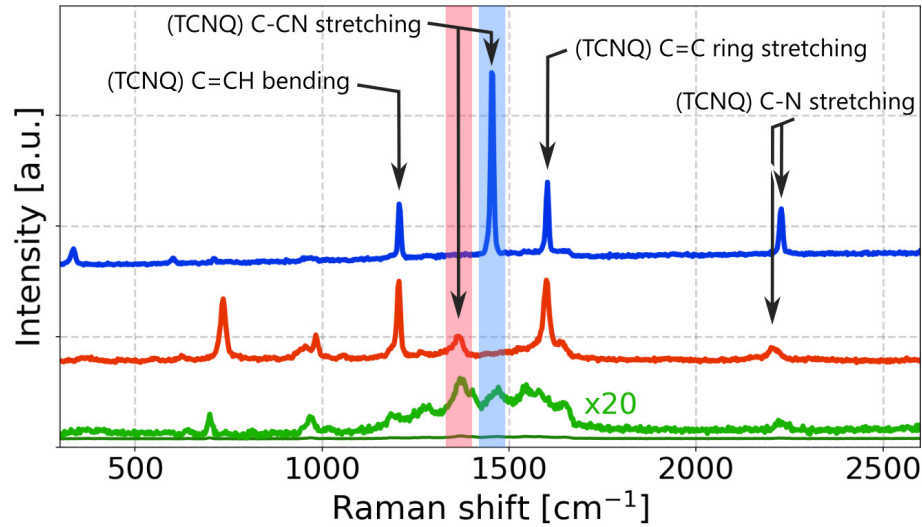


Figure 5.8: Raman spectra at three different positions on the Cu-HHTP-TCNQ film. Noncoordinated TCNQ molecules have a prominent peak at 1450 cm^{-1} (blue box) based on the C–CN stretching mode, which shifts to 1380 cm^{-1} (red box) when coordinating to copper ions. The spectra are plotted with an offset for clarity and the green spectrum is also displayed with a multiplication factor of 20.

taken at the same position to increase the resolution. The acquired 2D intensity plots were then overlaid with the microscope images to map the signal from the ligands. Figure 5.9b shows the combined image for wavenumber $1380 \pm 30\text{ cm}^{-1}$, which represents the presence of TCNQ molecules coordinated to copper ions. Interestingly, a strong signal was measured where the cubic crystals were present. This clearly indicates the high concentration of coordinated TCNQ molecules in the cubes, which is also consistent with the enrichment of nitrogen known from the EDX measurements (Figure 5.7). A different picture is seen in the intensity plot at $1450 \pm 30\text{ cm}^{-1}$, shown in Figure 5.9c. There is no increased signal at sites with cubic crystals, implying that there are no noncoordinated TCNQ molecules accumulated there. Only a few random spots show a Raman signal at 1450 cm^{-1} , otherwise no strong intensity is measured, which implies that there is no significant amount of noncoordinated TCNQ.

When the Cu-HHTP-TCNQ film was viewed under a larger scale by optical microscopy, regions of different optical appearance were detected (Figure 5.10). A closer inspection via SEM reveals that this impression is due to an unequal density of crystalline cubes within the regions. The continuous film was more disrupted and less connected in the parts with higher concentrations of crystalline cubes. Raman scans in the border region revealed a stronger signal at 1380 cm^{-1} on one

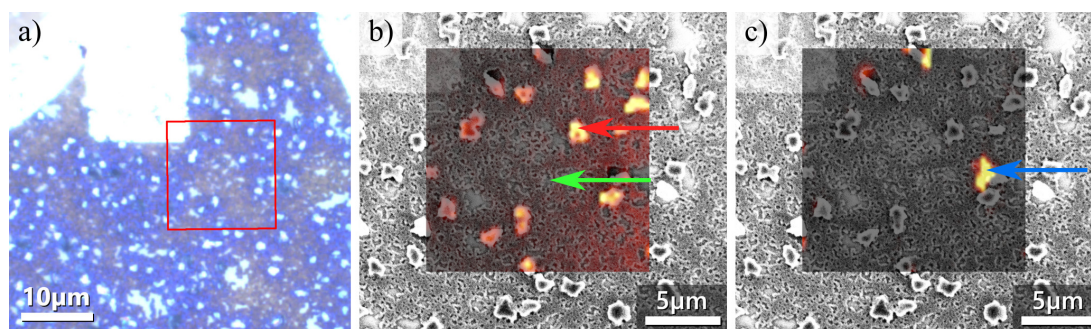


Figure 5.9: a) Optical microscopy image of Cu-HHTP-TCNQ film after 30 min reaction time. The bright signal on the top is a gold marker that allows alignment of SEM and Raman images. The red square indicates the area of the Raman scan. b,c) Overlays of SEM images and 2D Raman intensity plots at the wavenumbers $1380 \pm 30 \text{ cm}^{-1}$ (b) and $1450 \pm 30 \text{ cm}^{-1}$ (c). The Raman signal distribution at 1380 cm^{-1} affirms the accumulation of coordinated TCNQ molecules in the cubic crystals, whereas the distribution at 1450 cm^{-1} shows that noncoordinated TCNQ is present only in a few isolated spots. Colored arrows indicate the position of the single Raman spectra shown in Figure 5.8.

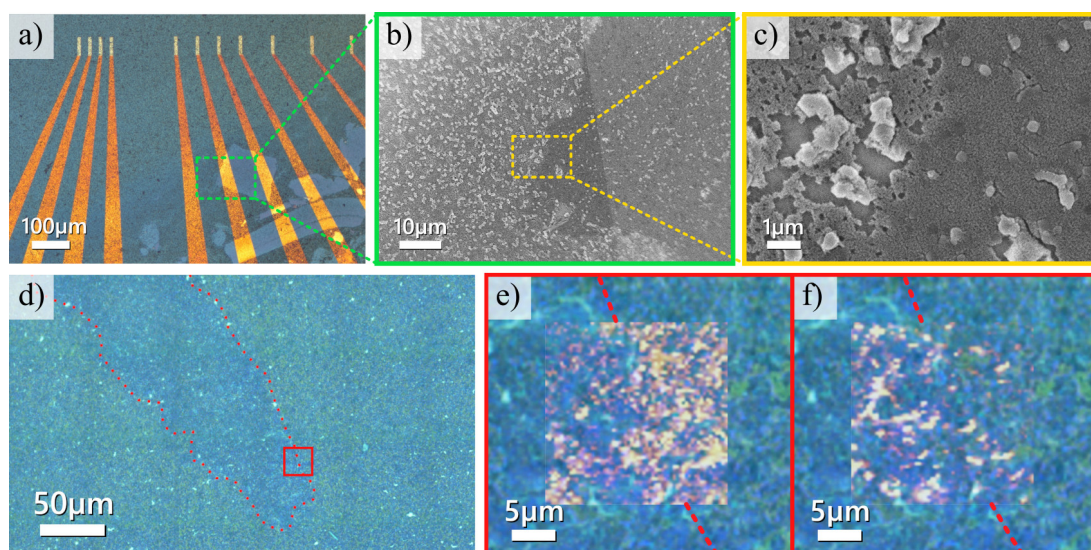


Figure 5.10: Optical (a) and SEM images (b,c) of Cu-HHTP-TCNQ film, displaying two regions with different visual appearance (80 min reaction time). The SEM images revealed unequal densities of crystalline cubes in the two regions. The parts with higher number of cubes seem to disrupt the continuous film resulting in different microscopy image contrasts. d) Optical microscopy image of Cu-HHTP-TCNQ film showing a region boundary marked by the red dotted line (45 min reaction time). The red square shows the area of the Raman scan. e,f) 2D Raman intensity plots at the wavenumbers 1380 cm^{-1} indicating coordinated TCNQ molecules (e), and 1450 cm^{-1} indicating noncoordinated TCNQ molecules (f). The concentration of noncoordinated TCNQ molecules seems to be higher at the film region on the left side, whereas the coordinated TCNQ molecules are more concentrated at the right region.

side of the border, indicating coordinated TCNQ in form of cubes, while the signal at 1450 cm^{-1} was predominant in the other region, indicating noncoordinated TCNQ molecules (Figure 5.10e,f). For a similar investigation and mapping of HHTP by Raman spectroscopy, the signal-to-noise ratio was too weak and the Raman signal was masked by the strong signal from TCNQ.

5.5 Electrical characterization

Conductivity evaluation

Glass chips with prepatterned gold electrodes were fabricated onto which the Cu-HHTP-TCNQ films were transferred to investigate the electrical properties of the MOFs. Details on the chip fabrication can be found in Appendix A.2. Figure 5.11a shows a dark-field microscopy image of a chip with a deposited MOF film. Each chip has N contacts in the center of the chip, which are connected to large pads on the outer edges by gold leads. The leads were covered by an insulating Al_2O_3 layer in order to prevent short circuits between adjacent contacts. The geometry and spacing of the contacts vary to test different contact performances.

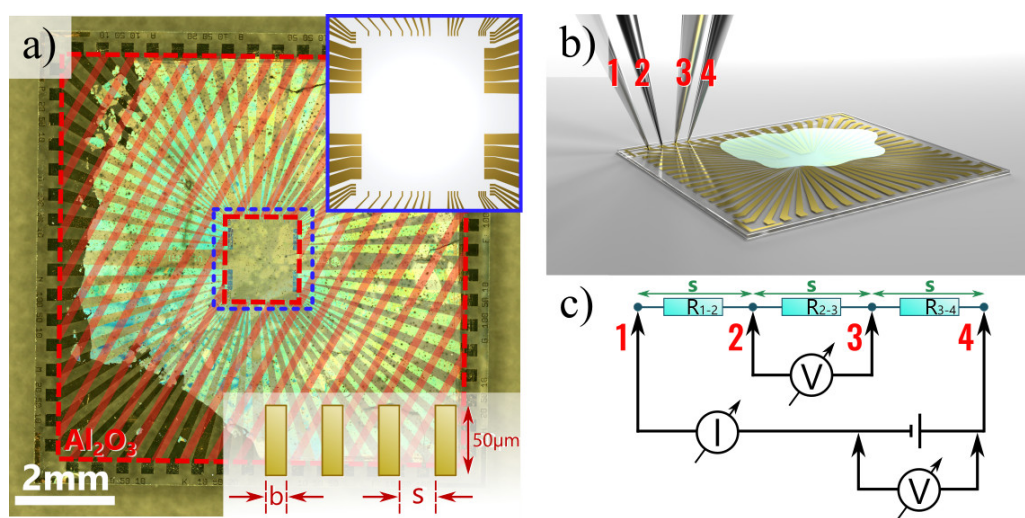


Figure 5.11: a) Dark-field microscopy image of a chip coated with Cu-HHTP-TCNQ film. The red dashed area indicates the insulating Al_2O_3 layer between chip and film preventing short circuits. Inset top: Illustrative zoom-in into inner contacts with different dimensions. Inset bottom: Schematic of inner contact geometries. The ratio between contact width, b , and distance, s , is changing. b) Geometry of the prepatterned glass chip with gold electrodes contacted by needle probe actuators in a four-point probe. Deposited Cu-HHTP-TCNQ film is colored in cyan. c) Simplified electrical circuit of configuration.

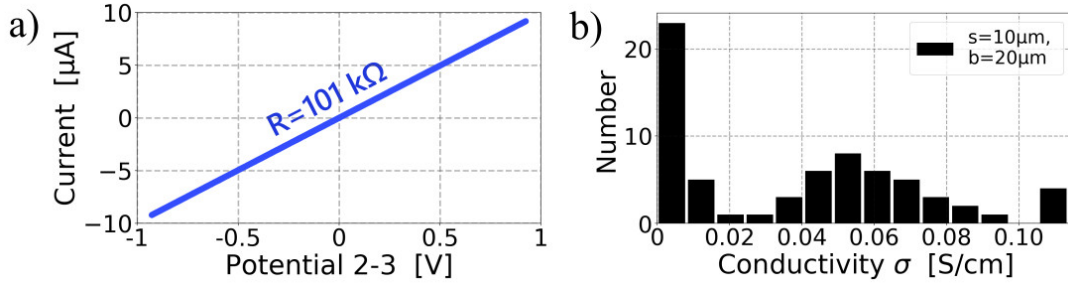


Figure 5.12: a) Typical IV-curve of Cu-HHTP-TCNQ film (in vacuum), synthesized at 0 °C for 45 min. Linear slope indicates Ohmic behavior (sweeping rate = 12 V s⁻¹). b) Histogram of film conductivities for one contact geometry ($s=10\ \mu\text{m}$, $b=20\ \mu\text{m}$).

The length of the contacts stays 50 μm , and the contact width b is 10 μm with one exception, in which the width is 20 μm . The contact spacing s varies from 10 μm to 100 μm . As shown in Figure 5.11, conductivity was then measured in a four-point probe geometry by applying a voltage to the two outer contacts that is swept over time. The inner contacts tapped the voltage drop of the driven current, which flows through the sample.

The IV trace of a representative sample is shown in Figure 5.12a and it shows a clear Ohmic behavior of the film, with a resistance of 100.8 k Ω in vacuum at room temperature. When measuring in a four-point probe geometry, the film resistivity ρ can be derived from the general formula $\rho = \frac{U}{I} \Gamma$. Here, U stands for the voltage in volt, I for the current in ampere and Γ is a geometrical correction factor of length dimension, taking into account the sample thickness. If the film is thin (means: $\frac{t}{s} \leq 0.5$) and has an infinite size (means: $d \geq 40s$) with thickness t , contact spacing s and limiting contour diameter d , the film resistivity can be given by $\rho = \frac{\pi}{\ln(2)} \frac{U}{I} t$.^{290–292} With the IV traces and the average film thicknesses determined by the AFM measurements, the resistivity values can be evaluated. In Figure 5.12b, the conductivity values $\sigma = \rho^{-1}$ for one specific contact geometry ($s=10\ \mu\text{m}$ and $b=20\ \mu\text{m}$) are shown as histogram. The plot contains data from several films with different reaction times. In order to take into account the reaction times ranging from 10 min up to 80 min, the measured conductivity values are plotted against their individual reaction time in Figure 5.13, considering the varying contact geometries. A total of 206 contacts were measured and at least five measurements were performed on each contact geometry in order to validate the reproducibility. The mean conductivity is $\sigma_{\text{mean}} = 0.033 \pm 0.006\ \text{S cm}^{-1}$. This value is comparable to known literature values for Cu-HHTP (Cu-HHTP pressed pellets: 0.045 S cm⁻¹).²⁵⁰ The found value displays an average quantity, since the

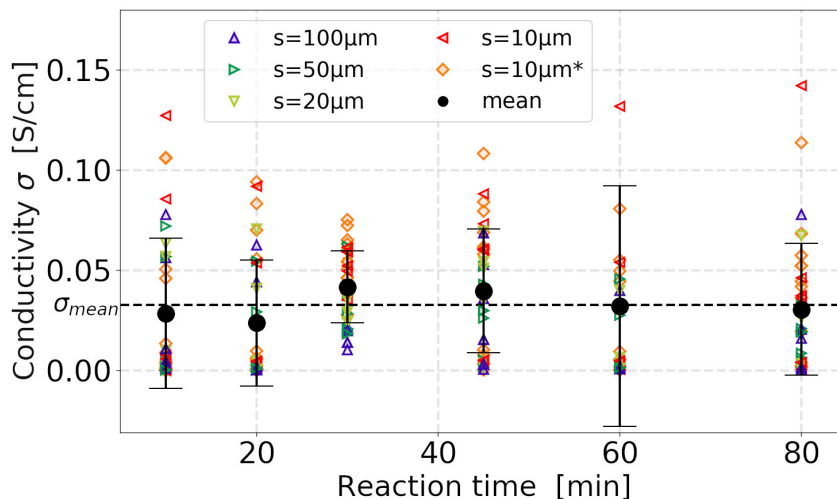


Figure 5.13: Conductivity values from transport measurements of Cu-HHTP-TCNQ films with varying reaction times at different contact geometries (sweeping rate = 12 V s^{-1}). Contact width $b=10 \mu\text{m}$ for all data depicted as triangles and $b=20 \mu\text{m}$ for data depicted as diamonds, also marked with *. Black circles display the mean values and error bars indicate standard deviations. One single outlier at $\sigma=0.306 \text{ S cm}^{-1}$ (time=60 min, $s=20 \mu\text{m}$) is not shown for better visibility. The dashed line represents the average conductivity.

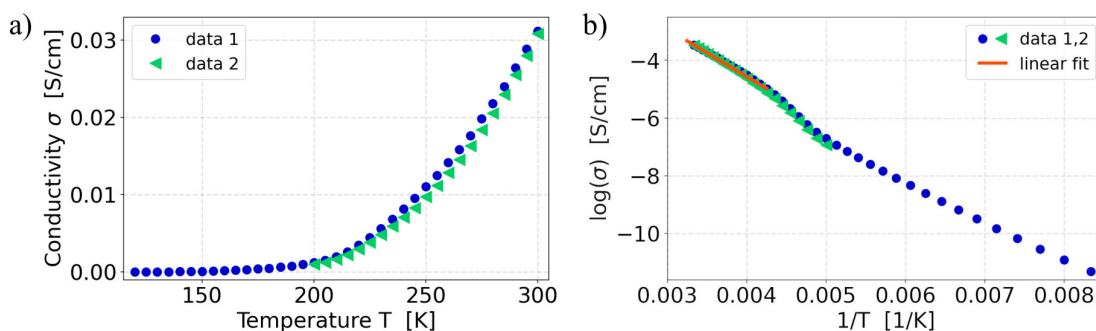


Figure 5.14: Temperature-dependent electrical measurements of two representative Cu-HHTP-TCNQ film samples (data 1 and data 2, respectively), synthesized at 0°C for 45 min (measured in vacuum at two different contact geometries with spacing $s=10 \mu\text{m}$). Conductivity is plotted against temperature in (a) an ordinary diagram and (b) as Arrhenius plot. The electrical conductivity between 240 K and 300 K can be described by a thermally activated process with an activation energy of $E_a=0.142 \text{ eV}$.

film consists of different phases with individual conducting properties (Cu-HHTP and Cu-TCNQ(I)). Also, the synthesis method leads to a variation in film thickness on the length scale of the measured inter-electrode area as well as film-to-film variations, probably caused by physical deposition issues or fluctuations in the synthesis of the different batches. These reasons are the source of the scattering of the data points in Figure 5.13. Similar findings are known from the literature.^{179,293} Conductivity was also measured at different temperatures, down to 120 K. For a film with 45 min reaction time and contact spacing $s = 10 \mu\text{m}$, the conductivity is plotted against temperature in Figure 5.14 as ordinary diagram and as Arrhenius plot. The temperature-dependent measurements demonstrate that the electrical conductivity of Cu-HHTP-TCNQ around room temperature can be described by a thermally activated process, indicating a hopping transport regime according to equation (4) in Chapter 2.3.3. The linear fit of the Arrhenius plot between 240 K and 300 K gives an activation energy of $E_a = 0.142 \text{ eV}$.

Sensing approaches

Basic chemiresistive response of the synthesized Cu-HHTP-TCNQ film was demonstrated. In addition to enhanced conductivity, a film is also advantageous for certain applications like gas sensing because it has an open structure and thus a high surface-to-volume ratio.^{154,294} As proof of principle, film resistance and pressure were monitored over time while the vacuum measurement chamber was flushed with nitrogen, dry air, and ambient air with a relative humidity of 41 %. The monitored values for a representative measurement with ambient air are shown in Figure 5.15a. The Supporting Information Figure 5.21 provides the traces of all gases applied to the Cu-HHTP-TCNQ film, synthesized at 0 °C for 45 min in all cases. In Figure 5.15b, the relative changes in resistance with respect to the vacuum level are displayed. Starting from low pressure, the resistances for each gas start to rise from about 10^{-1} mbar and go to saturation when atmospheric pressure is reached. The saturation values are indicated by small triangles. Small discrepancies at atmospheric pressure are the result of the delayed resistance changes at the same pressure. The higher energy required to remove the adsorbed gas molecules from the pores and surfaces could explain that hysteresis occurs in all curves after pumping down again. The kink between 10^{-2} mbar and 10^{-3} mbar can be explained by a measurement artifact originated from an ignition lag between the Pirani and cold-cathode element of the pressure gauge. The measurement results show that ambient air causes the strongest increase in film resistance, fol-

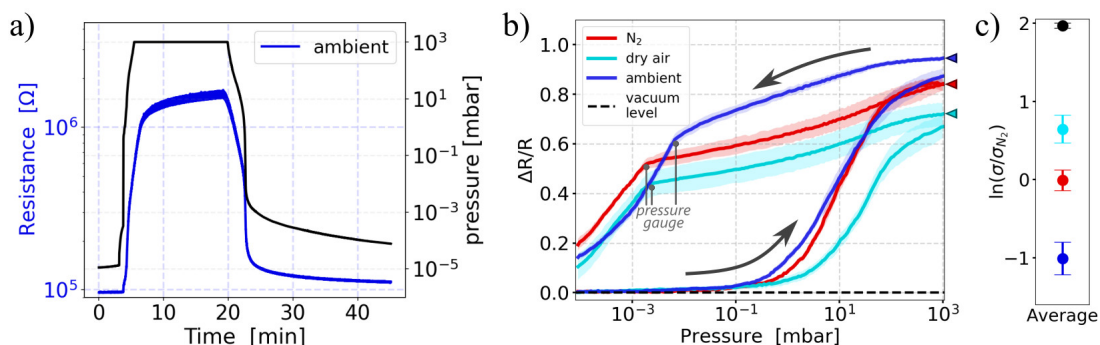


Figure 5.15: a) Pressure and device resistance of Cu-HHTTP-TCNQ film, synthesized at 0°C for 45 min, monitored over time when exposed to ambient air with relative humidity of 41% (contact spacing $s=20\ \mu\text{m}$). b) Relative response (change in film resistance) versus pressure during venting the vacuum chamber with nitrogen, dry air, and ambient air with relative humidity of 41% (average of $N=3$, colored area displays standard deviation; measured Cu-HHTTP-TCNQ film was the same as shown in Figure 5.12). Arrows indicate the cycling direction, starting at vacuum level. Triangles point to the saturation value. c) Normalized average film conductivities when exposed to different atmospheres. σ_{N_2} represents film conductivity in a nitrogen atmosphere.

lowed by pure nitrogen and dry air. One suggestion for the strong response toward ambient air is the interaction with water molecules owing to their polar character.⁵⁶ Beyond that effect of water, the difference in response between nitrogen and dry air suggests a chemiresistive effect that should be investigated in future studies. To relate the chemiresistive response of the Cu-HHTTP-TCNQ film to known results, the normalized average conductivities of the film under the different atmospheres were evaluated (Figure 5.15c). The values were normalized to σ_{N_2} which represents the film conductivity in a nitrogen atmosphere. Previous work demonstrated comparable chemiresistive responses of Cu-HHTTP films to ambient changes.²⁹⁵ This implies that our Cu-HHTTP-TCNQ film also has the potential to be applied as a chemiresistive material for future work on the development of Cu-HHTTP-TCNQ-based chemiresistive sensors.²⁹⁶

5.6 Conclusion and Outlook

With this work, we demonstrated a reliable synthesis of free-standing hybrid Cu-HHTTP-TCNQ MOF films. The interfacial assembly approach used has the advantage that it yields a uniform film thickness controlled by reaction time. Furthermore, the film is robust to physically deposit them on a variety of substrates. The hybrid Cu-HHTTP-TCNQ film was analyzed multiparametrically by different methods. Structure and morphology were studied by SEM and AFM. This

revealed that the film consists of filaments and cubic crystals formed by the coordination of Cu^{2+} -ions to the individual organic molecules. High resolution AFM measurements clarified the influence of reaction time on the thickness and surface roughness. The chemical composition and distribution of the organic ligands were analyzed by EDX and Raman spectroscopy, revealing the separation of the phases Cu-HHTP and Cu-TCNQ(I) embedded in a film structure coming along with low structural order. Also, the film showed an average electrical conductivity of 0.033 S cm^{-1} and a chemiresistive response toward ambient environmental shifts. In conclusion, the outcome of this work demonstrates a potentially good applicability of less ordered MOF structures as chemiresistive materials.

Author contributions

L.L. performed the chemical synthesis, electrical measurements, and Raman measurements. A.G. and M.S. designed and fabricated the glass chips with gold electrodes. A.G. built the electrical measurement setup. M.S. conducted SEM and EDX elemental analysis. J.O. and A.G. also carried out Raman measurements. P.N.N. performed AFM measurements and data analysis. D.B. supervised the temperature-dependent electrical measurements. A.S. characterized the samples with GISAXS. A.N. carried out XRD experiments and analyzed the diffraction data.

5.A Supporting Information

5.A.1 Additional Figures

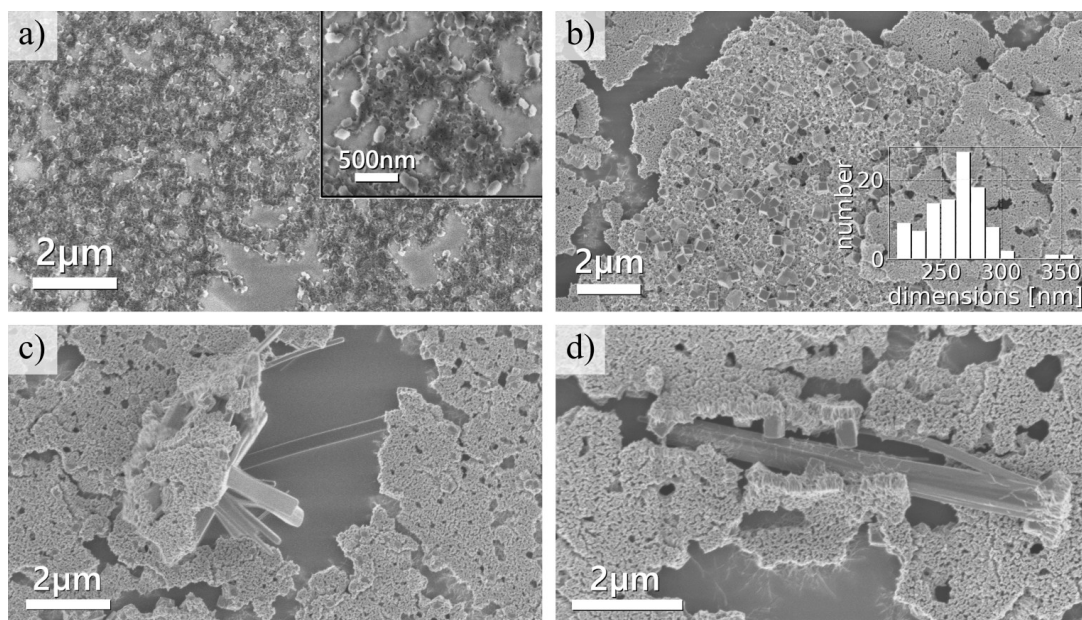


Figure 5.16: a) SEM image of Cu-HHTP-TCNQ film with reaction time 10 min. The film is holey and didn't grow together yet but shows already the presence of crystalline cubes. b) Turned-down part of Cu-HHTP-TCNQ film with reaction time 80 min. The bottom side is covered with cubic crystals. Inset: Size distribution of 102 measured cubes. c,d) SEM images of long crystals, which are formed at the bottom side of the film sticking out vertically, probably originated from the crystalline cubes (reaction time 80 min (c) and 60 min (d)). At the film border, filamentous features are apparent, which are substantially aligned in parallel.

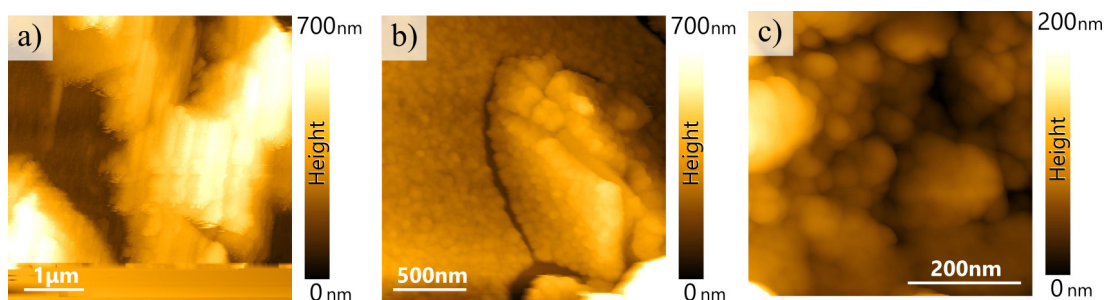


Figure 5.17: High resolution AFM area scans on Cu-HHTP-TCNQ films with 60 min reaction time. Magnification increases from (a) to (c).

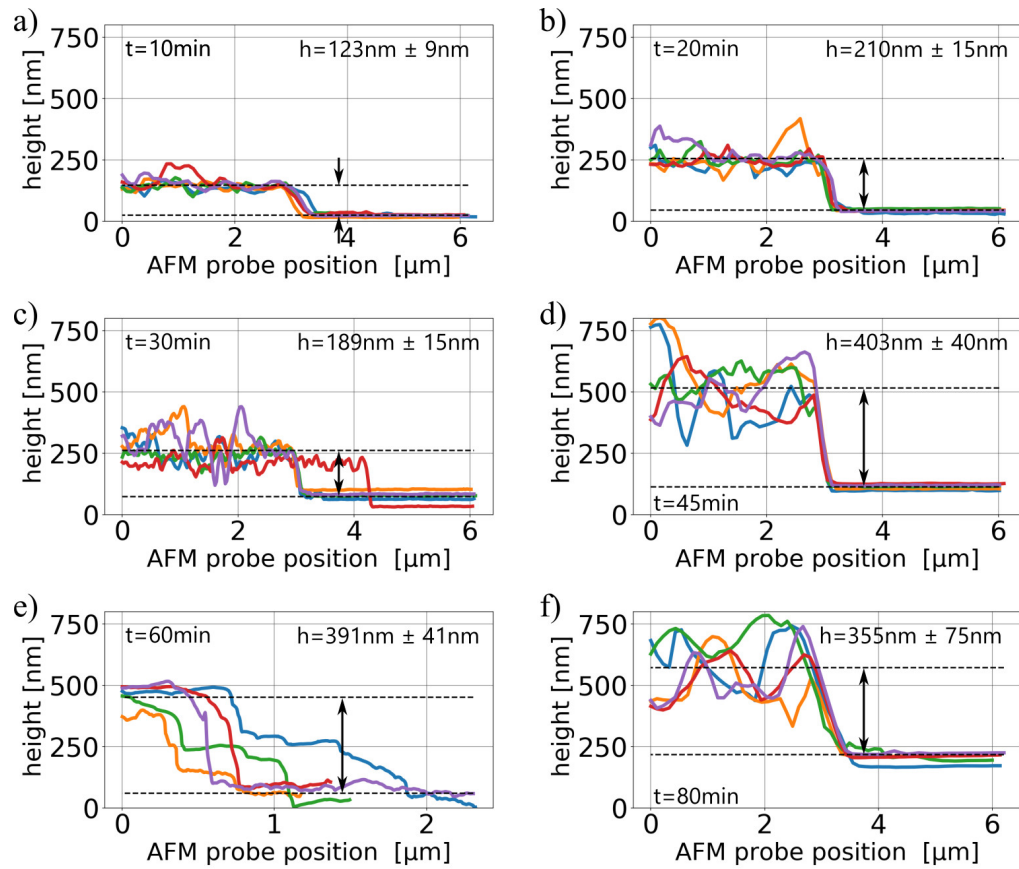


Figure 5.18: Line profile scans from AFM scans on Cu-HHTP-TCNQ films with different reaction time. Average film thickness is evaluated from the individual level differences at five different locations at the film border.

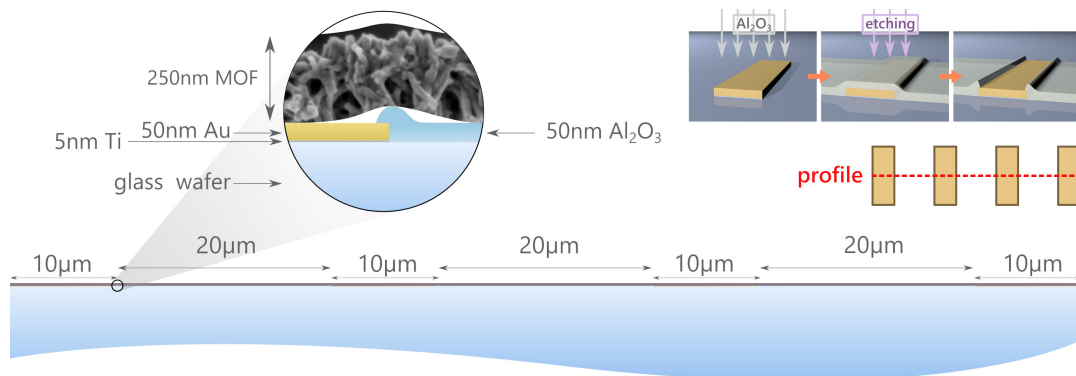


Figure 5.19: In-scale profile image of the chip contacts for electrical measurements with the contact geometry spacing $s=20\ \mu\text{m}$ and width $b=10\ \mu\text{m}$. A side image of the Cu-HHTP-TCNQ film is superimposed to estimate the proportions. The picture demonstrates the reasonable good contact between MOF film and gold surface. Small hills in the insulating Al_2O_3 layer at the edge of the gold contacts are a result of the fabrication process (see Inset for illustrated fabrication).

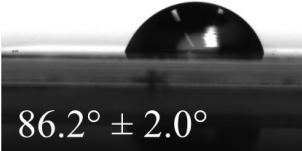
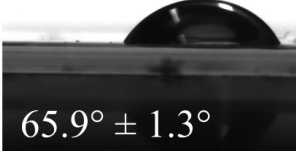
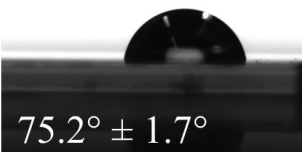

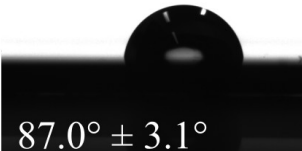
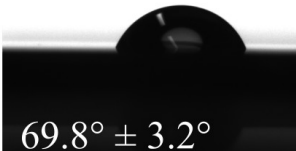
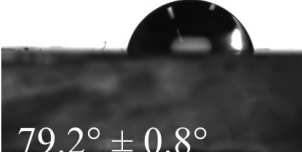
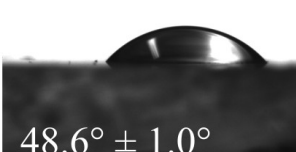
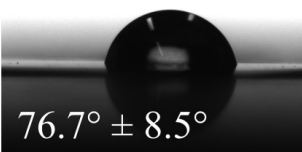

| Substrate | Standard | Plasma treatment |
|---|---|--|
| Al_2O_3 (on glass) |  $86.2^\circ \pm 2.0^\circ$ |  $65.9^\circ \pm 1.3^\circ$ |
| Al_2O_3 (on prepatterned chip) |  $75.2^\circ \pm 1.7^\circ$ |  $62.4^\circ \pm 1.1^\circ$ |
| Si/SiO ₂ (250nm) |  $87.0^\circ \pm 3.1^\circ$ |  $69.8^\circ \pm 3.2^\circ$ |
| PMMA |  $79.2^\circ \pm 0.8^\circ$ |  $48.6^\circ \pm 1.0^\circ$ |
| Capton |  $76.7^\circ \pm 8.5^\circ$ | |
| Glass (from microscope slides) |  $7.6^\circ \pm 1.4^\circ$ | |

Figure 5.20: Contact angle measurements of water droplets on different substrates to determine the surface wettability, which has an influence on the deposition of the MOF film onto the substrate of choice. Air plasma treatment for 5 min leads to surface activation with increased hydrophilicity, partly also due to removal of resist residues after chip fabrication.

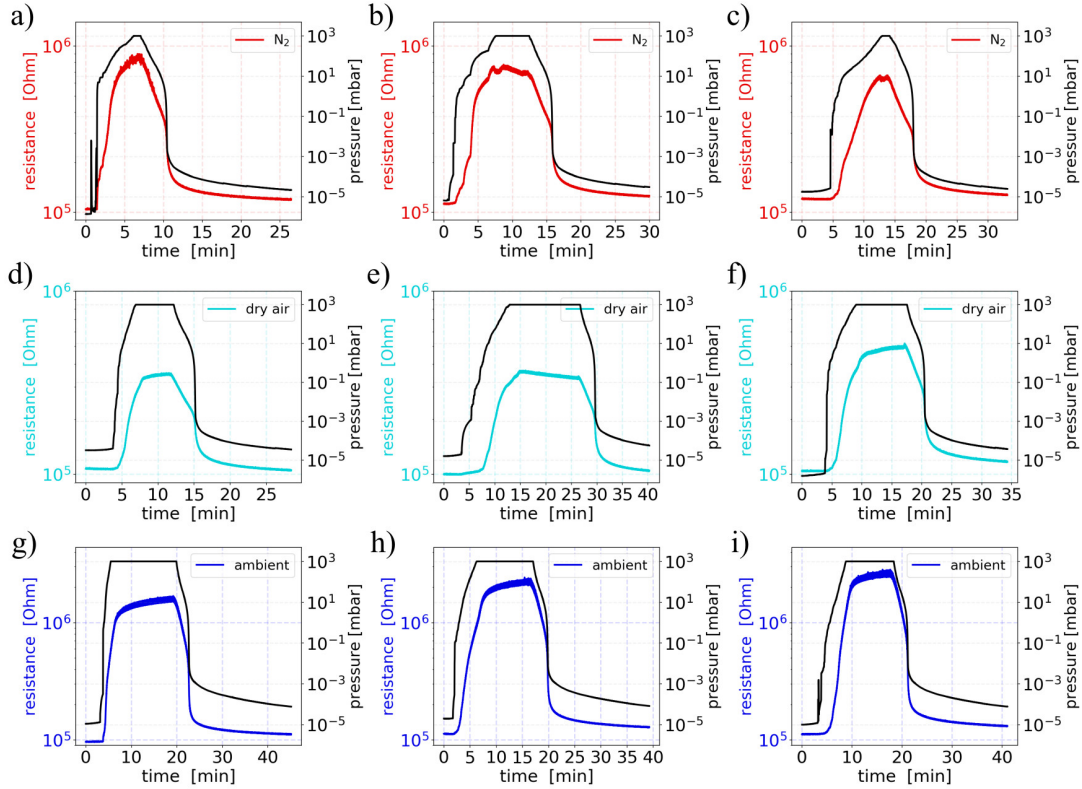


Figure 5.21: Device resistance and pressure over time. Resistance of Cu-HHTP-TCNQ film, synthesized at 0°C for 45 min, monitored over time when exposed to nitrogen (a,b,c), dry air (d,e,f) and ambient air with relative humidity of 41% (g,h,i) (contact spacing $s=20\ \mu\text{m}$).

5.A.2 Measurement details and parameters

AFM: For the AFM measurements, a Bruker Dimension Icon AFM equipped with a hybrid scanner was used. The AFM probe was a SCANASYST-AIR cantilever (BRUKER) with a tip apex radius of 2 nm and the AFM scan was performed in tapping mode under standard laboratory conditions without temperature or environmental control (resonant frequency: 70 kHz; force constant: $0.4\ \text{N m}^{-1}$). The cantilever was cleaned with acetone and isopropanol and dried with nitrogen before usage. The recorded AFM scan data was evaluated and leveled by Gwyddion software (version 2.55).

Raman: Raman spectra and corresponding optical images were acquired in ambient conditions using a WITec Alpha 300R confocal Raman microscope with a 100x objective (Zeiss EC Epiplan-Neofluar Dic, $\text{NA} = 0.9$) and a 300 mm lens-based spectrometer (grating: $600\ \text{g mm}^{-1}$) equipped with a TE-cooled charge-coupled device (Andor Newton). The linearly polarized laser excitation had the wave-

length $\lambda_{\text{exc}} = 488 \text{ nm}$ and a power of $P = 0.3 \text{ mW}$ measured before the objective. 2D Raman maps of size $15 \mu\text{m} \times 15 \mu\text{m}$ were acquired in backscattering geometry with an integration time of 1.6 s and a resolution of 3 pixels per μm . Single spectra were extracted from the area scans at representative positions and were displayed after polynomial background subtraction.

Electrical transport: For the electrical conductance measurements, a custom setup was used to monitor the current–voltage characteristics of the sample. The voltage was applied using a data acquisition card from National Instruments (model: NI 6289) and swept linearly over time (amplitude = 3 V, sweeping rate = 12 V s^{-1}). The current was monitored using a current amplifier (SP895/SP895a, University of Basel) and the measurement was controlled via a LabView program. I-V-measurements of electrically nonconducting devices (below the threshold of 1 nS) originated by, for example, lack of physical contact or film imperfections were not considered for the further data evaluation. The authors performed the pressure-dependent measurements (PXR 36X vacuum gauge from Pfeiffer Vacuum) using nitrogen (N_2 5.0) and compressed air (pressurized air, Sauerstoffwerk Lenzburg AG), taking care to flush the lines with the respective gas.

Temperature-dependent electrical transport: The temperature-dependent electrical conductivity was measured in a variable temperature cryostat (Lakeshore ST-500) using a Keithley 236 SMU controlled via Python pyvisa. The electrical conductivity was measured in a four-point collinear configuration. I-V-lines were taken by forcing a maximum current of 9 nA, with a sweeping rate of 0.1 nA s^{-1} . The temperature was controlled by a Lakeshore 336 temperature controller with resolution in the mK-range.

X-ray diffraction: Repeated synthesis of Cu-HHTP-TCNQ films (standard interfacial procedure at $T = 0^\circ\text{C}$ for 45 min) and subsequent merging led to a larger amount of powder for investigations by XRD. The sample was measured on a PANALYTICAL X’pert Powder instrument equipped with an imaging plate using a $\text{CuK}\alpha$ X-ray source with $\lambda = 1.5406 \text{ \AA}$ for 60 h. Data acquisition was conducted in reflection mode.

Crystallite sizes could be derived from the full width at half maximum of single indexed (nonoverlapping) reflections for selected crystal directions using the Scherrer equation ((200) for Cu-HHTP; (002) for Cu-TCNQ). The crystal elongation in the (100) and the (001) crystallographic direction for Cu-HHTP and Cu-TCNQ was calculated. For all other crystallographic directions, no single in-

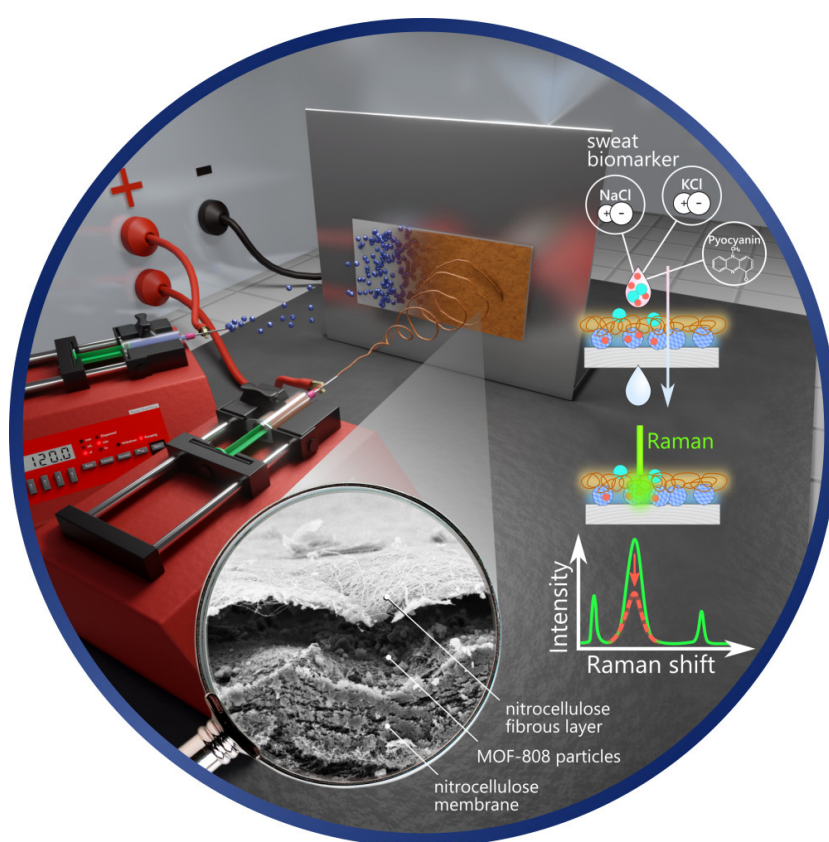
dexed lines were found. The instrumental peak broadening resolution was taken from the (111) reflection of the reference polycrystalline silicon.

For the analysis of the stability of Cu-HHTP-TCNQ toward washing and drying, thin films were synthesized (standard interfacial procedure at $T = 0^\circ\text{C}$ for 45 min) and then collected by a loop sample holder. Diffraction measurements were performed directly after synthesis by STOE IPDS II instrument equipped with an imaging plate using MoK α X-ray source ($\lambda = 0.7107 \text{ \AA}$) and compared with the data obtained from washed and dried samples. Data acquisition was conducted in transmission mode while the sample was rotating (beam diameter = 0.5 mm).

TEM: MOF films were synthesized for TEM imaging by the standard interfacial procedure at $T = 0^\circ\text{C}$ for 40 min and then fished onto a copper grid (G2400C, square 400 mesh, Cu 3.05 mm diameter). TEM images were taken using JEOL 2200FS equipment with energy of 200 keV and 0.3 s exposure time. SAED signals were recorded at corresponding positions with camera lengths of 100 cm and 60 cm, respectively, with a SAED aperture introduced in order to define the sample region.

GI-SAXS: MOF films were synthesized for GI-SAXS measurements by the standard interfacial procedure at $T = 0^\circ\text{C}$ for 40 min and then deposited onto a silicon wafer substrate (orientation (100), thickness of 500 μm with a 285 nm native SiO₂ layer on top). Silicon substrates were rinsed with deionized water and treated with air plasma for 5 min before being placed at the bottom of the vial. The GISAXS experiments were performed using a Nanostar X-ray Scattering equipment (Bruker AXS GmbH, Germany) equipped with 2D Xe-based gaseous avalanche detector (VANTEC-2000 detector) of x2048 pixels and the pixel size of 68 μm x 68 μm . A microfocused X-ray CuK α (wavelength $\lambda = 0.154 \text{ nm}$) source with Montel optics and two pinhole collimation systems provided a point-focused beam diameter of around 500 μm . The setup was calibrated for the sample to detector distance using a standard silver behenate powder sample. This setup benefits from a GISAXS stage which allows sample movements in all directions with a resolution of 0.01 mm as well as rotations around all sample axes with an angular resolution of 0.0001°. The incident grazing angles were tuned between 0.15° and 0.3°. All experiments were performed in vacuum ($\approx 0.01 \text{ mbar}$).

MOF-particle integration into fibrous layers for wearables



Wearable sensors equipped with stimuli responsive materials can non-invasively collect and detect biomarkers in body fluids such as sweat, providing valuable information about a patient's health status.

This chapter is about the integration of MOF-808 particles into nitrocellulose fibrous layers and its application for spectroscopic sensing of sweat biomarkers.

Parts of this chapter are currently being submitted to ACS Applied Nano Materials (Lüder et al.). Supporting information is included at the end of this chapter.

6.1 Introduction

The collection of physicochemical data such as the concentration of biomarkers in body fluids allows the reading of the fitness and health status of a patient. Well known body fluids for medical analysis are blood^{297,298} and cerebrospinal fluid (CSF)²⁹⁹, e.g. for the detection of neurodegenerative diseases, however, invasive methods are required to access these fluids and the abundance of biomarkers such as amyloid proteins in these body fluids makes them also complex.⁹

Other body fluids such as sweat^{300,301}, breath^{168,302}, saliva^{303,304} or wound exudate^{305,306} also contain a variety of biomarkers reflecting the patient's health status. These body fluids, unlike blood or CSF, can be collected noninvasively by wearables such as patch devices³⁰⁷, masks³⁰⁸ or wound dressings.^{14,309} Wearable sensors equipped with an active biosensor platform can accumulate certain biomarkers and allow simple and uncomplicated monitoring of the target analytes. For example, by measuring changes in the concentrations of metabolites, wearable sensors enable observation of the progression of a condition or providing information for early diagnosis of an existing disease, making them increasingly important in many fields ranging from medicine^{21,310} and fitness^{3,311} to military applications.^{214,312}

Accurate detection of low levels of various biomarkers requires versatile sensor platforms that offer high sensitivity and selectivity.^{20,313} We have already learned that MOFs can address these requirements, demonstrating good sensing efficiencies with low detection limits down to the femtomolar range.^{198,314,315} However, the successful integration of MOFs into textiles and polymer substrates poses a challenge if flexibility and functionality of the MOF are to be maintained, i.e. that the pores remain open, for example when applying coatings over the MOFs.

This work describes the integration of biocompatible MOF particles into a nitrocellulose membrane using a sequential electrospaying and electrospinning³¹⁶ process, where the MOFs are effectively entrapped and retained by the loose fiber mesh. Thereby, an open architecture is maintained so that MOF functionality is preserved and translucence is achieved, enabling the access to optical analytic methods. The fabricated MOF@nitrocellulose (MOF@NC) membranes were characterized by several techniques such as SEM, AFM or EDX to gain insight into the structure and integration capability. Optical Raman spectroscopy was then used as label-free analytical tool to evaluate the response of the MOF architectures upon exposure to various sweat biomarkers. One of the biomarkers

studied is sodium chloride, an indicator of cystic fibrosis and sweat rate, another is potassium chloride, which is an identifier of muscle activity.¹¹ A further investigation was performed using pyocyanin, which is a biomarker for the nosocomial pathogen *Pseudomonas aeruginosa*. Pyocyanin is released by the bacterium as signaling molecule for chemical communication, a phenomena known as quorum sensing³¹⁷, and the influence on the MOF-nitrocellulose architecture was studied to demonstrate the potential for infection detection. In summary, the presented integration method for our MOF@NC architecture, being independent of the type of MOF, provides a potential route for the realization of wearable sensing platforms and functional materials for versatile biomarker sensing with high sensitivity and selectivity.

6.2 Fabrication approach

For the fabrication of the MOF@NC architecture, a commercially available nitrocellulose membrane with a pore size of 0.45 μm was first utilized as a base layer. Then, MOF-808 particles, which were obtained from *novoMOF AG*, were distributed on the membrane surface by an electro spraying process. For this, the particles were suspended in isopropyl alcohol and the suspension was filled into a syringe. A high voltage was applied between the syringe needle and a metal plate electrode, causing the suspension to become charged and droplets to form, which were then released and attracted to the electrode. Thus, the MOF particles were sprayed onto the NC membrane attached to the metal plate (details on the electro spraying parameters in Appendix A.3).

Next, NC fibers were electro spun on top of the MOF particles. The procedure is similar to electro spraying, except that instead of the MOF suspension, a NC polymer solution was filled into the syringe. The solution was created by dissolving NC in a mixture of acetone/DMSO. Then, by applying a high voltage between the filled syringe and the metal plate, the charging effects led to the release of a thin jet. The jet was attracted to the plate electrode, with the solvent evaporating during flight and a thin polymer fiber being deposited on the sample. Electro spinning for several minutes resulted in a fibrous layer covering and physically entrapment of the MOF particles (details on the electro spinning parameters in Appendix A.4). The thickness of the fibrous layer is defined by the spinning time. In this case, sufficient coverage was achieved by a time of 20 min.

In the end, a layered sandwich structure was obtained in which the MOF particles

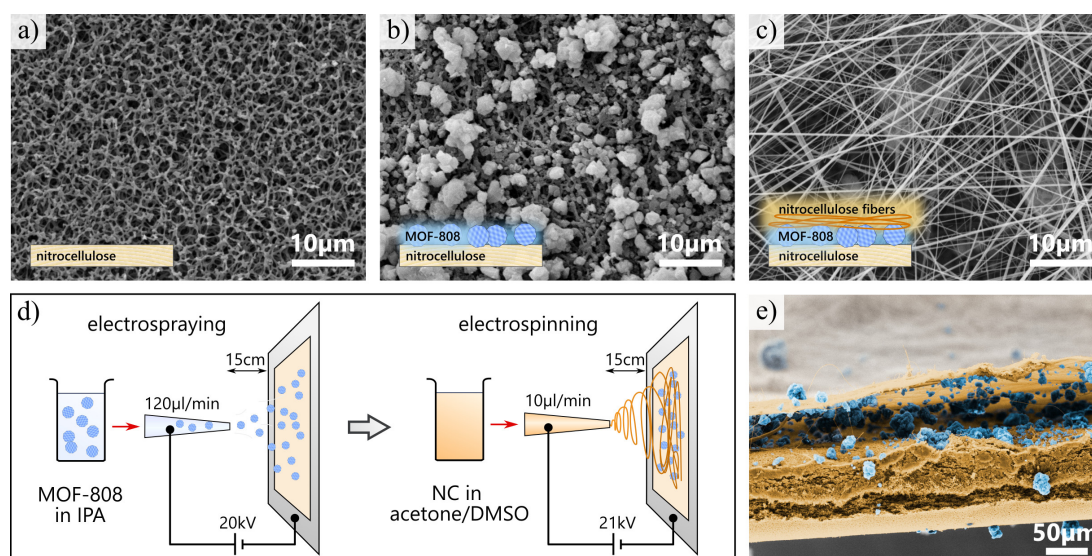


Figure 6.1: Integration process of MOF particles into fibrous nitrocellulose layers by using a sequential electrospaying and electrospinning procedure. SEM images taken at each intermediate step show the purchased pure NC membrane (a), the NC membrane with electrospayed MOF-808 particles (b), and with additional electrospun NC fibers on top (c). d) Schematic of the spraying and spinning process, illustrating the release of droplets of MOF suspension or jets of NC polymer solution due to charging effects when applying a high voltage between the filled syringe and the metal plate collector. The MOF and the NC fibers are deposited on the substrate of choice (here NC membrane) that is mounted on the metal plate. e) Color coded SEM image showing the profile of the final MOF@NC sandwich structure. Visible delamination and detachment of the top fibrous layer is the result of the cutting process, exclusively applied for imaging. MOF particles are colored in blue and NC in orange.

were integrated in between the nitrocellulose (referred to as MOF@NC). Figure 6.1 shows SEM images of each intermediate step of the fabrication and the final architecture, as well as a schematic of the electrospaying and electrospinning process (additional overview of the structure in Supporting Information Figure 6.16).

6.3 Characterization of MOF@NC layers

Examination of MOF-808 particles

The MOF-808 particles were first examined by X-ray diffraction (XRD) to verify their structure. Figure 6.2 shows the diffraction pattern of the MOF powder in clear agreement with known MOF-808 reflections from literature.^{318,319} Furthermore, the experimentally measured spectrum was compared with simulated data.

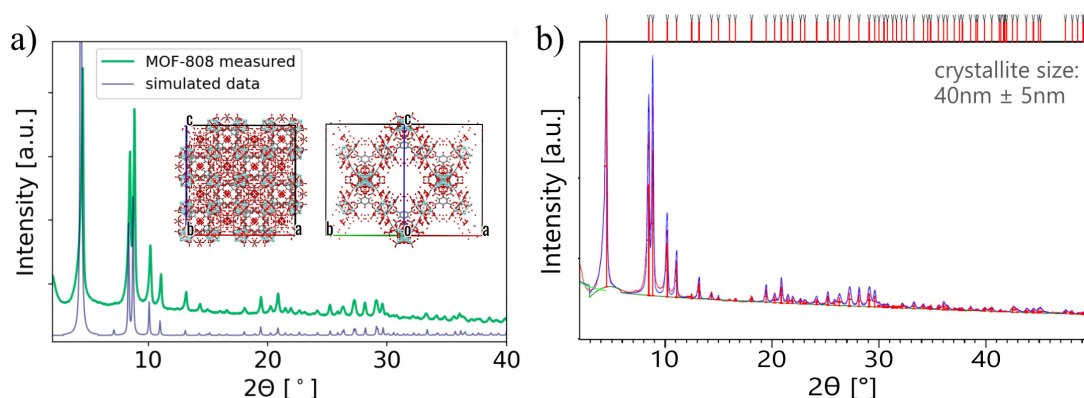


Figure 6.2: a) X-ray diffraction (XRD) patterns of measured and simulated MOF-808 particles. The inset shows the unit cell of MOF-808 under different angles. (Crystallographic data for structural representation and pattern calculation were obtained from Cambridge Crystallographic Data Center (CCDC)). b) Line profile analysis using the 'Williamson-Hall' approach for the crystallite size determination, giving a value of (40 ± 5) nm.

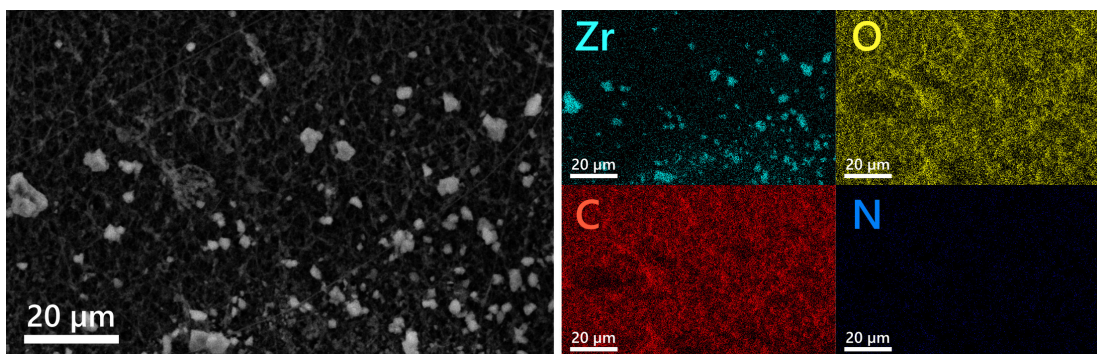


Figure 6.3: SEM image of MOF-808 particles after being electrospayed on a nitrocellulose membrane. The images on the right show the corresponding energy dispersive X-ray (EDX) spectroscopy maps. The position of the MOF particles can be well mapped from the elemental distribution of zirconium (Zr) contained in the metal cluster. Oxygen (O), carbon (C) and nitrogen (N) show uniform pictures and homogeneous distributions, with some local variations.

The crystallographic data were obtained from the Cambridge Crystallographic Data Center (CCDC) and yielded a spectrum that is in good agreement with the measured data (Figure 6.2a). Line profile analysis by the Williamson-Hall approach was used to determine the crystallite size of the MOF-808 particles.³²⁰ After background subtraction and peak assignment, a profile fitting has been performed, while taking the instrument contribution to the peak profile into account

by measuring and evaluating the line profile of the LaB_6 reference material. The line profile analysis gave a crystallite size of (40 ± 5) nm (Figure 6.2b).

Next, the sample was analyzed with energy dispersive X-ray spectroscopy (EDX). The MOF particles could be clearly mapped based on the elemental distribution of zirconium, because this element is present in the clusters of the metal nodes (Figure 6.3). Other elements such as oxygen, carbon and nitrogen show a quite homogeneous distribution with some local variations.

Investigation of the particle entrapment by the fibrous layer

To ensure effective entrapment of the MOF particles by the fibrous top layer, the fibrous layer should be dense enough to prevent the particles from leaching out without sacrificing the loose mesh structure. For this reason, the size distribution of the MOF particles and the polymer mesh spacings were analyzed. MOF particles were sprayed onto a pure aluminum foil and scanning electron microscopy (SEM) images were acquired. With the free computer software Fiji (developed by ImageJ), the images were analyzed by applying a brightness threshold and generating a black and white image. Thereafter, the Feret diameters (i.e. the largest dimension) of the particles were calculated; a total of 2308 particles were recorded (Figure 6.4a).

A possible influence on the particle size could be the treatment with ultrasound immediately before the electrospaying process. The MOF suspension is treated

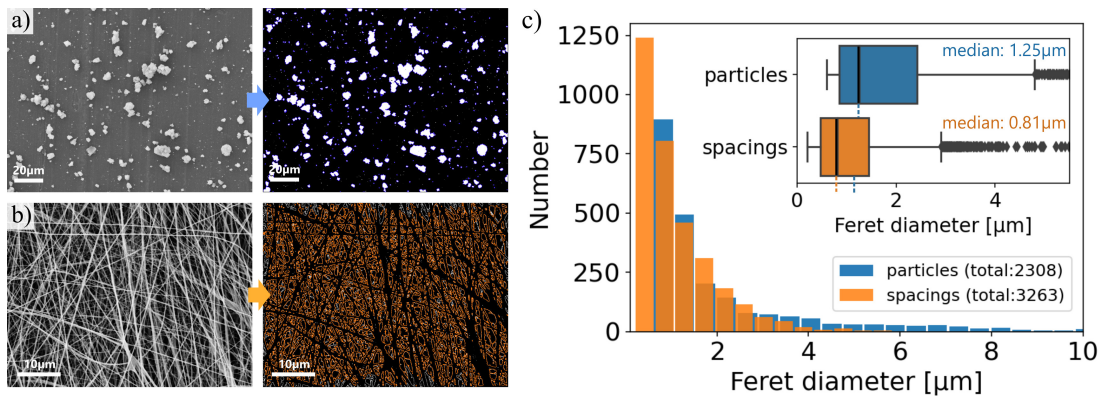


Figure 6.4: SEM and converted black and white images of electrospayed MOF-808 particles on alumina foil (a) and electrospun NC fibrous layer (spacing outlines were traced) (b). The image conversion and analysis was executed using Fiji image software. Blue outlines indicate the detected particles and orange outlines indicate the detected spacings. c) Feret diameter size distribution of the traced MOF particles (blue) and fibrous layer spacings (orange), showing an exponential reduction. Boxplots are shown as inset, providing the median values of $1.25 \mu\text{m}$ for particles and $0.81 \mu\text{m}$ for spacings.

in an ultrasonic bath to obtain a more stable and homogeneous suspension. It was tested, whether the duration of sonication from a minimum of 5 min to a maximum of 60 min had an influence on the particle size distribution. No significant effects on particle size were observed, except for the case without any ultrasonic treatment, since in this case the suspension was not stable and the particles sank rapidly, with the consequence that not all particles of the defined volume could be used in the electro spraying process (Supporting Information Figure 6.17).

Similar to the particles, the size of the NC mesh spacings were evaluated. Electrospinning of NC fibers on a blank substrate was executed for 20 min. The SEM images of the resulting fibrous layer were analyzed by the computer software Fiji. After conversion of the images into black and white, the outlines of the pores were traced and Feret diameters of a total of 3263 mesh spacings were calculated (Figure 6.4b).

In Figure 6.4c, the size distributions of the particles and the spacings were presented together, both showing an exponential reduction. The data is also plotted as boxplots and the medians were determined for quantification. The median of the particles is $1.25\ \mu\text{m}$ and that of the spacings is $0.81\ \mu\text{m}$, revealing that the fibrous layer has smaller mesh spacings than the size of the MOF particles. These are benchmark values, but they indicate the tendency for successful entrapment of

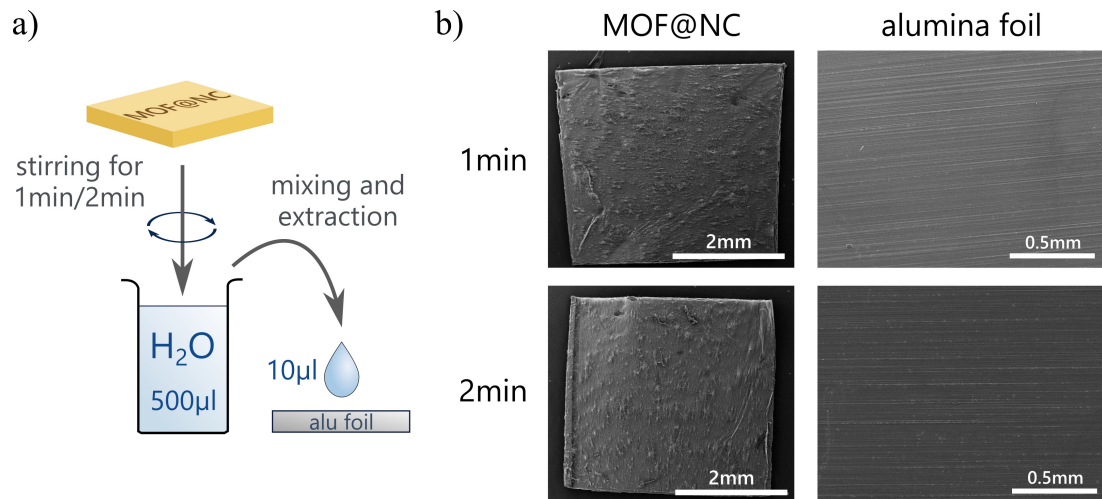


Figure 6.5: a) Schematic illustration of leaching tests of MOF@NC samples. MOF@NC substrates are strongly stirred in $500\ \mu\text{l}$ of deionized water for 1 min or 2 min respectively. After mixing, an extraction of $10\ \mu\text{l}$ is deposited on an alumina foil and air dried for SEM analysis. b) SEM images of the MOF@NC substrates as well as alumina foil after water droplet deposition. The substrates didn't show any changes compared to before treatment. Further, no significant leaching of particles is observed on the alumina foil demonstrating an efficient particle fixation by the fibrous layer.

the particles while still allowing open access to the MOF pores. Practical leaching tests, in which attempts were made to wash out the MOF particles by vigorously stirring the sample in water, confirmed the effective particle entrapment (Figure 6.5). MOF@NC samples were strongly stirred in deionized water and optically inspected afterwards by SEM, revealing no visible change compared to before treatment. Also, a droplet of the water was extracted after mixing and deposited on alumina foil. After air drying, several locations on the alumina foil were imaged by SEM, showing no significant leaching of particles through the fibrous layer. In addition, MOF@NC samples as well as control samples without MOF particles were measured by atomic force microscopy (AFM). The comparison between the area scans on samples without and samples with integrated MOF particles clearly show the roughening of the surface when MOF particles were involved (Figure 6.6). The roughening makes uniform large area scans on the MOF@NC samples difficult, while the control samples with their relatively uniform fibrous layer could be imaged without such issues. Line profile scans revealed an approximate thickness of the fibrous layer up to $3\mu\text{m}$.

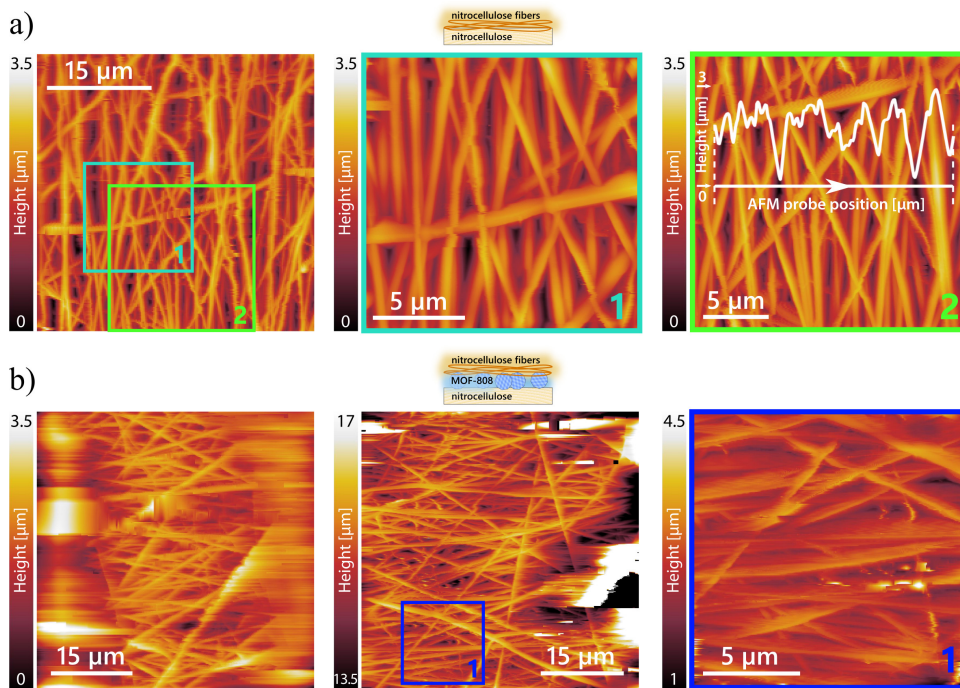


Figure 6.6: Atomic force microscopy (AFM) area scans on fibrous layers without (a) and with integrated MOF particles (b). The pure fibrous layer can be measured uniformly, giving an approximate thickness of up to $3\mu\text{m}$ by line profile scans. A clear difference compared to the samples with MOF particles can be seen, where the integration of the MOFs leads to a roughening of the surface making uniform AFM large area scans difficult.

6.4 Raman spectroscopy

Analysis of individual layers

Raman spectroscopy is used as an analytical sensing tool, enabled by the fact that the integrated MOF particles can be spotted through the loose NC mesh. After each fabrication step, the layers were examined with Raman spectroscopy, which then are the (i) pure NC membrane, (ii) NC membrane with MOF particles, (iii) NC membrane with MOF particles and electrospun fibrous NC layer on top (= 'active MOF@NC') and (iv) NC membrane with electrospun fibrous NC layer on top without MOF particles (= 'control') (Figure 6.7a).

The Raman spectra of nitrocellulose and MOF-808 are clearly distinguishable and agree with known data from literature.^{318,321} The most prominent peaks in the region between 800 cm^{-1} and 1700 cm^{-1} could be assigned to corresponding vibrational modes (Figure 6.7b). Depending on whether the layer contains MOF particles or not, the MOF signal or the NC signal predominates. Nitrocellulose has strong Raman intensities at 850 cm^{-1} and 1287 cm^{-1} , coming from the NO and the symmetric NO_2 stretching modes.³²¹ The peak at 1660 cm^{-1} belongs to

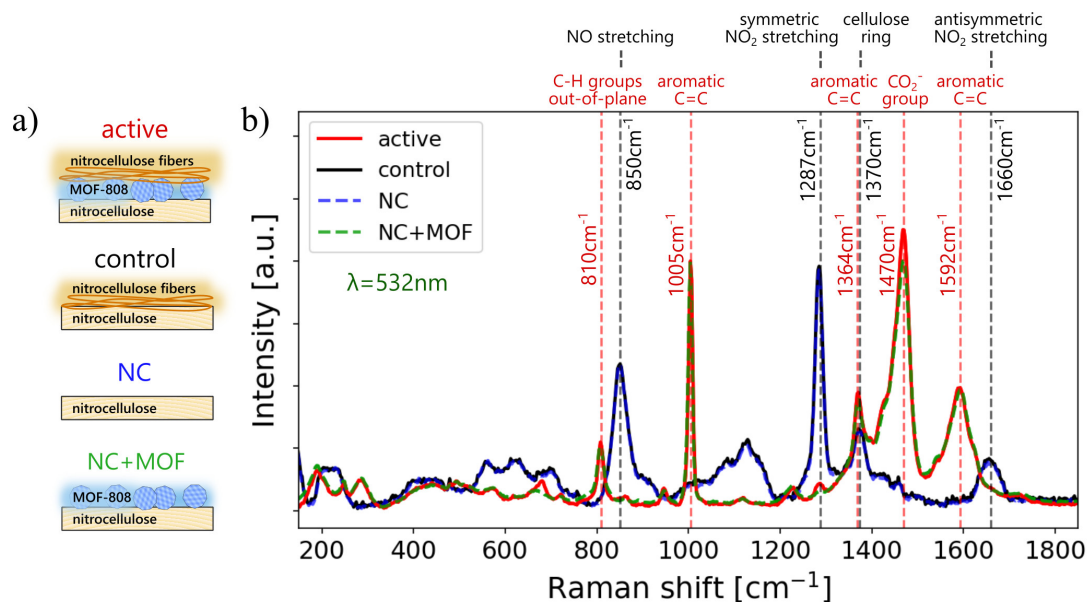


Figure 6.7: a) Schematic profile views of the different fabricated layers: NC+MOF+NC fibers (active), NC+NC fibers (control), NC+MOF and pure NC. b) Raman spectra of each individual layer. Samples with and without MOF particles show different Raman patterns, allowing a clear distinction. Minor variations between the active MOF sample and the MOF sample without top NC layer can be seen due to a slight spectrum superposition. (excitation wavelength $\lambda_{\text{exc}} = 532\text{ nm}$; grating with 600 g mm^{-1}).

the antisymmetric NO₂ stretching mode and 1370 cm⁻¹ is likely related to the cellulose ring.³²¹ For MOF-808, the organic ligand benzene tricarboxylate (BTC) is mainly involved in the Raman signal. The wavenumbers 1005 cm⁻¹, 1364 cm⁻¹ and 1592 cm⁻¹ show prominent Raman peaks associated with the C=C vibrations of the aromatic BTC ring.³¹⁸ The peak at 810 cm⁻¹ can be assigned to the C-H out-of-plane deformation mode, and the signal at 1470 cm⁻¹ is coming from the CO₂⁻ groups.³¹⁸ When viewing the Raman signal from samples containing MOFs, the focal point is adjusted to maximize the MOF signal at 1005 cm⁻¹. The comparison of the active MOF@NC spectrum with the MOF signal of the open NC+MOF shows a higher intensity of the MOF@NC architecture at certain wavenumbers, e.g. 675 cm⁻¹ (9x higher), 715 cm⁻¹ (6x higher) and 1287 cm⁻¹ (3.5x higher). This is due to a superimposed signal caused by the influence of the nitrocellulose that also extends into the focal volume of the laser beam and whose spectrum matches that of the peaks.

Objective focal size calculation

Depending on the objective used and thus the numerical aperture associated with it, the laser beam is focused on the sample with different dimensions of the lateral and axial focus during the Raman measurement. For a strong Raman signal, the object of interest (here our MOF particles) should be in the region of highest light intensity, i.e. in the focal volume of the focused laser beam. The choice of the objective determines the focal dimension and thus the extent to which MOF particles are located in the focus. A narrow focus reflects the measurement at one point, while a wider focus covers a slightly bigger range, also in axial direction. Since the MOF particles are integrated below a top NC layer, it was tested how the choice of the objective affects the Raman signal.

In Figure 6.8a, the Raman spectra of active MOF@NC samples as well as control samples without MOFs are shown for different objectives: magnification 50x long distance (LD), 100x long distance (LD) and 100x short distance. The measurements, all performed with an excitation wavelength of $\lambda_{\text{exc}} = 532$ nm, show a clear match of the signals from the 100x objectives. In contrast, the objective with magnification 50x shows deviations for both the active and the control sample. The MOF signal of the active sample contains peaks that correspond to the pattern of the NC. This superposition is due to the larger focal length of the 50x objective and thus a stronger influence of the NC extending into the focal volume of the laser beam.

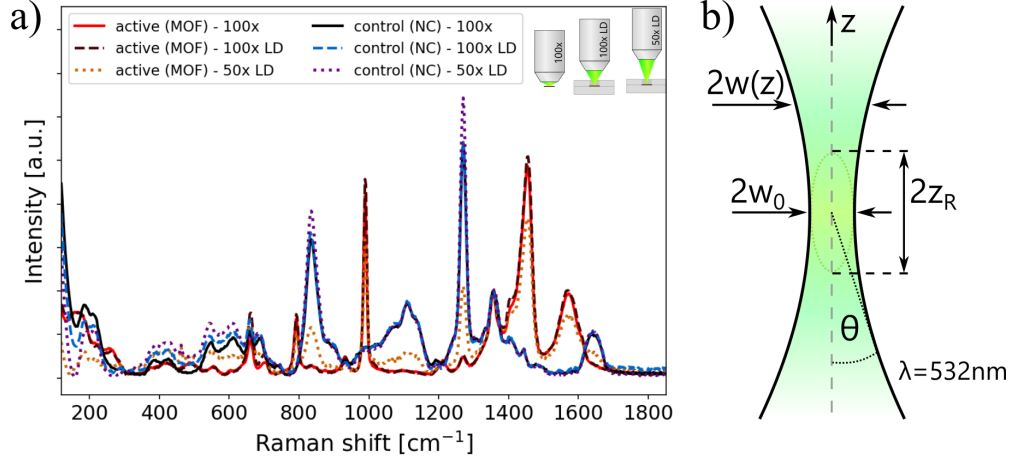


Figure 6.8: a) Raman spectra of active samples (with MOFs) and control samples (without MOFs) using different objectives with magnification 50x (long distance LD), 100x (long distance LD) and 100x (short distance). b) Schematic representation of a focused laser beam forming a beam waist with the beam radius $w(z)$, beam waist radius w_0 , Rayleigh length z_R and half divergence angle θ .

To support our findings, the depth of focus for each objective is to be calculated. The intensity of the laser beam has a Gaussian profile symmetrical to the propagation direction of the light and can be described using Gaussian optics.^{248,322–324} If a laser beam is focused along the direction z , a beam waist is formed (Figure 6.9b), whose radius $w(z)$ can be described by

$$w(z) = w_0 \sqrt{1 + \left(\frac{z}{z_R}\right)^2} \quad (20)$$

Here, w_0 is the beam waist radius, i.e. the narrowest spot with minimum beam diameter, which can be written as follows

$$w_0 = \sqrt{\frac{z_R \lambda}{\pi}} = \frac{\lambda}{\pi \tan(\theta)} \quad (21)$$

where θ is half the divergence angle given by the numerical aperture NA of the optical system

$$\text{NA} = n \sin(\theta) \quad (22)$$

z_R is the Rayleigh length, which is the distance at which the beam radius w widens to $\sqrt{2}$ times the beam waist w_0 (beam cross section doubles at z_R). Its dependence

on the beam waist and the laser wavelength λ is given by

$$z_R = \frac{\pi w_0^2}{\lambda} \quad (23)$$

An assessment of the depth of focus can be made by the double Rayleigh length $2z_R$, which is also called confocal parameter.^{322,325} For the setup used here with excitation wavelength of $\lambda_{\text{exc}} = 532 \text{ nm}$ and the given numerical apertures of the objectives 50x LD, 100x LD and 100x, the calculated values for waist diameter and depth of focus are listed in Table 1. It is evident that the depth of focus of

Table 1: Calculated values of waist diameter and depth of focus for different objectives and excitation wavelength $\lambda_{\text{exc}} = 532 \text{ nm}$.

| Objective magnification | numerical aperture NA | waist diameter $2w_0$ [μm] | depth of focus $2z_R$ [μm] |
|-------------------------|-----------------------|---|---|
| 50x LD | 0.55 | 0.58 | 1.00 |
| 100x LD | 0.75 | 0.40 | 0.47 |
| 100x | 0.9 | 0.30 | 0.27 |

the 50x objective is about twice or four times as large as that of the 100x LD or 100x objective. Thus, there is a greater probability that NC will reach into the focus and contribute to the MOF Raman signal. Since the MOF particles vary in size and are distributed over a wider area, a larger focal volume is advantageous to obtain a Raman signal from MOFs and achieve averaging, especially along the axial direction. The 50x objective was therefore used for the following Raman sensing experiments.

Additional Raman test measurements

Additional Raman measurements with an excitation wavelength of 488 nm and a different spectrometer grating were performed to get an insight into the very low wavenumber region at about $< 200 \text{ cm}^{-1}$) (details on the parameters in Section 6.A.2). The Raman spectra for an active MOF@NC sample and control sample are shown in Figure 6.9a. Compared to the excitation wavelength of 532 nm, the same Raman patterns are observed, although the signal-to-noise ratio is decreased, which is why the 532 nm laser is used for the following measurements.

Another test measurement concerns the influence of water on the MOF-808 Raman signal. Water was found to affect the MOF Raman spectra and mask the signal especially at low wavenumbers below $< 300 \text{ nm}$, as shown in Figure 6.9b. Since

changing environmental conditions with fluctuating moisture levels could influence the Raman results, the measurements were performed in a closed chamber under a nitrogen atmosphere. Prior to measurements, samples were heated to remove water to ensure uniform measurement conditions.

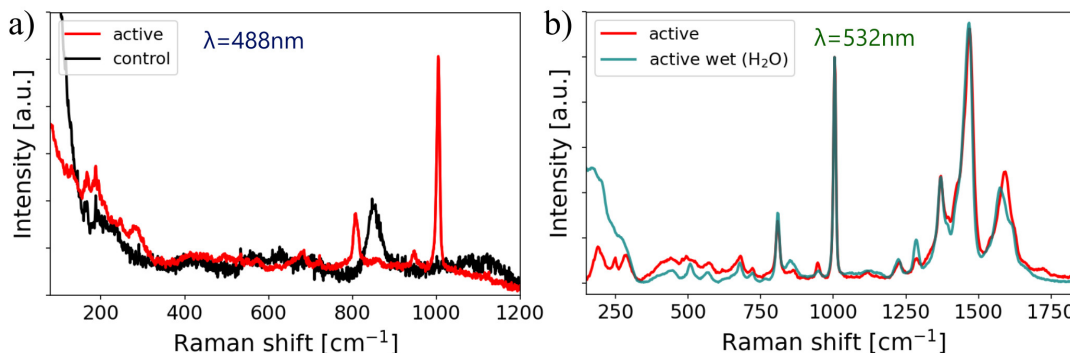


Figure 6.9: a) Raman spectra of active and control MOF@NC samples using an excitation wavelength of $\lambda_{\text{exc}} = 488 \text{ nm}$ to show the signal in the low wavenumber regime. b) Raman spectra of dry MOF@NC sample (measured after heating in N_2 environment) and wet active sample (measured at ambient conditions after moistened with $20 \mu\text{l}$ deionized water) with excitation wavelength of $\lambda_{\text{exc}} = 532 \text{ nm}$.

6.5 Sensing experiments

Ionic biomarkers

Raman spectroscopy was then used to test the active MOF@NC architecture for sensing of ionic sweat biomarkers such as sodium chloride (NaCl) and potassium chloride (KCl). It was investigated how the Raman spectrum of the integrated MOF-808 changes with the addition of different analyte solutions. In order to treat the MOF@NC samples in a structured multiwell-like approach with different analytes and concentrations, a sample holder (made of PEEK) was specially fabricated, in which the samples can be clamped (Figure 6.10a). The analyte solutions are added to the sample and the porous and hydrophilic nature of the fibrous layers enables good sample wetting with the aqueous solution. The idea is that the NC fibrous layer provides an additional filtering effect where larger particles are physically retained while smaller analytes such as the dissolved ions can pass through and may be trapped by interactions with the MOF. This then becomes apparent as changes in the Raman spectrum of the MOF due to modifications in the vibrational modes (Figure 6.10a).

First, the concentration and wavenumber range of interest are to be identified. Six individual active samples were treated with aqueous NaCl solutions of different concentrations, two of them with the same concentration (0.005 M, 0.05 M and 0.5 M). Before and after treatment, Raman measurements were performed on MOF particles at different positions to have statistical significance, in total 11-12 positions. The localization of MOF particles was possible because the particles shone through the top NC fibrous layer (Supporting Information Figure 6.18a). Figure 6.10b shows the full Raman spectra of the three samples before and after treatment. In particular, in the marked regions of interest I, II and III, a stronger signal reduction for certain peaks could be observed, the higher the NaCl concentration was. This becomes apparent when the data is presented as a differential plot, i.e. the spectrum before treatment is subtracted from the spectrum after treatment, as shown in the Supporting Information Figure 6.18. The differential approach simultaneously compensates for batch-to-batch variations and features the strongest intensity changes with increasing NaCl concentration at the positions 286 cm^{-1} , 1470 cm^{-1} , 1595 cm^{-1} , 2870 cm^{-1} and 2930 cm^{-1} . The intensity shift does not occur equally for all peaks, which can also be seen when zooming into region of interest I (low wavenumbers $120\text{-}340\text{ cm}^{-1}$) in Figure 6.10c, where the most pronounced variation occurs at 286 cm^{-1} (Figure 6.10d). A fit to the peaks with a Lorentzian curve was performed for this selected region of interest, and the intensity values were plotted against the NaCl concentration, showing an exponential course (Figure 6.10e). For lower concentrations up to about 0.05 M, an approximately linear dependence is observed.

Next, an active sample was treated several times in succession with aqueous NaCl solution to better quantify the intensity shift after treatment. In the process, the concentration was increased stepwise to 0.5 M to monitor the progression for a larger concentration range. The complete Raman spectra as well as the zoom of the windows of interest are shown in Figure 6.11. At the same time, a second sample was also treated successively with NaCl solutions, but with solutions of the same concentration of 0.01 M (Figure 6.12). All spectra shown are averaged spectra of three to six individual measurements at different locations (individual spectra for treatment with same concentrations of 0.01 M shown in Supporting Information Figure 6.19). Both series of measurements show the same behavior and confirm the different intensity variations for each peak. For a quantification, the peaks displayed were fitted to a Lorentzian curve for each individual spectra and the normalized intensity changes $I_{\text{norm}} = \Delta I / I_{\text{H}_2\text{O}}$ (with $\Delta I = I - I_{\text{H}_2\text{O}}$)

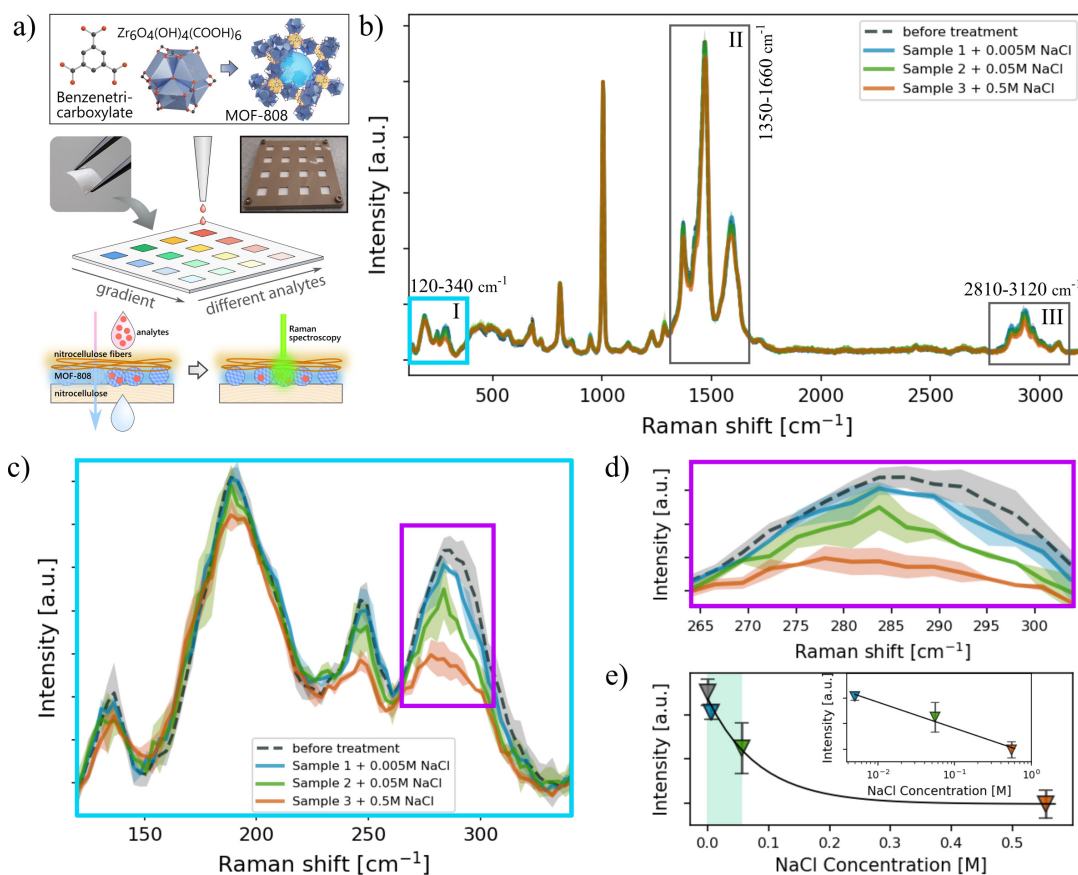

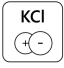
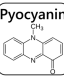


Figure 6.10: a) Top: Schematic of MOF-808, built by coordination of benzenetricarboxylate organic linker (BTC) and zirconium metallic cluster (pores illustrated as blue and yellow spheres). Middle: Illustration of sample holder for systematic treatment of MOF@NC samples with analytic solutions. Insets: photographs of a tweezer holding MOF@NC sample and filled sample holder. Bottom: Schematic of the sensing workflow: After treatment of MOF@NC samples with analyte solutions, Raman spectroscopy is performed for chemical analysis and detection of the trapped analytes by optical signal changes. b) Full range spectra of individual active MOF@NC samples after treatment with aqueous NaCl solutions of different concentrations (concentrations from 0.005 M to 0.5 M, droplet volume of 20 μ l, $\lambda_{\text{exc}}=532$ nm). Three regions of interest I, II and III with pronounced signal reduction after treatment are marked by boxes. c-e) Zoomed-in spectra in region I at 120-340 cm^{-1} (c) and 265-305 cm^{-1} (d), indicated by the cyan and violet box. The solid lines show the average spectra of 11-12 measurements performed on two different samples for each concentration. Standard deviation is displayed as colored area. e) Peak intensity values at 285 cm^{-1} for each sample, plotted against NaCl concentration. Inset shows the data on a logarithmic scale and green area highlights the regime of interest, with the linear dependence being further investigated.

were calculated and plotted against NaCl concentration (full range spectra and Lorentzian fits for treatment with same concentrations of 0.01 M shown in Supporting Information Figure 6.20). The plots of the normalized intensity changes are shown as insets in the Figures 6.11 and 6.12 and in Figure 6.11f-h for the full concentration range. The measurement with stepwise increase to higher concentration values shows an exponential course with approximately linear behavior

Table 2: Sensitivities (slopes) and R^2 -values of the linear fits of the normalized intensity changes $I_{\text{norm}} = \Delta I/I$ for all peaks after treatment with NaCl, KCl and pyocyanin.

| | | ◀ | ▲ | ▶ | ▼ | ⊗ | ⬠ | ■ | + | ⬡ | ● | ◆ | ⊗ | ◆ | ⬠ | ★ |
|--|---|-------|-------|-------|-------|------|-------|-------|-------|-------|-------|------|-------|-------|-------|-------|
| | wavenumber [cm ⁻¹] | 135 | 188 | 244 | 286 | 808 | 1004 | 1370 | 1425 | 1470 | 1595 | 1620 | 2870 | 2930 | 2970 | 3080 |
|  NaCl | $I_{\text{norm slope}}$ [a.u. μmol^{-1}] | -0.19 | -0.17 | -0.48 | -0.47 | | | -0.06 | -0.11 | -0.07 | -0.05 | 0.06 | -0.41 | -0.37 | -0.28 | -0.09 |
| | R^2 -value [%] | 48.8 | 70.9 | 97.0 | 97.9 | | | 77.0 | 83.7 | 82.9 | 77.5 | 29.4 | 83.4 | 63.7 | 49.2 | 70.2 |
|  KCl | $I_{\text{norm slope}}$ [a.u. μmol^{-1}] | 0.01 | 0.01 | -0.30 | -0.42 | | | -0.07 | -0.15 | -0.06 | -0.08 | 0.07 | -0.33 | -0.42 | -0.35 | 0.07 |
| | R^2 -value [%] | 0.4 | 1.1 | 72.7 | 94.2 | | | 64.6 | 92.1 | 66.3 | 66.7 | 86.5 | 71.7 | 74.7 | 69.5 | 28.3 |
|  Pyocyanin | $I_{\text{norm slope}}$ [a.u. μmol^{-1}] | | -1053 | -728 | -787 | -883 | -1120 | -826 | -750 | -1084 | -797 | -528 | | | | |
| | R^2 -value [%] | | 97.5 | 91.3 | 91.2 | 98.8 | 98.6 | 98.1 | 99.0 | 99.3 | 98.9 | 94.9 | | | | |

at concentrations in the range up to about 0.05 M, which lies in the concentration range of the second measurement with constant concentrations. In this linear range, regression lines were fitted for each peak and the linear slopes representing the sensitivity values were evaluated (slope values and coefficients of determination (R^2) are listed in Table 2). For NaCl, the largest slope values of -0.48 and -0.47 a.u. μmol^{-1} occur at the low wavenumber peaks at 244 cm^{-1} and 286 cm^{-1} , respectively. At 1595 cm^{-1} and 1370 cm^{-1} , only extremely weak changes in normalized intensity of -0.05 and -0.06 a.u. μmol^{-1} are observed. Also, at 1620 cm^{-1} , a small slope of 0.06 a.u. μmol^{-1} with a positive sign occurs, attributed to a peak shoulder whose intensity grows with increasing NaCl concentration. Furthermore, the relative intensity changes $I_{\text{rel}} = \Delta I/I$ for the peaks with the largest and smallest intensity reduction for each wavenumber region of interest were calculated. It further illustrates the different sensitivities of the various peaks and highlights the stronger relative intensity changes at the peaks 286 cm^{-1} (region I) and 2930 cm^{-1} (region III) compared to the peaks in the range between 1350 cm^{-1} and 1660 cm^{-1} (region II). Also, the peaks at 188 cm^{-1} or 3080 cm^{-1} demonstrate relative intensity changes of nearly zero. When the sample with successive NaCl treatment with solutions of same concentrations was subsequently treated with deionized water,

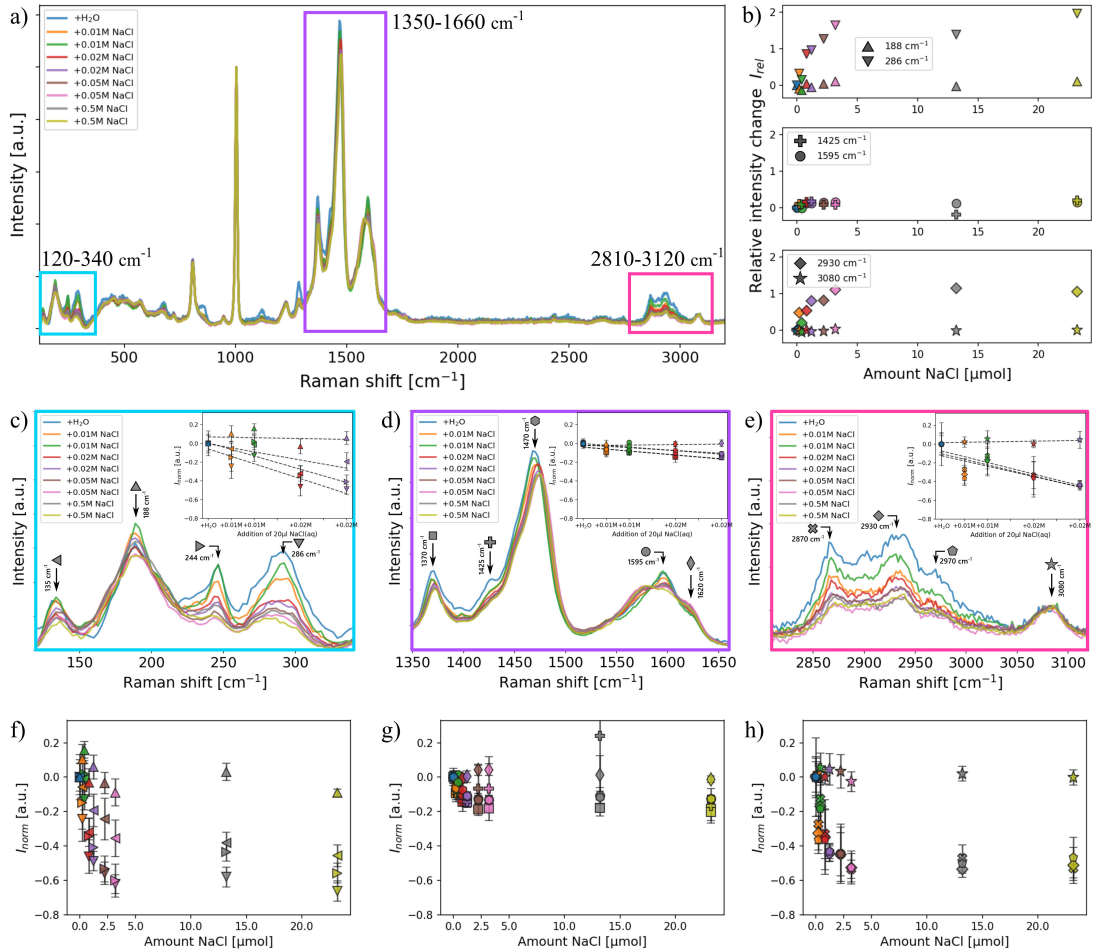


Figure 6.11: a) Full Raman spectra of MOF@NC after successive treatment with aqueous NaCl solutions (concentrations from 0.01 M to 0.5 M, droplet volume of 20 μ l). Regions of interest are marked by colored boxes. b) Relative intensity change $I_{rel} = \Delta I / I$ (with $\Delta I = I - I_{H_2O}$) for the peaks with the largest and smallest intensity reduction for each wavenumber region of interest. c-e) Zoomed-in spectra in the regions 120-340 cm⁻¹ (c, cyan), 1350-1660 cm⁻¹ (d, violet) and 2810-3120 cm⁻¹ (e, magenta). Prominent peaks (marked with symbol and wavenumber) are fitted with a Lorentzian curve, and the normalized intensity change $I_{norm} = \Delta I / I_{H_2O}$ of the peaks are evaluated and plotted against NaCl concentration, shown as inset for the linear range and in (f-h) for the full range. The error bars indicate the standard deviation and the dashed lines show the linear fits.

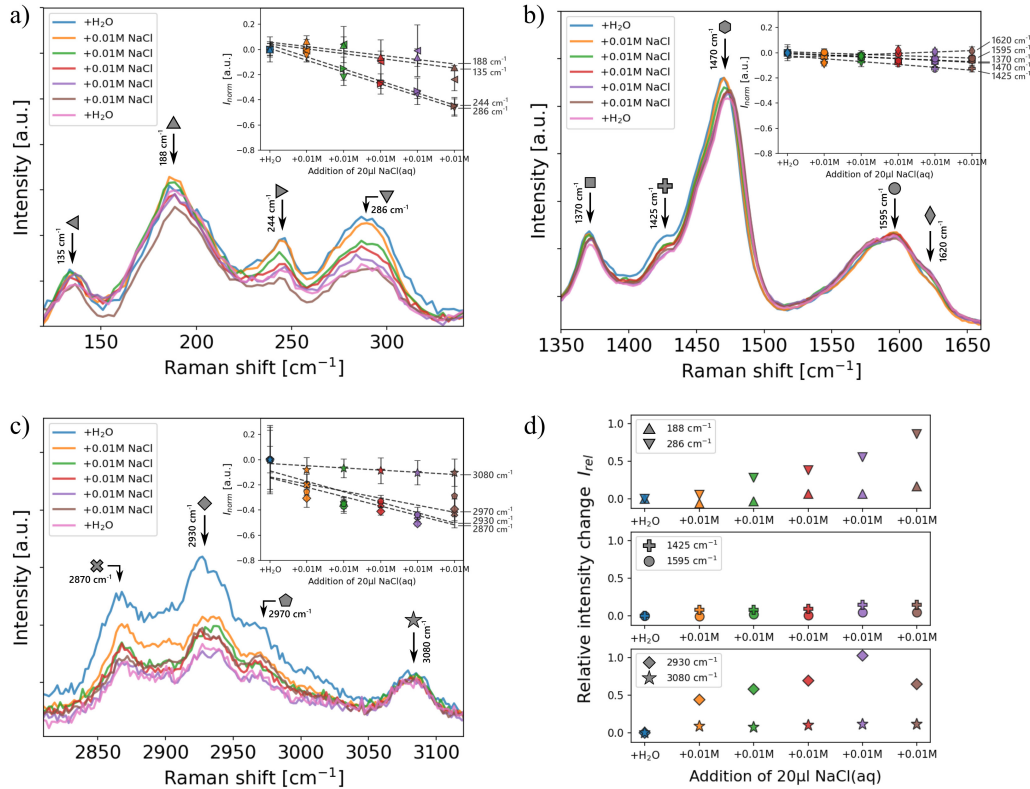


Figure 6.12: a-c) Raman spectra of MOF@NC after successive treatment with aqueous NaCl solutions (concentrations of 0.01 M, droplet volume of 20 μl) in the wavenumber regions of interest 120-340 cm^{-1} (a), 1350-1660 cm^{-1} (b) and 2810-3120 cm^{-1} (c). Prominent peaks (marked with symbol and wavenumber) are fitted with a Lorentzian curve, and the normalized intensity change $I_{\text{norm}} = \Delta I / I_{\text{H}_2\text{O}}$ (with $\Delta I = I - I_{\text{H}_2\text{O}}$) of the peaks are evaluated and plotted against NaCl concentration, shown as inset. The error bars indicate the standard deviation and the dashed lines show the linear fits. d) Relative intensity change $I_{\text{rel}} = \Delta I / I$ for the peaks with the largest and smallest intensity reduction for each wavenumber region of interest.

the Raman spectrum remains the same, so it can be assumed that no significant elution has occurred (Figure 6.12).

Besides sodium chloride, the ionic sweat biomarker potassium chloride (KCl) was also tested on our sensing architecture. As previously, an active MOF@NC sample was successively treated with KCl solutions of equal concentration (0.01 M) and measured by Raman spectroscopy. The resulting Raman spectra are shown in Figure 6.13, as a whole and zoomed-in. Possibly because of the equal chemical properties between the two salts, KCl shows a similar behavior of Raman intensity reduction as for the treatment with NaCl. This becomes evident after evaluating the normalized and relative intensity changes and comparing the sensitivity

values of the different peaks between NaCl and KCl in Table 2. Again, one of the largest slope value is found at the low wavenumber peak at 286 cm^{-1} with $-0.42\text{ a.u. }\mu\text{mol}^{-1}$, together with the peak at 2930 cm^{-1} , which is slightly higher compared to NaCl ($-0.37\text{ a.u. }\mu\text{mol}^{-1}$). No significant normalized intensity change is seen in the 135 cm^{-1} and 188 cm^{-1} peaks. The peak shoulder at 1620 cm^{-1} shows again a positive trend with increasing KCl concentration ($0.07\text{ a.u. }\mu\text{mol}^{-1}$), this time not as the only peak, as the peak at 3080 cm^{-1} shows the same positive slope. In this case, however, the course of the relative intensity change is almost zero and the coefficient of determination does not show a high value either, so it can be considered that there is no significant intensity change.

The results of NaCl and KCl are very similar and do not currently allow discrimination between the two salts from the data presented. The exact explanation of the trapping mechanism and the interactions between analyte and MOF can only be speculated without theoretical simulations. Possibly, the similar effect of the two salts on the Raman spectra after interaction with the MOF is due to the negatively charged chloride ion present in both salts. In other work, it has already been shown that negatively charged iodine (I_2^- or I_3^-) is adsorbed into the pores of MOF-808, thereby showing strong affinity to the terminal -OH groups of the Zr cluster and low affinity to BTC ligands.³²⁶ Whether the positively charged ions of sodium and potassium interact with the MOF is not clear, but they could also have a similar effect on the vibrational modes due to their chemical similarity.

Pyocyanin

In addition to ionic biomarkers, the potential to sense small chemical molecules with biological relevance was also demonstrated by testing pyocyanin on our MOF@NC architecture. Pyocyanin is a biomarker for the pathogen *Pseudomonas aeruginosa* and is water soluble. Aqueous solutions of concentration 0.01 mM were used for successive treatment of the active MOF@NC samples, which is in the concentration range found in biological fluids such as wound specimens, urine or human ear secretions.³²⁷ Initial Raman measurements using the laser with excitation wavelength of 532 nm lead to the appearance of fluorescence reducing the signal-to-noise ratio as well as to a laser damaging effect on pyocyanin even if the laser power is largely reduced to 4 mW (Supporting Information Figure 6.21). By changing the laser to a longer excitation wavelength of 785 nm , fluorescence background and laser damage to the organic material could be avoided.³²⁸ The 785 nm laser allowed the MOF@NC architecture to be measured without damage,

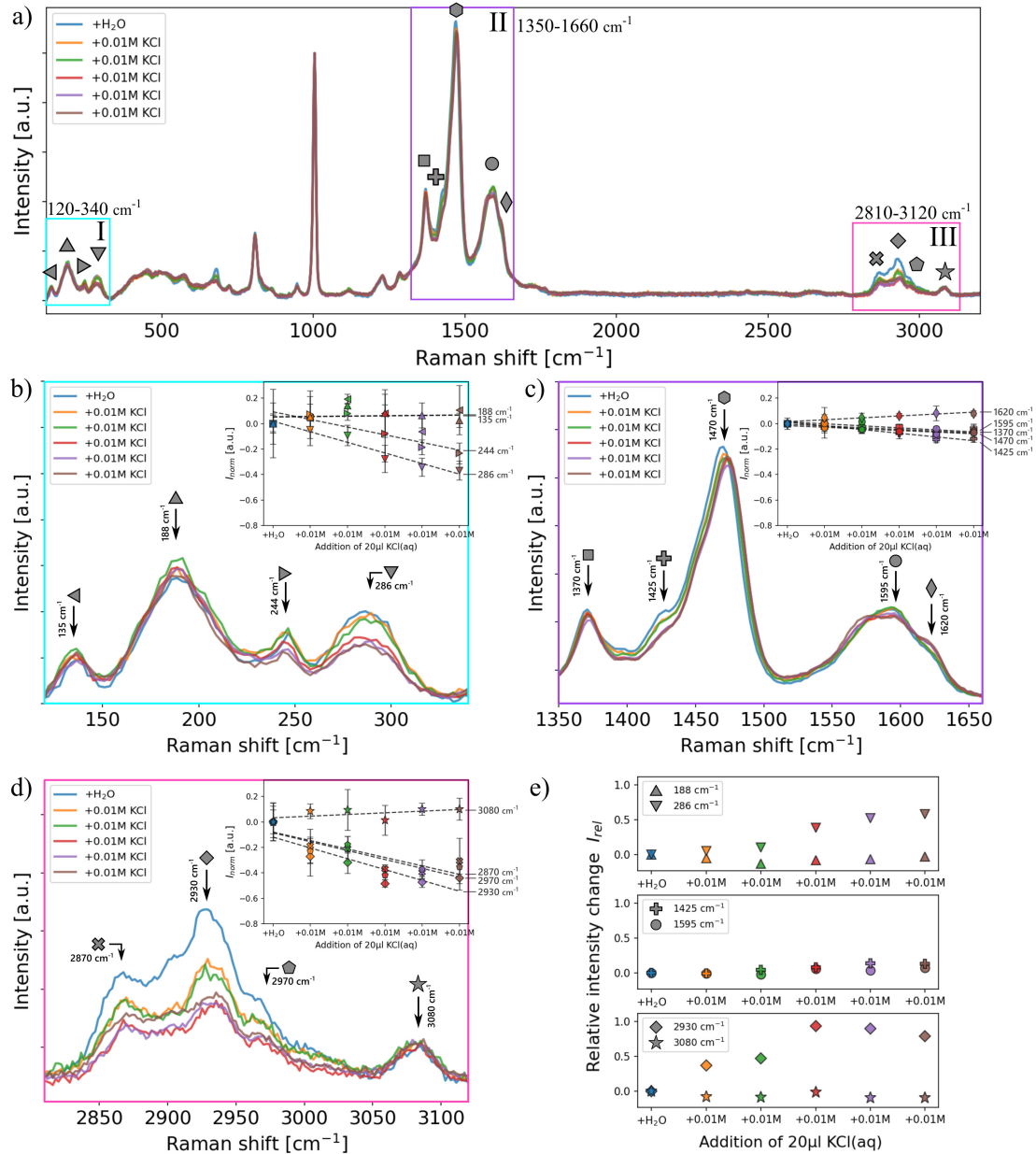


Figure 6.13: a) Full Raman spectra of MOF@NC after successive treatment with aqueous KCl solutions (concentrations of 0.01 M, droplet volume of 20 μ l). Regions of interest are marked by colored boxes. b-d) Zoomed-in Raman spectra in the wavenumber regions of interest 120-340 cm^{-1} (b), 1350-1660 cm^{-1} (c) and 2810-3120 cm^{-1} (d). Prominent peaks (marked with symbol and wavenumber) are fitted with a Lorentzian curve, and the normalized intensity change $I_{\text{norm}} = \Delta I / I_{\text{H}_2\text{O}}$ (with $\Delta I = I - I_{\text{H}_2\text{O}}$) of the peaks are evaluated and plotted against KCl concentration, shown as inset. The error bars indicate the standard deviation and the dashed lines show the linear fits. e) Relative intensity change $I_{\text{rel}} = \Delta I / I$ for the peaks with the largest and smallest intensity reduction for each wavenumber region of interest.

revealing the prominent MOF spectrum (the use of a 300 g mm^{-1} grating for this wavelength results in a smaller measurable spectral range).

The full Raman spectra as well as zoom of the wavenumber regions of interest are shown in Figure 6.14. A first observation indicates that with increasing pyocyanin concentration all peaks decrease significantly more than for the ionic solutions. Also, in contrast to the addition of the ionic solutions, the treatment with pyocyanin results not only in an intensity reduction of known peaks in the previous marked regions of interest, but also at the peaks at wavenumbers 808 cm^{-1} and 1004 cm^{-1} . The evaluation of the normalized intensity changes and linear fitting were performed as before and reveal the sensitivities for pyocyanin about four orders of magnitude larger than for the ionic NaCl and KCl solutions (Table 2). The largest slope occurs at the strong intensity peak at 1004 cm^{-1} with a value of $-1120\text{ a.u. }\mu\text{mol}^{-1}$. This is closely followed by $-1084\text{ a.u. }\mu\text{mol}^{-1}$ at the peak at 1470 cm^{-1} . The ionic solutions show a significantly different behavior, so that, for example, no significant change in intensity was observed at these peaks for NaCl and KCl. This becomes more evident when comparing the different Raman spectra visually at once. The Supporting Information Figure 6.22 compares the zoomed-in Raman spectra for low wavenumbers ($165\text{-}330\text{ cm}^{-1}$) and for large wavenumbers ($1350\text{-}1660\text{ cm}^{-1}$) after treatment with NaCl, KCl and pyocyanin. Here, the significantly stronger variation of the Raman spectrum after pyocyanin treatment, using a concentration lower by a factor of 1000 than for the ionic solutions, is clearly evident. The varying influence on the Raman spectrum of the MOF is due to the fact that pyocyanin is not an ion but a small molecule. Pyocyanin can enter the MOF because its molecular size is smaller than the 18 \AA wide pores of MOF-808.³²⁹ In the MOF, it is then likely to interact with the Zr clusters or organic ligands, probably in a different way than the ions do, which can then be distinguished in the Raman spectrum, but an exact mechanism of the interactions would require theoretical simulations. The fact that some arbitrary MOF without specific functionality is already able to discriminate different kind of biomarkers shows the great potential of our MOF@NC architecture as versatile sensing element using Raman spectroscopy as detection tool.

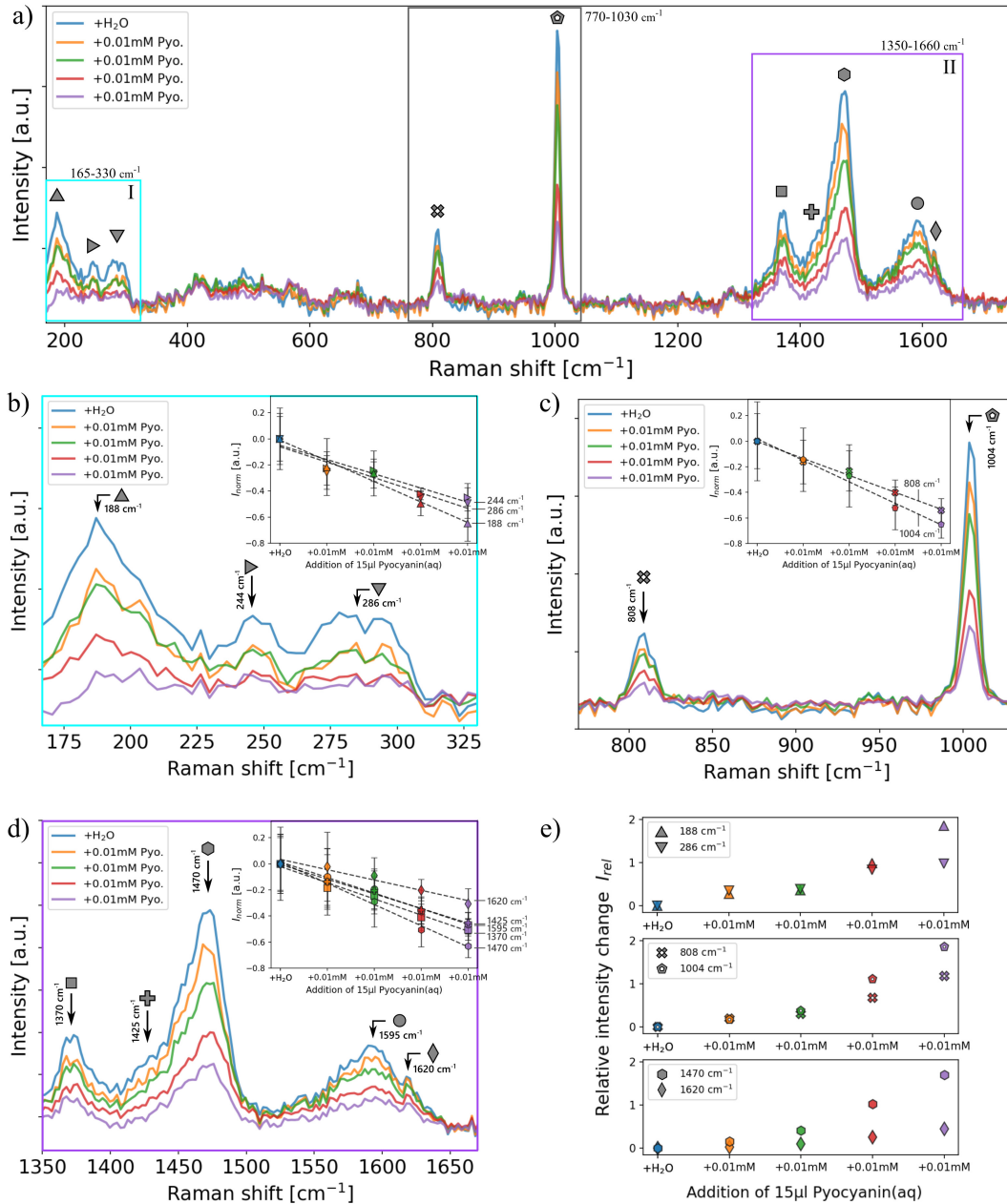


Figure 6.14: a) Full Raman spectra of MOF@NC after successive treatment with aqueous pyocyanin solutions (concentrations of 0.01 mM, droplet volume of 15 μ l). Regions of interest are marked by boxes. b-d) Zoomed-in Raman spectra in the wavenumber regions of interest 165-330 cm^{-1} (b), 770-1030 cm^{-1} (c) and 1350-1660 cm^{-1} (d). Prominent peaks (marked with symbol and wavenumber) are fitted with a Lorentzian curve, and the normalized intensity change $I_{norm} = \Delta I / I_{H_2O}$ (with $\Delta I = I - I_{H_2O}$) of the peaks are evaluated and plotted against pyocyanin concentration, shown as inset. The error bars indicate the standard deviation and the dashed lines show the linear fits. e) Relative intensity change $I_{rel} = \Delta I / I$ for the peaks with the largest and smallest intensity reduction for each wavenumber region of interest.

6.6 Conclusion and Outlook

In this work, we presented the fabrication of a biocompatible MOF@NC membrane for the sensing of biomarkers in solution. The integration of MOF-808 particles into a nitocellulose fibrous layer was realized by a sequential electro spraying and electro spinning process. This resulted in a loose mesh structure, that efficiently entrapped the MOF particles while keeping access to the pores open. The presented approach has the further advantage of being independent of the type of particles sprayed, such as different MOFs with individual functionality, as well as being able to choose the type of electro spun polymer as desired. After characterization by multiple methods such as SEM, AFM, EDX and Raman spectroscopy, the versatile sensing ability of our MOF@NC architecture was tested. The change in MOF Raman spectra upon exposure to NaCl, KCl and pyocyanin was investigated, with sensitivities for pyocyanin about four orders of magnitude greater than for the ionic biomarkers. Future theoretical simulations may provide deeper insight into the detailed mechanism of MOF-analyte interactions. In summary, this work has demonstrated the great potential of our MOF@NC architecture as a sensing platform for biomarkers in liquids, with high variability in the fabrication process and versatile tunability of chemical affinity to specific analytes in the future by adjusting MOF chemistry.

Author contributions

L.L. performed the sample fabrication, characterization, Raman measurements and sensing experiments. A.N. carried out XRD experiments and analyzed the diffraction data.

6.A Supporting Information

6.A.1 Additional Figures

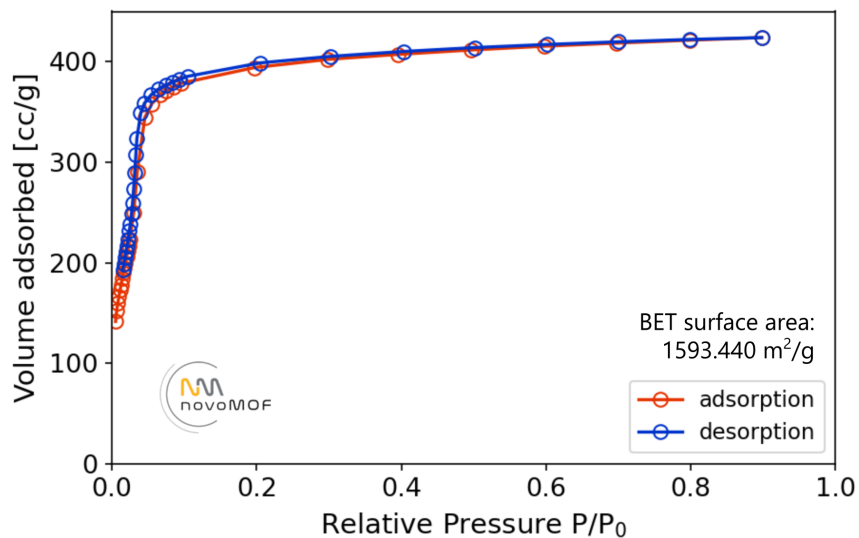


Figure 6.15: Nitrogen gas adsorption-desorption isotherms for MOF-808, executed by the company *novoMOF*. The evaluated specific BET surface area yields $1593.440 \text{ m}^2 \text{ g}^{-1}$ in agreement to known literature values.³³⁰

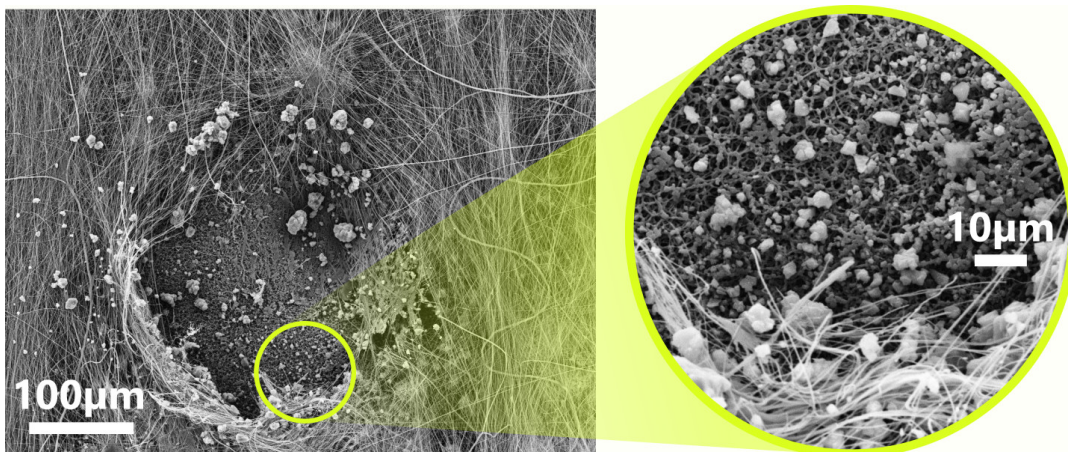


Figure 6.16: Scanning electron microscopy (SEM) image from the top of the MOF-808@nitrocellulose architecture. Electrospun NC fibers cover the MOF particles. The image shows an intentionally made hole in the fibrous layer, revealing the underlying MOF particles. The harsh procedure resulted in some particles being distributed outside.

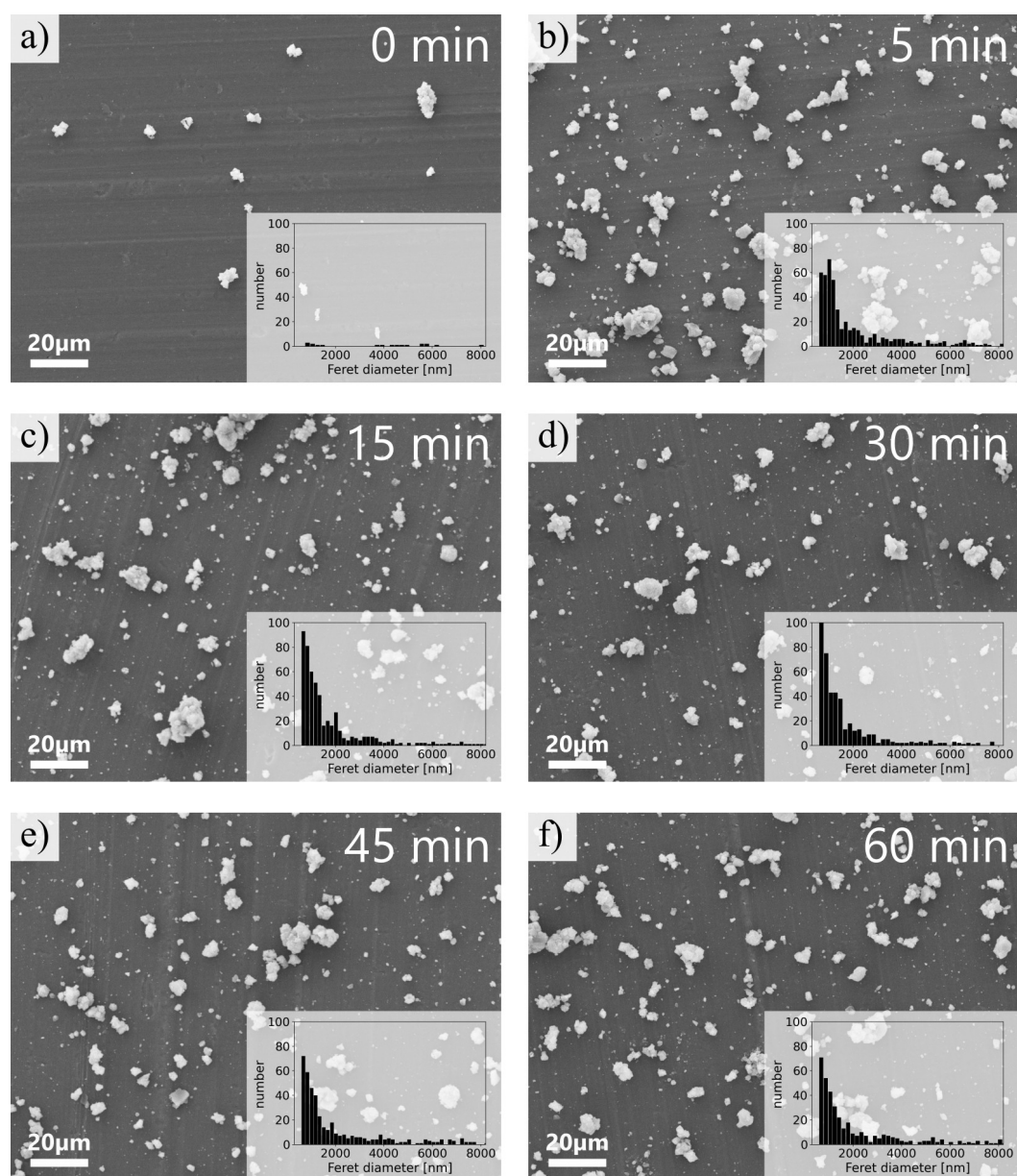


Figure 6.17: Study of influence of ultrasonication duration on the MOF particle size distribution after electro spraying. Immediately before electro spraying process, the MOF suspensions are treated by ultrasonication for different durations reaching from zero (a) to 60 min (f). SEM images show no significant influence on the particle size distribution for different ultrasonication times, except the test without any ultrasonic treatment due to a less stable suspension and a lower particle amount in the defined volume (a). Short ultrasonication of 5 min was enough to obtain a well-dispersed suspension and a consistent particle distribution.

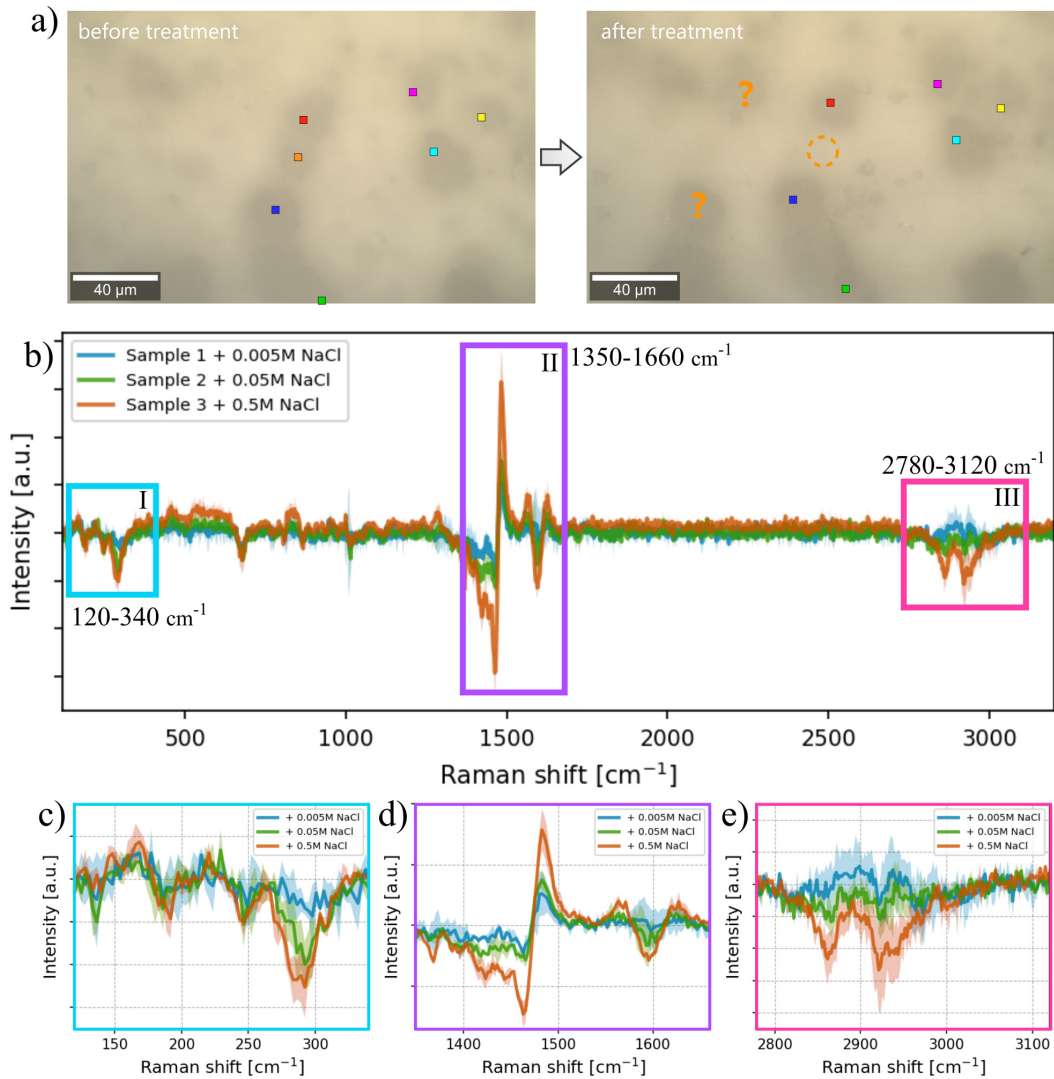


Figure 6.18: a) Optical microscopy images of active MOF@NC samples before and after treatment with aqueous NaCl solution. The MOF particles shine through the top NC fibrous layer, allowing localization of the measured areas. Colored squares indicate individual positions of Raman area scans at locations of maximum signal intensity for MOF-808. When particle positions change after treatment (see orange example), the differential approach is not executed. b) Differential representation of the Raman spectra after treatment with aqueous NaCl solutions of different concentrations, by subtracting the spectra before treatment from the spectra after treatment, performed individually for each sample. Regions of interest are marked by colored boxes. c-e) Zoomed-in spectra in the regions 120-340 cm⁻¹ (c, cyan), 1350-1660 cm⁻¹ (d, violet) and 2780-3120 cm⁻¹ (e, magenta).

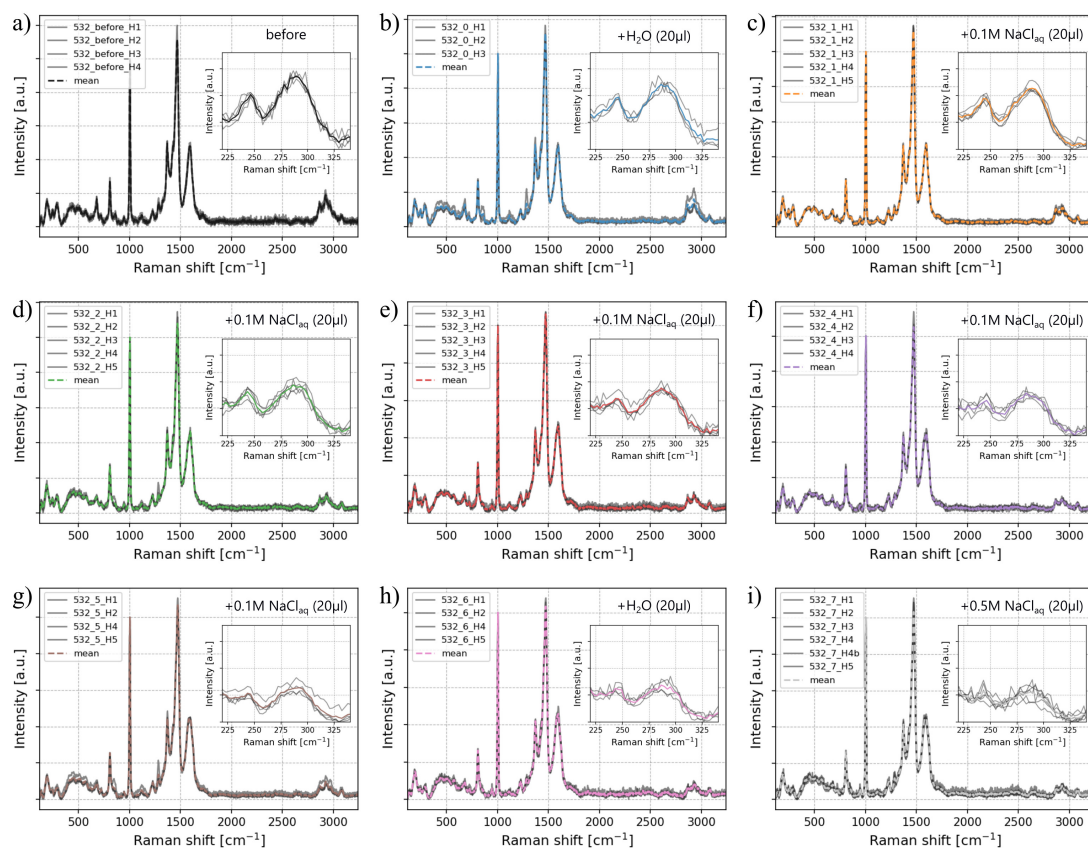


Figure 6.19: Individual (grey) and averaged (colored dashed line) Raman spectra of active MOF@NC sample, before any treatment (a), after treatment with H₂O (droplet volume of 20 μ l) (b), after 5x successive treatment with aqueous NaCl solutions (concentrations of 0.01 M, droplet volume of 20 μ l) (c-g), after second treatment with H₂O (droplet volume of 20 μ l) (h) and after treatment with aqueous NaCl solutions (concentrations of 0.05 M, droplet volume of 20 μ l) (i). Insets show the zoomed-in spectra in the region 220-340 cm^{-1} .

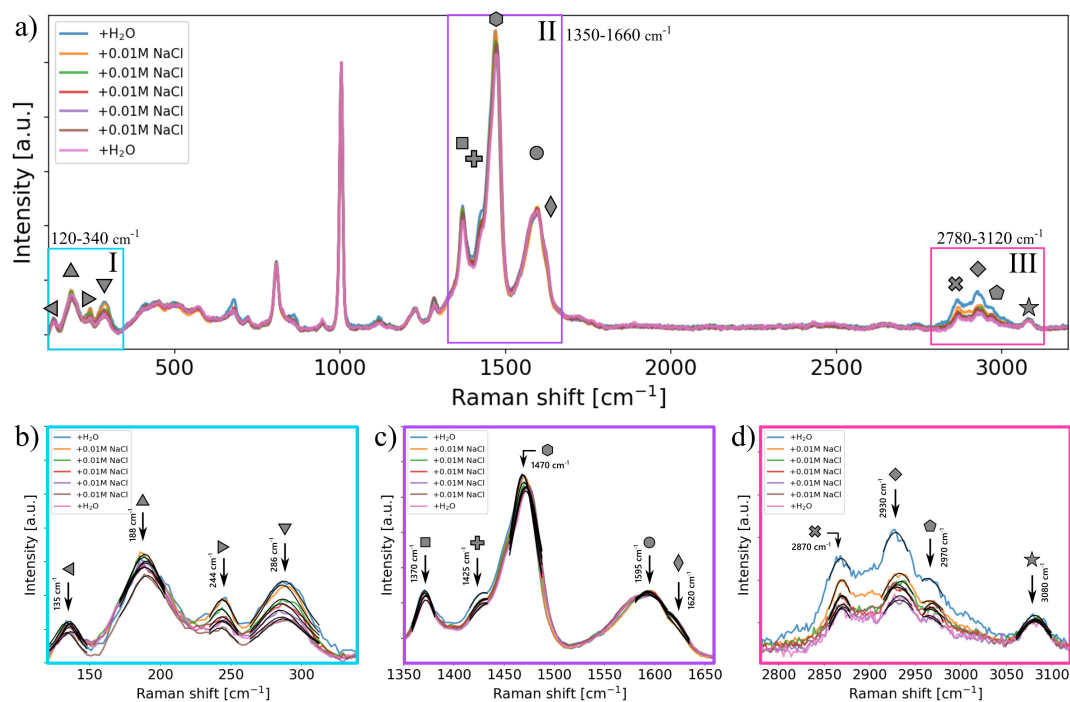


Figure 6.20: Full Raman spectra of MOF@NC after successive treatment with aqueous NaCl solutions (concentrations of 0.01 M, droplet volume of $20\ \mu\text{l}$). Regions of interest are marked by colored boxes. b-d) Zoomed-in Raman spectra in the wavenumber regions of interest $120\text{-}340\ \text{cm}^{-1}$ (b), $1350\text{-}1660\ \text{cm}^{-1}$ (c) and $2780\text{-}3120\ \text{cm}^{-1}$ (d). Prominent peaks (marked with symbol and wavenumber) are fitted with a Lorentzian curve, shown as black line.

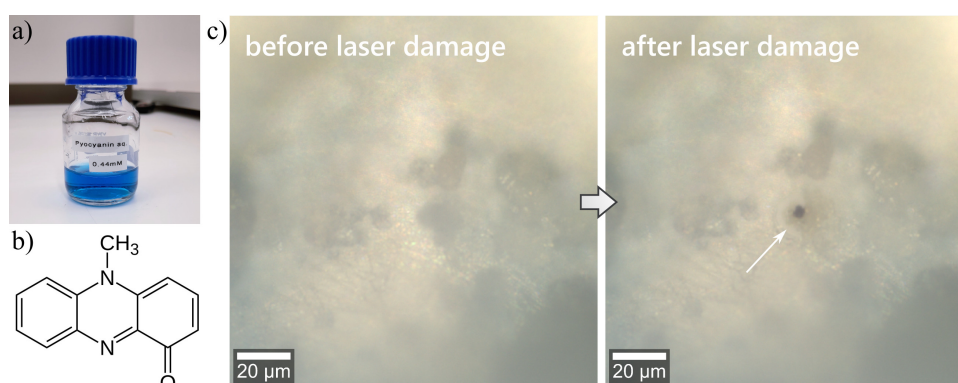


Figure 6.21: a) Aqueous pyocyanin solution (concentration 0.4 mM). b) Molecular structure of pyocyanin. c) Optical microscopy images of active MOF@NC samples after treatment with aqueous pyocyanin solution. The images demonstrate the damaging effect on pyocyanin after laser exposure during Raman measurements with wavelength $\lambda_{\text{exc}}=532\ \text{nm}$ (laser power $P=20\ \text{mW}$, area scan of size $3\ \mu\text{m} \times 3\ \mu\text{m}$ with integration time of 5 s and resolution of 2 pixels per μm). Damaging effect can be observed even when reducing the laser power to $P=4\ \text{mW}$.

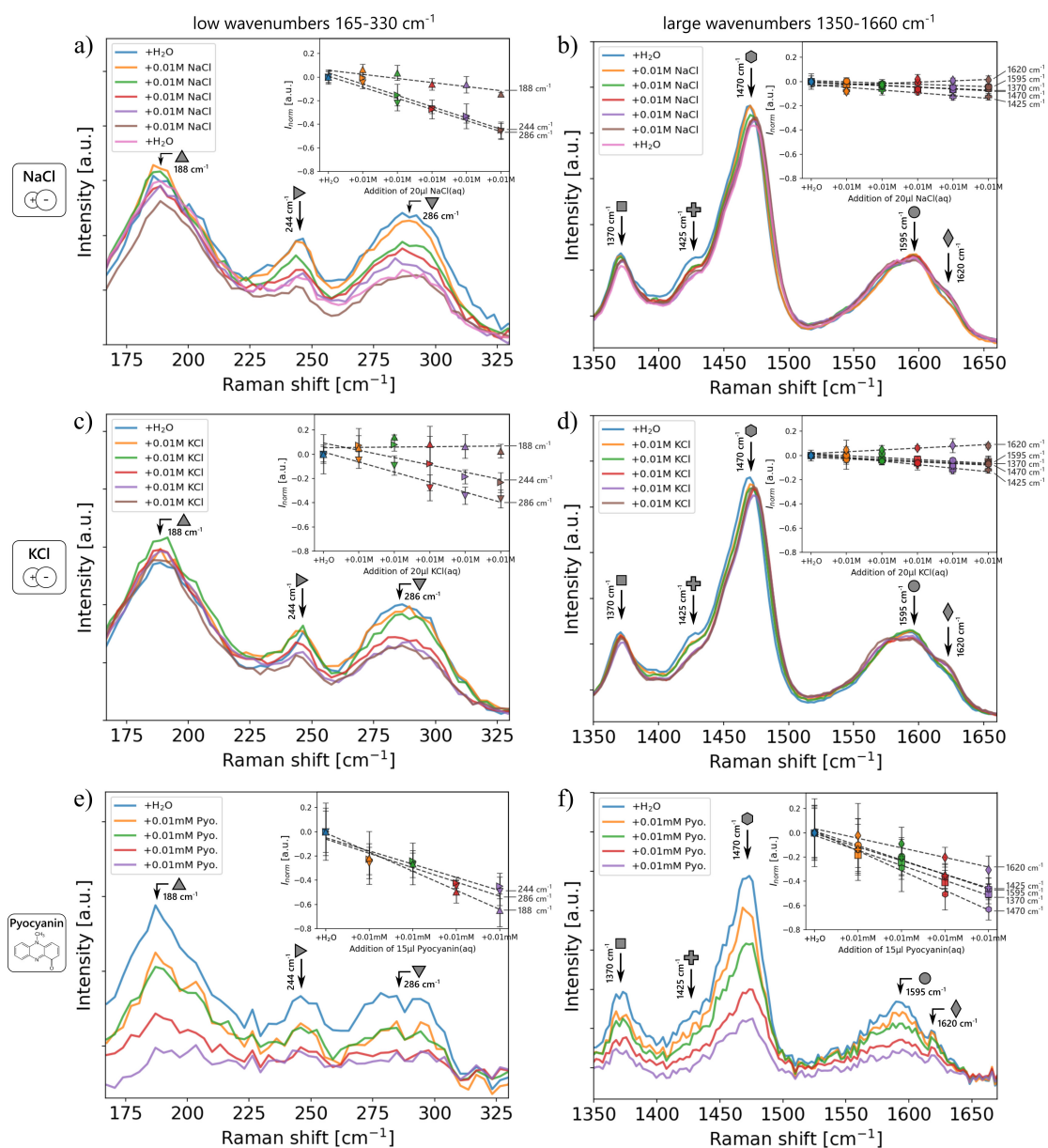


Figure 6.22: Comparison between MOF@NC Raman spectra after treatment with aqueous NaCl (a,b), KCl (c,d) and pyocyanin (e,f) solutions in the wavenumber regions $165\text{-}330\text{ cm}^{-1}$ and $1350\text{-}1660\text{ cm}^{-1}$ (NaCl and KCl: concentrations of 0.01 M, droplet volume of $20\text{ }\mu\text{l}$; pyocyanin: concentrations of 0.01 mM, droplet volume of $15\text{ }\mu\text{l}$). Prominent peaks (marked with symbol and wavenumber) are fitted with a Lorentzian curve, and the normalized intensity change $I_{\text{norm}} = \Delta I / I_{\text{H}_2\text{O}}$ (with $\Delta I = I - I_{\text{H}_2\text{O}}$) of the peaks are evaluated and plotted against concentration, shown as inset. The error bars indicate the standard deviation and the dashed lines show the linear fits.

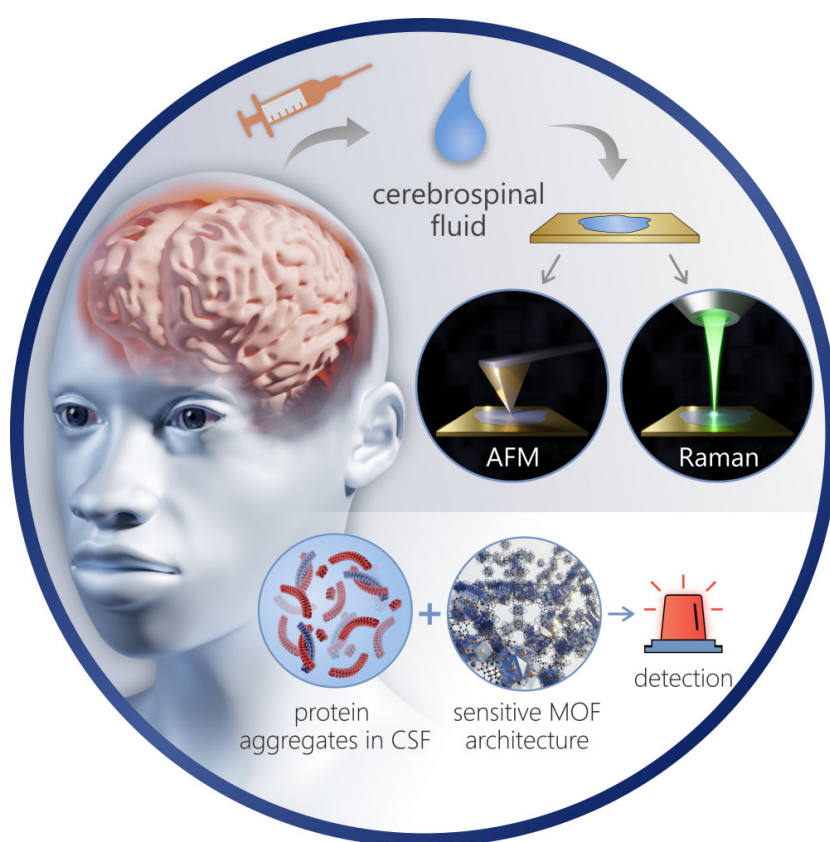
6.A.2 Measurement details and parameters

X-ray diffraction: MOF-808 powder was measured on a PANALYTICAL MPD instrument using a Bragg-Brentano setup equipped with an imaging plate using a $\text{CuK}\alpha$ X-ray source with $\lambda = 1.5406 \text{ \AA}$ in the range of 2° to 80° . Data collection was performed at room temperature and crystallite size could be derived using the Williamson-Hall approach. MOF-808 crystallographic data were obtained from Cambridge Crystallographic Data Center (CCDC): CSD entry is BOHWUS and deposition number is 1002672. Simulated XRD pattern and structure visualization was realized by CCDC Mercury software.

AFM: The AFM measurements were performed using a nanosurf NaniteAFM equipped with a tip scanner. The AFM probe was a Cyn190Al-10 cantilever (Nanosurf) with a tip apex radius $< 10 \text{ nm}$ and AFM scan was performed in tapping mode under standard laboratory conditions without temperature or environmental control (resonant frequency: 190 kHz ; force constant: 48 N m^{-1}). The recorded AFM scan data was evaluated by Gwyddion software (version 2.58).

Raman: Raman spectra and corresponding optical images were acquired using a WITec Alpha 300R confocal Raman microscope with a 50x objective (Zeiss EC Epiplan-Neofluar Dic, $\text{NA} = 0.55$) and a 300 mm lens-based spectrometer (grating: 600 g mm^{-1}) equipped with a TE-cooled charge-coupled device (Andor Newton). Samples were measured in a closed chamber under nitrogen atmosphere, where the samples were heated to 70°C for 30 min at nitrogen flow prior to measurements to remove water and ensure constant measurement conditions. The linearly polarized laser excitation had the wavelength $\lambda_{\text{exc}} = 532 \text{ nm}$ and a power of $P = 20 \text{ mW}$ read before the objective. Additional measurements with an excitation wavelength of $\lambda_{\text{exc}} = 488 \text{ nm}$ and grating with 1800 g mm^{-1} were performed to show the Raman signal at low wavenumbers below $< 1200 \text{ cm}^{-1}$. Pyocyanin measurements were performed with $\lambda_{\text{exc}} = 785 \text{ nm}$ and grating of 300 g mm^{-1} . 2D Raman maps of size $3 \text{ }\mu\text{m} \times 3 \text{ }\mu\text{m}$ were acquired in backscattering geometry with an integration time of 5 s and a resolution of 2 pixels per μm . Single spectra were extracted by averaging the area scans and are displayed after cosmic ray removal and polynomial background subtraction. Normalization takes place at the 1004 cm^{-1} peak (for pyocyanin experiments at 1285 cm^{-1}) which shows no change after treatment, using the formula $(y - y_{\text{min}})/(y_{\text{peak}} - y_{\text{min}})$, with y the intensity value, y_{min} the minimum intensity and y_{peak} the intensity value at the normalization peak.

Exploiting MOFs towards protein sensing in body fluids



Diverse proteins are biomarkers that provide information about pathological processes, such as amyloid proteins, which are an indicator of Alzheimer's disease. In this chapter, the morphological and chemical information of protein aggregates in the cerebrospinal fluid of people with Alzheimer's disease is studied and the possibilities for the use of MOFs for protein sensing are explored.

Parts of this chapter are currently undergoing external peer review at Nature Communications (Nirmalraj et al.). Supporting information is included at the end of this chapter.

7.1 Introduction

Neurodegenerative diseases such as Alzheimer's disease (AD) and Parkinson's disease (PD) are both characterized by a common phenomena of protein misfolding and aberrant aggregation leading to neuronal damage resulting in declining memory and cognitive skills in individuals.^{298,331–333} With about 40 million people affected worldwide, AD is the most prevalent cause of dementia and affects about 60–70% of all dementia cases.^{298,333} The exact causes of AD are not yet fully understood and are part of current research, but according to the amyloid cascade hypothesis, the pathological origin is the misfolding and aggregation of Amyloid-beta ($A\beta$) proteins in the brain to toxic oligomers and long insoluble fibrils (Figure 7.1).^{334–336} This process appears to trigger further changes in the brain, such as abnormal accumulation of tau protein in the form of neurofibrillary tangles (initiated by abnormal hyperphosphorylation³³⁷), chronic inflammation and atrophy.^{333,338}

A cure is not yet possible, but pathological processes can be detected 10–20 years before AD shows visible symptoms.³³⁹ Hence, if diagnosed earlier, the chances of delaying or mitigating the insidiously progressive disease by means of non-pharmacologic therapies and changes in lifestyle increase.^{298,333} However, diagnostic capabilities are still limited, with definitive diagnosis of AD possible only by post-mortem examination, which is why it is of interest to find biomarkers that allow screening and early detection of the disease.^{332,336} Currently, the detection of AD in living patients involves measuring levels of $A\beta$ (in particular the isoform $A\beta_{42}$ and the ratio between $A\beta_{42}/A\beta_{40}$) and tau proteins (total tau and phos-

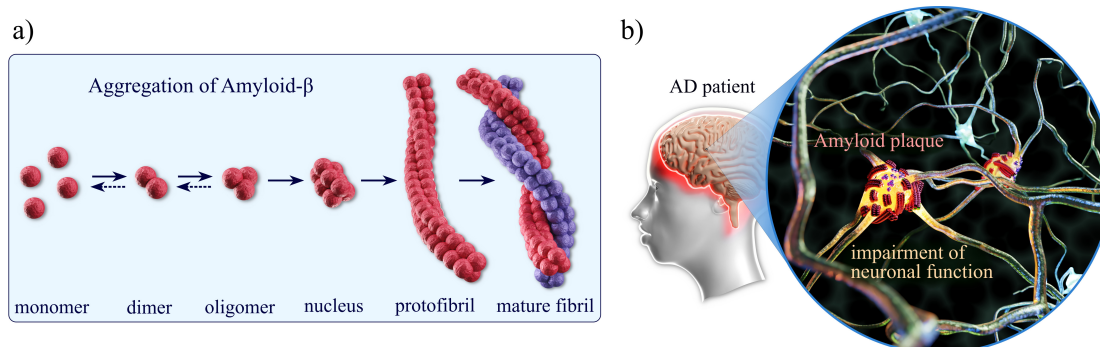


Figure 7.1: a) Schematic aggregation process of $A\beta$ protein from misfolded monomers to cytotoxic oligomers and long insoluble mature fibrils. b) Impaired cognitive function is observed in patients with AD due to neuronal damage in the brain caused by the accumulation of $A\beta$ oligomers and fibrils ($A\beta$ plaques) on the neurons.

phorylated tau) in cerebrospinal fluid (CSF).^{338,340,341} The use of MOFs as active material for CSF analytics could bring the known advantages for biomarker detection such as high selectivity and signal amplification, as already demonstrated in MOF-based detection of A β proteins by electrochemical sensing.^{201,342,343} It has also been previously shown that MOFs (e.g. HKUST-1, UiO-66, MIL-69) are capable of adsorbing A β to varying retention strengths depending on the type of MOF used.³⁴⁴ But before MOFs can be applied for the analysis of CSF, several steps must be performed up front to achieve a better nanoscopic understanding of the chemical composition of protein aggregates in CSF.

This work is about the examination of CSF samples from individuals with AD pathology using AFM, Raman spectroscopy and finally the assessment of MOFs as potential active material for detecting pathological proteins in CSF. Protein aggregates were studied to obtain the morphological and chemical information in high resolution and individual A β fibrils were analyzed for size, diameter and fibril orientation. Finally, the MOF@NC architecture presented in Chapter 6 was used for initial sensing tests on CSF by measuring the change in the Raman signal after treatment. Due to the complexity of the biological samples, CSF from a cognitively healthy individual was also studied as control to AD patients. In summary, the findings of this work yield deeper insights into the nature of protein aggregates in CSF and lay the groundwork for future sensing of AD biomarkers using MOF architectures.

7.2 Cerebrospinal fluid analytics

CSF is in contact with the brain and reflects occurring biochemical changes through the biomarkers it contains. A β and tau proteins that accumulate pathologically in the brain of patients with AD are therefore also found in CSF, making it an ideal source of biomarkers for AD.³³² As a concrete example, the load of amyloid fibrils and plaques in the brain can be inferred from the CSF level of A β_{42} , whereas the amount of total tau or phosphorylated tau proteins in CSF correlate with neuronal damage and the level of neurofibrillary tangles in the brain.³³⁸

Quantification of biomarkers is usually performed with immunoassays such as ELISA (enzyme-linked immunosorbent assay)³⁴⁵ or other methods involving capture antibodies (e.g. based on fluorescent beads³⁴⁶). Spectroscopic methods such as IR and Raman spectroscopy are gaining traction as tools to study protein aggregations without labeling.^{332,347,348} Although IR and Raman spectroscopy can

provide information on the polymorphic nature of the aggregated states of the proteins in CSF, the exact chemical identification of these proteins will require fluorescent labels to identify and classify the A β and tau protein isoforms.^{349–351} The basis for the spectroscopic detection is the protein misfolding and the change of the protein secondary structure during aggregation.³⁴⁸ The altered conformation, such as an enrichment in β -sheets, causes a change in the vibrational fingerprint which can be detected by Raman or IR spectroscopy.^{336,352} As example, primary, secondary and tertiary amides show characteristic absorption bands in IR spectroscopy (amide I, II and III) that shift in relation to β -sheet content and thus allow conclusions to be drawn about the proportion of misfolded A β proteins.^{336,348} Similar information about the overall secondary structure of proteins can be obtained by Raman spectroscopy.^{331,347}

CSF sample preparation

The analyzed CSF samples were provided by the Memory Clinic of the Department of Neurology at the Cantonal Hospital St. Gallen (KSSG) from patients with cognitive complaints. The preparation was identical for all samples before they were characterized by AFM for morphological information and Raman spectroscopy for chemical signature. CSF samples were obtained by lumbar puncture and stored at $-80\text{ }^{\circ}\text{C}$ at the laboratory Zentrum für Labormedizin in St. Gallen. Prior to deposition on substrates, the CSF samples were thawed under standard laboratory conditions. Commercially available mica substrates with a thin gold film were used as substrates, with an overall surface roughness $\leq 0.5\text{ nm}$ over an area of $5\text{ }\mu\text{m}^2$ (substrates from Phasis Inc., gold thickness ca. 100 nm (111), atomic flatness and surface roughness verified by Bruker Multimode 8 STM (Pt/Ir tip, E-scanner, constant current mode) and AFM (tapping mode) respectively). Substrates were cleaned by rinsing with acetone followed by isopropyl alcohol and blow dried with nitrogen. Then, $10\text{ }\mu\text{l}$ of CSF were drop-casted onto the gold surface and slowly dried in air.

Nanoscale imaging of CSF with AFM

First, CSF from a patient with severe AD pathology (AD-1) was studied with AFM. The patient was a 90-years-old man whose biomarker profile was clinically classified as A+T+N+ (A: amyloid, T: tau, N: neurodegeneration) according to the definition of the NIA-AA research framework.³⁴⁰ Figure 7.2a,b show large-area

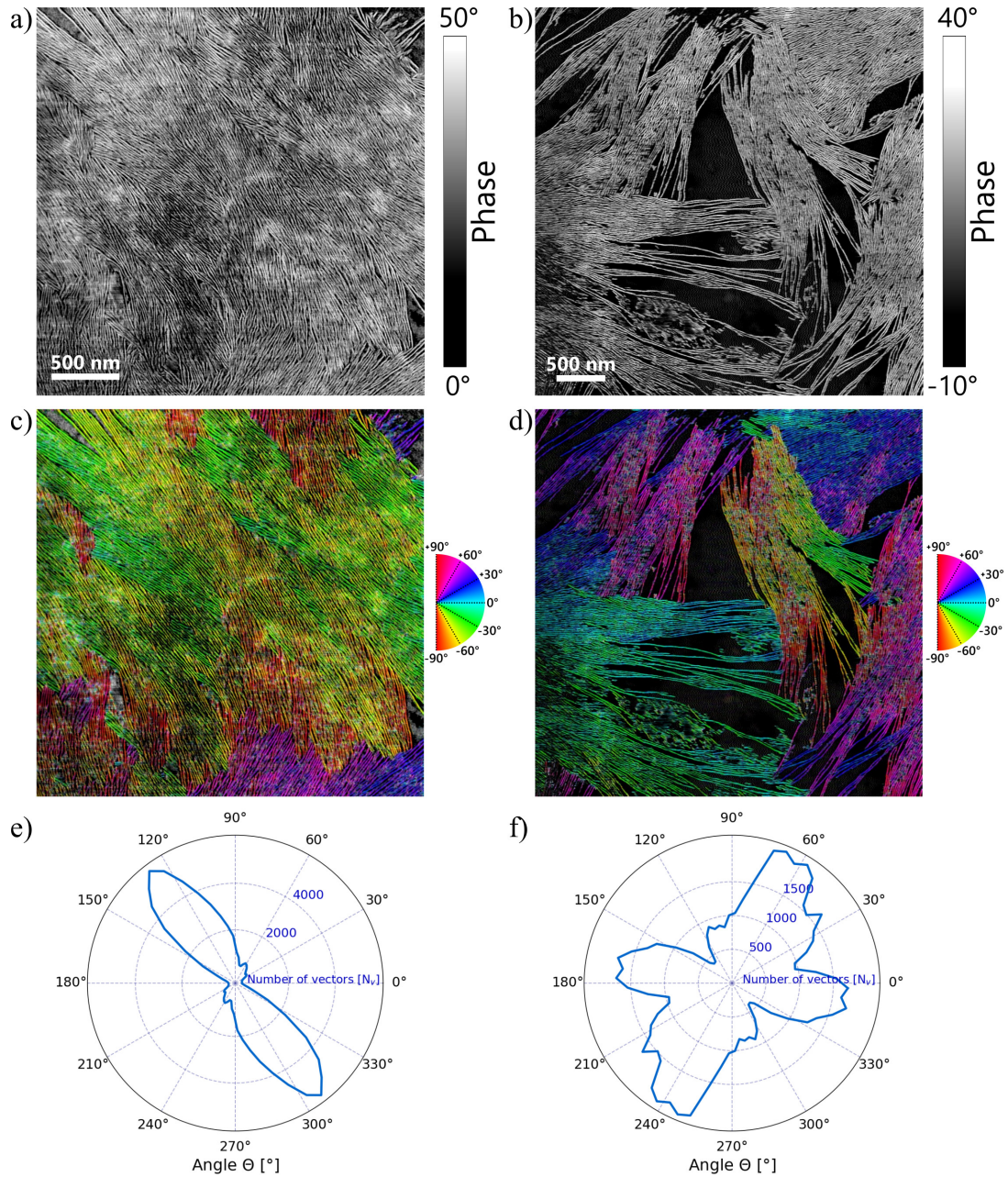


Figure 7.2: a-b) Large-area AFM phase-contrast images showing a dense network of fibrillar protein aggregates in the CSF of patient AD-1. c-d) Corresponding AFM images with color-coding of the fibril orientation as a function of the angle. e-f) Corresponding polar plots, showing the distribution of orientation angles of the fibrils.

phase-contrast scans at different locations. The images reveal long and densely packed amyloid fibrils present in the CSF. While in Figure 7.2a the fibrils are highly aligned over a large area, Figure 7.2b shows several bundles of aligned fibrils with varying orientation. The arrangement becomes more apparent when a qualitative analysis of the fibril orientation is performed using a color-coded map. Figure 7.2c,d show the same scan areas after coloring the fibrils depending on the orientation, illustrating the alignment that takes place. For quantification, all detectable fibrils within the scan areas were tracked using the software FiberApp³⁵³ and the orientation angles were studied. The polar plots with the distribution of orientation angles of the corresponding images are shown in Figure 7.2e,f. Therein, the more extensive orientation in one direction in the first image is evident, while the second image has multiple vector directions displaying the varying orientations.

Phase-contrast AFM scans of areas showing sparser fibril networks in CSF from the same patient AD-1 reveal the local fibril arrangement (Supporting Information Figure 7.5). Color-coding of the different fibril arrangements indicates that the fibrils were locally organized either in parallel (green), spliced (red) or in a T-junction format (blue). It is noted that the amyloid fibrils do not overlap for the most part on the gold surface, both in the close-packed network and in the sparse arrangement.

From the AFM scans presented, the average fibril length and diameter were calculated based on sectional analysis of approximately 3000 individual amyloid fibrils. The mean fibril length was $2.3 \pm 0.8 \mu\text{m}$ and was comparable to the lengths of other individuals with severe AD pathology (result from other patient with same AD classification A+T+N+: $2.25 \pm 0.58 \mu\text{m}$). The mean diameter was $4.4 \pm 2.1 \text{ nm}$, determined from the measured height (calculated from the height at the fibril middle section compared to the height of the underlying surface), considering that the observed fibril width from the AFM image is larger than the true width due to the convolution between the AFM tip and actual fibril width. The measured fibril height does not depend on the geometry of the AFM tip and allows an estimation of the fibril diameter based on the nearly cylindrical shape. Following the morphological information of the fibrils obtained by AFM, the chemical nature is to be identified in more detail, which cannot be explicitly determined by AFM alone.

Raman spectroscopy of CSF

After characterizing the morphological details of the fibrils in the CSF of patient AD-1 such as length, diameter and interfibrillar arrangement by AFM, the chemical signature of the aggregates was studied by Raman spectroscopy. CSF from two patients with severe AD pathology (AD-1 & AD-2) as well as CSF from a patient suffering from intracranial hypertension (IH) and a healthy control were analyzed by Raman spectroscopy (healthy control from a single donor, purchased from Innovative Research Inc.). For details on the Raman measurement parameters, refer to Section 7.A.2.

Figure 7.3a shows the averaged Raman spectra of the CSF samples from the patients AD-1 and AD-2 and the healthy control. In the region between 1200 cm^{-1} and 2000 cm^{-1} , the Raman spectra contain several distinct peaks that can be assigned to modes known from literature, such as amino acids like phenylalanine³⁵⁴ at 1600 cm^{-1} and tryptophan³⁵⁵ at 1358 cm^{-1} . A closer inspection shows that the signal from tryptophan is found in all cases, while for phenylalanine only the CSF from patient AD-1 has a much stronger peak intensity than the others. The Raman signal at the positions 1260 cm^{-1} and 1660 cm^{-1} refer to the amide III^{354–358} and amide I^{354–358} bands, respectively. Usually, the signal is broadened and extends over a small wavenumber range due to different conformations and multiple vibrational modes, here represented by a gray area. The amide III also shows a signal at wavenumber 1301 cm^{-1} . It is known that at this position a signal originates from the CH_2 twisting and wagging vibrations as well^{354–356,358}, showing a pronounced peak for patient AD-2. The peak at wavenumber 1420 cm^{-1} originates in the ring breathing modes of the DNA/RNA bases adenine and guanine^{356,358,359}, whereas the peaks at 1442 cm^{-1} and 1465 cm^{-1} refer to C–H vibrations, CH_2 wagging and CH_2/CH_3 deformations, respectively.^{355,356,358,360} The C–H vibrations are centered at about 1442 cm^{-1} but also occur in a broader region of wavenumbers between 1420 cm^{-1} and 1480 cm^{-1} . The 1732 cm^{-1} peak can be assigned to C=O stretching mode from ester.^{347,354,358} In general, the peak position changes slightly depending on the measurement conditions, such as the sample deposition, the temperature or if present the solvent.³⁴⁷ Certain signals may also be superpositions from multiple sources, as e.g. Raman peaks at 1301 cm^{-1} , 1449 cm^{-1} , 1660 cm^{-1} and 1732 cm^{-1} may correspond to the vibrations of lipids.^{347,354,358} Looking at the Raman signal from the patient with intracranial hypertension in Figure 7.3b, some of the same signatures can be seen, as for the wavenumbers

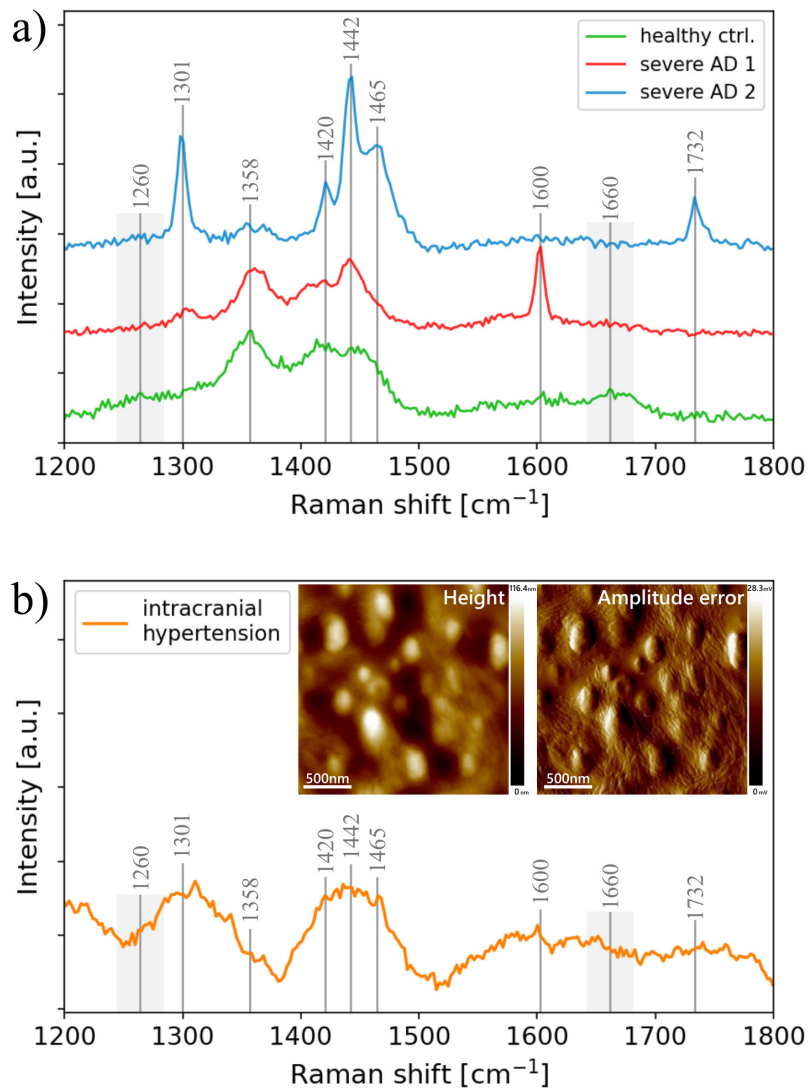


Figure 7.3: a) Average Raman spectra of CSF from two patients with severe AD pathology and one healthy control. Pronounced peaks originating from known vibrational modes are marked with gray lines and wavenumber. b) Average Raman spectrum of CSF from a patient suffering from intracranial hypertension (IH). Inset shows high-resolution AFM height and amplitude error scans of the patient's CSF, revealing aggregates of short fibrils arranged around larger spherical aggregates.

1301 cm⁻¹, between 1420 cm⁻¹ and 1465 cm⁻¹ and 1600 cm⁻¹. Some peaks are not very pronounced (e.g. amide III band at around 1260 cm⁻¹) or are insignificant compared to the spectra with AD pathology (e.g. at 1358 cm⁻¹). The study of AFM scans of the corresponding CSF sample reveals highly ordered fibrillar aggregates (Figure 7.3b inset, Supporting Information Figure 7.7). The blood of the same patient was also analyzed, but compared with the CSF, the blood showed no

accumulation of protein aggregates. Both AFM and Raman spectroscopy confirm the presence of mature fibrils in CSF, although further fluorescence spectroscopy is needed to identify whether the observed fibrils are amyloid or tau fibrils.

7.3 MOF-based protein analytics

To explore the applicability of the MOF@NC architecture from Chapter 6 for protein sensing, initial sensing tests on CSF were performed. CSF of a patient with AD pathology (A+T+N+) was added to the MOF architecture and it was studied how the MOF Raman signal changed after treatment. As a comparative experiment to the complex CSF, the effect of the protein ferritin was also tested (ferritin from human liver, Type IV, $10 \mu\text{g ml}^{-1}$, present in phosphate-buffered saline (PBS), Sigma Aldrich). Ferritin is a well-studied protein with various functions in the human body, ranging from storage and transport of iron to enzymatic properties, that when malfunctioning is also involved in the pathogenesis of neurodegenerative diseases.^{361,362} These results were compared with control experiments using pure PBS buffer solution and deionized water for the treatment of MOF@NC architectures.

Figure 7.4 shows the full MOF Raman spectrum after treatment of individual substrates with the different solutions. The spectra are averaged from four to eight measurements at different positions of two individual samples each (one sample for CSF treatment). The spectra after treatment with CSF and ferritin significantly differ from the control experiments with water and PBS at certain wavenumbers such as around 500 cm^{-1} , 1300 cm^{-1} and 2925 cm^{-1} . To make spectral differences clearer and to compensate for potential batch-to-batch variations, the data is plotted as a differential spectrum in Figure 7.4b ("after-before") and zoomed in closer in regions of interest in Figure 7.4c,d. It shows how the intensity of the peak at 286 cm^{-1} is significantly lower after treatment with CSF than after treatment with the other three solutions. Also at 1060 cm^{-1} CSF shows a different behavior after treatment, namely an increase in intensity, related to C–C ring vibrations.³⁶³ Further, there are Raman peaks that are similarly affected by CSF and ferritin. Examples are peaks at 404 cm^{-1} , 460 cm^{-1} , 535 cm^{-1} , 812 cm^{-1} , 1480 cm^{-1} , 1570 cm^{-1} , and 1630 cm^{-1} . Here, an increase of the Raman intensity is always shown in a comparable way. The origin of the vibrations can be assigned only partially, such as C–H group vibrations associated with 812 cm^{-1} and 1480 cm^{-1} associated with CO_2^- groups.³¹⁸ Other peaks show an increase in inten-

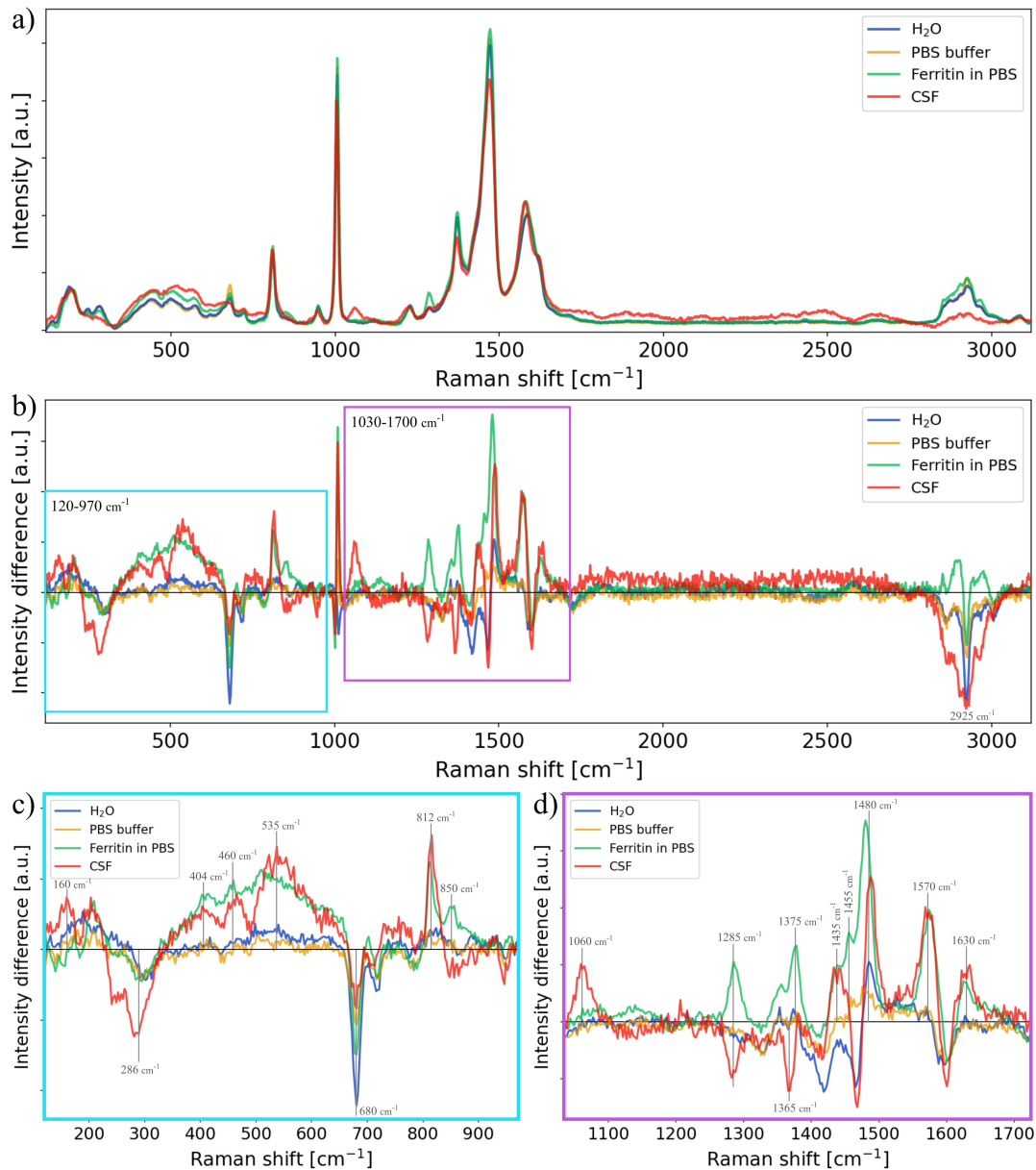


Figure 7.4: a) Full Raman spectra of MOF@NC after treatment with deionized water, PBS buffer solution, ferritin in PBS and CSF from patient with AD pathology (droplet volume of $10\ \mu\text{l}$). b) Differential Raman spectra of the MOF@NC architecture after different treatments by subtracting the spectra before treatment from the spectra after treatment, performed individually for each sample. Regions of interest are marked by boxes. c-d) Zoomed-in differential Raman spectra in the wavenumber regions of interest $120\text{-}970\ \text{cm}^{-1}$ (c) and $1030\text{-}1700\ \text{cm}^{-1}$ (d). Pronounced peaks indicating significant changes are marked with gray lines and wavenumber.

sity after treatment with ferritin solution, whereas CSF causes an intensity reduction, e.g. at 850 cm^{-1} , 1285 cm^{-1} , 1375 cm^{-1} , 1455 cm^{-1} and around 2925 cm^{-1} . The peaks at 1375 cm^{-1} and 1455 cm^{-1} can be assigned to the aromatic C=C and C-H vibrations, respectively.^{318,359} For the most part, water and PBS show no significant effects on the Raman spectrum. The peak at 680 cm^{-1} shows a reduction in intensity for each treatment, most pronounced for water. This may be an effect of residual moisture in the sample.

The first distinction that can be made by the different Raman spectra of the MOF after treatment with CSF and ferritin emphasizes the suitability of MOFs for the measurements since Raman on the MOF provides a well-defined spectrum with good signal strength. The MOF-808 used has no Raman signal enhancement effect, but may be a potential platform to condense proteins during the treatment process due to the interactions. This experiment using a MOF-based platform for protein treatment should be considered as an initial test experiment providing a demonstration of MOF-based protein sensing. With the results from Chapter 6, first differences in the MOF Raman spectrum can be seen depending on whether an ionic solution or a protein solution was added. The use of the Raman and AFM data allows to estimate the severity of the disease based on the nature and size of protein aggregations in CSF as an indicator of AD. However, it is not yet possible to draw any conclusions based on the available data, for example, the distinction between A β or tau proteins. This might be possible in future in combination with other methods such as IR spectroscopy and fluorescence microscopy e.g. for comparison of spectral bands.

7.4 Conclusion and Outlook

In summary, AFM and Raman spectroscopy are useful and label-free methods for analyzing body fluids such as CSF at the nanoscale to obtain clinically relevant information about the pathology of AD. The CSF of patients with AD has been shown to have abnormal aggregation of misfolded proteins to fibrils, which for this reason may be considered a hallmark of AD. Raman spectroscopy can reveal chemical differences between CSF of patients with different pathology and may together with AFM allow conclusions to be drawn about protein aggregation status.³⁴⁸ The use of machine learning in combination with chemical spectroscopy will help to detect small changes in the complex signals and to differentiate the samples, holding promise for the diagnosis of AD at an early stage.²⁹⁹ MOFs,

with their numerous benefits such as versatility, may be increasingly used in the future for body fluid analysis and biomarker sensing, as recently demonstrated in the detection of cancer exosomes from blood via MOF-based electrochemical liquid biopsy.³⁶⁴ It is also useful to discuss limitations or drawbacks of CSF as a source of AD biomarkers, e.g. the invasive procedure of lumbar puncture to collect CSF.^{365,366} Other more accessible biofluids such as blood may be considered as an alternative due to the presence of AD biomarkers in the plasma and prevalence of protein aggregates on red blood cells in AD patients.^{298,332} Also, in the context of neurodegeneration, the different aggregation stages of amyloid proteins should be studied in detail, as there is evidence that intermediate oligomers are much more cytotoxic than long fibrils.^{348,367,368} In conclusion, more than a hundred years after Alois Alzheimer first described the disease named after him³⁶⁹, the cause is still not fully understood and research must continue in the future, perhaps also looking beyond the confines of the amyloid cascade hypothesis.³⁷⁰

Author contributions

L.L. prepared the CSF samples, performed the Raman spectra analysis and supported P.N.N. in statistical analysis of fibril orientation. P.N.N. carried out the AFM measurements and data analysis. A.F. and T.S. recruited the patients and collected the clinical data.

This work was conducted within the framework of the collaborated project A3BAD between Empa and the neurology department at KSSG, which was ethically approved by the St. Gallen ethical commission (number: 202000558).

7.A Supporting Information

7.A.1 Additional Figures

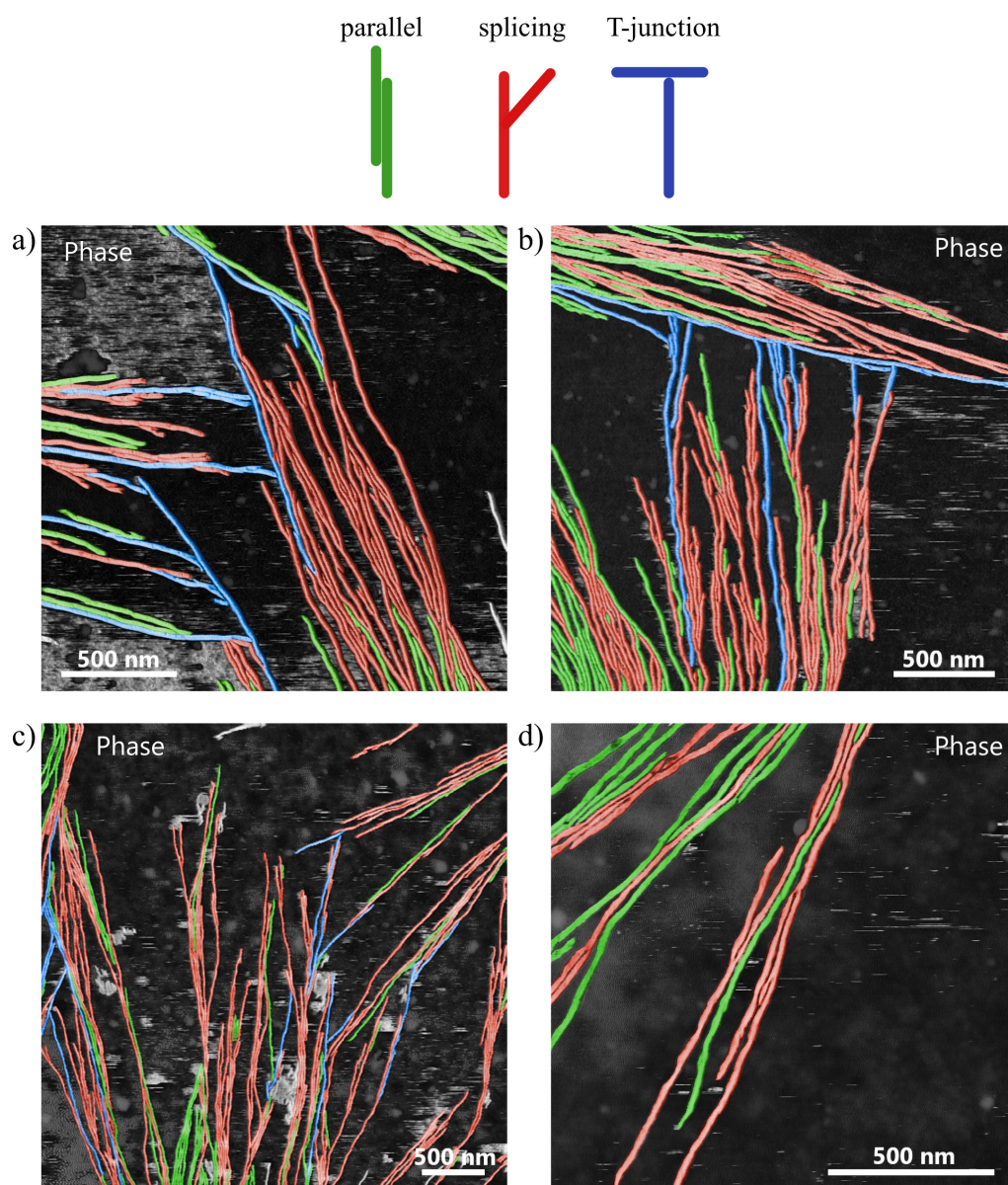


Figure 7.5: a-d) Color-coded phase-contrast AFM images of sparse fibril networks in the CSF of patient AD-1. The fibrils were locally organized either in parallel (green), spliced (red) or in a T-junction format (blue). Top: Schematic of the color-coding for the different fibril arrangements.

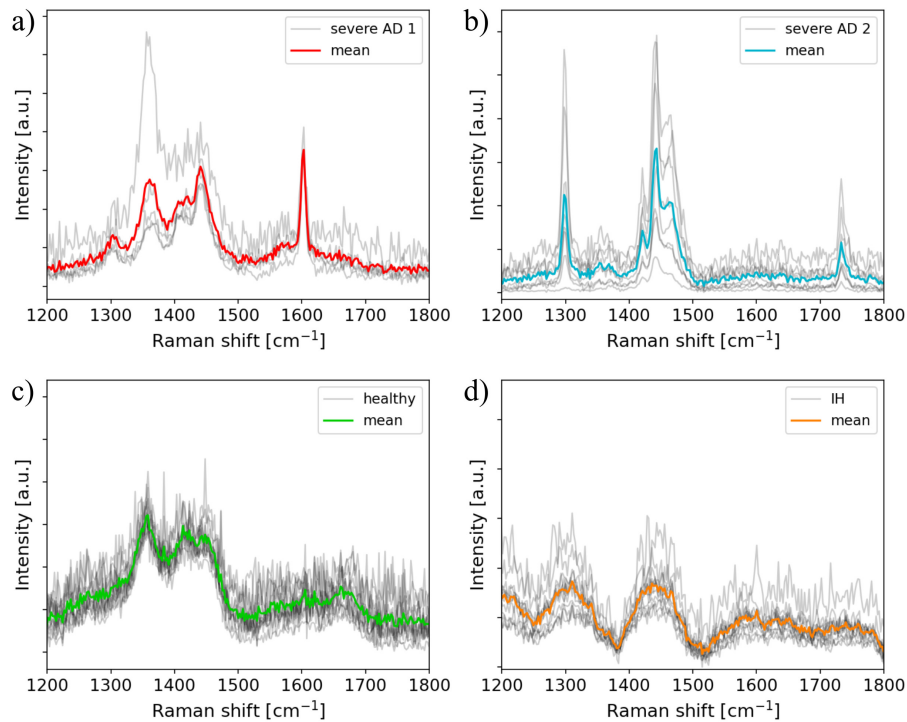


Figure 7.6: Individual (grey) and mean (colored line) Raman spectra of CSF from patients with severe AD pathology (a,b), healthy control (c) and patient with intracranial hypertension (d).

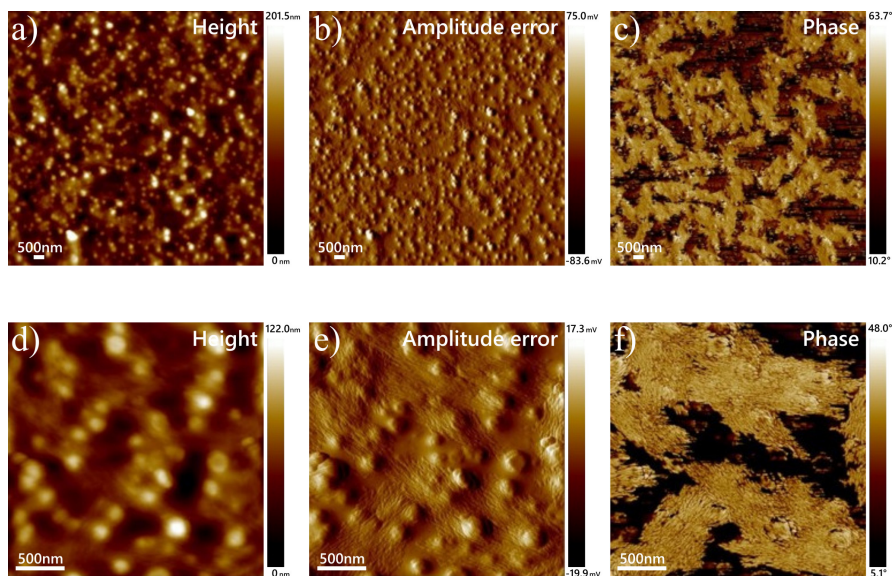


Figure 7.7: Simultaneously acquired AFM scans of CSF from a patient with intracranial hypertension (IH), showing height, amplitude error and phase contrast data (a-c and d-f). Patches of fibrillar aggregates are visible on top of spherical aggregates as seen from the amplitude error data (CSF drop-casted and air-dried on gold surface).

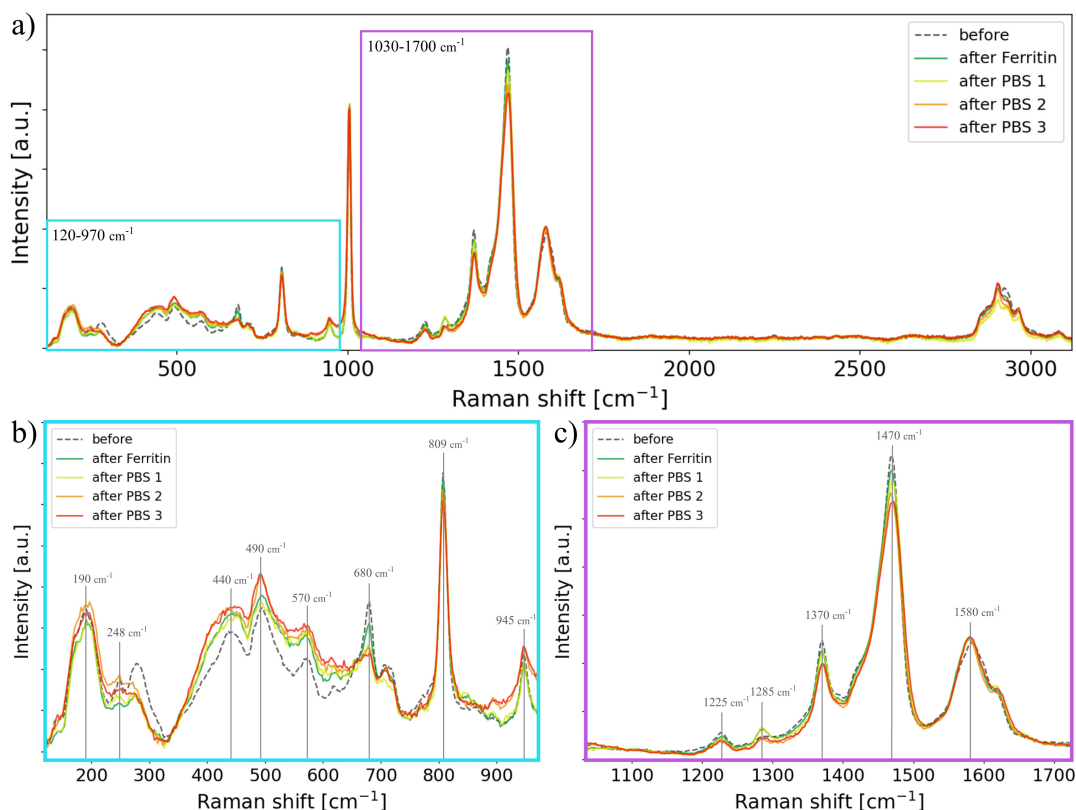


Figure 7.8: a) Full Raman spectra of MOF@NC after sequential treatment with ferritin in PBS and pure PBS buffer solutions (droplet volume of 10 μl). Regions of interest are marked by boxes. b-c) Zoomed-in Raman spectra in the wavenumber regions of interest 120-970 cm^{-1} (b) and 1030-1700 cm^{-1} (c). Pronounced peaks are marked with gray lines and wavenumber.

7.A.2 Measurement details and parameters

AFM: For the AFM measurements, a multimode 8 Bruker instrument equipped with an E-scanner was used. The AFM tip was a SCOUT 70 HAR silicon AFM tip with a high aspect ratio (gold reflective backside coating; cone angle of $< 15^\circ$ over the final 1 μm of the tip apex, NuNano) and the AFM scan was performed in tapping mode under standard laboratory conditions without temperature or environmental control (resonant frequency: 70 kHz; force constant: 2 N m^{-1}). The cantilever was cleaned with acetone and isopropanol and dried with nitrogen before usage. The recorded AFM scan data was evaluated and leveled by Nanoscope software (Bruker).

Raman: Raman spectroscopy on CSF samples was performed using a WITec Alpha 300R confocal Raman microscope with a 100x objective (Zeiss EC Epiplan-Neofluar Dic, NA = 0.9) and a 300 mm lens-based spectrometer with 600 g mm^{-1} grating, equipped with a TE-cooled charge-coupled device (Andor Newton). The laser light was linearly polarized and had an excitation wavelength of $\lambda_{\text{exc}} = 532 \text{ nm}$. The laser power was $P = 5 \text{ mW}$ for all samples and $P_{\text{ctrl}} = 30 \text{ mW}$ for the healthy control (all measured before the objective). On flat regions, 2D Raman maps of the sizes between $3 \mu\text{m} \times 3 \mu\text{m}$ and $10 \mu\text{m} \times 10 \mu\text{m}$ were acquired in backscattering geometry with an integration time of 1.0 s (5 s for one sample with severe AD) and a resolution of 3 pixels per μm . The acquired spectra were processed by WITec software, involving cosmic ray removal, polynomial background subtraction and averaging. The averaged spectra of several positions (between 5 and 12 positions) were normalized at 1002 cm^{-1} (phenylalanine signal³⁵⁹) and plotted with python software.

Conclusion and Outlook



Having presented the use of metal–organic frameworks in various ways for sensing applications in this research, a summary of the work and an outlook on possible follow-on projects in the future are given in this chapter.

In this research work, we aimed to explore the versatility of MOFs for biochemical sensing application. We worked with different metal–organic architectures and pursued individual approaches, such as the synthesis of hybrid MOF structures and the integration of MOF particles into polymer substrates. The focus in each project was on the application of our MOF as sensor material and the evaluation of the signal response upon exposure to relevant analytes. Overall, the work can be subdivided into three major sections.

In the first project, we used an electrically conductive MOF film as chemiresistive sensing material. The film was synthesized in-house by an interfacial approach and consisted of two different organic ligands HHTP and TCNQ. The resulting hybrid Cu-HHTP-TCNQ MOF was analyzed multiparametrically and was investigated for structural, chemical, and electrical properties by various methods such as SEM, AFM, EDX, XRD and Raman spectroscopy. The characterization revealed a coexistence of filaments and cubic crystals formed by the coordination of copper ions with the organic ligands. The associated amorphous film structure and poor long-range crystalline order did not impair the electrical conductivity substantially and an average conductivity of 0.033 S cm^{-1} was measured employing a four-wire configuration and specially fabricated glass chips with gold electrodes. We thus demonstrated a good compromise between conductivity and structural order of the hybrid MOF film by including different types of MOFs. Furthermore, we tested the chemiresistive response of the material to changes in the environment such as nitrogen or humidity and found a relative change in film resistance up to 94%. These results show the potentially good applicability and promise of our hybrid Cu-HHTP-TCNQ and generally less ordered MOF structures as chemiresistive materials.

For future work, the study of the electrical conduction pathway through our hybrid MOF may be relevant for further development. Since the Cu-HHTP-TCNQ film is composed of two different components, visualization of the film connectivity and conduction path would lead to a deeper understanding of the current flow through the hybrid film, similar to what was done for silver nanowire networks by voltage contrast imaging, for example.³⁷¹ Electron beam absorbed current (EBAC)³⁷² and conductive AFM³⁷³ could be used to nondestructively investigate and visualize the conduction pathways and the theory of electrical percolation could help to understand the mechanisms of charge transport.³⁷⁴ Another further project could be the detailed exploration of the chemiresistive behavior of our Cu-HHTP-TCNQ. The sensing response of the hybrid MOF upon exposure to different gases or classes

of organic substances (e.g. volatile organic compounds) could be systematically investigated, thereby revealing potential differences from previously studied pure Cu-HHTP.⁵⁶ The main challenge is probably to integrate the film into the device in a non-destructive manner. In the work shown, the Cu-HHTP-TCNQ film was deposited onto an open substrate after liquid-liquid interfacial synthesis, but this could be difficult if the device is not allowed to come into contact with the solution or does not fit into the reaction vessel. In that case, one may have to resort to alternative synthesis and growth methods, for example liquid-phase epitaxy and layer-by-layer assembly.²⁷⁸ This way, there is also the possibility to test further components and combinations for the production of conductive MOF films.

The second project focused on the integration of MOF particles into a polymer membrane and the exploration of their potential for the detection of sweat biomarkers using Raman spectroscopy. The integration was achieved and optimized by a specially developed sequential electrospaying and electrospinning process. MOF-808 particles were distributed on a nitrocellulose membrane and subsequently physically entrapped by spun nitrocellulose fibers, resulting in biocompatible MOF@NC architectures. The loose fiber mesh leaves access to the MOF pores open, thus retaining the MOF functionality, and allows analysis with optical analytic methods due to its translucence. We characterized the architecture by multiple techniques (SEM, AFM, EDX, Raman spectroscopy) and demonstrated the versatile sensing ability on various sweat biomarkers such as sodium chloride, potassium chloride and pyocyanin by changes in the Raman spectrum. For the treatment with pyocyanin, sensitivities were found to be four orders of magnitude greater than for the ionic biomarkers tested. These results demonstrate the great potential of our MOF@NC architectures as a wearable sensing platform and, more generally, as a functional material for the selective detection of biomarkers in body fluids such as sweat.

Some follow-up projects could provide further important information for the realization of a wearable sensing platform. Our presented integration method benefits from high variability and independence from the type of MOF and polymer. For example, other MOFs with different affinities could be used and tested on the architecture. The functionality of a particular MOF type could be adapted, such as the MOF-808 used by us by replacing the formate group on the zirconium cluster^{50,375} thus tuning the MOF chemistry and interaction with target analytes. The flexibility of this method also allows the sequences to be adjusted and, if necessary, several layers to be fabricated in series, for example to create multilay-

ers or combinations of several MOFs. Further, the analysis of sweat biomarkers can be extended as there are other analytes of interest, such as urea being an important sweat biomarker in patients with chronic kidney diseases³⁷⁶, or ammonia, which reflects e.g. exercise intensity and related metabolic stress.^{11,377} Our MOF@NC architecture is not limited to the analysis of sweat, but can also be used for other biomarker-containing body fluids like breath or urine. The complexity of the Raman spectra of biomarker-rich fluids could be addressed with computational tools. Machine learning and recognition algorithms could be used to classify spectral features of target analytes and build predictive models, enabling qualitative and quantitative analysis for biomarker sensing.^{299,378,379} It is also worthwhile to work on speeding up the acquisition of Raman data using computational methods by reading only the required part rather than the entire spectral information, known as compressive Raman.^{220,221} Compressive Raman can considerably increase the readout speed and enables rapid scanning of large sample areas in high resolution and even real-time imaging, which would take too long with the standard Raman scans (several days for one megapixel image).²²¹ Finally, the aspect of mobility should also be taken into account when considering the realization of a wearable sensor device. Analysis with Raman spectroscopy is not limited to a fixed benchtop instrument, but can now be performed on-site with mobile Raman spectrometers, e.g. on the human body.^{222,223} When using such a portable Raman instrument in combination with our MOF@NC architecture, its handling should be investigated in detail. In the distant future, when the challenges mentioned above have been successfully addressed, this approach may have the potential for eventual commercialization, perhaps in the format of a lateral flow assay (LFA) similar to a rapid antigen test.^{380,381} Instead of immobilized antibodies, integrated MOF particles with different functionalizations and affinities could serve as active platforms to detect target analytes in body fluids. Nitrocellulose membranes are already widely used as a base layer for LFAs or other blotting processes and are therefore suitable for use in the production. Upscaling the fabrication of MOF-integrated membranes is possible, which could make it a cost-effective process.

The third project explored the possibilities of using MOFs as active material for protein sensing, exemplified by pathological proteins in CSF for the diagnosis of Alzheimer's disease. For this purpose, CSF samples from several patients with different pathologies were first examined and analyzed label-free by AFM and Raman spectroscopy for their morphological and chemical properties. It was found

that abnormal aggregation of proteins occurred in patients with AD pathology and differences from healthy control samples were revealed. Finally, initial sensing experiments were performed on CSF from a patient with AD pathology using our MOF@NC architecture. The changes in Raman spectra after treatment with CSF were studied and compared with those after treatment with buffer (H₂O, PBS) and protein (ferritin) solutions.

Several steps remain to be taken before clinical application and diagnosis of AD can be achieved using our MOF-based sensing approach. To start with, an improved understanding of the composition of CSF and analytes present in it is needed. A major challenge will be to identify target proteins within each individual's collection and diversity of biomarkers. To generate statistics and learn spectral features, future work could involve studying high numbers of CSF samples from many patients with different neurodegenerative pathologies and the connection to the associated Raman spectra. Changes and overlaps of spectral features in the Raman spectrum of CSF of different biochemical composition can be analyzed with machine learning tools, thus building models that allow discrimination of the signal.²⁹⁹ Also, the interaction between MOFs and proteins should be investigated in more detail. Different MOFs with individual chemical affinities and properties could be employed to study the adsorption strength to the targeted protein, as has been done with A β peptide in other work.³⁴⁴ This approach could be extended to other proteins as well.

In conclusion, the rapid progress in the field of MOF research will enable further discoveries and pave the way for novel sensing applications using MOF technology. In this regard, the achievements presented in this work emphasize the great potential that metal–organic architectures have as active material for the sensing of biochemical analytes.

References

- [1] J. KIM, A. S. CAMPBELL, B. E.-F. DE ÁVILA, and J. WANG. Wearable biosensors for healthcare monitoring. *Nature biotechnology*, 37 (4), 389–406, **2019**.
- [2] M. M. RODGERS, V. M. PAI, and R. S. CONROY. Recent Advances in Wearable Sensors for Health Monitoring. *IEEE Sensors Journal*, 15 (6), 3119–3126, **2014**.
- [3] D. R. SESHADRI, R. T. LI, J. E. VOOS, J. R. ROWBOTTOM, C. M. ALFES, C. A. ZORMAN, and C. K. DRUMMOND. Wearable sensors for monitoring the internal and external workload of the athlete. *NPJ digital medicine*, 2 (71), 1–18, **2019**.
- [4] Y. YANG and W. GAO. Wearable and flexible electronics for continuous molecular monitoring. *Chemical Society Reviews*, 48 (6), 1465–1491, **2019**.
- [5] G. MATZEU, L. FLOREA, and D. DIAMOND. Advances in wearable chemical sensor design for monitoring biological fluids. *Sensors and Actuators B: Chemical*, 211, 403–418, **2015**.
- [6] J. ANDREU-PEREZ, D. R. LEFF, H. M. D. IP, and G.-Z. YANG. From Wearable Sensors to Smart Implants – Toward Pervasive and Personalized Healthcare. *IEEE Transactions on Biomedical Engineering*, 62 (12), 2750–2762, **2015**.
- [7] B. SENF, W.-H. YEO, and J.-H. KIM. Recent Advances in Portable Biosensors for Biomarker Detection in Body Fluids. *Biosensors*, 10 (9), 127, **2020**.
- [8] Y. Y. BROZA, X. ZHOU, M. YUAN, D. QU, Y. ZHENG, R. VISHINKIN, M. KHATIB, W. WU, and H. HAICK. Disease Detection with Molecular Biomarkers: From Chemistry of Body Fluids to Nature-Inspired Chemical Sensors. *Chemical reviews*, 119 (22), 11761–11817, **2019**.
- [9] H. LEE, Y. J. HONG, S. BAIK, T. HYEON, and D.-H. KIM. Enzyme-Based Glucose Sensor: From Invasive to Wearable Device. *Advanced healthcare materials*, 7 (8), 1701150, **2018**.
- [10] H. LEE, T. K. CHOI, Y. B. LEE, H. R. CHO, R. GHAFARI, L. WANG, H. J. CHOI, T. D. CHUNG, N. LU, T. HYEON, S. H. CHOI, and D.-H. KIM. A graphene-based electrochemical device with thermoresponsive microneedles for diabetes monitoring and therapy. *Nature nanotechnology*, 11 (6), 566–572, **2016**.
- [11] Z. SONNER, E. WILDER, J. HEIKENFELD, G. KASTING, F. BEYETTE, D. SWAILE, F. SHERMAN, J. JOYCE, J. HAGEN, N. KELLEY-LOUGHNANE, and R. NAIK. The microfluidics of the eccrine sweat gland, including biomarker partitioning, transport, and biosensing implications. *Biomicrofluidics*, 9 (3), 031301, **2015**.
- [12] M. CHUNG, W. H. SKINNER, C. ROBERT, C. J. CAMPBELL, R. M. ROSSI, V. KOUTSOS, and N. RADACSI. Fabrication of a Wearable Flexible Sweat pH Sensor Based on SERS-Active Au/TPU Electrospun Nanofibers. *ACS Applied Materials & Interfaces*, 13 (43), 51504–51518, **2021**.
- [13] Global Wearable Sensors Market Size 2018–2025, Industry Report, Grand View Research. <https://www.grandviewresearch.com/industry-analysis/global-wearable-sensor-market#>, **19.08.2022**.
- [14] D. A. JANKOWSKA, M. B. BANNWARTH, C. SCHULENBURG, G. FACCIO, K. MANIURA-WEBER, R. M. ROSSI, L. SCHERER, M. RICHTER, and L. F. BOESEL. Simultaneous detection of pH value and glucose concentrations for wound monitoring applications. *Biosensors and Bioelectronics*, 87, 312–319, **2017**.
- [15] G. PANZARASA, A. OSYPOVA, C. TONCELLI, M. T. BUHMANN, M. ROTTMAR, Q. REN, K. MANIURA-WEBER, R. M. ROSSI, and L. F. BOESEL. The pyranine-benzalkonium ion pair: A promising fluorescent system for the ratiometric detection of wound pH. *Sensors and Actuators B: Chemical*, 249, 156–160, **2017**.
- [16] J. KIM, S. IMANI, W. R. DE ARAUJO, J. WARCHALL, G. VALDÉS-RAMÍREZ, T. R. PAIXÃO, P. P. MERCIER, and J. WANG. Wearable salivary uric acid mouthguard biosensor with integrated wireless electronics. *Biosensors and Bioelectronics*, 74, 1061–1068, **2015**.

References

- [17] L.-C. TAI, T. S. LIAW, Y. LIN, H. Y. NYEIN, M. BARIYA, W. JI, M. HETTICK, C. ZHAO, J. ZHAO, L. HOU, Z. YUAN, Z. FAN, and A. JAVEY. Wearable Sweat Band for Noninvasive Levodopa Monitoring. *Nano letters*, 19 (9), 6346–6351, **2019**.
- [18] J. DIEFFENDERFER, H. GOODELL, S. MILLS, M. MCKNIGHT, S. YAO, F. LIN, E. BEPLER, B. BENT, B. LEE, V. MISRA, Y. ZHU, O. ORALKAN, J. STROHMAIER, J. MUTH, D. PEDEN, and A. BOZKURT. Low-Power Wearable Systems for Continuous Monitoring of Environment and Health for Chronic Respiratory Disease. *IEEE journal of biomedical and health informatics*, 20 (5), 1251–1264, **2016**.
- [19] O. SYNHAIVSKA, Y. MERMOUD, M. BAGHERNEJAD, I. ALSHANSKI, M. HUREVICH, S. YITZCHAIK, M. WIPF, and M. CALAME. Detection of Cu^{2+} Ions with GGH Peptide Realized with Si-Nanoribbon ISFET. *Sensors*, 19 (18), 4022, **2019**.
- [20] W. A. D. M. JAYATHILAKA, K. QI, Y. QIN, A. CHINNAPPAN, W. SERRANO-GARCÍA, C. BASKAR, H. WANG, J. HE, S. CUI, S. W. THOMAS, and S. RAMAKRISHNA. Significance of Nanomaterials in Wearables: A Review on Wearable Actuators and Sensors. *Advanced Materials*, 31 (7), 1805921, **2019**.
- [21] S. YAO, P. SWETHA, and Y. ZHU. Nanomaterial-Enabled Wearable Sensors for Healthcare. *Advanced healthcare materials*, 7 (1), 1700889, **2018**.
- [22] B. F. HOSKINS and R. ROBSON. Infinite Polymeric Frameworks Consisting of Three Dimensionally Linked Rod-like Segments. *Journal of the American Chemical Society*, 111 (15), 5962–5964, **1989**.
- [23] O. M. YAGHI and H. LI. Hydrothermal Synthesis of a Metal–Organic Framework Containing Large Rectangular Channels. *Journal of the American Chemical Society*, 117 (41), 10401–10402, **1995**.
- [24] I. M. HÖNICKE, I. SENKOVSKA, V. BON, I. A. BABURIN, N. BÖNISCH, S. RASCHKE, J. D. EVANS, and S. KASKEL. Balancing Mechanical Stability and Ultrahigh Porosity in Crystalline Framework Materials. *Angewandte Chemie International Edition*, 57 (42), 13780–13783, **2018**.
- [25] Z. CHEN, P. LI, R. ANDERSON, X. WANG, X. ZHANG, L. ROBISON, L. R. REDFERN, S. MORIBE, T. ISLAM-OGU, D. A. GÓMEZ-GUALDRÓN, T. YILDIRIM, J. F. STODDART, and O. K. FARHA. Balancing volumetric and gravimetric uptake in highly porous materials for clean energy. *Science*, 368 (6488), 297–303, **2020**.
- [26] M. EDDAOUDI, J. KIM, N. ROSI, D. VODAK, J. WACHTER, M. O’KEEFFE, and O. M. YAGHI. Systematic Design of Pore Size and Functionality in Isorecticular MOFs and Their Application in Methane Storage. *Science*, 295 (5554), 469–472, **2002**.
- [27] Y. KOBAYASHI, B. JACOBS, M. D. ALLENDORF, and J. R. LONG. Conductivity, Doping, and Redox Chemistry of a Microporous Dithiolene-Based Metal–Organic Framework. *Chemistry of Materials*, 22 (14), 4120–4122, **2010**.
- [28] A. JUSTIN, J. ESPIN, I. KOCHETYGOV, M. ASGARI, O. TRUKHINA, and W. L. QUEEN. A Two Step Post-synthetic Modification Strategy: Appending Short Chain Polyamines to $\text{Zn-NH}_2\text{-BDC}$ MOF for Enhanced CO_2 Adsorption. *Inorganic Chemistry*, 60 (16), 11720–11729, **2021**.
- [29] O. M. YAGHI, M. O’KEEFFE, N. W. OCKWIG, H. K. CHAE, M. EDDAOUDI, and J. KIM. Reticular synthesis and the design of new materials. *Nature*, 423 (6941), 705–714, **2003**.
- [30] Y. KINOSHITA, I. MATSUBARA, T. HIGUCHI, and Y. SAITO. The Crystal Structure of Bis(adiponitrilo)copper(I) Nitrate. *Bulletin of the Chemical Society of Japan*, 32 (11), 1221–1226, **1959**.
- [31] H. LI, M. EDDAOUDI, T. L. GROU, and O. M. YAGHI. Establishing Microporosity in Open Metal–Organic Frameworks: Gas Sorption Isotherms for $\text{Zn(BDC)(BDC=1,4-Benzenedicarboxylate)}$. *Journal of the American Chemical Society*, 120 (33), 8571–8572, **1998**.
- [32] H. LI, M. EDDAOUDI, M. O’KEEFFE, and O. M. YAGHI. Design and synthesis of an exceptionally stable and highly porous metal–organic framework. *nature*, 402 (6759), 276–279, **1999**.

- [33] T. J. MCCARTHY, T. A. TANZER, and M. G. KANATZIDIS. A New Metastable Three-Dimensional Bismuth Sulfide with Large Tunnels: Synthesis, Structural Characterization, Ion-Exchange Properties, and Reactivity of KBi_3S_5 . *Journal of the American Chemical Society*, 117 (4), 1294–1301, **1995**.
- [34] S. SUBRAMANIAN and M. J. ZAWOROTKO. Porous Solids by Design: $[\text{Zn}(4,4'\text{-bpy})_2(\text{SiF}_6)]_n \cdot x \text{DMF}$, a Single Framework Octahedral Coordination Polymer with Large Square Channels. *Angewandte Chemie International Edition in English*, 34 (19), 2127–2129, **1995**.
- [35] O. M. YAGHI, M. J. KALMUTZKI, and C. S. DIERCKS. *Introduction to Reticular Chemistry: Metal-Organic Frameworks and Covalent Organic Frameworks*. Wiley-VCH: Weinheim, **2019**.
- [36] S. KASKEL. *The Chemistry of Metal-Organic Frameworks: Synthesis, Characterization, and Applications*, vol. 1&2. John Wiley & Sons, **2016**.
- [37] D. J. TRANCHEMONTAGNE, J. L. MENDOZA-CORTÉS, M. O'KEEFFE, and O. M. YAGHI. Secondary building units, nets and bonding in the chemistry of metal-organic frameworks. *Chemical Society Reviews*, 38 (5), 1257–1283, **2009**.
- [38] E. LONGO and F. D. A. LA PORTA. *Recent Advances in Complex Functional Materials*. Springer, **2017**.
- [39] M. J. KALMUTZKI, N. HANIKEL, and O. M. YAGHI. Secondary building units as the turning point in the development of the reticular chemistry of MOFs. *Science advances*, 4 (10), eaat9180, **2018**.
- [40] H.-Q. ZHENG, C.-Y. LIU, X.-Y. ZENG, J. CHEN, J. LÜ, R.-G. LIN, R. CAO, Z.-J. LIN, and J.-W. SU. MOF-808: A Metal-Organic Framework with Intrinsic Peroxidase-Like Catalytic Activity at Neutral pH for Colorimetric Biosensing. *Inorganic chemistry*, 57 (15), 9096–9104, **2018**.
- [41] R. KRISHNA and J. M. VAN BATEN. A comparison of the CO_2 capture characteristics of zeolites and metal-organic frameworks. *Separation and Purification Technology*, 87, 120–126, **2012**.
- [42] Y. TAO, H. KANO, L. ABRAMS, and K. KANEKO. Mesopore-Modified Zeolites: Preparation, Characterization, and Applications. *Chemical reviews*, 106 (3), 896–910, **2006**.
- [43] R. C. PULLAR, R. M. NOVAIS, A. P. CAETANO, M. A. BARREIROS, S. ABANADES, and F. A. C. OLIVEIRA. A Review of Solar Thermochemical CO_2 Splitting Using Ceria-Based Ceramics With Designed Morphologies and Microstructures. *Frontiers in chemistry*, 7, 601, **2019**.
- [44] S. BRUNAUER, P. H. EMMETT, and E. TELLER. Adsorption of Gases in Multimolecular Layers. *Journal of the American chemical society*, 60 (2), 309–319, **1938**.
- [45] S. BRUNAUER, L. S. DEMING, W. E. DEMING, and E. TELLER. On a Theory of the van der Waals Adsorption of Gases. *Journal of the American Chemical society*, 62 (7), 1723–1732, **1940**.
- [46] S. YANG, V. V. KARVE, A. JUSTIN, I. KOCHETYGOV, J. ESPIN, M. ASGARI, O. TRUKHINA, D. T. SUN, L. PENG, and W. L. QUEEN. Enhancing MOF performance through the introduction of polymer guests. *Coordination Chemistry Reviews*, 427, 213525, **2021**.
- [47] R. BANERJEE, A. PHAN, B. WANG, C. KNOBLER, H. FURUKAWA, M. O'KEEFFE, and O. M. YAGHI. High-Throughput Synthesis of Zeolitic Imidazolate Frameworks and Application to CO_2 Capture. *Science*, 319 (5865), 939–943, **2008**.
- [48] Z. HU, Y. PENG, Z. KANG, Y. QIAN, and D. ZHAO. A Modulated Hydrothermal (MHT) Approach for the Facile Synthesis of UiO-66-Type MOFs. *Inorganic chemistry*, 54 (10), 4862–4868, **2015**.
- [49] K. EUM, K. C. JAYACHANDRABABU, F. RASHIDI, K. ZHANG, J. LEISEN, S. GRAHAM, R. P. LIVELY, R. R. CHANCE, D. S. SHOLL, C. W. JONES, and S. NAIR. Highly Tunable Molecular Sieving and Adsorption Properties of Mixed-Linker Zeolitic Imidazolate Frameworks. *Journal of the American Chemical Society*, 137 (12), 4191–4197, **2015**.
- [50] Y. PENG, H. HUANG, Y. ZHANG, C. KANG, S. CHEN, L. SONG, D. LIU, and C. ZHONG. A versatile MOF-based trap for heavy metal ion capture and dispersion. *Nature communications*, 9 (187), 1–9, **2018**.

References

- [51] Y.-B. ZHANG, H. FURUKAWA, N. KO, W. NIE, H. J. PARK, S. OKAJIMA, K. E. CORDOVA, H. DENG, J. KIM, and O. M. YAGHI. Introduction of Functionality, Selection of Topology, and Enhancement of Gas Adsorption in Multivariate Metal–Organic Framework-177. *Journal of the American Chemical Society*, 137 (7), 2641–2650, **2015**.
- [52] M. DINCĂ, A. DAILLY, Y. LIU, C. M. BROWN, D. A. NEUMANN, and J. R. LONG. Hydrogen Storage in a Microporous Metal–Organic Framework with Exposed Mn^{2+} Coordination Sites. *Journal of the American Chemical Society*, 128 (51), 16876–16883, **2006**.
- [53] M. Y. MASOOMI, A. MORSALI, A. DHAKSHINAMOORTHY, and H. GARCIA. Mixed-Metal MOFs: Unique Opportunities in Metal–Organic Framework (MOF) Functionality and Design. *Angewandte Chemie*, 131 (43), 15330–15347, **2019**.
- [54] R. ZHAO, Z. LIANG, R. ZOU, and Q. XU. Metal–Organic Frameworks for Batteries. *Joule*, 2 (11), 2235–2259, **2018**.
- [55] E. M. MINER, T. FUKUSHIMA, D. SHEBERLA, L. SUN, Y. SURENDRANATH, and M. DINCĂ. Electrochemical oxygen reduction catalysed by $\text{Ni}_3(\text{hexaiminotriphenylene})_2$. *Nature communications*, 7 (10942), 1–7, **2016**.
- [56] M. G. CAMPBELL, S. F. LIU, T. M. SWAGER, and M. DINCĂ. Chemiresistive Sensor Arrays from Conductive 2D Metal–Organic Frameworks. *Journal of the American Chemical Society*, 137 (43), 13780–13783, **2015**.
- [57] L. LÜDER, A. GUBICZA, M. STIEFEL, J. OVERBECK, D. BERETTA, A. SADEGHPOUR, A. NEELS, P. N. NIRMALRAJ, R. M. ROSSI, C. TONCELLI, and M. CALAME. Conductive Hybrid Cu-HHTP-TCNQ Metal–Organic Frameworks for Chemiresistive Sensing. *Advanced Electronic Materials*, 8 (3), 2100871, **2021**.
- [58] L. SUN, M. G. CAMPBELL, and M. DINCĂ. Electrically Conductive Porous Metal–Organic Frameworks. *Angewandte Chemie International Edition*, 55 (11), 3566–3579, **2016**.
- [59] L. S. XIE, G. SKORUPSKII, and M. DINCĂ. Electrically Conductive Metal–Organic Frameworks. *Chemical reviews*, 120 (16), 8536–8580, **2020**.
- [60] N. F. MOTT. Conduction in Non-crystalline Materials: III. Localized States in a Pseudogap and Near Extremities of Conduction and Valence Bands. *Philosophical Magazine*, 19 (160), 835–852, **1969**.
- [61] N. APSLEY and H. P. HUGHES. Temperature- and field-dependence of hopping conduction in disordered systems. *Philosophical Magazine*, 30 (5), 963–972, **1974**.
- [62] S. ROTH and D. CARROLL. *One-Dimensional Metals: Conjugated Polymers, Organic Crystals, Carbon Nanotubes and Graphene*. John Wiley & Sons, **2015**.
- [63] R. GROSS and A. MARX. *Festkörperphysik*. De Gruyter Oldenbourg, **2014**.
- [64] J.-H. DOU, L. SUN, Y. GE, W. LI, C. H. HENDON, J. LI, S. GUL, J. YANO, E. A. STACH, and M. DINCĂ. Signature of Metallic Behavior in the Metal–Organic Frameworks $\text{M}_3(\text{hexaiminobenzene})_2$ ($\text{M} = \text{Ni}, \text{Cu}$). *Journal of the American Chemical Society*, 139 (39), 13608–13611, **2017**.
- [65] W.-H. LI, W.-H. DENG, G.-E. WANG, and G. XU. Conductive MOFs. *EnergyChem*, 2 (2), 100029, **2020**.
- [66] N. F. MOTT and E. A. DAVIS. *Electronic Processes in Non-Crystalline Materials*, 2nd edition. Oxford University Press, **2012**.
- [67] C. F. LEONG, P. M. USOV, and D. M. D’ALESSANDRO. Intrinsically conducting metal–organic frameworks. *MRS Bulletin*, 41 (11), 858–864, **2016**.
- [68] L. SUN, T. MIYAKAI, S. SEKI, and M. DINCĂ. $\text{Mn}_2(2,5\text{-disulfhydrylbenzene-1,4-dicarboxylate})$: A Microporous Metal–Organic Framework with Infinite $(-\text{Mn}-\text{S}-)_\infty$ Chains and High Intrinsic Charge Mobility. *Journal of the American Chemical Society*, 135 (22), 8185–8188, **2013**.

- [69] L. SUN, C. H. HENDON, M. A. MINIER, A. WALSH, and M. DINCĂ. Million-Fold Electrical Conductivity Enhancement in Fe₂(DEBDC) versus Mn₂(DEBDC) (E= S, O). *Journal of the American Chemical Society*, 137 (19), 6164–6167, **2015**.
- [70] B. J. HOLLIDAY and T. M. SWAGER. Conducting metallopolymers: the roles of molecular architecture and redox matching. *Chemical communications*, (1), 23–36, **2005**.
- [71] M. KO, L. MENDECKI, and K. A. MIRICA. Conductive two-dimensional metal–organic frameworks as multifunctional materials. *Chemical Communications*, 54 (57), 7873–7891, **2018**.
- [72] Z. JIN, J. YAN, X. HUANG, W. XU, S. YANG, D. ZHU, and J. WANG. Solution-processed transparent coordination polymer electrode for photovoltaic solar cells. *Nano Energy*, 40, 376–381, **2017**.
- [73] M. HMADEH, Z. LU, Z. LIU, F. GÁNDARA, H. FURUKAWA, S. WAN, V. AUGUSTYN, R. CHANG, L. LIAO, F. ZHOU, E. PERRE, V. OZOLINS, K. SUENAGA, X. DUAN, B. DUNN, Y. YAMAMOTO, O. TERASAKI, and O. M. YAGHI. New Porous Crystals of Extended Metal-Catecholates. *Chemistry of Materials*, 24 (18), 3511–3513, **2012**.
- [74] D. SHEBERLA, L. SUN, M. A. BLOOD-FORSYTHE, S. ER, C. R. WADE, C. K. BROZEK, A. ASPURU-GUZIK, and M. DINCĂ. High Electrical Conductivity in Ni₃(2,3,6,7,10,11-hexamino-triphenylene)₂, a Semiconducting Metal–Organic Graphene Analogue. *Journal of the American Chemical Society*, 136 (25), 8859–8862, **2014**.
- [75] R. DONG, P. HAN, H. ARORA, M. BALLABIO, M. KARAKUS, Z. ZHANG, C. SHEKHAR, P. ADLER, P. S. PETKOV, A. ERBE, S. C. B. MANNSFELD, C. FELSER, T. HEINE, M. BONN, X. FENG, and E. CÁNOVAS. High-mobility band-like charge transport in a semiconducting two-dimensional metal–organic framework. *Nature materials*, 17 (11), 1027–1032, **2018**.
- [76] C. S. GRANGE, A. J. H. M. MEIJER, and M. D. WARD. Trinuclear ruthenium dioxolene complexes based on the bridging ligand hexahydroxytriphenylene: electrochemistry, spectroscopy, and near-infrared electrochromic behaviour associated with a reversible seven-membered redox chain. *Dalton Transactions*, 39 (1), 200–211, **2010**.
- [77] L. S. XIE, L. SUN, R. WAN, S. S. PARK, J. A. DEGAYNER, C. H. HENDON, and M. DINCĂ. Tunable Mixed-Valence Doping toward Record Electrical Conductivity in a Three-Dimensional Metal–Organic Framework. *Journal of the American Chemical Society*, 140 (24), 7411–7414, **2018**.
- [78] T. C. NARAYAN, T. MIYAKAI, S. SEKI, and M. DINCĂ. High Charge Mobility in a Tetrathiafulvalene-Based Microporous Metal–Organic Framework. *Journal of the American Chemical Society*, 134 (31), 12932–12935, **2012**.
- [79] S. S. PARK, E. R. HONTZ, L. SUN, C. H. HENDON, A. WALSH, T. VAN VOORHIS, and M. DINCĂ. Cation-Dependent Intrinsic Electrical Conductivity in Isostructural Tetrathiafulvalene-Based Microporous Metal–Organic Frameworks. *Journal of the American Chemical Society*, 137 (5), 1774–1777, **2015**.
- [80] G. ZHANG, L. JIN, R. ZHANG, Y. BAI, R. ZHU, and H. PANG. Recent advances in the development of electronically and ionically conductive metal–organic frameworks. *Coordination Chemistry Reviews*, 439, 213915, **2021**.
- [81] A. A. TALIN, A. CENTRONE, A. C. FORD, M. E. FOSTER, V. STAVILA, P. HANEY, R. A. KINNEY, V. SZALAI, F. EL GABALY, H. P. YOON, F. LÉONARD, and M. D. ALLENDORF. Tunable Electrical Conductivity in Metal–Organic Framework Thin-Film Devices. *Science*, 343 (6166), 66–69, **2014**.
- [82] C. K. CHIANG, C. R. FINCHER JR, Y. W. PARK, A. J. HEEGER, H. SHIRAKAWA, E. J. LOUIS, S. C. GAU, and A. G. MACDIARMID. Electrical Conductivity in Doped Polyacetylene. *Physical review letters*, 39 (17), 1098, **1977**.
- [83] J. N. COLEMAN, S. CURRAN, A. B. DALTON, A. P. DAVEY, B. MCCARTHY, W. BLAU, and R. C. BARKLIE. Physical Doping of a Conjugated Polymer with Carbon Nanotubes. *Synthetic metals*, 102 (1-3), 1174–1175, **1999**.

References

- [84] M. GOEL, M. SIEGERT, G. KRAUSS, J. MOHANRAJ, A. HOCHGESANG, D. C. HEINRICH, M. FRIED, J. PFLAUM, and M. THELAKKAT. HOMO–HOMO Electron Transfer: An Elegant Strategy for p-Type Doping of Polymer Semiconductors toward Thermoelectric Applications. *Advanced Materials*, 32 (43), 2003596, **2020**.
- [85] A. M. GLAUDELL, J. E. COCHRAN, S. N. PATEL, and M. L. CHABINYC. Impact of the Doping Method on Conductivity and Thermopower in Semiconducting Polythiophenes. *Advanced Energy Materials*, 5 (4), 1401072, **2015**.
- [86] M. D. ALLENDORF, C. A. BAUER, R. BHAKTA, and R. HOUK. Luminescent metal–organic frameworks. *Chemical Society Reviews*, 38 (5), 1330–1352, **2009**.
- [87] Y. CUI, Y. YUE, G. QIAN, and B. CHEN. Luminescent Functional Metal–Organic Frameworks. *Chemical reviews*, 112 (2), 1126–1162, **2012**.
- [88] M. KURMOO. Magnetic metal–organic frameworks. *Chemical Society Reviews*, 38 (5), 1353–1379, **2009**.
- [89] J. GUO, Y. YU, W. ZHU, R. E. SERDA, S. FRANCO, L. WANG, Q. LEI, J. O. AGOLA, A. NOUREDDINE, E. PLOETZ, S. WUTTKE, and C. J. BRINKER. Modular Assembly of Red Blood Cell Superstructures from Metal–Organic Framework Nanoparticle-Based Building Blocks. *Advanced Functional Materials*, 31 (10), 2005935, **2021**.
- [90] A. SCHNEEMANN, V. BON, I. SCHWEDLER, I. SENKOVSKA, S. KASKEL, and R. A. FISCHER. Flexible metal–organic frameworks. *Chemical Society Reviews*, 43 (16), 6062–6096, **2014**.
- [91] Z. WANG, K. MÜLLER, M. VALÁŠEK, S. GROSJEAN, S. BRÄSE, C. WÖLL, M. MAYOR, and L. HEINKE. Series of Photoswitchable Azobenzene-Containing Metal–Organic Frameworks with Variable Adsorption Switching Effect. *The Journal of Physical Chemistry C*, 122 (33), 19044–19050, **2018**.
- [92] S. HIRAIDE, Y. SAKANAKA, H. KAJIRO, S. KAWAGUCHI, M. T. MIYAHARA, and H. TANAKA. High-throughput gas separation by flexible metal–organic frameworks with fast gating and thermal management capabilities. *Nature communications*, 11 (3867), 1–15, **2020**.
- [93] N. CHANUT, A. GHOULI, M.-V. COULET, S. BOURRELLY, B. KUCHTA, G. MAURIN, and P. L. LLEWELLYN. Tailoring the separation properties of flexible metal–organic frameworks using mechanical pressure. *Nature communications*, 11 (1216), 1–7, **2020**.
- [94] L. J. MURRAY, M. DINCĂ, and J. R. LONG. Hydrogen storage in metal–organic frameworks. *Chemical Society Reviews*, 38 (5), 1294–1314, **2009**.
- [95] D. SUN, S. MA, Y. KE, D. J. COLLINS, and H.-C. ZHOU. An Interweaving MOF with High Hydrogen Uptake. *Journal of the American Chemical Society*, 128 (12), 3896–3897, **2006**.
- [96] A. CORMA, H. GARCÍA, and F. X. LLABRÉS I XAMENA. Engineering metal organic frameworks for heterogeneous catalysis. *Chemical reviews*, 110 (8), 4606–4655, **2010**.
- [97] J. LI, X. HAN, X. ZHANG, A. M. SHEVELEVA, Y. CHENG, F. TUNA, E. J. L. MCINNES, L. J. M. MCPHERSON, S. J. TEAT, L. L. DAEMEN, A. J. RAMIREZ-CUESTA, M. SCHRÖDER, and S. YANG. Capture of nitrogen dioxide and conversion to nitric acid in a porous metal–organic framework. *Nature chemistry*, 11 (12), 1085–1090, **2019**.
- [98] S.-Y. MOON, E. PROUSSALOGLOU, G. W. PETERSON, J. B. DECOSTE, M. G. HALL, A. J. HOWARTH, J. T. HUPP, and O. K. FARHA. Detoxification of Chemical Warfare Agents Using a Zr₆-Based Metal–Organic Framework/Polymer Mixture. *Chemistry—A European Journal*, 22 (42), 14864–14868, **2016**.
- [99] K. MA, T. ISLAMOGLU, Z. CHEN, P. LI, M. C. WASSON, Y. CHEN, Y. WANG, G. W. PETERSON, J. H. XIN, and O. K. FARHA. Scalable and Template-Free Aqueous Synthesis of Zirconium-Based Metal–Organic Framework Coating on Textile Fiber. *Journal of the American Chemical Society*, 141 (39), 15626–15633, **2019**.

- [100] K. ZHANG, Q. HUO, Y.-Y. ZHOU, H.-H. WANG, G.-P. LI, Y.-W. WANG, and Y.-Y. WANG. Textiles/Metal–Organic Frameworks Composites as Flexible Air Filters for Efficient Particulate Matter Removal. *ACS applied materials & interfaces*, 11 (19), 17368–17374, **2019**.
- [101] I. HOSSAIN, A. HUSNA, S. CHAEMCHUEN, F. VERPOORT, and T.-H. KIM. Cross-Linked Mixed-Matrix Membranes Using Functionalized UiO-66-NH₂ into PEG/PPG–PDMS-Based Rubbery Polymer for Efficient CO₂ Separation. *ACS Applied Materials & Interfaces*, 12 (52), 57916–57931, **2020**.
- [102] C. WANG, X. LIU, J. P. CHEN, and K. LI. Superior removal of arsenic from water with zirconium metal–organic framework UiO-66. *Scientific reports*, 5 (1), 16613, **2015**.
- [103] W. XU and O. M. YAGHI. Metal–Organic Frameworks for Water Harvesting from Air, Anywhere, Anytime. *ACS central science*, 6 (8), 1348–1354, **2020**.
- [104] N. HANIKEL, M. S. PRÉVOT, F. FATHIEH, E. A. KAPUSTIN, H. LYU, H. WANG, N. J. DIERCKS, T. G. GLOVER, and O. M. YAGHI. Rapid Cycling and Exceptional Yield in a Metal–Organic Framework Water Harvester. *ACS central science*, 5 (10), 1699–1706, **2019**.
- [105] M. J. KALMUTZKI, C. S. DIERCKS, and O. M. YAGHI. Metal–Organic Frameworks for Water Harvesting from Air. *Advanced Materials*, 30 (37), 1704304, **2018**.
- [106] H. KIM, S. YANG, S. R. RAO, S. NARAYANAN, E. A. KAPUSTIN, H. FURUKAWA, A. S. UMANS, O. M. YAGHI, and E. N. WANG. Water harvesting from air with metal–organic frameworks powered by natural sunlight. *Science*, 356 (6336), 430–434, **2017**.
- [107] P. YANG, D. S. CLARK, and O. M. YAGHI. Envisioning the "Air Economy"–Powered by Reticular Chemistry and Sunlight for Clean Air, Clean Energy, and Clean Water. *Molecular Frontiers Journal*, 5 (1), 1–8, **2021**.
- [108] A. J. CLOUGH, J. W. YOO, M. H. MECKLENBURG, and S. C. MARINESCU. Two-Dimensional Metal–Organic Surfaces for Efficient Hydrogen Evolution from Water. *Journal of the American Chemical Society*, 137 (1), 118–121, **2015**.
- [109] J. DUAN, S. CHEN, and C. ZHAO. Ultrathin metal–organic framework array for efficient electrocatalytic water splitting. *Nature communications*, 8 (15341), 1–7, **2017**.
- [110] K. WADA, K. SAKAUSHI, S. SASAKI, and H. NISHIHARA. Multielectron-Transfer-based Rechargeable Energy Storage of Two-Dimensional Coordination Frameworks with Non-Innocent Ligands. *Angewandte Chemie*, 130 (29), 9024–9028, **2018**.
- [111] D. FENG, T. LEI, M. R. LUKATSKAYA, J. PARK, Z. HUANG, M. LEE, L. SHAW, S. CHEN, A. A. YAKOVENKO, A. KULKARNI, J. XIAO, K. FREDRICKSON, J. B. TOK, X. ZOU, Y. CUI, and Z. BAO. Robust and conductive two-dimensional metal–organic frameworks with exceptionally high volumetric and areal capacitance. *Nature Energy*, 3 (1), 30–36, **2018**.
- [112] D. SHEBERLA, J. C. BACHMAN, J. S. ELIAS, C.-J. SUN, Y. SHAO-HORN, and M. DINCĂ. Conductive MOF electrodes for stable supercapacitors with high areal capacitance. *Nature materials*, 16 (2), 220–224, **2017**.
- [113] E. A. DOLGOPOLOVA and N. B. SHUSTOVA. Metal–organic framework photophysics: Optoelectronic devices, photoswitches, sensors, and photocatalysts. *MRS Bulletin*, 41 (11), 890–896, **2016**.
- [114] Y.-C. LUO, K.-L. CHU, J.-Y. SHI, D.-J. WU, X.-D. WANG, M. MAYOR, and C.-Y. SU. Heterogenization of Photochemical Molecular Devices: Embedding a Metal–Organic Cage into a ZIF-8-Derived Matrix To Promote Proton and Electron Transfer. *Journal of the American Chemical Society*, 141 (33), 13057–13065, **2019**.
- [115] M. C. SO, G. P. WIEDERRECHT, J. E. MONDLOCH, J. T. HUPP, and O. K. FARHA. Metal–organic framework materials for light-harvesting and energy transfer. *Chemical Communications*, 51 (17), 3501–3510, **2015**.
- [116] M.-S. WANG, S.-P. GUO, Y. LI, L.-Z. CAI, J.-P. ZOU, G. XU, W.-W. ZHOU, F.-K. ZHENG, and G.-C. GUO. A Direct White-Light-Emitting Metal–Organic Framework with Tunable Yellow-to-White Photoluminescence.

References

- cence by Variation of Excitation Light. *Journal of the American Chemical Society*, 131 (38), 13572–13573, **2009**.
- [117] D. KOTTILL, M. GUPTA, C. VIJAYAN, P. K. BHARADWAJ, and W. JI. Multiphoton-Pumped Highly Polarized Polariton Microlasers from Single Crystals of a Dye-Coordinated Metal–Organic Framework. *Advanced Functional Materials*, 30 (32), 2003294, **2020**.
- [118] J. YANG and Y.-W. YANG. Metal–Organic Frameworks for Biomedical Applications. *Small*, 16 (10), 1906846, **2020**.
- [119] P. HORCAJADA, C. SERRE, M. VALLET-REGÍ, M. SEBBAN, F. TAULELLE, and G. FÉREY. Metal–Organic Frameworks as Efficient Materials for Drug Delivery. *Angewandte chemie*, 118 (36), 6120–6124, **2006**.
- [120] R. ETLINGER, N. MORENO, D. VOLKMER, K. KERL, and H. BUNZEN. Zeolitic Imidazolate Framework-8 as pH-Sensitive Nanocarrier for "Arsenic Trioxide" Drug Delivery. *Chemistry (Weinheim an der Bergstrasse, Germany)*, 25 (57), 13189, **2019**.
- [121] A. FOUCAULT-COLLET, K. A. GOGICK, K. A. WHITE, S. VILLETTE, A. PALLIER, G. COLLET, C. KIEDA, T. LI, S. J. GEIB, N. L. ROSI, and S. PETOUD. Lanthanide near infrared imaging in living cells with Yb³⁺ nano metal organic frameworks. *Proceedings of the National Academy of Sciences*, 110 (43), 17199–17204, **2013**.
- [122] Y.-W. CHO, S. JEE, I. R. SUHITO, J.-H. LEE, C. G. PARK, K. M. CHOI, and T.-H. KIM. Single metal-organic framework-embedded nanopit arrays: A new way to control neural stem cell differentiation. *Science Advances*, 8 (16), eabj7736, **2022**.
- [123] K. JIE, Y. ZHOU, H. P. RYAN, S. DAI, and J. R. NITSCHKE. Engineering Permanent Porosity into Liquids. *Advanced Materials*, 33 (18), 2005745, **2021**.
- [124] <https://chemistry.berkeley.edu/news/programmable-synthetic-materials>, **26.01.2022**.
- [125] <https://novomof.com/>, **22.05.2022**.
- [126] <https://wahainc.com/>, **22.05.2022**.
- [127] <https://www.porousliquidtechnologies.com/>, **22.05.2022**.
- [128] UN-WATER. *The United Nations World Water Development Report 2021: Valuing Water*. UNESCO: Paris, France, **2021**.
- [129] N. O'REILLY, N. GIRI, and S. L. JAMES. Porous Liquids. *Chemistry—A European Journal*, 13 (11), 3020–3025, **2007**.
- [130] Y.-H. ZOU, Y.-B. HUANG, D.-H. SI, Q. YIN, Q.-J. WU, Z. WENG, and R. CAO. Porous Metal–Organic Framework Liquids for Enhanced CO₂ Adsorption and Catalytic Conversion. *Angewandte Chemie*, 133 (38), 21083–21088, **2021**.
- [131] D. WANG, Y. XIN, D. YAO, X. LI, H. NING, H. ZHANG, Y. WANG, X. JU, Z. HE, Z. YANG, W. FAN, P. LI, and Y. ZHENG. Shining Light on Porous Liquids: From Fundamentals to Syntheses, Applications and Future Challenges. *Advanced Functional Materials*, 32 (1), 2104162, **2021**.
- [132] Z. JI, T. LI, and O. M. YAGHI. Sequencing of metals in multivariate metal–organic frameworks. *Science*, 369 (6504), 674–680, **2020**.
- [133] T. M. O. POPP and O. M. YAGHI. Sequence-Dependent Materials. *Acc. Chem. Res.*, 50 (3), 532–534, **2017**.
- [134] J. D. EVANS, V. BON, I. SENKOVSKA, H.-C. LEE, and S. KASKEL. Four-dimensional metal–organic frameworks. *Nature Communications*, 11 (2690), 1–11, **2020**.
- [135] M.-S. YAO, K.-I. OTAKE, Z.-Q. XUE, and S. KITAGAWA. Concluding remarks: current and next generation MOFs. *Faraday Discussions*, 231, 397–417, **2021**.

- [136] S. HORIKE, S. S. NAGARKAR, T. OGAWA, and S. KITAGAWA. A New Dimension for Coordination Polymers and Metal–Organic Frameworks: Towards Functional Glasses and Liquids. *Angewandte Chemie International Edition*, 59 (17), 6652–6664, **2020**.
- [137] I. STASSEN, N. BURTCH, A. TALIN, P. FALCARO, M. ALLENDORF, and R. AMELOOT. An updated roadmap for the integration of metal–organic frameworks with electronic devices and chemical sensors. *Chemical Society Reviews*, 46 (11), 3185–3241, **2017**.
- [138] B. R. EGGINS. *Chemical sensors and biosensors*, vol. 2. John Wiley & Sons, **2002**.
- [139] E. HERING and G. SCHÖNFELDER. *Sensoren in Wissenschaft und Technik*. Springer, **2012**.
- [140] L. E. KRENO, K. LEONG, O. K. FARHA, M. ALLENDORF, R. P. VAN DUYN, and J. T. HUPP. Metal–Organic Framework Materials as Chemical Sensors. *Chemical reviews*, 112 (2), 1105–1125, **2012**.
- [141] N. BHALLA, P. JOLLY, N. FORMISANO, and P. ESTRELA. Introduction to biosensors. *Essays Biochem*, 60 (1), 1–8, **2016**.
- [142] A. J. SAAH and D. R. HOOVER. 'Sensitivity' and 'Specificity' Reconsidered: The Meaning of These Terms in Analytical and Diagnostic Settings, **1997**.
- [143] M. LIESS. A description of properties and errors of simple and stacked sensors. *Measurement Science and Technology*, 14 (3), 301, **2003**.
- [144] D. A. ARMBRUSTER, M. D. TILLMAN, and L. M. HUBBS. Limit of Detection (LOD)/Limit of Quantitation (LOQ): Comparison of the Empirical and the Statistical Methods Exemplified with GC-MS Assays of Abused Drugs. *Clinical chemistry*, 40 (7), 1233–1238, **1994**.
- [145] F.-Y. YI, D. CHEN, M.-K. WU, L. HAN, and H.-L. JIANG. Chemical Sensors Based on Metal–Organic Frameworks. *ChemPlusChem*, 81 (8), 675, **2016**.
- [146] J. F. OLORUNYOMI, S. T. GEH, R. A. CARUSO, and C. M. DOHERTY. Metal–organic frameworks for chemical sensing devices. *Materials Horizons*, 8 (9), 2387–2419, **2021**.
- [147] M. A. ANDRÉS, M. T. VIJAPU, S. G. SURYA, O. SHEKHAH, K. N. SALAMA, C. SERRE, M. EDDAOUDI, O. ROUBEAU, and I. GASCÓN. Methanol and Humidity Capacitive Sensors Based on Thin Films of MOF Nanoparticles. *ACS Applied Materials & Interfaces*, 12 (3), 4155–4162, **2020**.
- [148] O. YASSINE, O. SHEKHAH, A. H. ASSEN, Y. BELMABKHOUT, K. N. SALAMA, and M. EDDAOUDI. H₂S Sensors: Fumarate-Based fcu-MOF Thin Film Grown on a Capacitive Interdigitated Electrode. *Angewandte Chemie*, 128 (51), 16111–16115, **2016**.
- [149] J. H. CAVKA, S. JAKOBSEN, U. OLSBYE, N. GUILLOU, C. LAMBERTI, S. BORDIGA, and K. P. LILLERUD. A New Zirconium Inorganic Building Brick Forming Metal Organic Frameworks with Exceptional Stability. *Journal of the American Chemical Society*, 130 (42), 13850–13851, **2008**.
- [150] H. SHAO, Y. HUANG, H. GUO, Y. LIU, Y. GUO, and Y. WANG. Thermally stable Ni MOF catalyzed MgH₂ for hydrogen storage. *International Journal of Hydrogen Energy*, 46 (76), 37977–37985, **2021**.
- [151] M. SARAF, R. RAJAK, and S. M. MOBIN. A fascinating multitasking Cu-MOF/rGO hybrid for high performance supercapacitors and highly sensitive and selective electrochemical nitrite sensors. *Journal of Materials Chemistry A*, 4 (42), 16432–16445, **2016**.
- [152] I. STASSEN, B. BUEKEN, H. REINSCH, J. F. M. OUDENHOVEN, D. WOUTERS, J. HAJEK, V. VAN SPEYBROECK, N. STOCK, P. M. VEREECKEN, R. VAN SCHAIJK, D. DE VOS, and R. AMELOOT. Towards metal–organic framework based field effect chemical sensors: UiO-66-NH₂ for nerve agent detection. *Chemical science*, 7 (9), 5827–5832, **2016**.
- [153] R. XU, Y. WANG, X. DUAN, K. LU, D. MICHERONI, A. HU, and W. LIN. Nanoscale Metal–Organic Frameworks for Ratiometric Oxygen Sensing in Live Cells. *Journal of the American Chemical Society*, 138 (7), 2158–2161, **2016**.

References

- [154] X. FANG, B. ZONG, and S. MAO. Metal–Organic Framework-Based Sensors for Environmental Contaminant Sensing. *Nano-micro letters*, 10 (64), 1–19, **2018**.
- [155] Y. TAKASHIMA, V. M. MARTÍNEZ, S. FURUKAWA, M. KONDO, S. SHIMOMURA, H. UEHARA, M. NAKAHAMA, K. SUGIMOTO, and S. KITAGAWA. Molecular decoding using luminescence from an entangled porous framework. *Nature communications*, 2 (168), 1–8, **2011**.
- [156] Y. CUI, H. XU, Y. YUE, Z. GUO, J. YU, Z. CHEN, J. GAO, Y. YANG, G. QIAN, and B. CHEN. A Luminescent Mixed-Lanthanide Metal–Organic Framework Thermometer. *Journal of the American Chemical Society*, 134 (9), 3979–3982, **2012**.
- [157] Y. YU, X.-M. ZHANG, J.-P. MA, Q.-K. LIU, P. WANG, and Y.-B. DONG. Cu(I)-MOF: naked-eye colorimetric sensor for humidity and formaldehyde in single-crystal-to-single-crystal fashion. *Chemical Communications*, 50 (12), 1444–1446, **2014**.
- [158] H.-L. JIANG, D. FENG, K. WANG, Z.-Y. GU, Z. WEI, Y.-P. CHEN, and H.-C. ZHOU. An Exceptionally Stable, Porphyrinic Zr Metal–Organic Framework Exhibiting pH-Dependent Fluorescence. *Journal of the American Chemical Society*, 135 (37), 13934–13938, **2013**.
- [159] A. ZRIBI and J. FORTIN. *Functional Thin Films and Nanostructures for Sensors: Synthesis, Physics and Applications*. Springer Science & Business Media, **2009**.
- [160] Z.-Z. LU, R. ZHANG, Y.-Z. LI, Z.-J. GUO, and H.-G. ZHENG. Solvatochromic Behavior of a Nanotubular Metal–Organic Framework for Sensing Small Molecules. *Journal of the American Chemical Society*, 133 (12), 4172–4174, **2011**.
- [161] S.-I. OHIRA, Y. MIKI, T. MATSUZAKI, N. NAKAMURA, Y.-K. SATO, Y. HIROSE, and K. TODA. A fiber optic sensor with a metal organic framework as a sensing material for trace levels of water in industrial gases. *Analytica chimica acta*, 886, 188–193, **2015**.
- [162] K.-J. KIM, P. LU, J. T. CULP, and P. R. OHODNICKI. Metal–Organic Framework Thin Film Coated Optical Fiber Sensors: A Novel Waveguide-Based Chemical Sensing Platform. *ACS sensors*, 3 (2), 386–394, **2018**.
- [163] L. E. KRENO, J. T. HUPP, and R. P. VAN DUYN. Metal–Organic Framework Thin Film for Enhanced Localized Surface Plasmon Resonance Gas Sensing. *Analytical chemistry*, 82 (19), 8042–8046, **2010**.
- [164] J. AN, C. M. SHADE, D. A. CHENGELIS-CZEGAN, S. PETOUD, and N. L. ROSI. Zinc-Adeninate Metal–Organic Framework for Aqueous Encapsulation and Sensitization of Near-infrared and Visible Emitting Lanthanide Cations. *Journal of the American Chemical Society*, 133 (5), 1220–1223, **2011**.
- [165] Z. XIE, L. MA, K. E. DEKRAFFT, A. JIN, and W. LIN. Porous Phosphorescent Coordination Polymers for Oxygen Sensing. *Journal of the American Chemical Society*, 132 (3), 922–923, **2010**.
- [166] X.-Y. DONG, Y. SI, J.-S. YANG, C. ZHANG, Z. HAN, P. LUO, Z.-Y. WANG, S.-Q. ZANG, and T. C. W. MAK. Ligand engineering to achieve enhanced ratiometric oxygen sensing in a silver cluster-based metal–organic framework. *Nature communications*, 11 (3678), 1–9, **2020**.
- [167] S. PRAMANIK, C. ZHENG, X. ZHANG, T. J. EMGE, and J. LI. New Microporous Metal–Organic Framework Demonstrating Unique Selectivity for Detection of High Explosives and Aromatic Compounds. *Journal of the American Chemical Society*, 133 (12), 4153–4155, **2011**.
- [168] X. QIAO, B. SU, C. LIU, Q. SONG, D. LUO, G. MO, and T. WANG. Selective Surface Enhanced Raman Scattering for Quantitative Detection of Lung Cancer Biomarkers in Superparticle@MOF Structure. *Advanced Materials*, 30 (5), 1702275, **2018**.
- [169] H. SUN, S. CONG, Z. ZHENG, Z. WANG, Z. CHEN, and Z. ZHAO. Metal–Organic Frameworks as Surface Enhanced Raman Scattering Substrates with High Tailorability. *Journal of the American Chemical Society*, 141 (2), 870–878, **2018**.

- [170] M. TCHALALA, P. BHATT, K. CHAPPANDA, S. TAVARES, K. ADIL, Y. BELMABKHOUT, A. SHKURENKO, A. CADIAU, N. HEYMANS, G. DE WEIRELD, ET AL. Fluorinated MOF platform for selective removal and sensing of SO₂ from flue gas and air. *Nature communications*, 10 (1328), 1–10, **2019**.
- [171] A. L. ROBINSON, V. STAVILA, T. R. ZEITLER, M. I. WHITE, S. M. THORNBERG, J. A. GREATHOUSE, and M. D. ALLENDORF. Ultrasensitive Humidity Detection Using Metal–Organic Framework-Coated Microsensors. *Analytical chemistry*, 84 (16), 7043–7051, **2012**.
- [172] J. ZHANG, W. KOSAKA, Y. KITAGAWA, and H. MIYASAKA. A metal–organic framework that exhibits CO₂-induced transitions between paramagnetism and ferrimagnetism. *Nature Chemistry*, 13 (2), 191–199, **2021**.
- [173] P. BATAILLARD. Calorimetric sensing in bioanalytical chemistry: principles, applications and trends. *TrAC Trends in Analytical Chemistry*, 12 (10), 387–394, **1993**.
- [174] S. WANG, J. LIU, H. ZHAO, Z. GUO, H. XING, and Y. GAO. Electrically Conductive Coordination Polymer for Highly Selective Chemiresistive Sensing of Volatile Amines. *Inorganic chemistry*, 57 (2), 541–544, **2018**.
- [175] A. GUPTA, S. K. SHARMA, V. PACHAURI, S. INGEBRANDT, S. SINGH, A. L. SHARMA, and A. DEEP. Sensitive impedimetric detection of troponin i with metal–organic framework composite electrode. *RSC Advances*, 11 (4), 2167–2174, **2021**.
- [176] N. INGLE, P. SAYYAD, G. BODKHE, M. MAHADIK, T. AL-GAHOUARI, S. SHIRSAT, and M. D. SHIRSAT. ChemFET Sensor: nanorods of nickel-substituted Metal–Organic framework for detection of SO₂. *Applied Physics A*, 126 (9), 1–9, **2020**.
- [177] L. MENDECKI and K. A. MIRICA. Conductive Metal–Organic Frameworks as Ion-to-Electron Transducers in Potentiometric Sensors. *ACS applied materials & interfaces*, 10 (22), 19248–19257, **2018**.
- [178] M. WIPF, R. L. STOOP, A. TARASOV, K. BEDNER, W. FU, I. A. WRIGHT, C. J. MARTIN, E. C. CONSTABLE, M. CALAME, and C. SCHONENBERGER. Selective Sodium Sensing with Gold-Coated Silicon Nanowire Field-Effect Transistors in a Differential Setup. *ACS nano*, 7 (7), 5978–5983, **2013**.
- [179] M. KO, L. MENDECKI, A. M. EAGLETON, C. G. DURBIN, R. M. STOLZ, Z. MENG, and K. A. MIRICA. Employing Conductive Metal–Organic Frameworks for Voltammetric Detection of Neurochemicals. *Journal of the American Chemical Society*, 142 (27), 11717–11733, **2020**.
- [180] H. WANG, Y. JIAN, Q. KONG, H. LIU, F. LAN, L. LIANG, S. GE, and J. YU. Ultrasensitive electrochemical paper-based biosensor for microRNA via strand displacement reaction and metal-organic frameworks. *Sensors and Actuators B: Chemical*, 257, 561–569, **2018**.
- [181] M. G. CAMPBELL, D. SHEBERLA, S. F. LIU, T. M. SWAGER, and M. DINCĂ. Cu₃(hexaiminotriphenylene)₂: An Electrically Conductive 2D Metal–Organic Framework for Chemiresistive Sensing. *Angewandte Chemie International Edition*, 54 (14), 4349–4352, **2015**.
- [182] M. KO, A. AYKANAT, M. K. SMITH, and K. A. MIRICA. Drawing Sensors with Ball-Milled Blends of Metal–Organic Frameworks and Graphite. *Sensors*, 17 (10), 2192, **2017**.
- [183] T. M.-H. LEE. Over-the-Counter Biosensors: Past, Present, and Future. *Sensors*, 8 (9), 5535–5559, **2008**.
- [184] R. D. SCHMID and U. BILITEWSKI. Biosensoren. *Chemie in Unserer Zeit*, 26 (4), 163–174, **1992**.
- [185] X. ZENG, Z. SHEN, and R. MERNAUGH. Recombinant antibodies and their use in biosensors. *Analytical and bioanalytical chemistry*, 402 (10), 3027–3038, **2012**.
- [186] D.-W. LEE, J. LEE, I. Y. SOHN, B.-Y. KIM, Y. M. SON, H. BARK, J. JUNG, M. CHOI, T. H. KIM, C. LEE, and N.-E. LEE. Field-effect transistor with a chemically synthesized MoS₂ sensing channel for label-free and highly sensitive electrical detection of DNA hybridization. *Nano Research*, 8 (7), 2340–2350, **2015**.

References

- [187] E. MICHELINI and A. RODA. Staying alive: new perspectives on cell immobilization for biosensing purposes. *Analytical and bioanalytical chemistry*, 402 (5), 1785–1797, **2012**.
- [188] L. C. CLARK JR and C. LYONS. Electrode systems for continuous monitoring in cardiovascular surgery. *Annals of the New York Academy of sciences*, 102 (1), 29–45, **1962**.
- [189] J. D. NEWMAN and A. P. F. TURNER. Home blood glucose biosensors: a commercial perspective. *Biosensors and bioelectronics*, 20 (12), 2435–2453, **2005**.
- [190] B. VAN DORST, J. MEHTA, K. BEKAERT, E. ROUAH-MARTIN, W. DE COEN, P. DUBRUEL, R. BLUST, and J. ROBBENS. Recent advances in recognition elements of food and environmental biosensors: A review. *Biosensors and Bioelectronics*, 26 (4), 1178–1194, **2010**.
- [191] M. THOMPSON and U. J. KRULL. Biosensors and the Transduction of Molecular Recognition. *Analytical chemistry*, 63 (7), 393A–405A, **1991**.
- [192] R. L. STOOP, M. WIPF, S. MÜLLER, K. BEDNER, I. A. WRIGHT, C. J. MARTIN, E. C. CONSTABLE, A. FANGET, C. SCHÖNENBERGER, and M. CALAME. Implementing Silicon Nanoribbon Field-Effect Transistors as Arrays for Multiple Ion Detection. *Biosensors*, 6 (2), 21, **2016**.
- [193] Q.-Y. XU, Z. TAN, X.-W. LIAO, and C. WANG. Recent advances in nanoscale metal-organic frameworks biosensors for detection of biomarkers. *Chinese Chemical Letters*, 33 (1), 22–32, **2021**.
- [194] J. ZHANG, Y. LI, F. CHAI, Q. LI, D. WANG, L. LIU, B. Z. TANG, and X. JIANG. Ultrasensitive point-of-care biochemical sensor based on metal-AIEgen frameworks. *Science advances*, 8 (30), eabo1874, **2022**.
- [195] S. CARRASCO. Metal–Organic Frameworks for the Development of Biosensors: A Current Overview. *Biosensors*, 8 (4), 92, **2018**.
- [196] Z. LIU and Y. LIU. Metal–Organic Frameworks as Sensors of Biomolecules. In *Metal–Organic Frameworks for Environmental Sensing*, pp. 1–31. ACS Publications, **2021**.
- [197] N. BHARDWAJ, S. K. BHARDWAJ, J. MEHTA, K.-H. KIM, and A. DEEP. Mof–Bacteriophage Biosensor for Highly Sensitive and Specific Detection of Staphylococcus aureus. *ACS applied materials & interfaces*, 9 (39), 33589–33598, **2017**.
- [198] M. HU, L. ZHU, Z. LI, C. GUO, M. WANG, C. WANG, and M. DU. CoNi bimetallic metal–organic framework as an efficient biosensing platform for miRNA 126 detection. *Applied Surface Science*, 542, 148586, **2021**.
- [199] C.-S. LIU, Z.-H. ZHANG, M. CHEN, H. ZHAO, F.-H. DUAN, D.-M. CHEN, M.-H. WANG, S. ZHANG, and M. DU. Pore modulation of zirconium–organic frameworks for high-efficiency detection of trace proteins. *Chemical Communications*, 53 (28), 3941–3944, **2017**.
- [200] Y. JIA, G. ZHOU, X. WANG, Y. ZHANG, Z. LI, P. LIU, B. YU, and J. ZHANG. A metal–organic framework/aptamer system as a fluorescent biosensor for determination of aflatoxin B1 in food samples. *Talanta*, 219, 121342, **2020**.
- [201] Y. ZHOU, C. LI, X. LI, X. ZHU, B. YE, and M. XU. A sensitive aptasensor for the detection of β -amyloid oligomers based on metal–organic frameworks as electrochemical signal probes. *Analytical Methods*, 10 (36), 4430–4437, **2018**.
- [202] J. LIANG and K. LIANG. Biocatalytic Metal–Organic Frameworks: Prospects Beyond Bioprotective Porous Matrices. *Advanced Functional Materials*, 30 (27), 2001648, **2020**.
- [203] B. THAKUR, V. V. KARVE, D. T. SUN, A. L. SEMRAU, L. J. K. WEISS, L. GROB, R. A. FISCHER, W. L. QUEEN, and B. WOLFRUM. An Investigation into the Intrinsic Peroxidase-Like Activity of Fe-MOFs and Fe-MOFs/Polymer Composites. *Advanced Materials Technologies*, 6 (5), 2001048, **2021**.
- [204] M. ADEEL, K. ASIF, M. M. RAHMAN, S. DANIELE, V. CANZONIERI, and F. RIZZOLIO. Glucose Detection Devices and Methods Based on Metal–Organic Frameworks and Related Materials. *Advanced Functional Materials*, 31 (52), 2106023, **2021**.

- [205] M. GIMÉNEZ-MARQUÉS, T. HIDALGO, C. SERRE, and P. HORCAJADA. Nanostructured metal–organic frameworks and their bio-related applications. *Coordination Chemistry Reviews*, 307, 342–360, **2016**.
- [206] C. TAMAMES-TABAR, D. CUNHA, E. IMBULUZQUETA, F. RAGON, C. SERRE, M. J. BLANCO-PRIETO, and P. HORCAJADA. Cytotoxicity of nanoscaled metal–organic frameworks. *Journal of Materials Chemistry B*, 2 (3), 262–271, **2014**.
- [207] G. WYSZOGRODZKA, B. MARSZALEK, B. GIL, and P. DOROŻYŃSKI. Metal–organic frameworks: mechanisms of antibacterial action and potential applications. *Drug Discovery Today*, 21 (6), 1009–1018, **2016**.
- [208] T. SIMON-YARZA, A. MIELCAREK, P. COUVREUR, and C. SERRE. Nanoparticles of Metal–Organic Frameworks: On the Road to In Vivo Efficacy in Biomedicine. *Advanced Materials*, 30 (37), 1707365, **2018**.
- [209] S. LI, L. TAN, and X. MENG. Nanoscale Metal–Organic Frameworks: Synthesis, Biocompatibility, Imaging Applications, and Thermal and Dynamic Therapy of Tumors. *Advanced Functional Materials*, 30 (13), 1908924, **2020**.
- [210] Y. ZHAO, H. OUYANG, S. FENG, Y. LUO, Q. SHI, C. ZHU, Y.-C. CHANG, L. LI, D. DU, and H. YANG. Rapid and selective detection of Fe (III) by using a smartphone-based device as a portable detector and hydroxyl functionalized metal–organic frameworks as the fluorescence probe. *Analytica Chimica Acta*, 1077, 160–166, **2019**.
- [211] Z. XU, Z. LIU, M. XIAO, L. JIANG, and C. YI. A smartphone-based quantitative point-of-care testing (POCT) system for simultaneous detection of multiple heavy metal ions. *Chemical Engineering Journal*, 394, 124966, **2020**.
- [212] X. ZHU, S. YUAN, Y. JU, J. YANG, C. ZHAO, and H. LIU. Water Splitting-Assisted Electrocatalytic Oxidation of Glucose with a Metal–Organic Framework for Wearable Nonenzymatic Perspiration Sensing. *Analytical chemistry*, 91 (16), 10764–10771, **2019**.
- [213] N. P. FROMME, Y. LI, M. CAMENZIND, C. TONCELLI, and R. M. ROSSI. Metal-Textile Laser Welding for Wearable Sensors Applications. *Advanced Electronic Materials*, 7 (4), 2001238, **2021**.
- [214] H. SHI, H. ZHAO, Y. LIU, W. GAO, and S.-C. DOU. Systematic Analysis of a Military Wearable Device Based on a Multi-Level Fusion Framework: Research Directions. *Sensors*, 19 (12), 2651, **2019**.
- [215] C. V. RAMAN and K. S. KRISHNAN. A New Type of Secondary Radiation. *Nature*, 121 (3048), 501–502, **1928**.
- [216] J. ZHANG, M. L. PERRIN, L. BARBA, J. OVERBECK, S. JUNG, B. GRASSY, A. AGAL, R. MUFF, R. BRÖNNIMANN, M. HALUSKA, C. ROMAN, C. HIEROLD, M. JAGGI, and M. CALAME. High-speed identification of suspended carbon nanotubes using raman spectroscopy and deep learning. *Microsystems & nanoengineering*, 8 (19), 1–9, **2022**.
- [217] J. OVERBECK, G. BORIN BARIN, C. DANIELS, M. L. PERRIN, L. LIANG, O. BRAUN, R. DARAWISH, B. BURKHARDT, T. DUMSLAFF, X.-Y. WANG, A. NARITA, K. MÜLLEN, V. MEUNIER, R. FASEL, M. CALAME, and P. RUFFIEUX. Optimized Substrates and Measurement Approaches for Raman Spectroscopy of Graphene Nanoribbons. *physica status solidi (b)*, 256 (12), 1900343, **2019**.
- [218] P. VECERA, J. C. CHACÓN-TORRES, T. PICHLER, S. REICH, H. R. SONI, A. GÖRLING, K. EDELTHALHAMMER, H. PETERLIK, F. HAUKE, and A. HIRSCH. Precise determination of graphene functionalization by in situ Raman spectroscopy. *Nature communications*, 8 (15192), 1–9, **2017**.
- [219] K. KONG, C. KENDALL, N. STONE, and I. NOTINGHER. Raman spectroscopy for medical diagnostics – From in-vitro biofluid assays to in-vivo cancer detection. *Advanced drug delivery reviews*, 89, 121–134, **2015**.
- [220] B. M. DAVIS, A. J. HEMPHILL, D. CEBECI MALTAS, M. A. ZIPPER, P. WANG, and D. BEN-AMOTZ. Multivariate Hyperspectral Raman Imaging Using Compressive Detection. *Analytical chemistry*, 83 (13), 5086–5092, **2011**.

References

- [221] D. CEBECI, B. R. MANKANI, and D. BEN-AMOTZ. Recent Trends in Compressive Raman Spectroscopy Using DMD-Based Binary Detection. *Journal of Imaging*, 5 (1), 1–15, **2018**.
- [222] E. GUEVARA, J. C. TORRES-GALVÁN, M. G. RAMÍREZ-ELÍAS, C. LUEVANO-CONTRERAS, and F. J. GONZÁLEZ. Use of Raman spectroscopy to screen diabetes mellitus with machine learning tools. *Biomedical Optics Express*, 9 (10), 4998–5010, **2018**.
- [223] M. JERMYN, K. MOK, J. MERCIER, J. DESROCHES, J. PICHETTE, K. SAINT-ARNAUD, L. BERNSTEIN, M.-C. GUIOT, K. PETRECCA, and F. LEBLOND. Intraoperative brain cancer detection with Raman spectroscopy in humans. *Science translational medicine*, 7 (274), 274ra19–274ra19, **2015**.
- [224] K. KNEIPP, Y. WANG, H. KNEIPP, L. T. PERELMAN, I. ITZKAN, R. R. DASARI, and M. S. FELD. Single Molecule Detection Using Surface-Enhanced Raman Scattering (SERS). *Physical review letters*, 78 (9), 1667, **1997**.
- [225] R. S. DAS and Y. K. AGRAWAL. Raman spectroscopy: Recent advancements, techniques and applications. *Vibrational spectroscopy*, 57 (2), 163–176, **2011**.
- [226] J. TOPORSKI, T. DIEING, and O. HOLLRICHER. *Confocal Raman Microscopy*, vol. 66. Springer, 2 edn., **2018**.
- [227] J. R. FERRARO, K. NAKAMOTO, and C. W. BROWN. *Introductory Raman Spectroscopy*. Elsevier, **2003**.
- [228] D. A. LONG. *The Raman Effect: A Unified Treatment of the Theory of Raman Scattering by Molecules*, vol. 8. Wiley Chichester, **2002**.
- [229] E. C. LE RU and P. G. ETCHEGOIN. *Principles of Surface-Enhanced Raman Spectroscopy: and related plasmonic effects*. Elsevier, **2008**.
- [230] E. C. LE RU, E. BLACKIE, M. MEYER, and P. G. ETCHEGOIN. Surface Enhanced Raman Scattering Enhancement Factors: A Comprehensive Study. *The Journal of Physical Chemistry C*, 111 (37), 13794–13803, **2007**.
- [231] S. NIE and S. R. EMORY. Probing Single Molecules and Single Nanoparticles by Surface-Enhanced Raman Scattering. *science*, 275 (5303), 1102–1106, **1997**.
- [232] K. I. HADJIIVANOV, D. A. PANAYOTOV, M. Y. MIHAYLOV, E. Z. IVANOVA, K. K. CHAKAROVA, S. M. ANDONOVA, and N. L. DRENCHEV. Power of Infrared and Raman Spectroscopies to Characterize Metal–Organic Frameworks and Investigate Their Interaction with Guest Molecules. *Chemical Reviews*, 121 (3), 1286–1424, **2020**.
- [233] Y. CHEN, J. ZHANG, J. LI, and J. V. LOCKARD. Monitoring the Activation of a Flexible Metal–Organic Framework Using Structurally Sensitive Spectroscopy Techniques. *The Journal of Physical Chemistry C*, 117 (39), 20068–20077, **2013**.
- [234] S. PAL, S. MAITI, U. N. MAITI, and K. K. CHATTOPADHYAY. Scalable approach for the realization of garland shaped 3D assembly of CuTCNQ nanorods: an efficient electron emitter. *Journal of Materials Chemistry C*, 2 (20), 4005–4011, **2014**.
- [235] T. D. PETERSEN, G. BALAKRISHNAN, and C. L. WEEKS. Mof crystal growth: UV resonance Raman investigation of metal–ligand binding in solution and accelerated crystal growth methods. *Dalton Transactions*, 44 (28), 12824–12831, **2015**.
- [236] D. Y. SIBERIO-PÉREZ, A. G. WONG-FOY, O. M. YAGHI, and A. J. MATZGER. Raman Spectroscopic Investigation of CH₄ and N₂ Adsorption in Metal–Organic Frameworks. *Chemistry of materials*, 19 (15), 3681–3685, **2007**.
- [237] N. NIJEM, P. THISSEN, Y. YAO, R. C. LONGO, K. ROODENKO, H. WU, Y. ZHAO, K. CHO, J. LI, D. C. LANGRETH, and Y. J. CHABAL. Understanding the Preferential Adsorption of CO₂ over N₂ in a Flexible Metal–Organic Framework. *Journal of the American Chemical Society*, 133 (32), 12849–12857, **2011**.

- [238] H. LAI, G. LI, F. XU, and Z. ZHANG. Metal–organic frameworks: opportunities and challenges for surface-enhanced Raman scattering—a review. *Journal of Materials Chemistry C*, 8 (9), 2952–2963, **2020**.
- [239] W. ZHOU, R. APKARIAN, Z. L. WANG, and D. JOY. Fundamentals of Scanning Electron Microscopy (SEM). In *Scanning Microscopy for Nanotechnology*, pp. 1–40. Springer, **2006**.
- [240] W.-H. LI, K. DING, H.-R. TIAN, M.-S. YAO, B. NATH, W.-H. DENG, Y. WANG, and G. XU. Conductive Metal–Organic Framework Nanowire Array Electrodes for High-Performance Solid-State Supercapacitors. *Advanced Functional Materials*, 27 (27), 1702067, **2017**.
- [241] X. HUANG, P. SHENG, Z. TU, F. ZHANG, J. WANG, H. GENG, Y. ZOU, C.-A. DI, Y. YI, Y. SUN, W. XU, and D. ZHU. A two-dimensional π -d conjugated coordination polymer with extremely high electrical conductivity and ambipolar transport behaviour. *Nature communications*, 6 (7408), 1–8, **2015**.
- [242] Y. ZHANG, S. YUAN, X. FENG, H. LI, J. ZHOU, and B. WANG. Preparation of Nanofibrous Metal–Organic Framework Filters for Efficient Air Pollution Control. *Journal of the American Chemical Society*, 138 (18), 5785–5788, **2016**.
- [243] M. SCHELLING, M. KIM, E. OTAL, and J. HINESTROZA. Decoration of Cotton Fibers with a Water-Stable Metal–Organic Framework (UiO-66) for the Decomposition and Enhanced Adsorption of Micropollutants in Water. *Bioengineering*, 5 (1), 14, **2018**.
- [244] D. C. BELL and A. J. GARRATT-REED. *Energy Dispersive X-Ray Analysis in the Electron Microscope*. Garland Science, **2003**.
- [245] P. LAMAGNI, M. MIOLA, J. CATALANO, M. S. HVID, M. A. H. MAMAKHEL, M. CHRISTENSEN, M. R. MADSEN, H. S. JEPPESEN, X.-M. HU, K. DAASBJERG, T. SKRYDSTRUP, and N. LOCK. Restructuring Metal–Organic Frameworks to Nanoscale Bismuth Electrocatalysts for Highly Active and Selective CO₂ Reduction to Formate. *Advanced Functional Materials*, 30 (16), 1910408, **2020**.
- [246] Q. XIA, Z. LI, C. TAN, Y. LIU, W. GONG, and Y. CUI. Multivariate Metal–Organic Frameworks as Multifunctional Heterogeneous Asymmetric Catalysts for Sequential Reactions. *Journal of the American Chemical Society*, 139 (24), 8259–8266, **2017**.
- [247] A. F. GROSS, E. SHERMAN, S. L. MAHONEY, and J. J. VAJO. Reversible Ligand Exchange in a Metal–Organic Framework (MOF): Toward MOF-Based Dynamic Combinatorial Chemical Systems. *The Journal of Physical Chemistry A*, 117 (18), 3771–3776, **2013**.
- [248] E. HECHT. *Optik 5., verbesserte Auflage*. Oldenbourg Verlag, München, **2009**.
- [249] L. MENG, B. YU, and Y. QIN. Templated interfacial synthesis of metal-organic framework (MOF) nano- and micro-structures with precisely controlled shapes and sizes. *Communications Chemistry*, 4 (1), 1–10, **2021**.
- [250] B. HOPPE, K. D. J. HINDRICKS, D. P. WARWAS, H. A. SCHULZE, A. MOHMEYER, T. J. PINKVOS, S. ZAILSKAS, M. R. KREY, C. BELKE, S. KÖNIG, M. FRÖBA, R. J. HAUG, and P. BEHRENS. Graphene-like metal–organic frameworks: morphology control, optimization of thin film electrical conductivity and fast sensing applications. *CrystEngComm*, 20 (41), 6458–6471, **2018**.
- [251] T. D. BENNETT and A. K. CHEETHAM. Amorphous Metal–Organic Frameworks. *Accounts of chemical research*, 47 (5), 1555–1562, **2014**.
- [252] N. MASCIOCCHI, F. CASTELLI, P. M. FORSTER, M. M. TAFOYA, and A. K. CHEETHAM. Synthesis and Characterization of Two Polymorphic Crystalline Phases and an Amorphous Powder of Nickel (II) Bisimidazolate. *Inorganic chemistry*, 42 (19), 6147–6152, **2003**.
- [253] Y. LIU, Z. NG, E. A. KHAN, H.-K. JEONG, C.-B. CHING, and Z. LAI. Synthesis of continuous MOF-5 membranes on porous α -alumina substrates. *Microporous and Mesoporous Materials*, 118 (1-3), 296–301, **2009**.

- [254] E. BIEMMI, C. SCHERB, and T. BEIN. Oriented Growth of the Metal Organic Framework $\text{Cu}_3(\text{BTC})_2(\text{H}_2\text{O})_3 \cdot x\text{H}_2\text{O}$ Tunable with Functionalized Self-Assembled Monolayers. *Journal of the American Chemical Society*, 129 (26), 8054–8055, **2007**.
- [255] R. N. WIDMER, G. I. LAMPRONTI, N. CASATI, S. FARSANG, T. D. BENNETT, and S. A. T. REDFERN. X-ray radiation-induced amorphization of metal–organic frameworks. *Physical Chemistry Chemical Physics*, 21 (23), 12389–12395, **2019**.
- [256] V. A. HACKLEY, M. A. ANDERSON, and S. SPOONER. A small-angle x-ray scattering study of microstructure evolution during sintering of sol-gel-derived porous nanophase titania. *Journal of materials research*, 7 (9), 2555–2571, **1992**.
- [257] T. NARAYANAN, M. SZTUCKI, P. VAN VAERENBERGH, J. LÉONARDON, J. GORINI, L. CLAUSTRE, F. SEVER, J. MORSE, and P. BOESECKE. A multipurpose instrument for time-resolved ultra-small-angle and coherent X-ray scattering. *Journal of applied crystallography*, 51 (6), 1511–1524, **2018**.
- [258] P. MÜLLER-BUSCHBAUM. Probing Organic Solar Cells with Grazing Incidence Scattering Techniques. *Synchrotron Radiation in Materials Science: Light Sources, Techniques, and Applications*, 1, 191–238, **2018**.
- [259] P. MÜLLER-BUSCHBAUM. Grazing incidence small-angle X-ray scattering: an advanced scattering technique for the investigation of nanostructured polymer films. *Analytical and bioanalytical chemistry*, 376 (1), 3–10, **2003**.
- [260] F. J. GIESSIBL. Advances in atomic force microscopy. *Reviews of modern physics*, 75 (3), 949, **2003**.
- [261] D. RUGAR and P. HANSMA. Atomic Force Microscopy. *Physics today*, 43 (10), 23–30, **1990**.
- [262] N. JALILI and K. LAXMINARAYANA. A review of atomic force microscopy imaging systems: application to molecular metrology and biological sciences. *Mechatronics*, 14 (8), 907–945, **2004**.
- [263] R. DONG, T. ZHANG, and X. FENG. Interface-Assisted Synthesis of 2D Materials: Trend and Challenges. *Chemical reviews*, 118 (13), 6189–6235, **2018**.
- [264] V. RUBIO-GIMÉNEZ, M. GALBIATI, J. CASTELLS-GIL, N. ALMORA-BARRIOS, J. NAVARRO-SÁNCHEZ, G. ESCORCIA-ARIZA, M. MATTERA, T. ARNOLD, J. RAWLE, S. TATAY, E. CORONADO, and C. MARTÍ-GASTALDO. Bottom-Up Fabrication of Semiconductive Metal–Organic Framework Ultrathin Films. *Advanced Materials*, 30 (10), 1704291, **2018**.
- [265] K.-W. KIM, S. H. JI, B. S. PARK, and J. S. YUN. High surface area flexible zeolite fibers based on a core-shell structure by a polymer surface wet etching process. *Materials & Design*, 158, 98–105, **2018**.
- [266] P. CUBILLAS, M. W. ANDERSON, and M. P. ATTFIELD. Crystal Growth Mechanisms and Morphological Control of the Prototypical Metal–Organic Framework MOF-5 Revealed by Atomic Force Microscopy. *Chemistry—A European Journal*, 18 (48), 15406–15415, **2012**.
- [267] B. M. WECKHUYSEN, Z. ÖZTÜRK, R. P. BRAND, J. M. BOEREBOOM, and F. MEIRER. Vibrational Fingerprinting of Defects Sites in Thin Films of Zeolitic Imidazolate Frameworks. *Chemistry—A European Journal*, 25 (34), 8070–8084, **2019**.
- [268] J. LI, H. WANG, X. YUAN, J. ZHANG, and J. W. CHEW. Metal–organic framework membranes for wastewater treatment and water regeneration. *Coordination Chemistry Reviews*, 404, 213116, **2020**.
- [269] U. SCHMIDT, S. HILD, W. IBACH, and O. HOLLRICHER. Characterization of Thin Polymer Films on the Nanometer Scale with Confocal Raman AFM. In *Macromolecular symposia*, vol. 230, pp. 133–143. Wiley Online Library, **2005**.
- [270] E. ENRÍQUEZ, M. A. DE LA RUBIA, A. DEL CAMPO, F. RUBIO-MARCOS, and J. F. FERNANDEZ. Characterization of Carbon Nanoparticles in Thin-Film Nanocomposites by Confocal Raman Microscopy. *The Journal of Physical Chemistry C*, 118 (19), 10488–10494, **2014**.

- [271] D. A. GÓMEZ-GUALDRÓN, P. Z. MOGHADAM, J. T. HUPP, O. K. FARHA, and R. Q. SNURR. Application of Consistency Criteria To Calculate BET Areas of Micro-And Mesoporous Metal–Organic Frameworks. *Journal of the American Chemical Society*, 138 (1), 215–224, **2016**.
- [272] K. S. SING. Reporting Physisorption Data for Gas/Solid Systems with Special Reference to the Determination of Surface Area and Porosity (Recommendations 1984). *Pure and applied chemistry*, 57 (4), 603–619, **1985**.
- [273] I. LANGMUIR. The adsorption of gases on plane surfaces of glass, mica and platinum. *Journal of the American Chemical society*, 40 (9), 1361–1403, **1918**.
- [274] J. ROUQUEROL, P. LLEWELLYN, and F. ROUQUEROL. Is the BET equation applicable to microporous adsorbents. *Stud. Surf. Sci. Catal*, 160 (07), 49–56, **2007**.
- [275] S. LOWELL, J. E. SHIELDS, M. A. THOMAS, and M. THOMMES. *Characterization of Porous Solids and Powders: Surface Area, Pore Size and Density*. Springer Science & Business Media, **2004**.
- [276] D. A. GÓMEZ-GUALDRÓN, T. C. WANG, P. GARCÍA-HOLLEY, R. M. SAWELEWA, E. ARGUETA, R. Q. SNURR, J. T. HUPP, T. YILDIRIM, and O. K. FARHA. Understanding volumetric and gravimetric hydrogen adsorption trade-off in metal–organic frameworks. *ACS applied materials & interfaces*, 9 (39), 33419–33428, **2017**.
- [277] K. MÜLLEN. Molecular defects in organic materials. *Nature Reviews Materials*, 1 (15013), 1–2, **2016**.
- [278] J. LIU and C. WÖLL. Surface-supported metal–organic framework thin films: fabrication methods, applications, and challenges. *Chemical Society Reviews*, 46 (19), 5730–5770, **2017**.
- [279] T. D. BENNETT and S. HORIKE. Liquid, glass and amorphous solid states of coordination polymers and metal–organic frameworks. *Nature Reviews Materials*, 3 (11), 431–440, **2018**.
- [280] T. D. BENNETT, A. L. GOODWIN, M. T. DOVE, D. A. KEEN, M. G. TUCKER, E. R. BARNEY, A. K. SOPER, E. G. BITHELL, J.-C. TAN, and A. K. CHEETHAM. Structure and Properties of an Amorphous Metal–Organic Framework. *Physical review letters*, 104 (11), 115503, **2010**.
- [281] M. KALAJ, K. C. BENTZ, S. AYALA JR, J. M. PALOMBA, K. S. BARCUS, Y. KATAYAMA, and S. M. COHEN. MOF-Polymer Hybrid Materials: From Simple Composites to Tailored Architectures. *Chemical Reviews*, 120 (16), 8267–8302, **2020**.
- [282] T. TIAN, Z. ZENG, D. VULPE, M. E. CASCO, G. DIVITINI, P. A. MIDGLEY, J. SILVESTRE-ALBERO, J.-C. TAN, P. Z. MOGHADAM, and D. FAIREN-JIMENEZ. A sol–gel monolithic metal–organic framework with enhanced methane uptake. *Nature materials*, 17 (2), 174–179, **2018**.
- [283] W. LING, G. LIEW, Y. LI, Y. HAO, H. PAN, H. WANG, B. NING, H. XU, and X. HUANG. Materials and Techniques for Implantable Nutrient Sensing Using Flexible Sensors Integrated with Metal–Organic Frameworks. *Advanced Materials*, 30 (23), 1800917, **2018**.
- [284] C. LIU, J. WANG, J. WAN, and C. YU. MOF-on-MOF hybrids: Synthesis and applications. *Coordination Chemistry Reviews*, 432, 213743, **2021**.
- [285] R. AMELOOT, F. VERMOORTELE, W. VANHOVE, M. B. J. ROEFFAERS, B. F. SELS, and D. E. DE VOS. Interfacial synthesis of hollow metal–organic framework capsules demonstrating selective permeability. *Nature chemistry*, 3 (5), 382–387, **2011**.
- [286] R. A. HEINTZ, H. ZHAO, X. OUYANG, G. GRANDINETTI, J. COWEN, and K. R. DUNBAR. New Insight into the Nature of Cu(TCNQ): Solution Routes to Two Distinct Polymorphs and Their Relationship to Crystalline Films That Display Bistable Switching Behavior. *Inorganic chemistry*, 38 (1), 144–156, **1999**.
- [287] K. XIAO, J. TAO, Z. PAN, A. A. PURETZKY, I. N. IVANOV, S. J. PENNYCOOK, and D. B. GEOHEGAN. Single-Crystal Organic Nanowires of Copper–Tetracyanoquinodimethane: Synthesis, Patterning, Characterization, and Device Applications. *Angewandte Chemie*, 119 (15), 2704–2708, **2007**.

References

- [288] L. HU, T. XIONG, R. LIU, Y. HU, Y. MAO, M.-S. BALOGUN, and Y. TONG. Co₃O₄ Cu-Based Conductive Metal–Organic Framework Core–Shell Nanowire Electrocatalysts Enable Efficient Low-Overall-Potential Water Splitting. *Chemistry–A European Journal*, 25 (26), 6575–6583, **2019**.
- [289] M. MAHAJAN, S. K. BHARGAVA, and A. P. O’MULLANE. Reusable surface confined semi-conducting metal-TCNQ and metal-TCNQF 4 catalysts for electron transfer reactions. *RSC advances*, 3 (13), 4440–4446, **2013**.
- [290] H. TOPSOE. Geometric factors in four point resistivity measurement. *Bulletin*, 472 (13), 63, **1968**.
- [291] F. M. SMITS. Measurement of Sheet Resistivities with the Four-Point Probe. *Bell System Technical Journal*, 37 (3), 711–718, **1958**.
- [292] R. A. WELLER. An algorithm for computing linear four-point probe thickness correction factors. *Review of scientific instruments*, 72 (9), 3580–3586, **2001**.
- [293] G. SKORUPSKII, B. A. TRUMP, T. W. KASEL, C. M. BROWN, C. H. HENDON, and M. DINČĂ. Efficient and tunable one-dimensional charge transport in layered lanthanide metal–organic frameworks. *Nature chemistry*, 12 (2), 131–136, **2020**.
- [294] G. LU, O. K. FARHA, W. ZHANG, F. HUO, and J. T. HUPP. Engineering ZIF-8 Thin Films for Hybrid MOF-Based Devices. *Advanced Materials*, 24 (29), 3970–3974, **2012**.
- [295] V. RUBIO-GIMÉNEZ, N. ALMORA-BARRIOS, G. ESCORCIA-ARIZA, M. GALBIATI, M. SESSOLO, S. TATAY, and C. MARTÍ-GASTALDO. Origin of the Chemiresistive Response of Ultrathin Films of Conductive Metal–Organic Frameworks. *Angewandte Chemie*, 130 (46), 15306–15310, **2018**.
- [296] M.-S. YAO, J.-W. XIU, Q.-Q. HUANG, W.-H. LI, W.-W. WU, A.-Q. WU, L.-A. CAO, W.-H. DENG, G.-E. WANG, and G. XU. Van der Waals Heterostructured MOF-on-MOF Thin Films: Cascading Functionality to Realize Advanced Chemiresistive Sensing. *Angewandte Chemie*, 131 (42), 15057–15061, **2019**.
- [297] E. STERN, A. VACIC, N. K. RAJAN, J. M. CRISCIONE, J. PARK, B. R. ILIC, D. J. MOONEY, M. A. REED, and T. M. FAHMY. Label-free biomarker detection from whole blood. *Nature nanotechnology*, 5 (2), 138–142, **2010**.
- [298] P. N. NIRMALRAJ, T. SCHNEIDER, and A. FELBECKER. Spatial organization of protein aggregates on red blood cells as physical biomarkers of Alzheimer’s disease pathology. *Science advances*, 7 (39), eabj2137, **2021**.
- [299] E. RYZHIKOVA, N. M. RALBOVSKY, V. SIKIRZHYTSKI, O. KAZAKOV, L. HALAMKOVA, J. QUINN, E. A. ZIMMERMAN, and I. K. LEDNEV. Raman spectroscopy and machine learning for biomedical applications: Alzheimer’s disease diagnosis based on the analysis of cerebrospinal fluid. *Spectrochimica Acta Part A: Molecular and Biomolecular Spectroscopy*, 248, 119188, **2021**.
- [300] H. Y. Y. NYEIN, M. BARIYA, B. TRAN, C. H. AHN, B. J. BROWN, W. JI, N. DAVIS, and A. JAVEY. A wearable patch for continuous analysis of thermoregulatory sweat at rest. *Nature communications*, 12 (1823), 1–13, **2021**.
- [301] Z. WANG, Z. HAO, X. WANG, C. HUANG, Q. LIN, X. ZHAO, and Y. PAN. A Flexible and Regenerative Aptameric Graphene–Nafion Biosensor for Cytokine Storm Biomarker Monitoring in Undiluted Biofluids toward Wearable Applications. *Advanced Functional Materials*, 31 (4), 2005958, **2021**.
- [302] A. VASILESCU, B. HRINCZENKO, G. M. SWAIN, and S. F. PETEU. Exhaled breath biomarker sensing. *Biosensors and Bioelectronics*, 182, 113193, **2021**.
- [303] W. TAN, L. SABET, Y. LI, T. YU, P. R. KLOKKEVOLD, D. T. WONG, and C.-M. HO. Optical protein sensor for detecting cancer markers in saliva. *Biosensors and Bioelectronics*, 24 (2), 266–271, **2008**.
- [304] V. MANI, T. BEDUK, W. KHUSHAIM, A. E. CEYLAN, S. TIMUR, O. S. WOLFBEIS, and K. N. SALAMA. Electrochemical sensors targeting salivary biomarkers: A comprehensive review. *TrAC Trends in Analytical Chemistry*, 135, 116164, **2021**.

- [305] A. PUSTA, M. TERTIS, C. CRISTEA, and S. MIREL. Wearable Sensors for the Detection of Biomarkers for Wound Infection. *Biosensors*, 12 (1), 1, **2021**.
- [306] E. GIANINO, C. MILLER, and J. GILMORE. Smart Wound Dressings for Diabetic Chronic Wounds. *Bioengineering*, 5 (3), 51, **2018**.
- [307] T. TERSE-THAKOOR, M. PUNJIYA, Z. MATHARU, B. LYU, M. AHMAD, G. E. GILES, R. OWYEUNG, F. ALAIMO, M. SHOJAEI BAGHINI, T. T. BRUNYÉ, and S. SONKUSALE. Thread-based multiplexed sensor patch for real-time sweat monitoring. *NPJ Flexible Electronics*, 4 (1), 1–10, **2020**.
- [308] P. ESCOBEDO, M. D. FERNÁNDEZ-RAMOS, N. LÓPEZ-RUIZ, O. MOYANO-RODRÍGUEZ, A. MARTÍNEZ-OLMOS, I. M. PÉREZ DE VARGAS-SANSALVADOR, M. A. CARVAJAL, L. F. CAPITÁN-VALVEY, and A. J. PALMA. Smart facemask for wireless CO₂ monitoring. *Nature Communications*, 13 (72), 1–12, **2022**.
- [309] X. LIU and P. B. LILLEHOJ. Embroidered electrochemical sensors on gauze for rapid quantification of wound biomarkers. *Biosensors and Bioelectronics*, 98, 189–194, **2017**.
- [310] W. YANG, W. HAN, H. GAO, L. ZHANG, S. WANG, L. XING, Y. ZHANG, and X. XUE. Self-powered implantable electronic-skin for in situ analysis of urea/uric-acid in body fluids and the potential applications in real-time kidney-disease diagnosis. *Nanoscale*, 10 (4), 2099–2107, **2018**.
- [311] Y. SHI, X. WEI, K. WANG, D. HE, Z. YUAN, J. XU, Z. WU, and Z. L. WANG. Integrated All-Fiber Electronic Skin toward Self-Powered Sensing Sports Systems. *ACS Applied Materials & Interfaces*, 13 (42), 50329–50337, **2021**.
- [312] H. B. LIM, D. MA, B. WANG, Z. KALBARCZYK, R. K. IYER, and K. L. WATKIN. A Soldier Health Monitoring System for Military Applications. In *2010 International Conference on Body Sensor Networks*, pp. 246–249. IEEE, **2010**.
- [313] Z. WANG, T. LIU, Y. YU, M. ASIF, N. XU, F. XIAO, and H. LIU. Coffee Ring-Inspired Approach toward Oriented Self-Assembly of Biomimetic Murray MOFs as Sweat Biosensor. *Small*, 14 (45), 1802670, **2018**.
- [314] Z. GUO, A. FLOREA, C. CRISTEA, F. BESSUEILLE, F. VOCANSON, F. GOUTALAND, A. ZHANG, R. SĂNDULESCU, F. LAGARDE, and N. JAFFREZIC-RENAULT. 1,3,5-Trinitrotoluene detection by a molecularly imprinted polymer sensor based on electropolymerization of a microporous-metal-organic framework. *Sensors and Actuators B: Chemical*, 207, 960–966, **2015**.
- [315] Ü. ANIK, S. TIMUR, and Z. DURSUN. Metal organic frameworks in electrochemical and optical sensing platforms: a review. *Microchimica Acta*, 186 (3), 1–15, **2019**.
- [316] J. SCHOELLER, F. ITEL, K. WUERTZ-KOZAK, G. FORTUNATO, and R. M. ROSSI. pH-Responsive Electrospun Nanofibers and Their Applications. *Polymer Reviews*, 62 (2), 351–399, **2022**.
- [317] Y. LI, Y. HU, T. CHEN, Y. CHEN, Y. LI, H. ZHOU, and D. YANG. Advanced detection and sensing strategies of *Pseudomonas aeruginosa* and quorum sensing biomarkers: A review. *Talanta*, p. 123210, **2022**.
- [318] S. BISWAS, Q. LAN, Y. XIE, X. SUN, and Y. WANG. Label-Free Electrochemical Immunosensor for Ultrasensitive Detection of Carbohydrate Antigen 125 Based on Antibody-Immobilized Biocompatible MOF-808/CNT. *ACS Applied Materials & Interfaces*, 13 (2), 3295–3302, **2021**.
- [319] M. SAMY, M. G. IBRAHIM, M. FUJII, K. E. DIAB, M. ELKADY, and M. G. ALALM. CNTs/MOF-808 painted plates for extended treatment of pharmaceutical and agrochemical wastewaters in a novel photocatalytic reactor. *Chemical Engineering Journal*, 406, 127152, **2021**.
- [320] B. HIMABINDU, N. L. DEVI, and B. R. KANTH. Microstructural parameters from X-ray peak profile analysis by Williamson-Hall models; A review. *Materials Today: Proceedings*, 47, 4891–4896, **2021**.
- [321] M. LÓPEZ-LÓPEZ, J. J. DELGADO, and C. GARCIA-RUIZ. Ammunition Identification by Means of the Organic Analysis of Gunshot Residues Using Raman Spectroscopy. *Analytical chemistry*, 84 (8), 3581–3585, **2012**.

References

- [322] J. N. DAMASK. *Polarization Optics in Telecommunications*, vol. 101. Springer Science & Business Media, **2004**.
- [323] F. PEDROTTI, L. PEDROTTI, W. BAUSCH, and H. SCHMIDT. *Optik für Ingenieure*. Springer, **2005**.
- [324] R. RIGLER, Ü. METS, J. WIDENGREN, and P. KASK. Fluorescence correlation spectroscopy with high count rate and low background: analysis of translational diffusion. *European Biophysics Journal*, 22 (3), 169–175, **1993**.
- [325] S. D. BRORSON. What is the Confocal Parameter? *IEEE journal of quantum electronics*, 24 (3), 512–515, **1988**.
- [326] P. CHEN, X. HE, M. PANG, X. DONG, S. ZHAO, and W. ZHANG. Iodine Capture Using Zr-Based Metal–Organic Frameworks (Zr-MOFs): Adsorption Performance and Mechanism. *ACS applied materials & interfaces*, 12 (18), 20429–20439, **2020**.
- [327] X. WU, J. CHEN, X. LI, Y. ZHAO, and S. M. ZUGHAIER. Culture-free diagnostics of *Pseudomonas aeruginosa* infection by silver nanorod array based SERS from clinical sputum samples. *Nanomedicine: Nanotechnology, Biology and Medicine*, 10 (8), 1863–1870, **2014**.
- [328] S. YANG, B. LI, M. N. SLIPCHENKO, A. AKKUS, N. G. SINGER, Y. N. YENI, and O. AKKUS. Laser wavelength dependence of background fluorescence in Raman spectroscopic analysis of synovial fluid from symptomatic joints. *Journal of Raman spectroscopy*, 44 (8), 1089–1095, **2013**.
- [329] E. PLESSERS, G. FU, C. Y. X. TAN, D. E. DE VOS, and M. B. J. ROEFFAERS. Zr-Bbased MOF-808 as Meerwein–Ponndorf–Verley Reduction Catalyst for Challenging Carbonyl Compounds. *Catalysts*, 6 (7), 104, **2016**.
- [330] M. W. LOGAN, S. LANGEVIN, and Z. XIA. Reversible Atmospheric Water Harvesting Using Metal–Organic Frameworks. *Scientific reports*, 10 (1492), 1–11, **2020**.
- [331] O. SYNHAIVSKA, S. BHATTACHARYA, S. CAMPIONI, D. THOMPSON, and P. N. NIRMALRAJ. Single-Particle Resolution of Copper-Associated Annular α -Synuclein Oligomers Reveals Potential Therapeutic Targets of Neurodegeneration. *ACS chemical neuroscience*, 13 (9), 1410–1421, **2022**.
- [332] M. PARASKEVAIDI, C. L. MORAIS, K. M. LIMA, J. S. SNOWDEN, J. A. SAXON, A. M. RICHARDSON, M. JONES, D. M. MANN, D. ALLSOP, P. L. MARTIN-HIRSCH, and F. L. MARTIN. Differential diagnosis of Alzheimer’s disease using spectrochemical analysis of blood. *Proceedings of the National Academy of Sciences*, 114 (38), E7929–E7938, **2017**.
- [333] A. ASSOCIATION. 2020 Alzheimer’s disease facts and figures. *Alzheimers Dementia*, 16 (3), 391–460, **2020**.
- [334] J. A. HARDY and G. A. HIGGINS. Alzheimer’s Disease: The Amyloid Cascade Hypothesis. *Science*, 256 (5054), 184–185, **1992**.
- [335] P. N. NIRMALRAJ, J. LIST, S. BATTACHARYA, G. HOWE, L. XU, D. THOMPSON, and M. MAYER. Complete aggregation pathway of amyloid β (1-40) and (1-42) resolved on an atomically clean interface. *Science advances*, 6 (15), eaaz6014, **2020**.
- [336] A. NABERS, J. OLLESCH, J. SCHARTNER, C. KÖTTING, J. GENIUS, H. HAFERMANN, H. KLAFKI, K. GERWERT, and J. WILTFANG. Amyloid- β -Secondary Structure Distribution in Cerebrospinal Fluid and Blood Measured by an Immuno-Infrared-Sensor: A Biomarker Candidate for Alzheimer’s Disease. *Analytical chemistry*, 88 (5), 2755–2762, **2016**.
- [337] I. GRUNDKE-IQBAL, K. IQBAL, Y.-C. TUNG, M. QUINLAN, H. M. WISNIEWSKI, and L. I. BINDER. Abnormal phosphorylation of the microtubule-associated protein τ (tau) in Alzheimer cytoskeletal pathology. *Proceedings of the National Academy of Sciences*, 83 (13), 4913–4917, **1986**.
- [338] K. BLENNOW, H. HAMPEL, M. WEINER, and H. ZETTERBERG. Cerebrospinal fluid and plasma biomarkers in Alzheimer disease. *Nature Reviews Neurology*, 6 (3), 131–144, **2010**.

- [339] H. BRAAK and E. BRAAK. Frequency of Stages of Alzheimer-Related Lesions in Different Age Categories. *Neurobiology of aging*, 18 (4), 351–357, **1997**.
- [340] C. R. JACK JR, D. A. BENNETT, K. BLENNOW, M. C. CARRILLO, B. DUNN, S. B. HAEBERLEIN, D. M. HOLTZMAN, W. JAGUST, F. JESSEN, J. KARLAWISH, E. LIU, J. L. MOLINUEVO, T. MONTINE, C. PHELPS, K. P. RANKIN, C. C. ROWE, P. SCHELTENS, E. SIEMERS, H. M. SNYDER, and R. SPERLING. NIA-AA Research Framework: Toward a biological definition of Alzheimer’s disease. *Alzheimer’s & Dementia*, 14 (4), 535–562, **2018**.
- [341] O. HANSSON, S. LEHMANN, M. OTTO, H. ZETTERBERG, and P. LEWCZUK. Advantages and disadvantages of the use of the CSF Amyloid β ($a\beta$) 42/40 ratio in the diagnosis of Alzheimer’s disease. *Alzheimer’s research & therapy*, 11 (34), 1–15, **2019**.
- [342] L. YIN, Y. WANG, R. TAN, H. LI, and Y. TU. Determination of β -amyloid oligomer using electrochemiluminescent aptasensor with signal enhancement by AuNP/MOF nanocomposite. *Microchimica Acta*, 188 (2), 1–8, **2021**.
- [343] C. WANG, N. ZHANG, Y. LI, L. YANG, D. WEI, T. YAN, H. JU, B. DU, and Q. WEI. Cobalt-based metal–organic frameworks as co-reaction accelerator for enhancing electrochemiluminescence behavior of N-(aminobutyl)-N-(ethylisoluminol) and ultrasensitive immunosensing of amyloid- β protein. *Sensors and Actuators B: Chemical*, 291, 319–328, **2019**.
- [344] Z. L. MENSINGER, B. L. COOK, and E. L. WILSON. Adsorption of Amyloid Beta Peptide by Metal–Organic Frameworks. *ACS omega*, 5 (51), 32969–32974, **2020**.
- [345] K. BLENNOW and H. HAMPEL. CSF markers for incipient Alzheimer’s disease. *The Lancet Neurology*, 2 (10), 605–613, **2003**.
- [346] A. OLSSON, H. VANDERSTICHELE, N. ANDREASEN, G. DE MEYER, A. WALLIN, B. HOLMBERG, L. ROSENGREN, E. VANMECHELEN, and K. BLENNOW. Simultaneous Measurement of β -Amyloid_(1–42), Total Tau, and Phosphorylated Tau (Thr¹⁸¹) in Cerebrospinal Fluid by the xMAP Technology. *Clinical chemistry*, 51 (2), 336–345, **2005**.
- [347] G. DEVITT, K. HOWARD, A. MUDHER, and S. MAHAJAN. Raman Spectroscopy: An Emerging Tool in Neurodegenerative Disease Research and Diagnosis. *ACS chemical neuroscience*, 9 (3), 404–420, **2018**.
- [348] F. S. RUGGERI, G. LONGO, S. FAGGIANO, E. LIPIEC, A. PASTORE, and G. DIETLER. Infrared nanospectroscopy characterization of oligomeric and fibrillar aggregates during amyloid formation. *Nature communications*, 6 (7831), 1–9, **2015**.
- [349] M. PITSCHKE, R. PRIOR, M. HAUPT, and D. RIESNER. Detection of single amyloid β -protein aggregates in the cerebrospinal fluid of Alzheimer’s patients by fluorescence correlation spectroscopy. *Nature medicine*, 4 (7), 832–834, **1998**.
- [350] A. NABERS, J. OLLESCH, J. SCHARTNER, C. KÖTTING, J. GENIUS, U. HAUSSMANN, H. KLAFKI, J. WILTFANG, and K. GERWERT. An infrared sensor analysing label-free the secondary structure of the A β peptide in presence of complex fluids. *Journal of biophotonics*, 9 (3), 224–234, **2016**.
- [351] C. C. DE LASSICHÈRE, T. D. MAI, and M. TAVERNA. Antibody-free detection of amyloid beta peptides biomarkers in cerebrospinal fluid using capillary isotachopheresis coupled with mass spectrometry. *Journal of Chromatography A*, 1601, 350–356, **2019**.
- [352] M. SUNDE, L. C. SERPELL, M. BARTLAM, P. E. FRASER, M. B. PEPYS, and C. C. F. BLAKE. Common Core Structure of Amyloid Fibrils by Synchrotron X-ray Diffraction. *Journal of molecular biology*, 273 (3), 729–739, **1997**.
- [353] I. USOV and R. MEZZENGA. Fiberapp: An Open-Source Software for Tracking and Analyzing Polymers, Filaments, Biomacromolecules, and Fibrous Objects. *Macromolecules*, 48 (5), 1269–1280, **2015**.

References

- [354] Z. HUANG, A. MCWILLIAMS, H. LUI, D. I. MCLEAN, S. LAM, and H. ZENG. Near-infrared Raman spectroscopy for optical diagnosis of lung cancer. *International journal of cancer*, 107 (6), 1047–1052, **2003**.
- [355] W.-T. CHENG, M.-T. LIU, H.-N. LIU, and S.-Y. LIN. Micro-Raman Spectroscopy Used to Identify and Grade Human Skin Pilomatrixoma. *Microscopy research and technique*, 68 (2), 75–79, **2005**.
- [356] J. W. CHAN, D. S. TAYLOR, T. ZWERDLING, S. M. LANE, K. IHARA, and T. HUSER. Micro-Raman Spectroscopy Detects Individual Neoplastic and Normal Hematopoietic Cells. *Biophysical journal*, 90 (2), 648–656, **2006**.
- [357] D. NAUMANN. Infrared and NIR Raman Spectroscopy in Medical Microbiology. In *Infrared spectroscopy: new tool in medicine*, vol. 3257, pp. 245–257. SPIE, **1998**.
- [358] I. NOTINGHER, C. GREEN, C. DYER, E. PERKINS, N. HOPKINS, C. LINDSAY, and L. L. HENCH. Discrimination between ricin and sulphur mustard toxicity in vitro using Raman spectroscopy. *Journal of the Royal Society Interface*, 1 (1), 79–90, **2004**.
- [359] Z. MOVASAGHI, S. REHMAN, and I. U. REHMAN. Raman Spectroscopy of Biological Tissues. *Applied Spectroscopy Reviews*, 42 (5), 493–541, **2007**.
- [360] G. ZHU, X. ZHU, Q. FAN, and X. WAN. Raman spectra of amino acids and their aqueous solutions. *Spectrochimica Acta Part A: Molecular and Biomolecular Spectroscopy*, 78 (3), 1187–1195, **2011**.
- [361] F. M. TORTI and S. V. TORTI. Regulation of ferritin genes and protein. *Blood*, 99 (10), 3505–3516, **2002**.
- [362] E. C. THEIL. Ferritin: The Protein Nanocage and Iron Biomineral in Health and in Disease. *Inorganic chemistry*, 52 (21), 12223–12233, **2013**.
- [363] E. Ó. FAOLÁIN, M. B. HUNTER, J. M. BYRNE, P. KELEHAN, M. MCNAMARA, H. J. BYRNE, and F. M. LYNG. A study examining the effects of tissue processing on human tissue sections using vibrational spectroscopy. *Vibrational Spectroscopy*, 38 (1-2), 121–127, **2005**.
- [364] Y. ZHANG, H. ZHU, Z. YING, X. GAO, W. CHEN, Y. ZHAN, L. FENG, C. C. LIU, and Y. DAI. Design and Application of Metal–Organic Framework ZIF-90-ZnO-MoS₂ Nanohybrid for an Integrated Electrochemical Liquid Biopsy. *Nano Letters*, 22 (16), 6833–6840, **2022**.
- [365] L. M. SHAW, J. ARIAS, K. BLENNOW, D. GALASKO, J. L. MOLINUEVO, S. SALLOWAY, S. SCHINDLER, M. C. CARRILLO, J. A. HENDRIX, A. ROSS, J. ILLES, C. RAMUS, and S. FIFER. Appropriate use criteria for lumbar puncture and cerebrospinal fluid testing in the diagnosis of Alzheimer’s disease. *Alzheimer’s & Dementia*, 14 (11), 1505–1521, **2018**.
- [366] J. C. LEE, S. J. KIM, S. HONG, and Y. KIM. Diagnosis of Alzheimer’s disease utilizing amyloid and tau as fluid biomarkers. *Experimental & molecular medicine*, 51 (5), 1–10, **2019**.
- [367] J. S. PEDERSEN, C. B. ANDERSEN, and D. E. OTZEN. Amyloid structure – one but not the same: the many levels of fibrillar polymorphism. *The FEBS journal*, 277 (22), 4591–4601, **2010**.
- [368] S. CAMPIONI, B. MANNINI, M. ZAMPAGNI, A. PENSALFINI, C. PARRINI, E. EVANGELISTI, A. RELINI, M. STEFANI, C. M. DOBSON, C. CECCHI, and F. CHITI. A causative link between the structure of aberrant protein oligomers and their toxicity. *Nature chemical biology*, 6 (2), 140–147, **2010**.
- [369] H.-J. MÖLLER and M. B. GRAEBER. The case described by Alois Alzheimer in 1911. *European archives of psychiatry and clinical neuroscience*, 248 (3), 111–122, **1998**.
- [370] A. MANDAVILLI. The amyloid code. *Nature Medicine*, 12 (7), 747–752, **2006**.
- [371] P. N. NIRMALRAJ, A. T. BELLEW, A. P. BELL, J. A. FAIRFIELD, E. K. MCCARTHY, C. O’KELLY, L. F. C. PEREIRA, S. SOREL, D. MOROSAN, J. N. COLEMAN, M. S. FERREIRA, and J. J. BOLAND. Manipulating Connectivity and Electrical Conductivity in Metallic Nanowire Networks. *Nano letters*, 12 (11), 5966–5971, **2012**.

-
- [372] L. CHANG, K. Y. WANG, S. T. C. WANG, and Y. P. CHANG. The Investigation of Active VC and EBAC Analysis Utilization on Test Structure. In *2015 IEEE 22nd International Symposium on the Physical and Failure Analysis of Integrated Circuits*, pp. 205–208. IEEE, **2015**.
- [373] H. HWANG, Y. KIM, J.-H. PARK, and U. JEONG. 2D Percolation Design with Conductive Microparticles for Low-Strain Detection in a Stretchable Sensor. *Advanced Functional Materials*, 30 (13), 1908514, **2020**.
- [374] J. LIAO, S. BLOK, S. J. VAN DER MOLEN, S. DIEFENBACH, A. W. HOLLEITNER, C. SCHÖNENBERGER, A. VLADYKA, and M. CALAME. Ordered nanoparticle arrays interconnected by molecular linkers: electronic and optoelectronic properties. *Chemical Society Reviews*, 44 (4), 999–1014, **2015**.
- [375] J. BAEK, B. RUNGTAWEEVORANIT, X. PEI, M. PARK, S. C. FAKRA, Y.-S. LIU, R. MATHEU, S. A. ALSHMIMRI, S. ALSHEHRI, C. A. TRICKETT, G. A. SOMORJAI, and O. M. YAGHI. Bioinspired Metal–Organic Framework Catalysts for Selective Methane Oxidation to Methanol. *Journal of the American Chemical Society*, 140 (51), 18208–18216, **2018**.
- [376] A. TRICOLI and G. NERI. Miniaturized Bio-and Chemical-Sensors for Point-of-Care Monitoring of Chronic Kidney Diseases. *Sensors*, 18 (4), 942, **2018**.
- [377] L. B. BAKER, M. D. ENGEL, and A. S. WOLFE. Sweat Biomarkers for Sports Science Applications. *Sports Science Exchange*, 35 (226), 1–9, **2022**.
- [378] I. OLAETXEA, A. VALERO, E. LOPEZ, H. LAFUENTE, A. IZETA, I. JAUNARENA, and A. SEIFERT. Machine Learning-Assisted Raman Spectroscopy for pH and Lactate Sensing in Body Fluids. *Analytical Chemistry*, 92 (20), 13888–13895, **2020**.
- [379] W. LEE, A. T. M. LENFERINK, C. OTTO, and H. L. OFFERHAUS. Classifying Raman spectra of extracellular vesicles based on convolutional neural networks for prostate cancer detection. *Journal of raman spectroscopy*, 51 (2), 293–300, **2020**.
- [380] X. MAO, Y. MA, A. ZHANG, L. ZHANG, L. ZENG, and G. LIU. Disposable Nucleic Acid Biosensors Based on Gold Nanoparticle Probes and Lateral Flow Strip. *Analytical chemistry*, 81 (4), 1660–1668, **2009**.
- [381] C.-H. T. YEW, P. AZARI, J. R. CHOI, F. LI, and B. PINGGUAN-MURPHY. Electrospin-coating of nitrocellulose membrane enhances sensitivity in nucleic acid-based lateral flow assay. *Analytica chimica acta*, 1009, 81–88, **2018**.

Fabrication recipes

A.1 Synthesis of Cu-HHTP-TCNQ films

Table 3: Purchased materials for Cu-HHTP-TCNQ film synthesis

| Material | CAS number | Company |
|--|-------------|-----------------------|
| copper nitrate $\text{Cu}(\text{NO}_3)_2 \cdot x\text{H}_2\text{O}$ | 13778-31-9 | Merck (Sigma Aldrich) |
| TCNQ 7,7,8,8-Tetracyanoquinodimethane | 1518-16-7 | Merck (Sigma Aldrich) |
| HHTP, 98% Triphenylene-2,3,6,7,10,11-hexaol | 865836-87-9 | abcr swiss AG |
| ethyl acetate | 141-78-6 | Merck (Sigma Aldrich) |

For the synthesis, all solvents were degassed with argon before using. The MOF thin films were synthesized in small glass vials ($V=15$ ml, $ND=22$) sealed and filled with argon and placed in an ice bath in order to keep reaction temperature at $T=0$ °C. The following synthesis steps are as follows:

1. add 2 ml of aqueous Cu(II) nitrate solution (10 mM)
2. add 1 ml of HHTP dissolved in ethyl acetate (0.4 mM)
 - ▷ water-organic solvent interface is formed
3. add 1 ml of TCNQ dissolved in ethyl acetate (4 mM)
 - ▷ MOF film formation starts at the interface and is visible with naked eye

For transfer of the MOF film, a substrate of choice was placed at the bottom of the vial before the reaction started. The used substrates were treated with air plasma for 5 min in order to remove any resist residues and to improve wetting properties. The synthesis reaction was stopped after the desired time by carefully removing all the liquid with a syringe and thus sinking the thin film down onto the substrate. After drying the film at air, the deposited film was washed in acetone and isopropyl alcohol, followed by second drying at air.

A.2 Fabrication of glass chips with gold electrodes

For patterning the electrodes of the chip, a mask for UV lithography was fabricated by direct laser writing (DWL). The process steps for patterning a fused silica wafer (4 inch, 500 μm thickness, MicroChemicals GmbH) are listed below:

1. spin-coating with AZ2020nlof resist at 4000 rpm for 40 s
2. soft baking for 1 min at 110 °C
3. exposure of pattern at a dose of 60 mJ cm^{-2}
4. post exposure bake for 1 min at 110 °C
5. development in AZ726mif for 30 s
6. evaporation of 5 nm titanium
7. evaporation of 50 nm gold
8. resist removal (lift-off) in dimethylsulfoxide (DMSO) for 1 h at 110 °C
9. deposition of insulating passivation Al_2O_3 layer (50 nm) using plasma-enhanced atomic layer deposition (ALD)

To form the final MOF contacts and probe pad openings, the following steps were carried out:

1. spin-coating with AZ1505 resist at 4000 rpm for 40 s
2. soft baking for 1 min at 110 °C
3. exposure of patterns for contact and probe pads at a dose of 20 mJ cm^{-2}
4. development of in AZ400k:H₂O (1:4) for 20 s
5. pattern transfer into the oxide by means of wet chemical etching in phosphoric acid (85%) at 55 °C for 105 s
6. spin-coating of wafer dicing protection layer with AZ1505 resist at 1500 rpm for 40 s
7. soft baking for 1 min at 110 °C

A.3 Electrospaying of MOF particles

For the electrospaying process, a suspension of MOF-808 particles in isopropyl alcohol (IPA) was prepared. The MOF-808 powder was ordered and specially synthesized by novoMOF AG company (Untere Brühlstrasse 4, 4800 Zofingen, Switzerland).

To realize a 12 wt% particle suspension, 0.2127 g of MOF-808 powder was suspended in 2 ml IPA ($\text{wt}\% = \frac{m_{\text{MOF}}}{m_{\text{MOF}} + m_{\text{IPA}}}$). The suspension was treated by ultrasonication for at least 30 min and gave a milky liquid with well-dispersed MOF particles. A 2 ml syringe with a 18G blunt needle was filled with the suspension directly after ultrasonication, which was then fixed in a syringe pump. A metal plate was used as the collector, which was placed at a distance of 15 cm from the needle opening. In order to spray on a particular substrate of choice, it was attached to the collector (here: alumina foil or nitrocellulose membrane). Electrospaying of MOF-808 particles was then initiated by applying a high voltage of 20 kV between the needle and the metal plate and the syringe pump flow rate was set to $120 \mu\text{l}/\text{min}^{-1}$ (environment temperature between 21°C to 22°C , relative humidity between 40% to 42%).

A.4 Electrospinning of nitrocellulose

A solution of nitrocellulose (NC) was prepared for the electrospinning process. NC membrane was purchased by Merck (Sigma Aldrich; article number GE106000112, AmershamTM Protran[®] Western-Blotting Nitrocellulose Membrane) and dissolved in acetone/DMSO.

To realize a 12 wt% NC solution, 0.365 g NC was dissolved in a mixture of 2 ml acetone and 1 ml DMSO ($\text{wt}\% = \frac{m_{\text{NC}}}{m_{\text{NC}} + m_{\text{solvent}}}$). The solution was stirred for about 1 h and gave a clear, slightly yellowish NC solution. A 2 ml syringe with a 18G blunt needle was filled with the solution, which was then fixed in a syringe pump. A metal plate was used as the collector, which was placed at a distance of 15 cm from the needle opening. In order to spin on a particular substrate of choice, it was attached to the collector (here: nitrocellulose membrane, potentially with dispersed MOF particles). Electrospinning of NC fibers was then initiated by applying a high voltage of 21 kV between the needle and the metal plate and the syringe pump flow rate was set to $10 \mu\text{l}/\text{min}^{-1}$ (environment temperature between 21°C to 22°C , relative humidity between 40% to 42%).

Curriculum Vitae

Lars Lüder, born 06.03.1993 in Heidenheim an der Brenz, Germany

Education

- 2018 – 2022 **PhD in Nanowissenschaften**
University of Basel, Switzerland
Thesis: Biochemical Sensing based on Metal–Organic Architectures
Prof. Michel Calame
- 2015 – 2018 **Master in Nanoscience (1.0)**
Eberhard-Karls-University Tübingen, Germany
Thesis: Coupling effects in hybrid systems made of plasmonic
gold nanocones and quantum dots as single photon source
Prof. Monika Fleischer
- 2012 – 2015 **Bachelor in Nanoscience (1.0)**
Eberhard-Karls-University Tübingen, Germany
Thesis: Application of plasmonic nanostructures onto flexible
PDMS substrates
Prof. Monika Fleischer
- 2003 – 2012 **High School, Abitur (1.0)**
Hellenstein-Gymnasium, Heidenheim an der Brenz, Germany

Additional Research Activities

- 2020 – 2022 **TecDay speaker** - Schweizer. Akademie der Techn. Wissenschaften
Modul Biosensing
- 2018 **Research visit** - Hebrew University of Jerusalem, Israel
Racah Institute of Physics & The Department of Applied Physics
Prof. Ronen Rapaport
- 2016 – 2017 **Internship semester** - Karlsruhe Institute of Technology
Institute of Microstructure Technology
Prof. Manfred Kohl
- 2015 – 2016 **Research assistant** - Eberhard-Karls-University Tübingen
Institute for Applied Physics - Plasmonic nanostructures
Prof. Monika Fleischer
- 2014 – 2015 **Tutor** - Eberhard-Karls-University Tübingen
Physics Basic Course 1

List of Publications

- **Lars Lüder**, Agnes Gubicza, Michael Stiefel, Jan Overbeck, Davide Beretta, Amin Sadeghpour, Antonia Neels, Peter N. Nirmalraj, René M. Rossi, Claudio Toncelli, and Michel Calame. Conductive Hybrid Cu-HHTP-TCNQ Metal–Organic Frameworks for Chemiresistive Sensing. *Advanced Electronic Materials*, 8(3), p. 2100871, 2021
<https://doi.org/10.1002/aelm.202100871>
- **Lars Lüder**, Peter N. Nirmalraj, Antonia Neels, René M. Rossi, and Michel Calame. Multiscale MOF architecture with control of porosity for wearable sensing.
to be submitted
- Peter N. Nirmalraj, Thomas Schneider, **Lars Lüder**, Ansgar Felbecker. Ultralong amyloid fibrils swarm cerebrospinal fluid in Alzheimer’s disease.
to be submitted
- Hamza Abudayyeh, Annika Mildner, Dror Liran, Boaz Lubotzky, **Lars Lüder**, Monika Fleischer, and Ronen Rapaport. Overcoming the Rate-Directionality Trade-off: A Room-Temperature Ultrabright Quantum Light Source. *ACS Nano*, 15(11), p. 17384–17391, 2021
<https://doi.org/10.1021/acsnano.1c08591>

Poster contributions

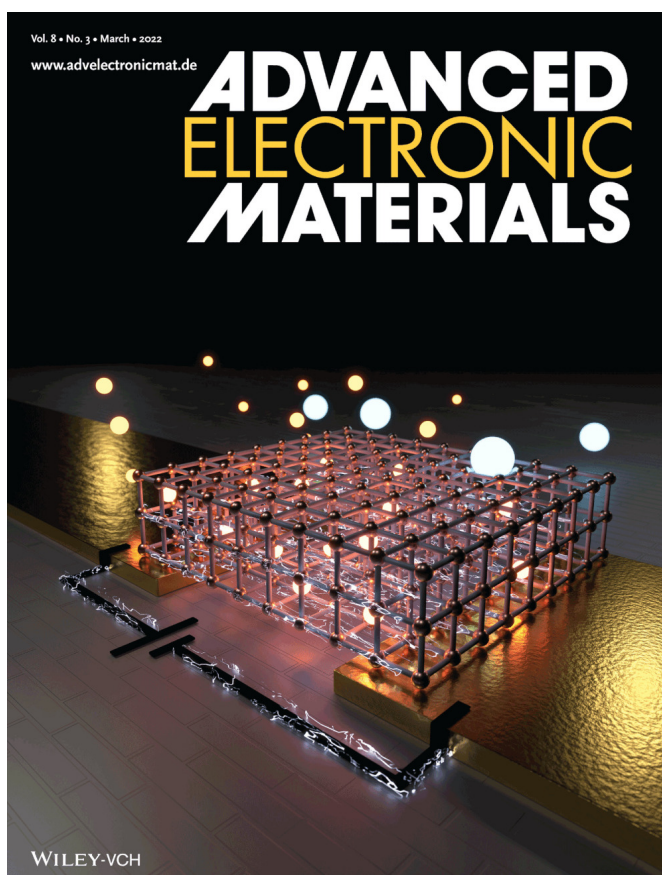
- NanoBio Tec, Montreux (Switzerland), October 2018, "*Synthesis of conductive metal–organic architectures for biochemical sensing*"
- EuroMOF 2019, Paris (France), October 2019, "*Synthesis of conductive metal–organic architectures for biochemical sensing*"
- SAOG 2020, Fribourg (Switzerland), January 2020, "*Conductive metal–organic architectures for biochemical sensing*"
- EuroMOF 2021, online (Krakow, Poland), September 2021, "*Synthesis and multiparametric analysis of conductive Cu-HHTP-TCNQ hybrid coordina-*

tion polymers"

- Swiss Sweat Science & Technology Symposium, Lausanne (Switzerland), June 2022, "*Multiscale MOF Architecture with Porosity Control for Wearable Sweat Sensing*"
- Swiss NanoConvention, Fribourg (Switzerland), July 2022, "*Multiscale MOF Architecture with Porosity Control for Wearable Sweat Sensing*"
→ **Best Poster Prize**

Journal Cover Images

- **Front cover:** Advanced Electronic Materials, volume 8, issue 3, March 2022



Front cover

Acknowledgements

Direct contributions

Ágnes Gubicza (A.G.), Michael Stiefel (M.S.), Jan Overbeck (J.O.), Davide Berretta (D.B.), Amin Sadeghpour (A.S.), Antonia Neels (A.N.), Thomas Schneider (T.S.), Ansgar Felbecker (A.F.), Peter N. Nirmalraj (P.N.N.), René M. Rossi (R.M.R.), Claudio Toncelli (C.T.), Michel Calame (M.C.)

During my time as a PhD student, I have met many nice people and helpful colleagues and I look back happily on the great experiences and friendships I made. Working here at Empa on the front lines of nanoscience research has taught me a lot of new things and I can truly say that I have grown along this journey. Certainly, this work would not have been possible without the support of many people in my environment, to whom I would like to express my gratitude.

First and foremost, I would like to thank *Prof. Michel Calame* for even giving me the opportunity to work on this exciting topic in his research group. Michel, I couldn't have asked for better supervision over the years and I am very grateful that you have always been there to help and advise me when needed. I was able to learn a lot from you and take it with me for my life and I thank you very much for your support and motivation at work, for the encouragement in my creative activities, in the work with the students, for the many beautiful moments I was able to experience here such as our group excursions and for your care.

Furthermore, I am very grateful to *Prof. Marcel Mayor* and *Prof. René Rossi* for the patience and time they invested in numerous meetings to provide me with valuable feedback and support for my work. A special thanks to René, who welcomed me very well in his group in St. Gallen, gave me support and a workspace there, but also made for nice moments at lab events or other occasions.

I would also like to thank *Prof. Wendy Queen*, who agreed to review my work and serve as my external expert.

A big thank you goes to *Dr. Peter Nirmalraj* for his support and care, for mentoring me over the years and for great advice not only on the job, but also beyond. Peter, thank you that I could always count on you and that you were at my side

when I needed you. With your positive attitude and friendly nature you gave me not only great motivation for the work, but also inspired me to do further things, such as the blender work. I will also keep our personal conversations in very good memory and I thank you for the great time in your group.

I am especially grateful for my colleagues in the Biosensing group, almost all of whom shared the office with me and with whom I was able to enjoy many wonderful and fun moments. The mindset of the group has always been positive and led to a joyful time at work, and I thank *Dr. Ágnes Gubicza* for her great supervision and training at the beginning of my PhD, *Dr. Yves Mermoud* for his friendship and strong collegiality as well as his valuable advice, *Dr. Olena Synhaiska* and *Talia Bergaglio* for the good teamwork, the deep conversations and help with experiments, and *Dr. Mathias Wipf* for the support when starting as PhD and especially for the TecDays contribution.

I would like to thank *Dr. Claudio Toncelli* for the good supervision in chemical synthesis at the beginning of my PhD, and also for his warm and friendly attitude that always motivated me.

I would also like to express my gratitude to *Prof. Antonia Neels* for her support with the X-ray experiments and their analyses.

Not only the people I worked directly with have made the working atmosphere very pleasant, but also the many great colleagues who were always cooperative and helpful and without whom the time here would certainly not have been so nice, which is why I would like to thank the entire team of the Transport at Nanoscale Interfaces Laboratory in Empa Dübendorf: *Daniel Aeppli*, *Dominik Bachmann*, *Dr. Davide Beretta*, *Dr. Oliver Braun*, *Dr. Rolf Brönnimann* (special thanks for various discussions and the support with electrical measurements), *Dr. Miklos Csontos*, *Fabien Dorey*, *Roman Furrer* (special thanks for Durak tutoring), *Jonas Gartmann*, *Dr. Matthias Grotevent*, *Dr. Erwin Hack*, *Marcel Held*, *Wenhao Huang*, *Nadia Jimenez-Olalla*, *Gökhan Kara* (special thanks for the motivating conversations and support), *Sebastian Kretschmer*, *André Kupferschmid*, *Dr. Fabio La Mattina*, *Sebastian Lohde*, *Dr. Eleni Mavrona* (special thanks for the nice coffee breaks), *Rico Muff*, *Jacopo Oswald*, *Dr. Jan Overbeck* (special thanks for the support with Raman measurements), *Dr. Tathagata Paul*, *Dr. Mickael Perrin* (special thanks for the Blender discussions), *Dr. Patrik Rohner*, *Philipp Scheidegger*, *Oliver Schmuck*, *Dr. Ivan Shorubalko* (special thanks for advice and nice discussions), *Michael Stiefel* (special thanks for the support in the lab and the cheerful conversations), *Dr. Lorenzo Valzania*, *Erfu Wu*, *Dr. Jian Zhang*, *Dr. Peter*

Zolliker and last but not least all apprentices.

I had the privilege to work not only at Empa Dübendorf, but also at Empa St. Gallen, which allowed me to have even more nice experiences and make friends there. Therefore, I would also like to thank my colleagues in St. Gallen and the people I had the chance to meet during my PhD, in particular the following people with whom I have worked and been in closer contact: *Jean Schoeller* (special thanks for tea and chess), *Dr. Konchang Wei* (special thanks for the support in the lab and the nice coffee meetings), *Dr. Fabian Itel*, *Dr. Salima Nedjari*, *Dr. Gordon Herwig*, *Dr. Nicola Migliore*, *Magda Plaga*, *Akin Gursej*, *Dr. Efe Armagan*, *Dr. Yifan Li*, *Dr. Fei Pan*, *Flora Bahrami*, *Urs Bünter*, *Urs Schütz*, *Lea Oberhänkli*, *Daniela Küttel* and *Annatonina Küttel*.

Also, I would like to give special thanks to the administrative staff for their years of support and assistance: *Ann-Christin Vetsch* (special thanks for the almonds), *Silvia Eppenberger*, *Natalie Aeschbach-Jones* and *Beatrix Spörri*.

Last but not least, I would like to thank my best friends and family from the bottom of my heart for all the unconditional support, no matter in which life situation: Pascal, thank you for accompanying me during my time in Switzerland and for always being able to inspire me for new things with your positive nature. Thank you Nils and Fabian for our eternal friendship and the many beautiful moments you shared with me. You have become a part of the family for me and I look forward to our next adventures together. Thanks Nils and Janin for your cheerful ways at home. I always keep our game evenings in good memory. Special thanks to you Ulf, for your support and advice in my work and life. I can always count on you and always enjoy our time together. And thank you Mom and Dad: Mom for your love and wisdom, for always having a sympathetic ear for me and much more, and Dad for always believing in me and giving me so much. Even though you unfortunately didn't live to see the end of my PhD, I know you were there for me, Dad. Danke, dass ihr alle immer für mich da gewesen seid!

"Jemand hat mir mal gesagt, die Zeit würde uns wie ein Raubtier ein Leben lang verfolgen. Ich möchte viel lieber glauben, dass die Zeit unser Gefährte ist, der uns auf unserer Reise begleitet und uns daran erinnert, jeden Moment zu genießen, denn er wird nicht wiederkommen. Was wir hinterlassen ist nicht so wichtig, wie die Art, wie wir gelebt haben. Denn letztlich [...] sind wir alle nur sterblich."

"Someone once told me that time was a predator that stalked us all our lives. But I rather believe that time is a companion who goes with us on the journey and reminds us to cherish every moment because they'll never come again. What we leave behind is not as important as how we lived. After all [...] we're only mortal."

Jean-Luc Picard